Université du Québec
Institut National de la Recherche Scientifique
Énergie, Matériaux et Télécommunications

INVESTIGATION OF POROUS NAFION/PTFE-BASED CATHODES FOR LOW TEMPERATURE DIRECT METHANOL FUEL CELLS

Par

Francesca Capitanio

Thèse présentée pour l'obtention du grade de
Philosophiae doctor (Ph.D.)
en sciences de l'énergie et des matériaux

Jury d'évaluation

Président du jury et examinateur interne	Professeur Mohamed Mohamedì INRS – EMT
Examinateur externe	Professeure Gessie Brisard Département de chimie Université de Sherbrooke
Examinateur externe	Professeure Elena Baranova Département de génie chimique et biologique Université d'Ottawa
Directeur de recherche	Professeure Ana Tavares INRS – EMT

“Hard times arouse an instinctive desire for authenticity.”

Coco Chanel

RÉSUMÉ

La réduction des émissions de CO_2 dans l'atmosphère et une meilleure utilisation des ressources naturelles sont les seules mesures visant à éviter un désastre environnemental. L'utilisation des combustibles fossiles doit laisser la place au développement des énergies alternatives telles que l'énergie éolienne, l'énergie solaire, l'énergie hydroélectrique et les piles à combustible. Parmi les piles à combustible, la Pile à Combustible au Méthanol (PCM) est la plus étudiée pour les applications portables. Néanmoins, la commercialisation de la PCM est aujourd'hui limitée par sa faible performance en raison de l'activité électrocatalytique réduite pour les Réactions de Réduction d'Oxygène (RRO) et d'Oxydation du Méthanol (ROM), la perméation du méthanol et son oxydation à la cathode, la faible pression partielle d'oxygène et l'accumulation d'eau à la cathode. La rétention d'eau à la cathode empêche le réactif d'atteindre les sites catalytiques, par conséquence les performances de la pile sont faibles. Donc, il est nécessaire d'évacuer plus d'eau de la cathode. Cette thèse vise donc à : a) minimiser l'accumulation d'eau à la cathode et b) développer une méthode de diagnostic pour prévoir le « flooding » de la PCM. Ces recherches utilisent deux stratégies :

a) la préparation des couches catalytiques de la cathode par déposition simultanée du Nafion et du PTFE; le Nafion est un ionomère couramment utilisé dans la préparation des couches catalytiques et il est responsable de l'accumulation d'eau dans la cathode. b) la caractérisation ex-situ des cathodes dans une solution d'acide sulfurique (« flooding » de la cathode).

La première partie du travail a été consacrée à la Spectroscopie d'Impédance Électrochimique (SIE), couramment utilisée pour la caractérisation des matériaux poreux. D'abord, on a identifié la procédure pour l'analyse des spectres enregistrés dans la solution d'acide sulfurique saturée en azote. À partir de ces spectres, la résistance à la conduction protonique dans la couche catalytique et la capacitance de la double couche ont été déterminées. Ensuite, la RRO a été étudiée et les spectres enregistrés dans la solution saturée en oxygène ont été simulés par un Circuit Électrique Équivalent (CEE) contenant la résistance au transfert de charge, la capacité de la double couche et l'élément de diffusion de Warburg. Cette approche a été particulièrement utile pour la détermination des paramètres cinétiques. Ensuite, les spectres complets des Assemblages-Membrane-Électrodes (AMEs) ont été enregistrés dans la pile au méthanol pour déterminer les

paramètres cinétiques de la cathode et de l'anode. Les spectres montraient deux demi-cercles déformés et se chevauchant. L'analyse des spectres enregistrés sous différentes conditions d'opération (potentiel de pile, concentration du méthanol, débit d'air, air/oxygène) a permit d'attribuer l'arc à basses fréquences à la cathode et l'arc à hautes fréquences à l'anode. Les spectres ont été modélisés par deux CEEs construits à partir des processus électrochimiques qui se produisent à la cathode et l'anode.

La deuxième partie du travail a été consacrée à la préparation de quatre couches catalytiques par déposition simultanée du Nafion et du PTFE, utilisée comme stratégie pour minimiser l'accumulation d'eau à la cathode. Les cathodes contenant Nafion/PTFE dans chaque rapport spécifique ont été caractérisées physico-chimiquement, électrochimiquement dans 0.5 M H_2SO_4 et dans la pile au méthanol. Les résultats ont montré que la présence du PTFE dans la couche catalytique est bénéfique pour prévenir l'accumulation d'eau dans la PCM travaillant à basse température, et spécifiquement la conduction protonique et l'apport d'oxygène sont garantis dans la cathode qui a une couche catalytique contenant 10 % massique de Nafion et 5 % massique de PTFE. Pour cette composition de Nafion / PTFE, la distribution du platine a été par la suite optimisée et concentrée plus en surface. L'utilisation du platine et la performance de la cathode dans la pile ont été améliorés (34% plus élevée à 0.1 V, 50 °C, 100% d'humidité relative à la cathode), mais la probabilité d'accumulation d'eau à la cathode a été aussi augmentée. Ce comportement peut s'expliquer par une macroporosité dominante de l'électrode.

La dernière partie du travail a été le développement d'une méthode de diagnostic pour prévenir le « flooding » de la PCM. La caractérisation des cathodes dans la solution d'acide sulfurique était proposée comme stratégie. Cette recherche s'est adressé à l'étude de la cathode contenant 15 % massique de PTFE (et pas de Nafion), qui avait montré une très faible résistance à la conduction protonique, un plus haute courant pour la RRO, mais de faibles performances dans la pile à combustible. À partir de cette cathode, trois cathodes ont été préparées par frittage de la cathode à 350 °C, déposition de la couche catalytique sur tissu de carbone traité avec du PTFE, couverture de la couche catalytique avec du Nafion (« Nafion coating »). Les résultats ont montré que les techniques de voltammetrie cyclique et de spectroscopie d'impédance électrochimique, utilisées pour étudier la RRO dans la solution d'acide sulfurique apportent une description qualitative de la performance de la cathode dans la pile à combustible. Par contre, les mesures d'absorption d'eau, et les mesures de résistance ionique et de capacitance de la double couche par

spectroscopie d’impédance électrochimique (solution saturée en azote) ne prédisent pas le comportement de la cathode dans la PCM.

Cette recherche s’est occupée aussi d’optimiser la pression d’assemblage membrane – électrodes. Il a été observé que la diminution de la pression d’assemblage de 500 à 375 livres pour centimètre quarré est favorable à une plus faible résistance de contact membrane – électrodes, une meilleure utilisation du platine et des performances plus élevées. Une réduction ultérieure de la pression d’assemblage n’est pas bénéfique à cause d'un mauvais contact entre la membrane et les électrodes.

ABSTRACT

The only way to avoid an environmental disaster is to reduce CO_2 emissions and improve the use of natural sources. The fossil fuel era should be ended with the development of alternative energies such as windpower, solar cells, geothermic, hydroelectric energy and fuel cells. Between the varieties of fuel cells, Direct Methanol Fuel Cells (DMFCs) are very interesting for portable applications. However, their commercialization is still limited by the low performance due to the low kinetics at the anode/cathode, the oxidation of crossover methanol to the cathode, the low oxygen partial pressure and the accumulation of water in the cathode. The flooding of the cathode prevents the reactant from reaching the catalyst' active sites, and then the fuel cell performance are drastically reduced. Therefore, it is necessary to improve the water removal during fuel cell operation. Based on these arguments, this thesis aims to a) minimize the water flooding in the DMFC Cathode Catalyst Layer (CCL) and b) develop a diagnostic method to anticipate the flooding in DMFC. To reach these objectives two strategies have been proposed :

a) the preparation of CCLs by partial substitution and simultaneous deposition of Nafion and PTFE binders; Nafion ionomer is commonly used in the preparation of CCLs and is responsible for the flooding of the cathodes.

b) the ex-situ electrochemical characterization in 0.5 M H_2SO_4 to simulate the severe flooding in DMFC.

The first part of the work was devoted to the use of Electrochemical Impedance Spectroscopy (EIS) as a characterization tool for measuring transport properties of porous materials. First, it was described the procedure for the analysis of the spectra acquired in nitrogen saturated sulphuric acid solution for the determination of the ionic resistance through the CCL and the double-layer capacitance. Then, the EIS was used to study the Oxygen Reduction Reaction (ORR). The spectra recorded in oxygen saturated H_2SO_4 were simulated using an Equivalent Electric Circuit (EEC) containing the charge-transfer resistance, the double-layer capacitance and the Warburg diffusion element. This approach was particular useful for the determination of the kinetic parameters. Then, the EIS was used for the direct analysis of total spectra recorded in fuel cell to determine the cathodic and anodic electrochemical parameters. The DMFC spectra showed two overlapped and distorted semicircles. By recording a series of EIS spectra under different conditions (cell potential, methanol concentration, air flow rate, air/oxygen feed) it was possible

to ascribe the low frequencies semicircle to the cathode and the high frequencies semicircle to the anode. The spectra were simulated using two EECs which take in consideration the electrochemical processes occurring at the anode and the cathode under different operative conditions.

The second part of the work concerned the investigation of four Nafion/PTFE-based cathodes to understand if the simultaneous deposition of the two binders in a specific ratio could improve the performance of the cathodes in terms of flooding. Physicochemical, ex-situ electrochemical and fuel cell techniques were used for the analysis. The results showed that the presence of PTFE in the CCL can be beneficial in preventing the early flooding of the low temperature DMFC. In particular, the proton conductivity in the CCL and the continuous supply of O_2 were ensured in the cathode with 10 wt% of Nafion and the 5 wt% of PTFE. This cathode was found suitable to work in a DMFC up to 50 °C without evidence of early flooding. For this specific Nafion / Teflon composition, the Pt distribution was optimized and concentrated more on the electrode surface. The DMFC characterization showed a higher catalyst utilization and better cathode performance (34% higher at 0.1 V, 50 °C, 100% of relative humidity at the cathode), but also higher probability of flooding. This behaviour could be attributed to a higher content of macro-pores which are known to behave as "water basins" and to promote flooding.

The third part of the work concerned the validation of the ex-situ electrochemical characterization in 0.5 M H_2SO_4 as a diagnostic tool to anticipate the flooding in DMFC. This research involved a further investigation of the PTFE-based cathode which showed the lowest ionic resistance to the proton conduction in the CCL, higher current for the ORR, but lower DMFC performance. Three cathodes were prepared through morphological variation of the PTFE-based cathode by sintering at 350 °C, deposition of the CCL on a TFE-treated carbon cloth support and Nafion coating. This study showed that the results obtained for the oxygen reduction reaction by cyclic voltammetry and electrochemical impedance spectroscopy in the oxygen saturated sulphuric acid solution are qualitatively consistent with the performance of the cathodes in DMFC. On the contrary, the results from the water uptake measurements, the values of ionic resistance and double-layer capacitance obtained by electrochemical impedance spectroscopy in the nitrogen saturated sulphuric acid solution (though correlated between them) are not useful to anticipate the behaviour of the cathodes in fuel cell.

This work was also addressed to the optimization of the pressure of the membrane - electrodes assembly. It was observed that a decrease of the assembly pressure from 500 lbs to 375 lbs is beneficial to decrease the serial resistance between the electrodes and the membrane, and to improve the catalyst utilization and the performance. Further reduction of the pressure assembly is not beneficial because of the worst contact electrodes-membrane.

SOMMAIRE RÉCAPITULATIF

Les émissions de gaz à effet de serre dans l'atmosphère sont la cause principale de l'augmentation rapide de la température de la planète. Réduire l'émission des gaz, et maintenir la température de la planète dans un « niveau de sécurité », est actuellement le plus grand défi environnemental. Le dioxyde de carbone (CO_2), principal produit de la combustion des produits pétroliers, est responsable de l'83 % de la totalité de gaz à effet de serre émis, comme le montre la Figure 1.1.

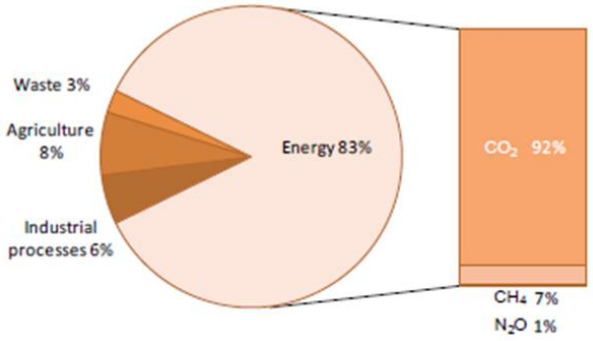

Figure 1.1 : Émission de gaz à effet de serre dans l'année 2009 (Chapitre 1 – Figure 1.1).

En réponse à cette problématique environnementale, il est impératif d'utiliser des énergies alternatives qui limitent la consommation des produits pétroliers et favorisent l'utilisation d'autres ressources naturelles et de préférence renovables. Les piles à combustible sont une des technologies envisages puisque elles utilisent de 'hydrogène et des biocarburants peuvent a la place des combustibles fossiles. Les piles à combustible couvrent une vaste gamme d'applications stationnaires, de transport et portable.

Parmi les piles à combustible, la Pile à Combustible au Méthanol (PCM) est la plus étudiée pour les applications portables car elles sont très compétitives par rapport à la batterie au lithium dans des dispositifs électroniques et de communication. Les avantages du méthanol comme combustible proviennent de sa grande densité énergétique (6 kW h kg^{-1}), de la simplicité associé à l'utilisation d'un combustible liquide et la possibilité de le produire par fermentation des produits agricoles. Les PMCs ont actuellement une faible puissance (30-100 mW cm^{-2}), mais sont capables de fournir cette puissance pour longtemps. Des simples calculs démontrent

qu'aujourd'hui un prototype de PMC pourrait alimenter un cellulaire pour quatre heures en utilisant seulement sept millilitres du méthanol.

Actuellement, la pile au méthanol est encore en état de développement car la faible performance de la pile et l'accumulation d'eau à la cathode limitent sa commercialisation. Dans la pile, l'eau est produite à la cathode par la réaction de réduction d'oxygène. En plus, l'eau est transportée de l'anode à la cathode par diffusion et électro-osmoses. À la cathode, l'eau est généralement éliminée par évaporation ou rétrodiffusion. Toutefois, si l'élimination n'est pas assez vite, l'eau s'accumule et limite drastiquement la performance de la pile. Pour conséquent, cette thèse s'est occupée de nouvelles couches catalytiques a fin de minimiser l'accumulation d'eau à la cathode. Plus précisément, les objectives de sont les suivants: a) étudier les propriétés de transport, texturales et activité électrocatalytique des électrodes préparées par déposition simultanée du Nafion et PTFE; b) développer une stratégie pour étudier l'accumulation de l'eau dans la cathode dans la PCM à basse température; et c) déterminer une méthode d'analyse des spectres d'impédance complets enregistrés dans la pile à combustible.

a) Étude de nouvelles couches catalytiques préparées par substitution partielle du Nafion par du PTFE.

Dans une pile combustible au méthanol, la couche catalytique de la cathode est une structure poreuse composé par des nanoparticules de platine supportées sur du carbone et par du Nafion. Comme montre la Figure 2, les particules de platine sont en contact avec le carbone qui fournit la conductivité électronique et avec le Nafion qui fournit la conduction ionique. Dans ces points triples a lieu la réaction de réduction d'oxygène.

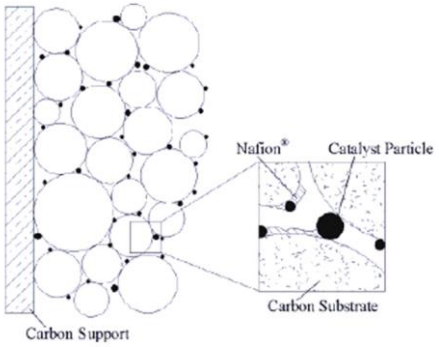

Figure 2: La couche catalytique de la cathode dans la pile au méthanol (Chapitre 1 – Figure 1.6).

Plusieurs études se sont attardées à l'optimisation de la composition de la couche catalytique en thermes de rapport Pt/C ou Pt/Nafion. Ces études ont montré que pour un contenu optimisé de Nafion, la résistance de la couche catalytique est plus faible et la performance de la pile est meilleure en termes de densité de puissance. Cependant, un contenu élevé de Nafion peut isoler les particules de platine, empêcher la diffusion du gaz vers les sites catalytiques et favoriser l'inondation de la cathode. En conséquence la performance de la pile décroit avec le temps.

La possibilité d'utiliser du PTFE dans la cathode a été aussi étudiée surtout pour les piles H_2/O_2. Des recherches conduites dans la pile à combustible à hydrogène ont montré que la présence du PTFE dans la couche de diffusion est bénéfique pour augmenter la pression hydraulique et favoriser un retour d'eau de la cathode vers l'anode. Une telle approche fournirait un moyen simple pour éliminer l'eau de la cathode sans utiliser des appareils auxiliaires. Dernièrement, deux études se sont attardées à l'utilisation du PTFE dans la couche catalytique pour réduire l'accumulation de l'eau dans cathode des PCM. Ces études ont montré qu'une couche catalytique plus hydrophobe est moins mouillée est moins empoisonnée par le méthanol. Toutefois, l'impact du PTFE sur la performance de la pile n'était pas bien défini, probablement parce que le contenu de PTFE, la composition de la couche catalytique et les méthodes de fabrication étaient différents dans les deux études.

Dans la présente étude, nous avons exploré la substitution partielle du Nafion par PTFE et la déposition simultanée des deux liants comme stratégie pour améliorer l'élimination de l'eau de la cathode, et pour garantir l'approvisionnement continu d'oxygène aux sites catalytiques. Néanmoins, nous avons établi également comme objectif de ne pas réduire la conductivité protonique dans la couche catalytique en remplaçant le Nafion par le PTFE. Dans la pratique, nous avons préparé des séries des cathodes à base de platine où I) le contenu massique de Nafion et PTFE été varié entre 0 et 15 % ; II) la distribution du platine dans une cathode avec du Nafion et PTFE a été modifiée ; III) la morphologie d'une cathode à base de PTFE a été modifiée par frittage à 350 °C, par couverture de la couche catalytique avec du Nafion ou par déposition de la couche catalytique sur un support traité avec du PTFE. Les cathodes ont été préparées par pulvérisation de la couche catalytique sur le tissu de carbone. La composition des cathodes est résumée dans la Tableau 1.

Tableau 1 : Description des cathodes étudiées (Chapitre 2 – Tableau 2.1).

	Pulvérisateur	*Nom*	*Contenu Pt/mgcm^{-2}*	*% massique Nafion*	*% massique PTFE*	*Support*
Séries I	TJR spray gun	N15/T00	2.94	15	0	Tissu de carbone
		N10/T05	2.82	10	5	Tissu de carbone
		N05/T10	2.86	5	10	Tissu de carbone
		N00/T15	2.87	0	15	Tissu de carbone
Séries II	airbrush	N10/T05-P	2.84	10	5	Tissu de carbone
Séries III	TJR spray gun	N00/T15-350	2.87	0	15	Tissu de carbone
		N00/T15-N05	2.87	5	15	Tissu de carbone
		N00/T15-TFE	3.3	0	15	Tissu de carbone traité avec PTFE

Comme cette recherche s'est occupé d'étudier l'accumulation d'eau à la cathode, aucune couche de diffusion n'a été utilisée dans la préparation des électrodes. Ce choix a été fait pour induire une accumulation excessive d'eau dans la cathode. En plus, la préparation des cathodes pour la pile au méthanol demande l'utilisation d'une grande quantité de catalyseur et donc les électrodes sont épais. Par conséquent, ce choix a visé à minimiser la résistance en série dans la pile.

Les cathodes ont subi des caractérisations physico-chimique, électrochimique (ex-situ) et dans la pile au méthanol (in-situ) comme décrit dans le tableau 2. Pour la caractérisation en pile, les cathodes ont été assemblées avec des membranes de Nafion 117 (DuPont) et des anodes commerciales (Electrochem.) contenant du catalyseur de Pt-Ru. Pour ce qui concerne la nomenclature, les Assemblages Membrane-Électrodes (AMEs) ont été identifié comme MEA-T où T est le nom de la cathode. Comme cette thèse contient également une étude sur l'effet de la pression d'assemblage, l'extension -500, -375 et -250 a été ajouté à MEA-T pour identifier la pression à laquelle l'AME a été pressée. La liste des AMEs étudiés dans cette thèse est montrée dans le Tableau 3.

Tableau 2: Techniques utilisées pour l'étude des cathodes et des assemblages membrane-électrodes (AMEs) (Chapitre 2 – Tableau 2.4).

	Technique	*Objectif*	*Paragraphe/Chapitre*
Cathodes ex-situ	MEB / EDS	Image de la surface et de la tranche Cartographie de la surface et de la tranche Analyse chimique quantitative	2.3.1.1
	RBS	Quantification du Pt and S dans les première 200 nm de la tranche	2.3.1.2
	DVS / Absorption d'eau – de hexane	Effet du contenu du Nafion/PTFE sur la hydrophilie/hydrophobie de la cathode	2.3.1.3 2.3.1.4
	Angle de contact	Mouillabilité de la surface de la cathode	2.3.1.5
	Adsorption d'azote	Volume total des micro-, méso- et macro-pores (jusqu'à 200 nm)	2.3.1.6
	Voltampérométrie Cyclique	Dans l'azote: surface électrochimique active, utilisation du Pt, fenêtre du potentiel de la double-couche Dans l'oxygène: performance pour la RRO, potentiel de demi-vague, courant limite.	2.3.2.2
	Chronoampérométrie	Formation d'une couche mince de l'électrolyte en contacte avec la cathode N 00 / T 15 / inondation de la cathode N 15 / T 00	2.3.2.3
	SI	Étude complète de la cathode dans la solution de l'acide sulfurique.	Chapitre 3
Cathodes Dans la PCM	SI (hautes fréquences)	Résistance de la pile	2.3.3.4
	Courbes E-j	Performance de la pile (PCO et densité de courant à 0.1 V)	2.3.3.5
	″O_2 gain″	Chute de potentiel à cause du transport de masse	2.3.3.6
	SI	Étude complète de la cathode dans la pile	Chapitre 3

Tableau 3: Liste des assemblages membrane-électrodes (AMEs) étudiés dans cette thèse (Chapitre 2 – Tableau 2.3).

AME	*Cathode*	*Type d'étude*	*Chapitre*
MEA - N15/T00	N15/T00	Effet du Nafion/PTFE	5
MEA - N10/T05	N10/T05	Effet du Nafion/PTFE	5
MEA - N05/T10	N05/T10	Effet Nafion/PTFE	5
MEA - N00/T15	N00/T15	Effet du Nafion/PTFE	5
MEA - N10/T05-P	N10/T05-P	Effet de la distribution du Pt	5
MEA - N00/T15 - 500	N00/T15	Effet de la pression d'assemblage	6
MEA - N00/T15 - 375	N00/T15	Effet de la pression d'assemblage	6
MEA - N00/T15 - 250	N00/T15	Effet de la pression d'assemblage	6
MEA -N00/T15-N05	N00/T15-N05	Effet de la morphologie de la cathode	6
MEA -N00/T15-TFE	N00/T15-TFE	Effet de la morphologie de la cathode	6
MEA – Pt/KB	Pt/KB-based	SI - Modélisation	3
MEA – Pt_3Co/KB	Pt_3Co/KB-based	SI - Modélisation	3
MEA – Pt/XC72	Commercial	SI - Modélisation	3

En plus des cathodes avec du Nafion/PTFE, le Tableau 3 contient également trois AMEs qui ont été préparées avec deux cathodes à base des catalyseurs Pt/KB et Pt3Co/KB (CNR-ITAE) et une cathode commerciale (Electrochem.). Ces AMEs ont été utilisés pour des études spécifiques de spectroscopie d'impédance électrochimique et qui sont décrits plus avant. Les détails sur la caractérisation in-situ des AMEs et les informations cherchées avec chacune technique sont également résumés dans le Tableau 2.

b) Développement d'une stratégie pour étudier l'accumulation de l'eau dans la cathode d'une PCM à basse température

Le problème d'accumulation d'eau dans la pile à combustible à hydrogène a été très étudié pendant les deux dernières décennies. Plusieurs méthodes expérimentales basées sur la spectroscopie d'impédance, la variation des paramètres expérimentaux (la température de la pile, le niveau d'humidité à l'anode et à la cathode), l'observation des chutes de tension ou de pression dans la pile ont été proposées comme des outils de diagnostic. Comme montre la Figure 3, l'inondation de la cathode par l'eau dans une pile H_2 / O_2 se produit en deux étapes. Durant la

première étape, l'eau s'accumule dans la couche de diffusion tandis que la tension de la pile diminue lentement. Pendant la deuxième étape, l'eau bloque la serpentine. Ceci conduit à une augmentation de la pression locale qui évacue rapidement l'eau en excès et restaure la densité de courant. Cependant, une fois l'eau accumulée ne peut être évacuée de manière efficace, l'accumulation d'eau amène à une augmentation de la résistance à la diffusion du réactif et induit une chute de tension.

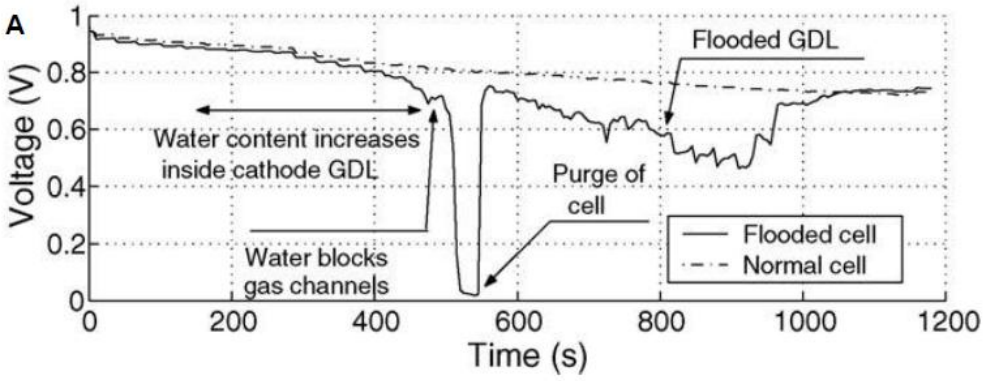

Figure 3: Accumulation d'eau dans une pile à hydrogène / oxygène (Chapitre 1 – Figure 1.7).

Différentes méthodes comme la visualisation directe, la résonance magnétique nucléaire (RMN) et la microscopie à fluorescence ont été utilisés pour observer l'accumulation d'eau dans la pile en état de travail. Cependant, ces méthodes ont donné seulement des informations qualitatives. Autres méthodes requièrent l'emploi de deux électrodes externes pour détecter l'inondation de la pile. Encore, des méthodes théoriques ont été utilisés pour simuler le mécanisme de transport d'eau dans les couches diffusive et catalytique.

Même si différents méthodes ont été proposées, il n'existe pas encore une simple et unique méthodologie pour étudier l'accumulation d'eau dans la pile à combustible. Par conséquent, dans le cadre de cette thèse il a été proposé une stratégie visant l'étude de l'accumulation d'eau dans la cathode de la pile à combustible au méthanol. On est parti du principe que la caractérisation électrochimique des cathodes dans une solution d'acide sulfurique peut être représentative de l'état d'inondation de la cathode dans la pile. Par conséquent, la caractérisation électrochimique ex-situ a été proposée pour étudier les cathodes avant des tests dans la pile à combustible. Cette procédure est moins longue et moins coûteuse, car elle ne nécessite pas de la préparation d'un assemblage membrane-électrodes (AME). Ensuite, les cathodes ont été testées dans une PCM.

Après l'activation, les courbes de polarisation et les spectres d'impédance ont été enregistrés avec de l'air et de l'oxygène humidifiés au 100 % et en faisant varier l'humidité relative à la cathode (50% HR et> 100% HR).

C) Spectroscopie d'Impédance Électrochimique

Une grande partie de cette thèse a été consacrée à l'utilisation de la Spectroscopie d'Impédance Électrochimique (SIE), une technique non invasive et bien utilisée dans de nombreux domaines de la recherche électrochimique, pour la caractérisation des matériaux poreux. La SIE est un outil très puissant pour étudier les propriétés de transport dans les matériaux poreux et les processus à l'interface électrode-solution. En SIE, le système étudié est soumis à une faible tension sinusoïdal à fréquence variable et la réponse en courant est mesuré, comme le montre la Figure 4. L'impédance est donnée par le rapport tension/courant en prenant en compte le déphasage. Comme le signal appliqué est très faible, le système analysé n'est pas perturbé de manière irréversible.

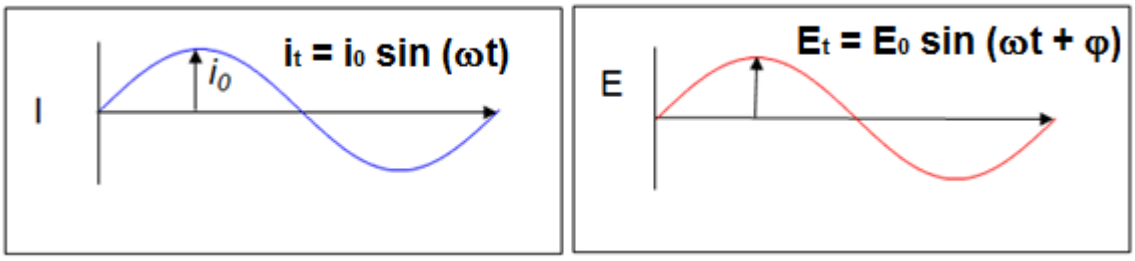

Figure 4: Tension sinusoïdale appliquée et courant sinusoïdal mesuré (Chapitre 3 – Figure 3.1).

$$Z = \frac{E_t}{i_t} = \frac{E_0 \sin(\omega t + \varphi)}{i_0 \sin(\omega t)} = Z_0 \frac{\sin(\omega t + \varphi)}{\sin(\omega t)} \qquad (\textbf{Equation 3.1})$$

c.1) Spectroscopie d'Impédance Électrochimique dans la solution d'acide sulfurique

Depuis la fin des années '80, la SIE a été employée dans les études sur les piles à combustible et pour la caractérisation des électrodes poreuses. Les modèles théoriques de Springer et Raistrick décrivant la structure d'une électrode poreuse et représentent les phénomènes qui se produisent dans les pores en présence de réactions électrochimiques ont été explorés. La spectroscopie

d’impédance électrochimique dans la solution d’acide sulfurique a été utilisée pour étudier la conduction protonique à travers la structure poreuse de la couche catalytique et pour caractériser le comportement d'électrodes poreuses ayant hydrophobie différentes.

Le spectre d'impédance typique d'une électrode poreuse, enregistré dans une solution d'acide sulfurique saturée en azote est montré dans le diagramme de Nyquist de la Figure 5. Le spectre d'impédance peut être divisé en deux régions. À hautes fréquences, le spectre comprend une ligne droite avec un angle de 45 degrés. Cette partie est connue comme l’impédance de Warburg, et correspond à la diffusion des ions à travers la couche catalytique. À basses fréquences, le graphique montre une ligne quasi vertical du à la capacité totale à l'interface pores - solution et à la résistance totale du pore.

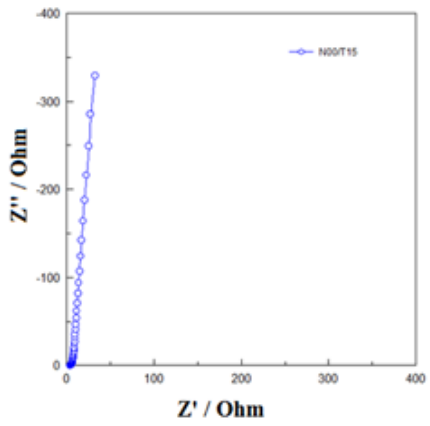

Figure 5: Spectre d’impédance pour la cathode N00/T15 enregistré dans une solution d’acide sulfurique saturée en azote (Chapitre 3 – Figure 3.7a).

Le spectre d'impédance typique d'une électrode poreuse, enregistré dans une solution d'acide sulfurique saturée en oxygène est montré dans la Figure 6. À hautes fréquences, le graphique montre une dépendance linéaire qui est modifié en demi-cercle dépressif en allant vers les basses fréquences. Encore une fois, le comportement à 45 degrés (région de Warburg) est lié à la diffusion dans la structure poreuse. Le demi-cercle à basses fréquences est liée à la réaction de réduction d'oxygène qui se produisant dans la structure poreuse à l'interface électrode-électrolyte. La distorsion et la dépression du demi-cercle a été attribuée à l'hétérogénéité de l'électrode poreuse.

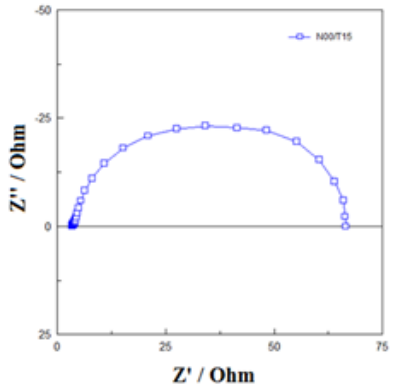

Figure 6: Spectre d'impédance pour la cathode N00/T15 enregistré dans une solution d'acide sulfurique saturée en oxygène (Chapitre 3 – Figure 3.7b).

Dans ce travail, on a identifié la procédure pour l'analyse des spectres d'impédance enregistrés dans les solutions d'acide sulfurique saturées en azote et en oxygène. Les deux cathodes, N 15 / T 00 et N 00 / T 15 (Tableau 1), ont été choisies pour présenter cette procédure. Les spectres enregistrés dans la solution saturée en azote (Figure 5) ont été utilisés pour déterminer la résistance ionique et la capacité de la double couche de la cathode en contact avec la solution d'électrolyte. La résistance ionique est obtenue à partir de la projection de la région de Warburg sur l'axe des réels (Z'), et est définie comme :

$$Z' = \frac{R_{ionic}}{3} \qquad (\boldsymbol{Equation\ 3.3})$$

L'extension de la région de Warburg a été déterminée par l'identification de l'intervalle de fréquence avec une pente de -1/2 dans le module et un angle de phase de 45 degrés dans les diagrammes de Bode, comme montre la Figure 7.

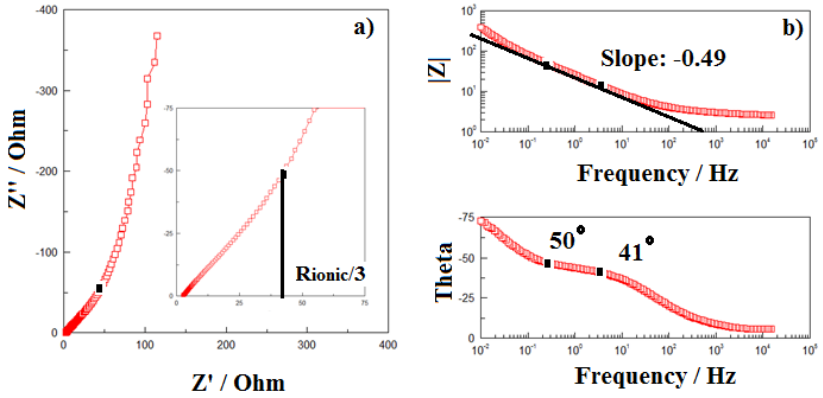

Figure 7: Spectres d'impédance pour la N15/T00 cathode enregistrés dans la solution d'acide sulfurique saturée en azote (Chapitre 3 – Figure 3.8).

Pour ce qui concerne la capacité de la double couche a été déterminée en utilisant la relation suivante:

$$C = -\frac{1}{Z''\omega} \qquad (\textbf{\textit{Equation}}\ \mathbf{3.4})$$

La capacité de la double couche a été déterminée graphiquement à partir de la zone du plateau, comme montré dans la Figure 8 :

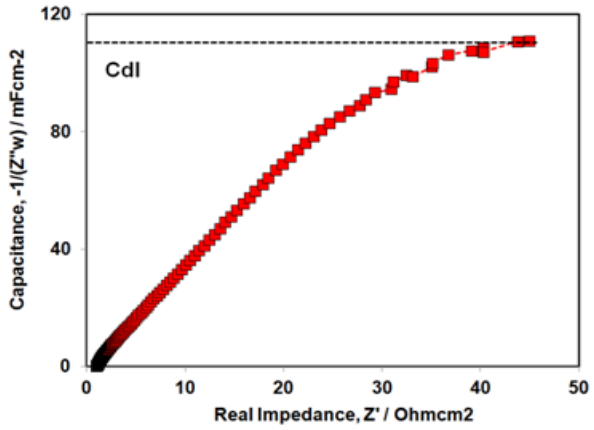

Figure 8: Capacité de la double couche de la N15/T00 cathode (Chapitre 3 – Figure 3.9).

Les spectres enregistrés dans la solution saturée en oxygène (Figure 6) ont été utilisés pour déterminer les paramètres cinétiques pour la RRO. Les spectres ont été modélisés par le Circuit Électrique Équivalent (CEE) montré dans la Figure 9. Le circuit contient la résistance d'électrolyte en série, R_s, la résistance au transfert de charge pour la RRO, R_{CT}, l'élément de phase constante, CPE, pour la capacité de la double couche (C_{dl}) et l'élément de Warburg, W_N, lié à la diffusion des protons et du réactif dans la structure poreuse de l'électrode.

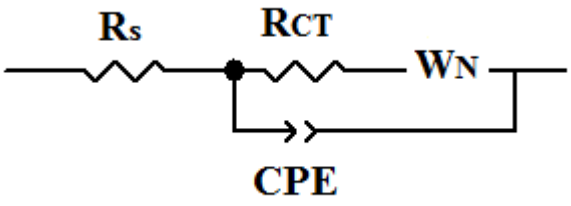

Figure 9: Circuit électrique équivalent (Chapitre 3 – Figure 3.11).

À titre d'exemple, on présent les résultats de la modélisation pour la cathode N 00 / T 15. La Figure 10 montre la variation de la résistance au transfert de charge et de la capacité de la double couche entre 0.7 V et 0.3 V. La résistance en série de l'électrolyte était constante pendant

l'expérience et égal à 1.20 ± 0.01 Ωcm^2. La résistance au transfert de charge diminue avec le potentiel (de 147.64 ± 2.77 Ωcm^2 à 6.78 ± 0.10 Ωcm^2) et commence à augmenter légèrement à partir de 0.4 V (8.00 ± 0.17 Ωcm^2). La capacité de la double couche monte avec le potentiel (de 35.79 ± 0.29 $mFcm^{-2}$ à 96.29 ± 0.23 $mFcm^{-2}$). L'augmentation de la capacité montre que la cathode n'était pas inondée par l'eau.

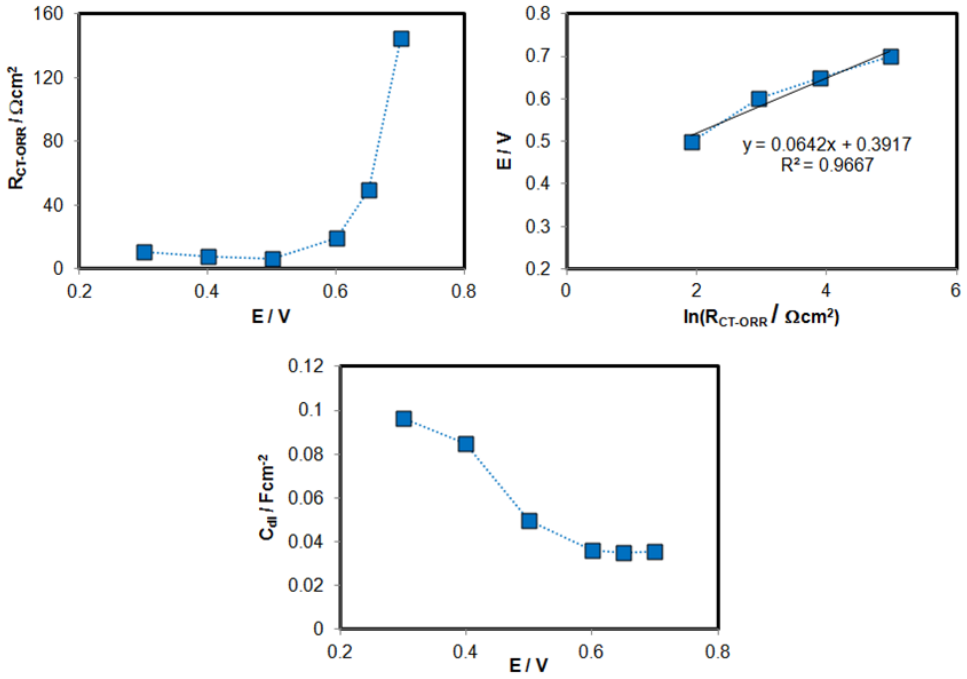

Figure 10: Paramètres cinétiques pour la cathode N00/T15 (Chapitre 3 – Figure 3.14).

c.2) Spectroscopie d'Impédance Électrochimique dans la pile au méthanol

Depuis son application dans les études de piles à combustible, la technique de spectroscopie d'impédance électrochimique a été principalement employée dans la recherche sur les piles à hydrogène pour mesurer la résistance de la membrane et étudier les effets de la déshydratation et de la compression sur la résistance de la membrane.

Pour ce qui concerne la recherche sur les piles au méthanol, l'utilisation de la SIE n'est pas facile. Par rapport à l'oxydation de l'hydrogène, la vitesse d'oxydation du méthanol n'est pas négligeable et les deux réactions anodique et cathodique contribuent au spectre d'impédance. L'oxydation du méthanol est une réaction à plusieurs étapes qui se produisent à travers la formation d'un intermédiaire (CO) qui empoisonne facilement le catalyseur et limite son activité.

En outre, le méthanol traverse la membrane Nafion (cross-over) et affecte considérablement la performance de la cathode. Comme résultat de tous ces processus simultanés, l'analyse de spectres d'impédance n'est pas simple. Traditionnellement, les spectres sont analysés en utilisant la méthodologie de Müller and Urban et les impédances de l'anode et de la cathode sont séparées comme montré dans la Figure 11. D'abord, le spectre complet de la PCM est enregistré. En suite, la cathode est alimentée avec de l'hydrogène (électrode de référence) pour enregistrer le spectre de l'anode. Enfin, le spectre de la cathode est calculé par différence.

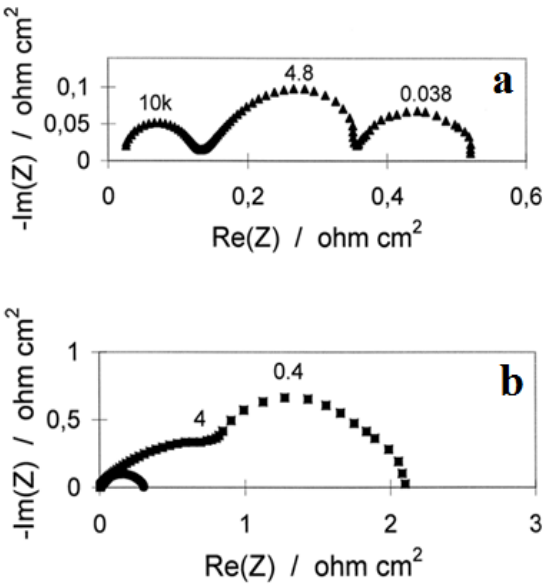

Figure 11: Spectres d'impédances de la PCM a) anode b) cathode (Chapitre 3 – Figure 3.15).

Une méthode simple et unique pour l'analyse des spectres complets n'existe pas encore. Par conséquent, l'objectif de cette étude était de trouver une approche facile et rapide pour analyser les spectres complets de la PCM. Les spectres complets de deux assemblages membrane-électrodes, MEA-Pt_3Co/KB and MEA-Pt/KB (Tableau 3), ont été étudiés en premier. Les AMEs étaient construits avec la même anode, la même membrane mais deux différentes cathodes; un AME contenant une cathode à base de Pt_3Co et l'autre avec une cathode à base de Pt. Les spectres ont été enregistrés sous différentes conditions expérimentales (en fonction du potentiel, du débit d'air, de la concentration du méthanol et en présence d'air et d'oxygène) comme le montre la Figure 12. L'analyse de ces spectres a montré que l'arc à basses fréquences est relatif aux processus occurrent à la cathode.

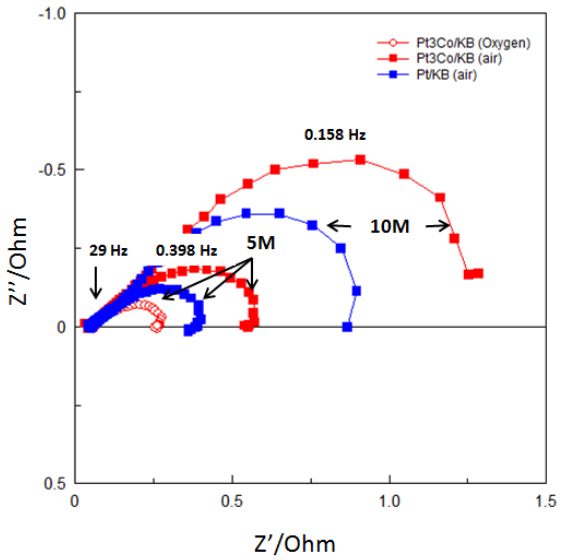

Figure 12: Spectres d'impédances complètes analysées (Chapitre 3 – Figure 3.20).

Les spectres complets ont été modélisés par des circuits électriques équivalents qui ont été construits à partir des processus électrochimiques qui se produisent à la cathode, à l'anode et à la membrane échangeuse d'ions. Les circuits sont montrés dans la Figure 13. Ils sont composés de la résistance en série (Rs), le circuit anodique et le circuit cathodique. Étant donné que l'objectif principal de cette thèse concerne l'étude de cathodes pour la PCM, l'impédance de relaxation liée à l'adsorption du CO sur le catalyseur de PtRu n'a pas été considérée dans le circuit anodique. Le premier circuit cathodique, Figure 13a, a été construit en considérant que deux réactions ont lieu simultanément à la cathode: la réaction de réduction d'oxygène (RRO) et la réaction parasite d'oxydation du méthanol (ROM). Comme l'adsorption de l'intermédiaire de CO affecte considérablement la performance du catalyseur à la cathode, l'impédance de relaxation est ajoutée en parallèle au circuit $Rct\text{-}_{cathode}$ - $CPE_{cathode}$. Le deuxième circuit cathodique, Figure 13b, a été construit en considérant que le cross-over du méthanol est faible à haute surtension. Sous cette condition, l'empoisonnement du catalyseur à la cathode peut être négligé et le circuit cathodique devient un circuit parallèle $Rct\text{-}_{cathode}$ - $CPE_{cathode}$. Les paramètres cinétiques pour les deux AMEs on été déterminés.

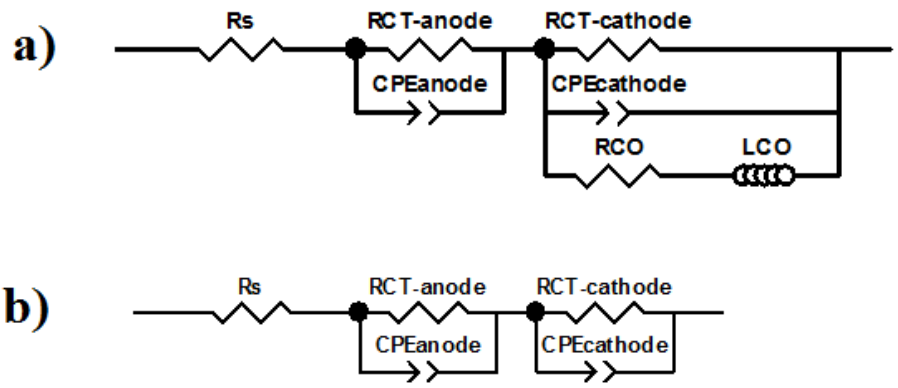

Figure 13: CEEs utilisés pour l'analyse des spectres d'impédance (Chapitre 3 – Figure 3.23).

En suite, la procédure de modélisation était étendue aux AMEs qui sont le sujet de cette thèse. Les deux MEA-Pt/XC72 and MEA-N00/T15 (Tableau 3) on été étudiés. Les spectres complets des AMEs sont montrés dans la Figure 14.

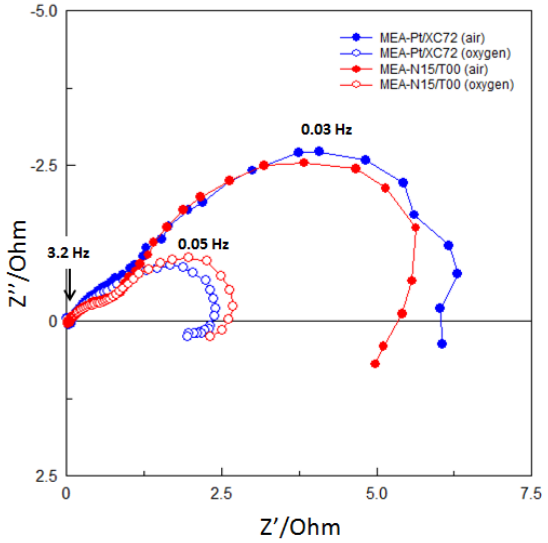

Figure 14: Spectres d'impédances complètes analysées (Chapitre 3 – Figure 3.21).

L'analyse des spectres d'impédance a montré que les modèles utilisés ont correctement attribué l'impédance cathodique au demi-cercle à basses fréquences et l'impédance anodique au demi-cercle à hautes fréquences. Les paramètres cathodiques ont répondu de manière cohérente à la variation de potentiel de pile, au type de réactif (air/O_2), au débit d'air et à la composition de la cathode. Au contraire, les paramètres anodiques n'ont pas montré des variations significatives avec les conditions expérimentales. Ceci était prévu à cause de la stœchiométrie élevée de méthanol utilisée dans ces expériences.

Résultats :

Déposition simultanée du Nafion et PTFE dans les cathodes à base du platine

Quatre cathodes contenant du Nafion/PTFE (Tableau 1) ont été étudiées pour comprendre si la déposition simultanée du Nafion et PTFE dans un rapport spécifique peut réduire l'accumulation d'eau à la cathode.

La caractérisation physico-chimique a montré que le remplacement partiel du Nafion par PTFE dans la couche catalytique ne produit pas une variation significative de l'épaisseur de la cathode. Par contre, il y a une réduction de le caractère hydrophile de la cathode avec le contenu du PTFE (de 32.46 ± 1.86 % pour la cathode N 15 / T 00 à 16.53 ± 1.46 % pour la cathode N 00 / T 15) et une variation du volume totale des pores des cathodes (0,109 cm^3g^{-1} pour la cathode N 15 / T 00 et 0.061 cm^3g^{-1} pour la cathode N 10 / T 05), comme montré dans la Figure 15.

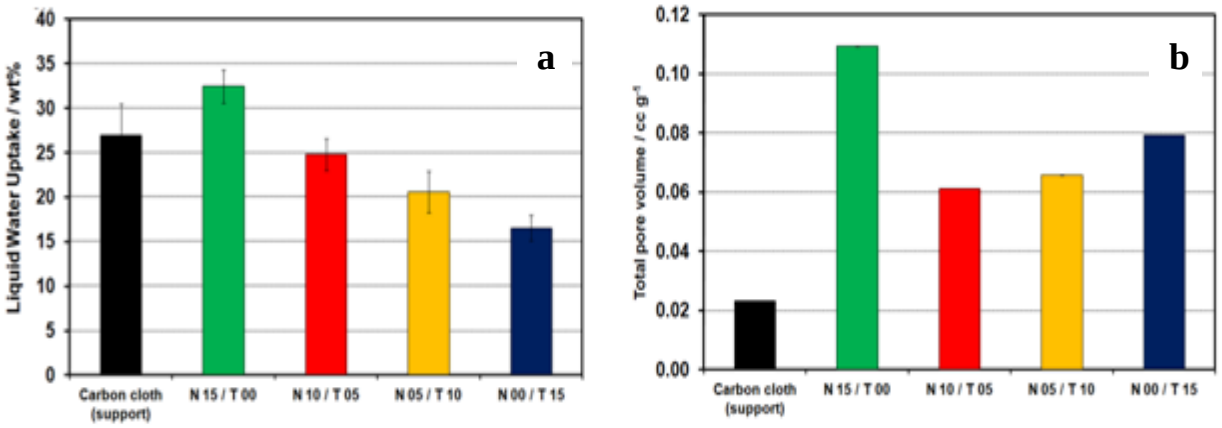

Figure 15: a) Mesures d'absorption d'eau et b) porosité totale (Chapitre 4 – Figures 4.3 et 4.5).

Comme attendu, la caractérisation électrochimique dans la solution d'acide sulfurique saturée en azote a montré que l'utilisation du platine et la capacité de la double couche augmentent avec l'hydrophilie des cathodes. La Figure 16 présente les maxima de 25,50 ± 0,70% pour l'utilisation du platine et de 104,00 ± 5,70 $mFcm^{-2}$ pour la capacité de la double couche pour la cathode N 15 / T 00.

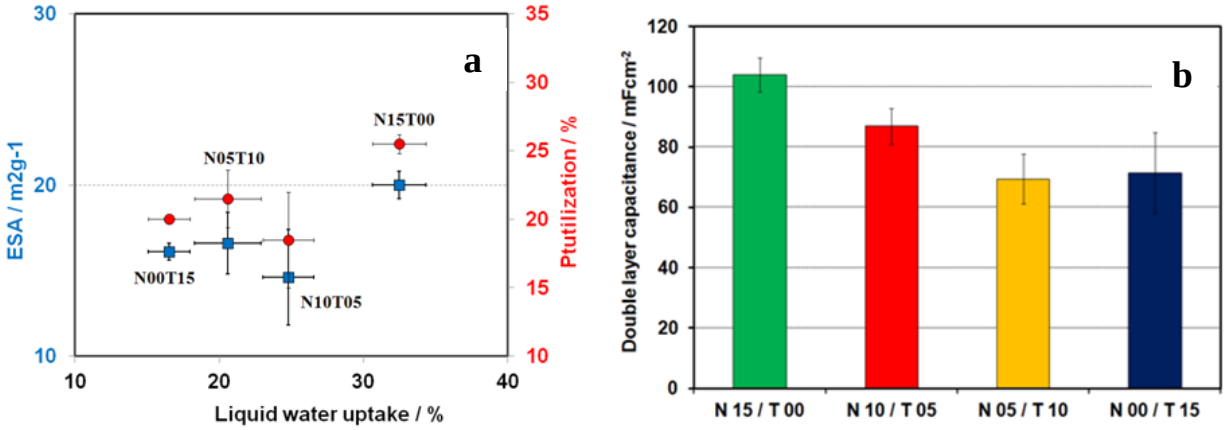

Figure 16: a) Utilisation de platine et b) capacité de la double couche (Chapitre 4 – Figures 4.8 et 4.10).

Mais, les avantages d'avoir compris le PTFE dans la couche catalytique de la cathode se sont bien mis en évidence dans la valeur de densité de courant pour la réaction de réduction d'oxygène. La Figure 17 montre que la RRO se produit plus facilement sur la cathode N 15 / T 00, mais l'accumulation d'eau limite drastiquement le valeur du courant. La densité de courant limite augmente avec le contenu de PTFE dans la couche catalytique et une valeur plus élevée est observée pour la cathode N 00 / T 15 (38 $mAcm^{-2}$ à 0,2 V).

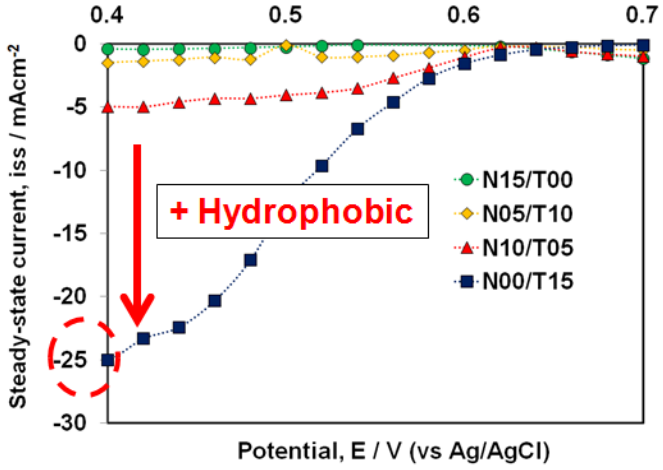

Figure 17: Courbes de polarisation pour la RRO (Chapitre 4 – Figure 4.11).

Ces résultats ont été confirmés par les mesures de spectroscopie d'impédance. Comme montré dans la Figure 18, la cathode N 10 / T 05 a une valeur de résistance de transfert de charge plus faible (36,86 ± 0,47 Ωcm^2) et une valeur de capacité de la double couche plus élevée (48,74 ± 0,40 $mFcm^{-2}$). Les résultats ont suggéré que le bon équilibre entre le 10 % massique du Nafion et 5 % massique du PTFE a assuré la conduction protonique dans la couche catalytique et l'apport

d’oxygène dans les sites actifs pour la RRO.

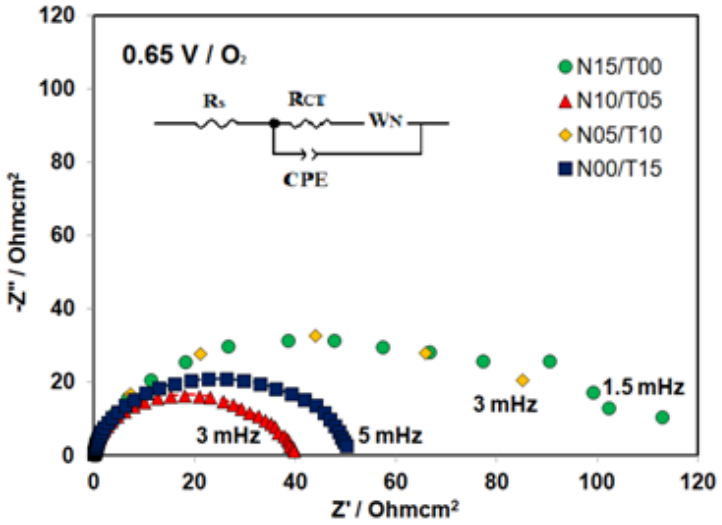

Figure 18: Spectres d’impédance enregistrés dans 0.5 M H_2SO_4 saturée en O_2 (Chapitre 4 – Figure 4.15).

Les cathodes ont subi aussi une caractérisation in-situ dans la pile au méthanol. Des courbes de polarisation ont été enregistrées à différentes températures (dans le range 25 – 80 °C), avec une alimentation d’air et d’oxygène à la cathode. Comme attendu, les AMEs avec les cathodes contenant du Nafion ont montré des performances plus élevées. La différence de potentiel entre les courbes de polarisation enregistrées en présence d’oxygène et le courbes enregistrées en présence d’air, le « oxygène gain », a été calculée. Une valeur plus faible a été observé pour le MEA – N 10 / T 05, liée probablement à un meilleur transport de masse dans la structure poreuse de la cathode N 10 / T 05. Ce résultat était confirmé par les mesures de spectroscopie d’impédance électrochimique, comme le montre la Figure 19. Pour le MEA – N 10 / T 05, l’arc à basses fréquences ferme toujours, indépendamment de l’alimentation à la cathode. Par contre, le MEA – N 15 / T 00 montre des évidents problèmes de transport de masse spécialement quand la cathode est alimentée avec l’oxygène et à basses valeurs du potentiel de pile (diagramme de Bode).

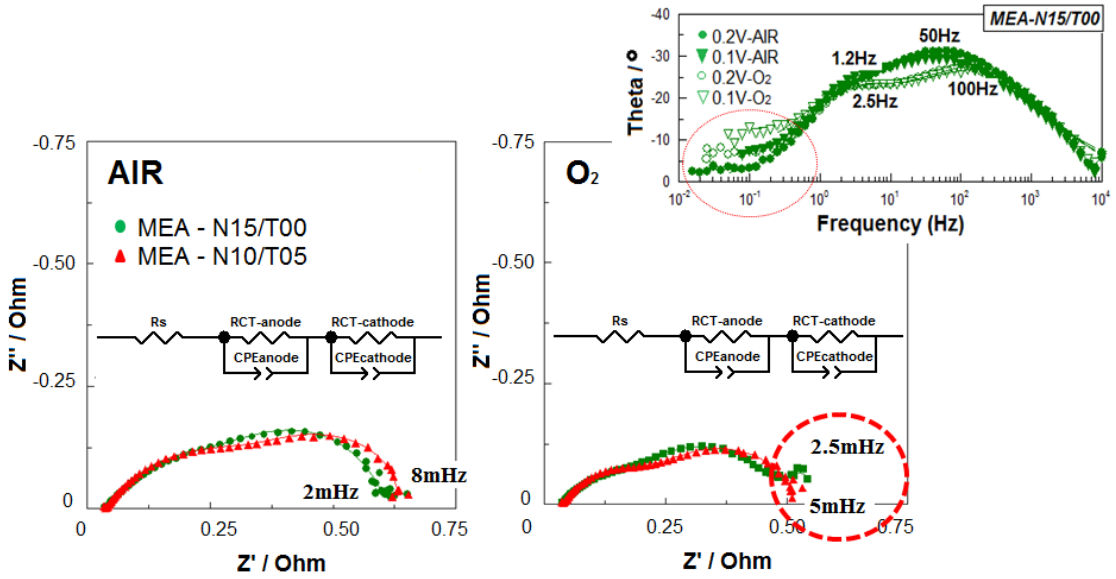

Figure 19: Spectres d'impédance enregistrés dans la PCM (Chapitre 4 – Figures 4.21 et 4.22).

Autres tests ont été réalisés à des valeurs différentes de humidité relative (50 % - 100 % - plus de 100 % HR). Les courbes de polarisation enregistrées à 50 °C, à une humidité relative de plus de 100% et avec une alimentation d'air à la cathode sont montrés dans la Figure 20. L'AME avec la cathode N 10 / T 05 montre une performance plus élevée que l'AME avec la cathode N 15 / T 00. Ces résultats confirment l'hypothèse faite avant et démontrent que la cathode N 10 / T 05 est apte à travailler dans un PCM à basse température sans problèmes d'accumulation d'eau dans la couche catalytique.

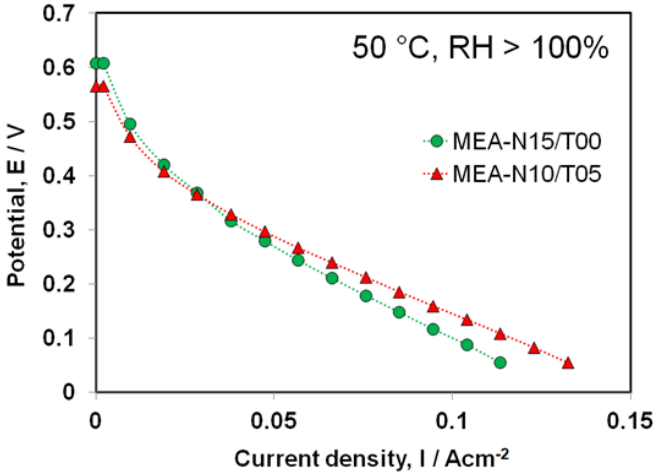

Figure 20: Courbes de polarisation à plus de 100 % HR (Chapitre 4 – Figure 4.23).

Optimisation de la distribution du Pt pour la cathode N 10 / T 05

Il a été pensé que la performance de la cathode N 10 / T 05 aurait pu être améliorée en optimisant l'utilisation du catalyseur. Par conséquent, dans une nouvelle cathode, N 10 / T 05 – P, la distribution du platine a été concentrée davantage sur la surface de la cathode, comme montré dans les images EDS et MEB de la Figure 21.

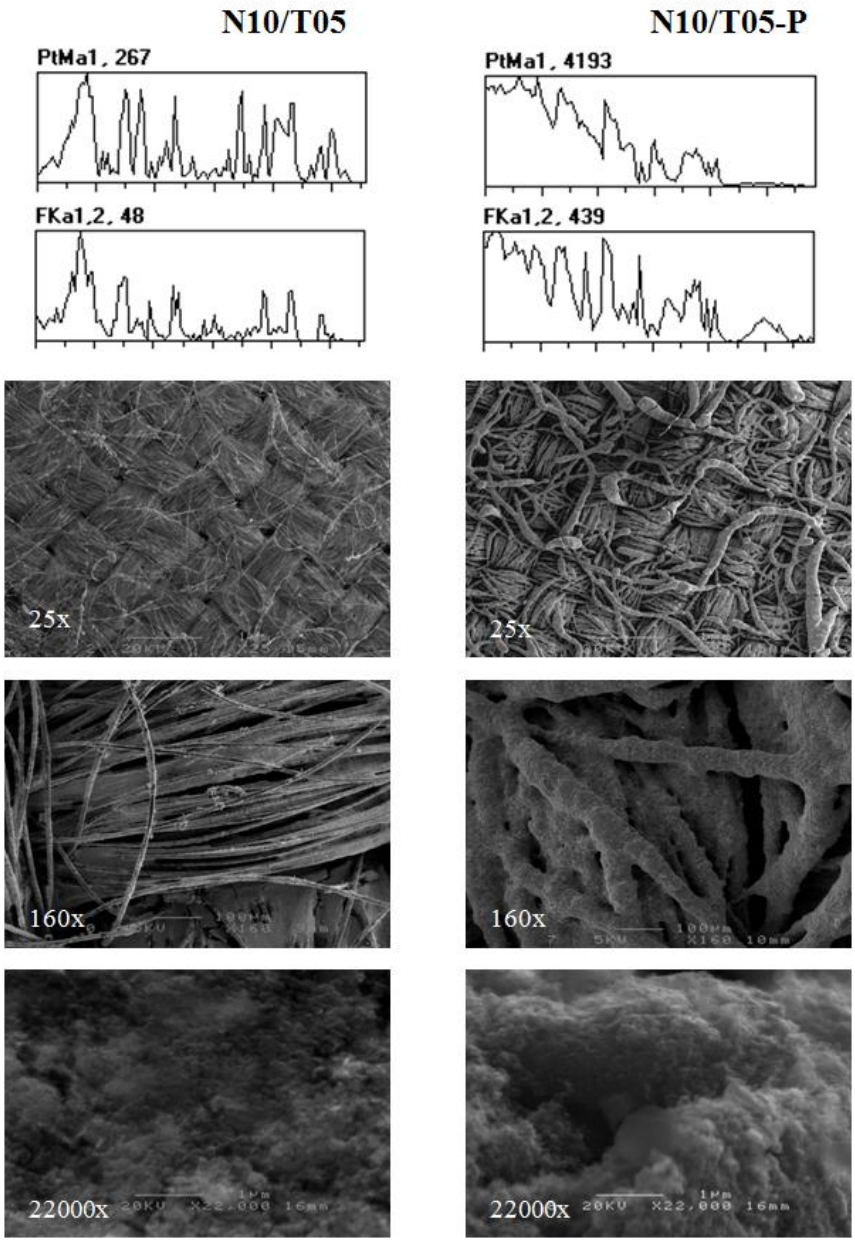

Figure 21: Images EDS et MEB pour les cathodes N10/T05, N10/T05-P (Chapitre 4 – Figure 4.24).

Par rapport à la cathode N 10 / T 05, la nouvelle cathode a montré une absorption d'eau légèrement supérieure (27.0 ± 1,5 % versus 24.8 ± 1.8 %) et une plus grande épaisseur (502 ± 72 μm versus 443 ± 49 μm). Depuis les deux cathodes ont la même composition chimique et aucune variation du volume total des micro-et méso-pores n'a pas été observée (0.061 cm^3g^{-1}). On a donc supposé que l'augmentation de l'épaisseur doit être liée à une macroporosité de la couche catalytique plus élevée dans le cas de la nouvelle cathode (N 10 / T 05 – P). Cependant, cette hypothèse devra être vérifiée par des mesures de porosimétrie au mercure. La caractérisation en pile de l'AME contenant la nouvelle cathode a montré une plus grande utilisation de catalyseur et plus haute performance, mais aussi une plus forte probabilité d'accumulation d'eau lorsque la pile a été opérée à basse température (50 °C) et à haute humidité relative (plus de 100%), comme montré dans la Figure 22. Il est bien connu que les macro-pores améliorent le transport de masse, mais, dans cette configuration cathodique (pas de couche de diffusion) et dans ces conditions expérimentales (basse température), il a été constaté que les macro-pores se sont comportés comme des "bassins d'eau" et ont favorisé l'accumulation l'eau.

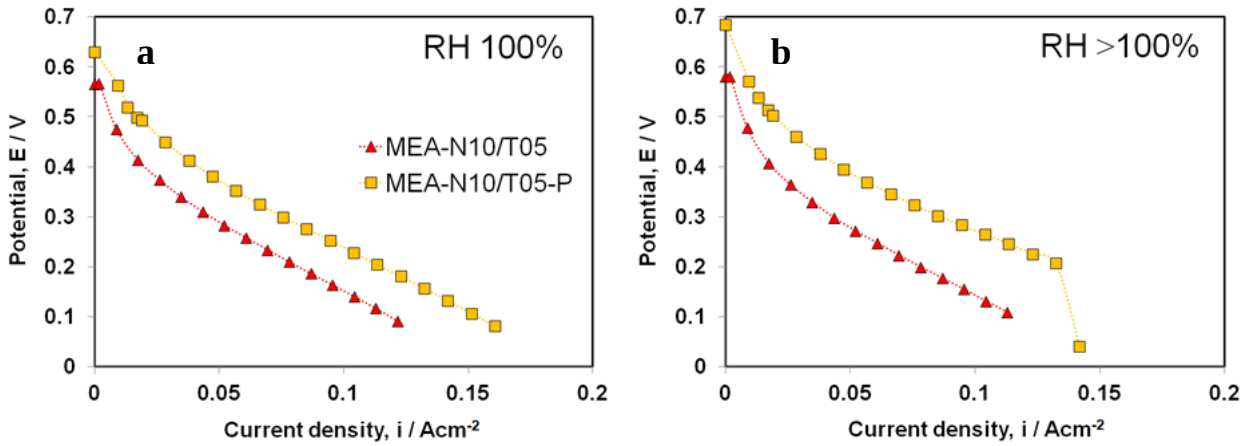

Figure 22: Courbes de polarisation à 50 °C, a) 100% HR, b) plus de 100% HR (Chapitre 4 – Figure 4.28).

La caractérisation des cathodes contenant du Nafion et PTFE a montré que la présence du PTFE dans la couche catalytique de la cathode est utile pour réduire l'accumulation d'eau dans la cathode de la PCM qui travaille à basse température. Mais nous résultats ont aussi suggéré que la solution au problème d'accumulation d'eau de la cathode est renfermée dans la porosité de la de la couche catalytique plus que dans sont caractère hydrophile/hydrophobe. La dimension appropriée des pores est crucial pour le développement de une cathode résistante à l'accumulation d'eau.

Modification de la morphologie de la cathode N 00 / T 15

La dernière partie de ce travail s'est occupée d'étudier plus en détails la cathode à base de PTFE. La performance de l'AME contenant cette cathode était considérablement faible, en particulier quand la cathode était alimentée avec l'air. Cependant, la résistance à la conduction protonique tels que mesure ex-situ était la plus faible de la série de cathodes Nafion / Teflon. En plus, le courant limite pour la réaction de réduction d'oxygène était le plus élevé. Ces résultats ont fait de la cathode N 00 / T 15 un sujet intéressant pour vérifier si la caractérisation électrochimique dans la solution d'acide sulfurique est la bonne stratégie pour prévoir l'accumulation d'eau dans la cathode de la PCM à basse température. Dans cette prospective, la morphologie de la cathode N 00 / T 15 a été modifiée par a) frittage à 350 °C (N 00 / T 15 – 350), b) couverture de la couche catalytique avec du Nafion (N 00 / T 15 - N 05) et c) déposition de la couche catalytique sur un support traité avec du PTFE (N 00 / T 15 - TFE) (Tableau 1).

Les résultats de la caractérisation physico-chimique ont montré que les traitements appliqués à la cathode N 00 / T 15 ont produit une variation significative de l'épaisseur et de la porosité totale des cathodes, comme le montre la Figure 23. Il y a un effet positif en couvrir la couche catalytique avec du Nafion où en la déposer sur un tissu de carbone traitée avec du PTFE. En fait, l'absorption d'eau de les deux cathodes N 00 / T 15 - N 05 et N 00 / T 15 - TFE est meilleure (33.80 ± 0.90 % et 21.60 ± 1.60 %). Par contre, le traitement de frittage à 350 ° C n'amène aucun résultat positif. La capacité d'absorption d'eau de cette cathode s'est réduite du 60%.

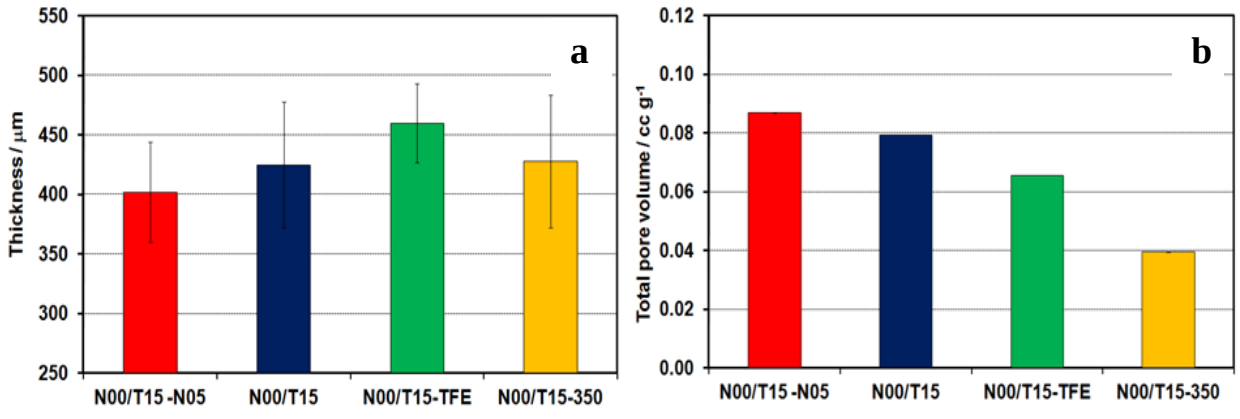

Figure 23: a) Épaisseur et b) porosité totale (Chapitre 5 – Figures 5.13 et 5.16).

La caractérisation électrochimique dans la solution d'acide sulfurique saturée en azote a montré

que la résistance à la conduction protonique dans la couche catalytique et la capacité de la double couche augmentent avec l'hydrophilie des cathodes. La cathode N 00 / T 15 – N 05 a montré la plus faible résistance ionique (3.20 ± 0.80 Ωcm^2). Par contre, le traitement de frittage à 350 ° C a minimisé la capacité de la double couche (6.89 ± 0.04 $mFcm^{-2}$). Comme attendu, l'utilisation du platine varie avec l'hydrophilie et la porosité totale des cathodes. La cathode N 00 / T 15 - N 05 a une plus grande utilisation du catalyseur (31.70 ± 4.40 %), comme montré dans la Figure 24.

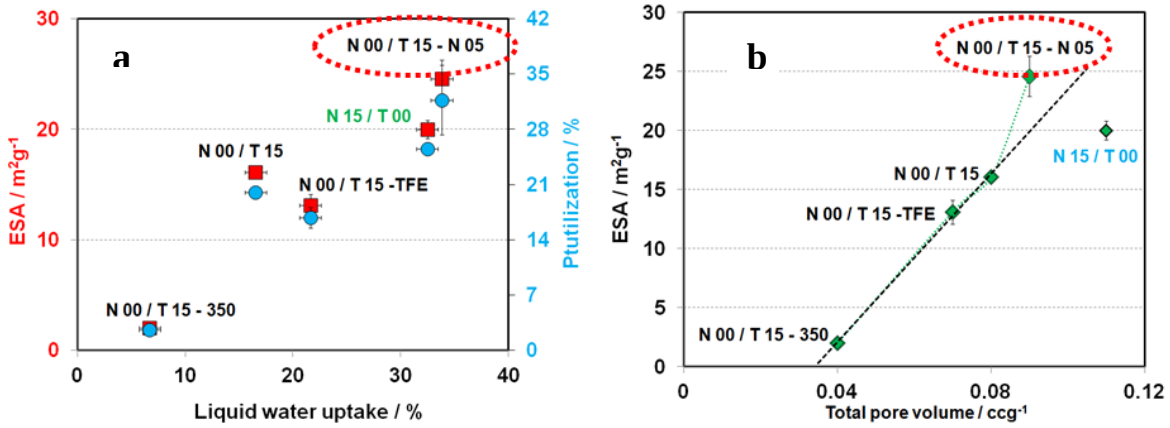

Figure 24: SEA versus a) absorption d'eau et b) porosité totale (Chapitre 5 – Figures 5.19 et 5.20).

Les avantages de la variation morphologique de la cathode N 00 / T 15 se sont aussi montrés dans la valeur de densité de courant pour la réaction de réduction d'oxygène. La Figure 25 montre que la RRO se produit facilement sur la cathode N 00 / T 15 – N 05. Dans ce cas, la densité de courant augmente avec l'hydrophilie de les cathodes et une valeur plus élevée est observé pour la cathode N 00 / T 15 – N 05 (300 $mAcm^{-2}$ à 0.1 V).

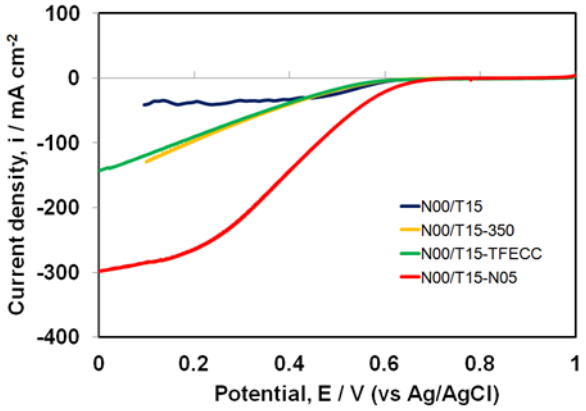

Figure 25: Courbes de polarisation pour la RRO (Chapitre 5 – Figure 5.23).

Ces résultats étaient confirmés par les mesures de spectroscopie d'impédance électrochimique.

Comme montré dans la Figure 26, la cathode N 00 / T 15 – N 05 a une valeur de résistance de transfert de charge plus faible (25.61 ± 1.02 Ωcm^2) et une valeur de capacité de la double couche plus élevée (116 ± 0.02 $mFcm^{-2}$). La Figure 26b montre les spectres d'impédance pour la cathode N 00 / T 15 – N 05 enregistrés à différentes valeurs de potentiel. La résistance au transfert de charge diminue avec le potentiel et à faibles potentiels (0.4 V et 0.3 V) la cathode fait preuve de problèmes de transport de masse.

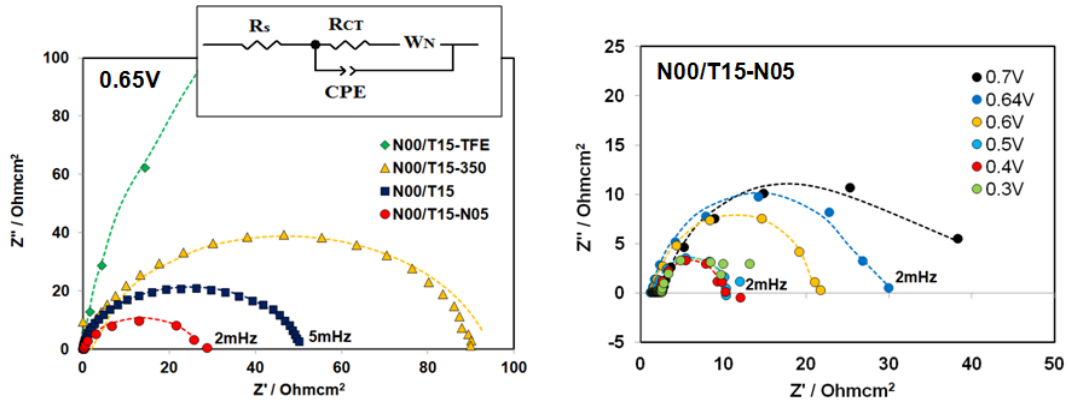

Figure 26: Spectres d'impédance enregistrés dans 0.5 M H_2SO_4 saturée en O_2 (Chapitre 5 – Figure 5.25).

Les cathodes ont subi aussi une caractérisation in-situ dans la pile au méthanol. Les courbes de polarisation enregistrées à 40 degrés, à une humidité relative de 100%, avec une alimentation d'air et d'oxygène à la cathode sont montrées dans la Figure 27. Les courbes montrent une amélioration de la performance pour l'AME avec la cathode N 00 / T 15 – N 05 du 33 % dans l'air et 8.4 % dans l'oxygène. Ce résultat confirme les résultats obtenus dans les courbes de polarisation pour la RRO dans l'acide sulfurique.

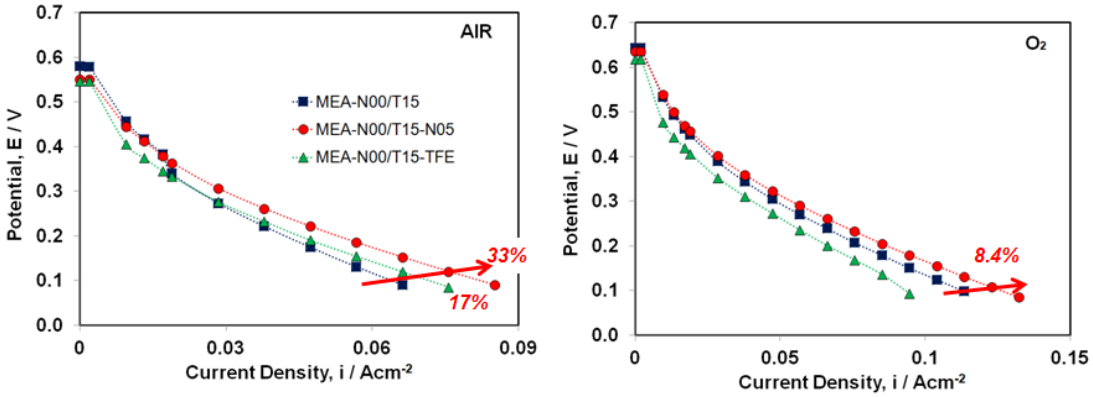

Figure 27: Courbes de polarisation à 40 °C dans l'air et oxygène (Chapitre 5 – Figures 5.29 et 5.32).

Ces résultats ont été confirmés par les mesures de spectroscopie d'impédance électrochimique. L'AME avec la cathode N 00 / T 15 – N 05 a la valeur de résistance de transfert de charge la plus faible (6.51 ± 0.42 Ωcm^2 à 0.5 V). Ce résultat est cohérent avec les résultats de spectroscopie d'impédance électrochimique obtenus dans l'acide sulfurique.

La caractérisation des cathodes préparées par variation morphologique de la cathode N 00 / T 15 a amené des conclusions intéressantes sur la validité de la caractérisation électrochimique dans la solution d'acide sulfurique pour anticiper l'accumulation dans la pile à combustible au méthanol. On peut conclure que les études pour la RRO (courbes de polarisation et spectroscopie d'impédance électrochimique) décrivent qualitativement la performance des cathodes dan la pile à combustible. Par contre, les mesures d'absorption d'eau, de résistance ionique dans la couche catalytique et de la capacité de la double couche ne sont pas utiles pour ce type des études.

Optimisation de la pression d'assemblage

Une partie de ce travail était consacrée à l'étude de l'effet de la pression d'assemblage sur la performance de l'AME dans la pile à méthanol. La pression d'assemblage a été diminuée afin de réduire la compression de la cathode lors de la fabrication de l'AME et pour maximiser le volume des pores disponible dans la cathode. Trois AMEs ont été préparés en utilisant les valeurs de pression suivantes: 500 lb - 375 lb - 250 lb (Tableau 2). Les résultats des tests dans la pile à combustible ont montré que une basse pression d'assemblage peut être bénéfique pour améliorer les performances de l'AME contenant la cathode N 00 / T 15. En effet, la résistance en série est variée entre 0.47 Ωcm^2 et 0.52 Ωcm^2, avec le minimum pour l'AME pressé à 375 lb. L'oxygène et les protons diffusent plus facilement à travers la couche catalytique résultant en un meilleur utilisation du catalyseur à l'anode et à la cathode. Pour ces raisons, les meilleurs résultats ont été reportés pour l'AME pressé à 375 lbs: des potentiels à circuit ouvert plus élevés à tous les températures (0,58 - 0,63 - 0,67 V à 40, 60 et 80 °C), une utilisation de catalyseur plus élevé dans les courbes E-j enregistrées à 40 ° C en présence d'air et d'oxygène, des performances supérieures dans les entières courbes E-J à 60 °C et 80 °C (132 $mAcm^{-2}$ and 151 $mAcm^{-2}$ at 0.1 V). Ces résultats sont montrés en bas dans la Figure 28.

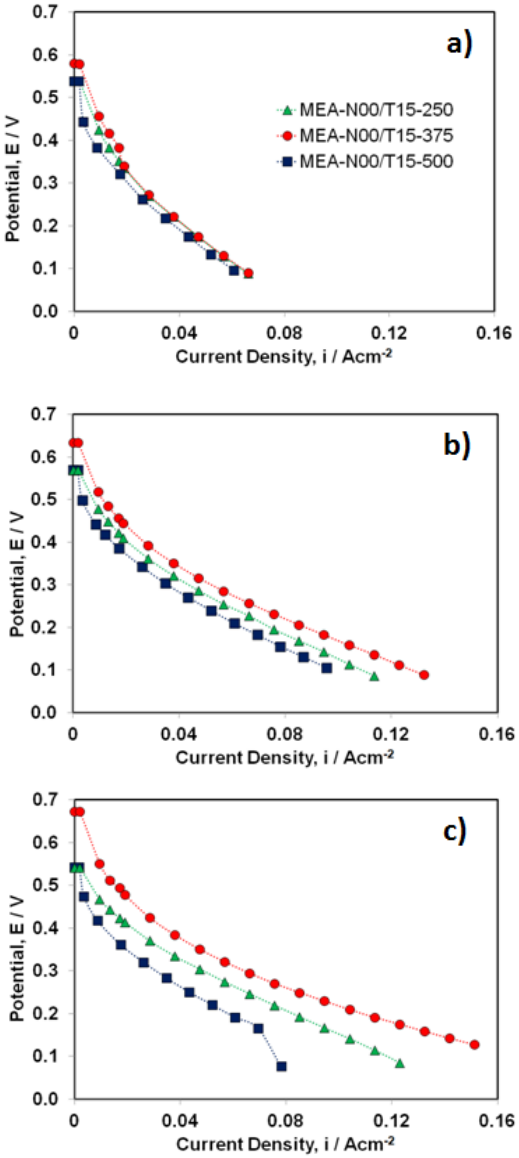

Figure 28: Courbes de polarisation à a) 40 °C, b) 60 °C, c) 80 °C (Chapitre 5 – Figure 5.3).

La performance de l'AME pressé à 350 lb a été aussi comparé avec celui de la MEA - N 15 / T 00. La comparaison a été faite à 0,4 V. A 40 °C, les AEMs montrent les mêmes performances (16 $mAcm^{-2}$), mais à plus haute température, 80 °C, le MEA - N 15 / T 00 a montré des meilleures performances (43 vs. 32$mAcm^{-2}$), comme prévu par la meilleur hydratation de la couche catalytique à base de Nafion. Il a été conclu que l'optimisation de la pression d'assemblage est bénéfique pour améliorer l'utilisation du catalyseur des cathodes N 00 / T 15; cependant d'autres approches sont nécessaires pour améliorer encore plus la performance de la cathode dans la région des hautes densités de courant.

Perspectives Future

La macroporosité de la couche catalytiques de cathodes présentées dans ce travail a était jugé responsable de l'accumulation d'eau dans les électrodes. Cependant, comme il a été mentionné à plusieurs reprises dans cette thèse, elle doit être quantifiée par la technique de porosimétrie au mercure.

Le caractère hydrophile et hydrophobe des cathodes a été mesuré par l'absorption d'eau liquide et d'hexane. Malheureusement, aucune absorption significative n'a été observée dans le cas de l'hexane. Ce résultat a suggéré que le choix d'un solvant non polaire pour mesurer l'hydrophobie des cathodes n'était pas approprié. Probablement l'hydrophobie de la molécule d'hexane empêché la cathode de se mouiller. En alternative, la mouillabilité des cathodes pourra être étude avec différents solvants organiques polaires (méthanol, 1-butanol, 4-octanol, le 1-décanol) et par des mesures d'angle de contact interne qui semblent donner une meilleure idée de l'hydrophilie des échantillons.

Enfin, pour les cathodes à base de PTFE présentées dans le chapitre 5, il est suggéré une analyse plus approfondie des spectres d'impédance enregistrés dans la solution d'acide sulfurique saturée d'azote. En effet, ces cathodes ne présentent pas une région de diffusion de Warburg dans les spectres Bode. Ce comportement peut être lié soit à une distribution non homogène sur les pores dans la cathode ou à la présence de pores obstrués qui ne comptent pas pour la diffusion de protons. Donc deux modèles différents peuvent être prisent en considération pour l'analyse des spectres d'impédance.

Les résultats reportés dans cette thèse ont démontré que l'augmentation de l'hydrophobicité de la couche catalytique de la cathode ne suffit pas pour empêcher l'accumulation d'eau dans l'électrode. En fait, dans cette configuration cathodique les macro-pores se sont comportés comme des bassins d'eau. Il faudrait utiliser des couches de diffusion dans la préparation des cathodes pour mieux contrôler la morphologie de la cathode car celle-ci contient des pores plus petits que ceux du tissu de carbone que a utilise dans ce travail.

Enfin, ce travail a visé à établir une base pour la préparation de cathodes en utilisant des copolymères non-fluorés. Cette approche s'adresse à la fabrication des AMEs avec des nouvelles membranes composites à base de zéolithes fonctionnalisées par des groupes d'acide sulfonique et en polyéthylène comme liant polymère que celles développées dans notre groupe.

TABLE OF CONTENTS

LIST OF FIGURES

LIST OF TABLES

CHAPTER 1 : INTRODUCTION

1.1. The Energy Revolution

Since the middle of the 20th century the world is facing the hugest environmental challenge, the climate change. The fast rising of the global temperature is threatening scientists but also specialists, engineers and economists because of the possible implications on the natural resources, the world's social and economic stability and in particular, on the way we produce our energy. As established in the Copenhagen Accord (December 2009), the increase of the global temperature should be kept to the "safe level" of warming (below 2 °C) and limited to 1.5 °C by 2015 as high risks for wildfires, melting ice sheets (partial de-glaciations of Greenland and West Antarctic) and floods may derive from the rising temperature. In addition, some changes in the climate may be irreversible and would compromise the equilibrium of the entire ecosystem.

The observed increase in the global temperature is very likely due to the constant raise of the anthropogenic greenhouse gas concentrations (GHGs), such as CO_2, N_2O, CH_4 and fluorinates, which are the main products of the energetic, agricultural and not-energetic industrial sectors. These pollutants accumulate in the atmosphere and, by trapping infrared radiation, they have an overall warming effect. Taking in consideration only the energy sector, as shown in Figure 1.1, the carbon dioxide dominates and it counts for the 83 % of the total greenhouse gases released in the atmosphere (1).

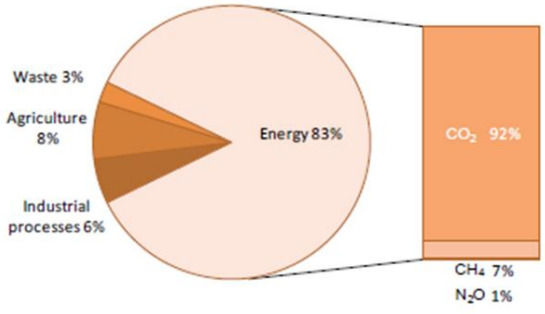

Figure 1.1 : Greenhouse gases emission in developed countries in 2009 (1).

Compared to the preindustrial era, the level of CO_2 in the atmosphere has been increasing over the past century, with the fastest growth occurring in the last ten years (1.9 ppmv/year in the period 1995-2005) and reaching in 2005 the concentration of 379 ppmv, a value 35 % higher than

in the mid-1800s (1). Given the long lifetime of CO_2 in the atmosphere, large reductions of global CO_2 emissions from current levels are required to stabilize the concentrations of greenhouse gases.

Among all the human activities responsible for the CO_2 production, the use of energy represents the main source of emissions. Two sectors, electricity/heat and transport are the main contributors and produced nearly two-thirds of global CO_2 emissions in 2009 (1). The sector of electricity and heat has been the largest producer of greenhouse gas, contributing for the 41 % of the total emission(1). Given the higher demand for electricity, due to the increasing request in the developing countries and the rising number of electrical devices used in homes and commercial buildings, the future development of this sector strongly depends on the fuels used to generate electricity and on the share of the alternative sources such as renewable energies and nuclear power. Concerning the transport, this sector contributes with the 23 % to the total CO_2 emission. Since the global demand for transport appears unlikely to decrease in the foreseeable future, the vehicle efficiency must be improved. Policies that encourage a shift from cars to public transportation may also be adopted and a shift to new, preferably low-carbon fuels, should be encouraged.

Worldwide, the energy sector relies heavily on coal which combustion provides between 68 % and 94 % of the electricity and heat. As shown in Figure 1.2, though coal represents only one-quarter of the global total primary energy supply (TPES), during the 2009, it accounted for the 43 % of the global CO_2 emissions due to its heavy carbon content per unit of energy released, whereas the emissions from oil and gas were estimated to be 37 % and 20 %, respectively. Despite 2009 was the year of the economical crisis, the economy is expected to re-increase again and with that the release of greenhouse gases from the fuel combustion to reach the frightening value of 35.4 Gt by 2035 (1).

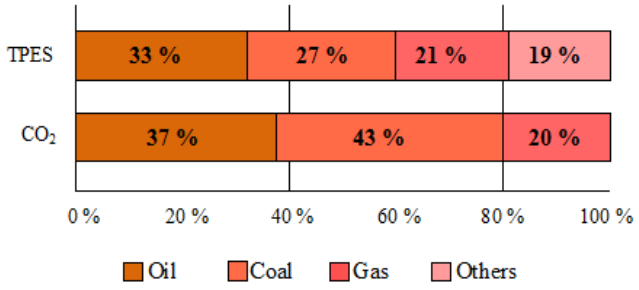

Figure 1.2 : World primary energy supply and CO_2 emissions (1).

The response to the announced environmental disaster and to the rapidly fluctuation of the oil prices (average oil price per barrel: 147 $ in July 2008 – 34 $ in December 2008 - 70 $ during the year 2009(2)) relies on the occurring energy revolution. This revolution aims to reduce the CO_2 emissions within 80 % by 2050 by limiting the fossil fuel utilization and decreasing the energy consumption through energy efficiency measures. While maintaining the steady global economic development, a better use of the natural resources is investigated together with the creation of millions of new green job positions (2). The energy revolution promotes the development of different alternative energies including windpower, solar photovoltaic, geothermal, electrical energy, hydrogen and biofuels. Windpower, solar photovoltaic and geothermal energies are used to supply power (electricity and heat) but they do not find application in the transport sector where electrical energy, hydrogen and biofuels can easier substitute the fossil fuels. Nowadays, the recent advances in electrochemical energy conversion allow hydrogen and biofuels to have an important impact on the applicability of the alternative energies. In this context, fuel cells found their application.

1.2. Fuel Cells

Fuel cells are electrochemical devices that continuously and directly convert the chemical energy of a fuel into electrical energy with the aid of an oxidant(3; 4). The basic structure of a fuel cell is shown in Figure 1.3. It consists of a liquid or solid electrolyte in contact with two porous electrodes, an anode and a cathode, on either side. Reactants are blown into the cell from each side, the ionic conduction occurs through the electrolyte and products are removed from the anode and the cathode.

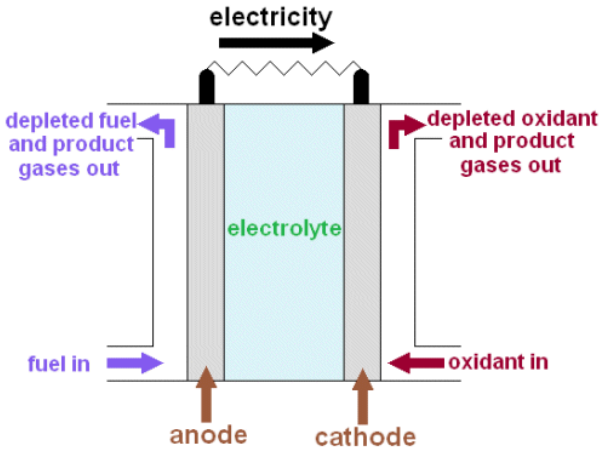

Figure 1.3 : Basic structure of a fuel cell system (5).

Typically, the anode is continuously fed with the fuel and the cathode with the oxidant. The electrochemical reactions occur at the electrodes to produce electricity which is driven in the external circuit. In principle, the energy is produced as long as the reactants are supplied.

1.2.1. Type of fuel cells

According to the choice of electrolyte which determines the type of ions crossing the electrolyte, Figure 1.4, fuel cells are classified as:

- Phosphoric acid fuel cells (PAFCs)
- Polymer electrolyte membrane fuel cells (PEMFCs)
- Alkaline fuel cells (AFCs)
- Molten carbonate fuel cells (MCFCs)
- Solid oxide fuel cells (SOFC)

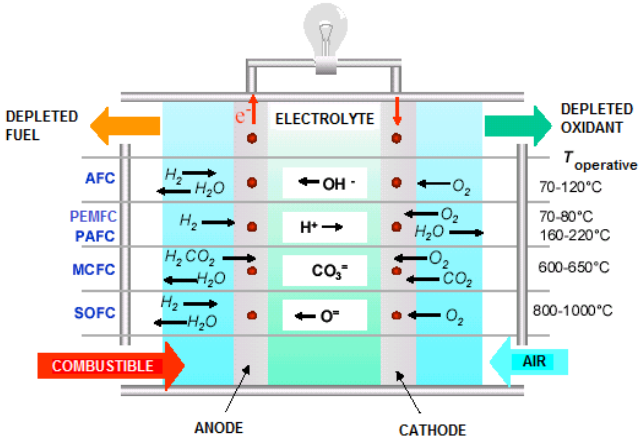

Figure 1.4 : Classification of fuel cell systems based on the type of electrolyte used.

Even if gaseous hydrogen is the most common fuel because of its high reactivity, other types of liquid fossil and renewable fuels can be directly used in the fuel cell system. The principal types of fuel cells are briefly presented in the next paragraphs (6) and their main characteristics are reported in Table 1.1.

Table 1.1 : Characteristics of different types of fuel cells.

	Low temperature			***Medium Temperature***	***High Temperature***	
Type of Fuel Cell	**PAFC**	**PEMFC**		**AFC**	**MCFC**	**SOFC**
		Hydrogen	**DMFC**			
Anode	Pt/C	Pt/C	PtRu/C	Ni, Ag, oxides, Pt	Ni alloy	Ni cerment
Anodic Reaction	$H_2 \rightarrow 2H^+ + 2e^-$	$H_2 \rightarrow 2H^+ + 2e^-$	$CH_3OH + H_2O \rightarrow CO_2 + 6H^+ + 6^-$	$H_2 + 2OH^- \rightarrow 2H_2O + 2e^-$	$H_2 + CO_3^{2-} \rightarrow CO_2 + 2H_2O + 2e^-$	$H_2 + O^{2-} \rightarrow H_2O + 2e^-$
Electrolyte	H_3PO_4	Nafion	Nafion	KOH	Molten mixture of alkali carbonates in $LiOAlO_2$ matrix	Y_2O_3 doped ZrO_2 (YSZ)
Cathode	Pt/C	Pt/C	Pt/C	Ni, Ag, oxides, Pt	NiO	$LaSrMnO_3$
Cathodic Reaction	$½O_2 + 2H^+ + 2e^- \rightarrow H_2O$	$½O_2 + 2H^+ + 2e^- \rightarrow H_2O$	$½O_2 + 2H^+ + 2e^- \rightarrow H_2O$	$½O_2 + 2e^- + 2H_2O \rightarrow 2OH^-$	$½O_2 + 2e^- + CO_2 \rightarrow CO_3^{2-}$	$½O_2 + 2e^- \rightarrow O^{2-}$
Operating Temperature (°C)	150 – 220	60 - 120	Up to 80	60 - 250	650	600 - 1000
Electrical Efficiency (%)	40	40 – 50	40	50	45 – 55	50- 60
Power Range (kW)	$50\text{-}10^3$	$10^{-3}\text{-}10^3$	5	$1\text{-}10^2$	$10^2\text{-}10^6$	$10\text{-}10^6$
Applications	Stationary power stations	Portable Stationary Transport	Portable	Aerospace industry	Stationary and military	Stationary

PHOSPHORIC ACID FUEL CELLS (PAFCs) : In Phosphoric Acid Fuel Cells (PAFCs), the liquid phosphoric acid electrolyte (H_3PO_4) is placed between the two porous graphite electrodes coated with platinum catalyst. Since the electrolyte is a poor ionic conductor at low temperatures and it undergoes to unfavorable phase transition over 210 °C, the PAFCs are generally operated in the range 150 – 220 °C. The fuel and the oxidant are hydrogen and air/oxygen. When the cell is run on a reformed, the anodic Pt catalyst is susceptible to carbon monoxide and sulphur

poisoning. The CO tolerance can be high as 0.5-1.5 %, whereas the H_2S tolerance is generally 50 ppm.

The PAFCs are mostly developed for stationary power stations and are one of the few fuel cell systems that are available for purchase. The electrical efficiencies of PAFC are around 40 % and with combined heat and power units a 70 % efficiency can be achieved. Commercial 200 kW-PAFCs able to supply clean power at a range of locations such as a NY police station, a post office in Alaska, a credit-card system facility in Nebraska, a science center in Japan are provided from UTC Fuel Cell company, one of leader in fuel cells production.

ALKALINE FUEL CELLS (AFCs) : The Alkaline Fuel Cells (AFCs) employ an aqueous potassium hydroxide electrolyte (KOH) and an OH^- anion is conducted from the anode to cathode. A wide range of electro-catalysts can be used at both the electrodes (Ni, Ag, metal oxides, noble and non precious metals). Depending on the concentration of KOH, the AFC can operate between 60 and 250 °C. Water is consumed at the cathode and produced twice as fast at the anode. Since it can dilute the electrolyte and cause performance degradation, a fast water removal is necessary. The electrolyte is also sensitive to the CO_2 and even the small amount of CO_2 in air should be considered as a potential poison for alkaline fuel cell. Consequently, the fuel supply is limited to non-reactive constituents such as pure hydrogen and pure oxygen.

Because of the high sensitivity to CO_2, the application of AFCs to terrestrial applications is very challenging and quite limited. However, important applications concern the aerospace industry. The alkaline fuel cells were used as primary electric power for the Apollo space missions. The units were rated to 1.5 kW with a peak power capability of 2.2 kW and exemplary performance were reported: 10000h of operation in 18 missions without an in-flight accident (6).

MOLTEN CARBONATE FUEL CELLS (MCFCs) : The Molten Carbonate Fuel Cells (MCFCs) use as electrolyte a molten mixture of alkali carbonates (Li_2CO_3 and K_2CO_3) immobilized in a $LiOAlO_2$ matrix and CO_3^{2-} ions are the mobile charge carriers. In MCFCs, the CO_2 is produced at the nickel alloy anode and consumed at the nickel oxide cathode. Therefore, CO_2 must be extracted from the anode and circulated in the cathode. The MCFCs can run on hydrogen, simple hydrocarbons (like methane) and simple alcohols. The CO tolerance is not an issue for MCFCs, indeed the CO acts as a fuel instead as a poison.

Due to the relative high operating temperature, 650 °C, and the long start-up times, MCFCs are best suited for stationary, continuous power applications and for military applications. The electrical efficiency of a single unit is near 50 %, whereas in combined heat and power applications efficiencies could reach the 90 %.

SOLID OXIDE FUEL CELLS (SOFCs) : The Solid Oxide Fuel Cells (SOFCs) employ a solid ceramic electrolyte such as yttria (Y_2O_3)-stabilized zirconia (ZrO_2) (YSZ), which is an oxygen ion (O^{2-}) conductor. The anode is made of Ni-ZrO_2 cerment, whereas the cathode is a mixed conducting ceramic (Sr-doped $LaMnO_3$). The operating temperature of SOFCs is currently between 600 and 1000 °C with electrical efficiency 50-60 %. Due to the continuous progresses made in their development, the SOFCs are now considered for a wide range of applications, including stationary power generation, mobile power and auxiliary power units in vehicles.

POLYMER ELECTROLYTE MEMBRANE FUEL CELLS (PEMFCs) : The Polymer Electrolyte Membrane Fuel Cells (PEMFCs) contain a thin (20-200 μm) proton-conducting polymer electrolyte membrane (Nafion). Each side of the membrane is coated with a thin-layer of platinum-based catalyst and porous carbon electrode as supporting material. For a proper functioning the membrane needs to be fully hydrated, therefore the operating temperature of PEMFCs is generally limited to 120 °C. Concerning the fuel, PEMFCs can be operated with hydrogen or liquid fuels such as methanol (DMFC) or formic acid (DFAFC). The operation of a fuel cell system with a liquid fuel has become very attractive because of the high energy density and convenience of liquid fuels. However, the electrochemical reactivity is more sluggish than for hydrogen, therefore the fuel cell performance (power density/efficiency) are lower.

Hydrogen-PEMFCs provide the highest power density of all the fuel cell types (300-1000 mW/cm^2) and the best fast-start and on-off cycling characteristics. For these reasons, they are well suited for stationary, transport and portable applications. Many developers are now focused on the automotive sector. The first fuel cell car available for commercial lease was the Honda FCX (6). In the first model (2005), the fuel cell (two PEMFC stacks) was providing 86 kW of electricity and a capacitor was used for the start-up, acceleration, and to store electricity. In the advanced model (2008), the capacitor 0was substituted with a Li-battery and the fuel cell stack was improved to 100 kW power and a single higher capacity hydrogen tank with a capacity of 170 L of hydrogen at 350 atm. The power unity of this model was 400 pounds lighter, 45 % smaller, and 20 % more fuel efficient of the previous model.

At the state of the art, DMFCs exhibit low power density (30-100 $mWcm^{-2}$). For this reason, DMFCs have been widely investigated as portable power sources, to replace the rechargeable Li-ion batteries in electronic and communication devices and in battery charging. The idea of using micro-DMFCs for powering cellular phones was born in the Los Alamos National Laboratories and others companies such as Motorola, Toshiba, Sony, NEC, Jet Propulsion Laboratory, General Motors followed in the studies (7). In 2001, Smart Fuel Cell company presented a camcorder powered by a DMFC capable of running the system for approximately 8 hours with one tank of methanol (8). Recently, two prototypes, a 20 W DMFC notebook computer charger and a 2 W cell phone charger has been presented by Samsung company (6).

1.2.2. The competing technology for portable applications: the battery

The chemical energy stored in several hydrocarbons is much higher than that found in common battery materials(9). The specific energy of methanol is around 6000 $Whkg^{-1}$ (10); however, not all the energy is converted into electrical energy when methanol is fed into a fuel cell system. First, fuel cells are operated under the 100% efficiency since low cell voltages are associated to useful power densities (0.3 V to achieve 60 $mWcm^{-2}$ (11)). Then, some of the fuel is wasted at the cathode therefore the fuel utilisation is typically around 80 % (11). This results in an effective energy content of the fuel around the 22 %, which correspond to 1.0 $Whcm^{-3}$. For this reason, low temperature methanol fuel cells are basically in the development stage to replace the rechargeable lithium-ion batteries which have an established market position in cellular phones, notebook computers and other portable devices (12; 13).

The Li-ion batteries are the second generation of small rechargeable batteries that made their entrance on the market with the nickel-based batteries. For long time, the *nickel-cadmium (Ni/Cd) battery* has been the only battery available for power tools. But, the high toxicity of Cd and the high manufacturing cost promoted the development of a second Ni-based battery, the *nickel-metal hydride (Ni-MH) battery* characterized by higher energy density and lighter weight. However, from the moment it was available on the market, the *lithium ion (Li) battery* has been the choice for portable electronic devices because of the higher energy density and energy efficiency with respect to the Ni-based batteries. Made of a carbon/graphite anode, a $LiCoO_2$ cathode and an organic electrolyte with a Li-based salt, the Li-ion battery was introduced in 1991

by Sony company. During the years many improvements have been made in the capacity, performance and shape of the battery to make it more suitable for small cellular phones and notebook computers. In 2003, the Li-ion batteries dominated the market of rechargeable batteries with 3500 millions of dollars (12).

As mentioned above, direct methanol fuel cells are well suited for applications where the average power is only a few watts because of their potential to provide that power for long time. Some simple calculations show that DMFCs can very competitive with Li-ion batteries in terms of durability. A rechargeable Li-ion battery applied in a cell phone owns a nominal capacity of 900 mAh and nominal voltage of 3.7 V. By supposing a power consumption of 2 W to function the mobile in "talkative mode", the battery can be operative for almost 2 hours. A small DMFC fed with 7 ml of methanol (energy density 0.792 kgL^{-1}) and operated at 22 % of its efficiency shows an energy density of 6.76 Wh and can run the mobile for at least 3 hours. This is one of the advantages of using a DMFC; indeed it also does not require any time for recharging (~ 90 minutes for a Li-ion battery) and it can be maintained operative just by adding fuel in the tank.

1.3. Issues in DMFCs: the flooding

At the state of the art, the commercialization of direct methanol fuel cells is strongly limited by their low performance. There are few challenging problems to the development of such systems. In first place, the kinetics of the methanol oxidation reaction (MOR) at the anode and the oxygen reduction reaction (ORR) at the cathode (Table 1.1) are very slow and the electrodes suffer from high activations over potential (14; 15). The ORR is further complicated by the simultaneous methanol electro-oxidation due to the migration of methanol from anode to cathode through the permeable Nafion membrane (crossover). The presence of methanol in the cathode lowers the cathode potential, consumes oxygen and acts as poisoning for the Pt catalyst (14; 15; 16; 17). The cathode performance is also drastically lowered when air is used due to the low oxygen partial pressure and blanketing effect of nitrogen (14), and due to the accumulation of water in the porous structure(18; 17; 19).

The sources of water in DMFCs are the product water formed in the cathode and the water in the anode due to the utilization of diluted methanol. For each molecule of methanol involved in the oxidation reaction at the anode, one molecule of water is consumed and three water molecules are

produced in the cathode with a net of two molecules. Water is also transported from the anode to the cathode by diffusion, hydraulic permeation and electro-osmotic drag mechanisms (17; 20; 21; 22), as shown in Figure 1.5. Diffusion occurs under concentration gradients, hydraulic permeation is caused by gradients of pressure through the membrane and electro-osmotic drag is due to the protons which carry water molecules while diffusing from the anode to the cathode. Assuming that the electro-osmotic drag coefficient of water is equal to 2.5 per proton, fifteen water molecules are dragged from the anode to the cathode by the six protons involved in the electrochemical oxidation-reduction reactions(18).

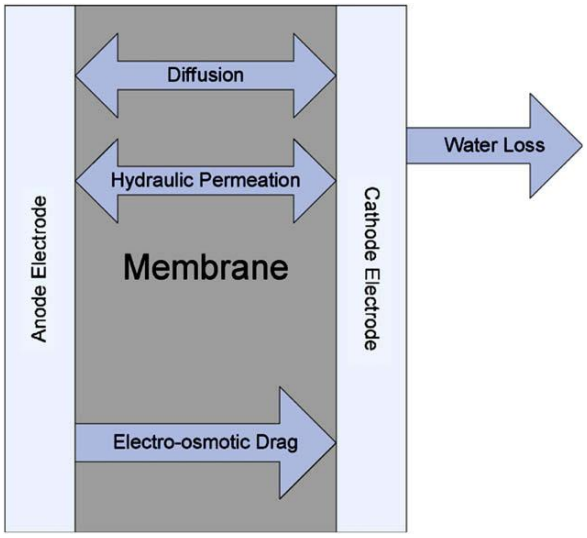

Figure 1.5 : Water transport mechanisms through Nafion membrane in DMFC (20).

The water produced and dragged into the cathode is usually removed out of the porous electrode via evaporation, water-vapor diffusion through the backing layer into the flow channels or by water back-diffusion through the membrane to the anode. However, if the rate of water removal is too low, water will accumulate resulting in the flooding of the cathode. The presence of a large amount of water prevents the reactant from reaching the catalyst' active sites, therefore the fuel cell performance are drastically reduced (18; 17; 21).

The water management is an important challenge in DMFCs. Increasing the fuel cell operating temperature is beneficial for improving the water evaporation and preventing the flooding but the final applications for which DMFCs are investigated strongly limit the operating temperature (~ 40 °C(8)). Generally high gas flow rates are used to remove the excess of water and to prevent the flooding of the cathode. However, this approach requires the use of external water coolers to condense the water and feed it back to the anode. This results in higher power consumption and

increases the complexity of the DMFC system(18; 17). Obviously the water management is even more challenging for the case of air-breathing systems in which the cathode is fed with air from the surrounding (no other auxiliaries) and only diffusion and natural convection are the transport mechanisms for removing water from the cathode (23).

Another simple approach to remove water from the cathode without auxiliaries consists in using PTFE-treated backing layers as supports for the cathode. Generally, the PTFE coating treatment ensures that the pores will not be congested with liquid water (15; 24; 25). However, it was found that after the treatment a portion of the pores of the backing layers were blocked by PTFE film (25; 26). This not only induced a higher oxygen transport resistance, but also hindered the liquid water removal. As a result, the PTFE-treated backing layer yielded lower performance and significant fluctuations in current density.

The use of microporous gas diffusion layers (GDL) as a strategy to improve the water removal has also been explored (27; 28; 24; 26). The presence of the hydrophobic microporous layers showed to be beneficial to reduce the flooding of the cathode. However, excessive PTFE content in the microporous layer decreases its porosity, increases the oxygen transport resistance and reduces the fuel cell performance. Therefore, an optimum PTFE content and proper thickness of the microporous layer should be determined to achieve the best results.

Another approach for a better water removal concerns the incorporation of the PTFE component in the cathode catalyst layer (29). This approach will be explained in the next paragraph after a brief description of the cathode catalyst layer structure.

1.4. Subject of this thesis

As previously discussed, the recent advances in the electrochemical energy conversion allow hydrogen and several hydrocarbons to have an important impact on the applicability of the alternative energies. Liquid fuels have become very attractive because of the high energy density of the fuel and convenient use in portable devices. In this context, methanol fuel cells are the promising candidates to replace the rechargeable Li-ion batteries in electronic and communication devices. However, at the state of the art, the commercialization of methanol fuel cells is yet limited by their low performance and specifically by the water accumulation in the

cathode. For this reason, this work is focused on the cathode flooding phenomenon and on improving the water removal from the cathode by increasing the hydrophobic character of the catalyst layer but without reducing the proton conductivity and the extent of the three-phase boundary. For this purpose, the simultaneous deposition of the Nafion and PTFE binders was explored as a strategy to prepare new cathode catalyst layers. These electrodes were characterized for their hydrophilicity, wettability, total pore volume, electrochemically in sulfuric acid solution, and under DMFC configuration.

1.4.1. Strategies used in this research project

A. Preparation of DMFC cathode catalyst layer by simultaneous deposition of Nafion and PTFE Binders

The DMFC cathode catalyst layer is a porous structure formed by Pt particles supported on carbon and Nafion ionomer, and its structure comes directly from the PEMFC technology (30). This is the active layer and location of the oxygen reduction reaction. The typical structure of a catalyst layer is reported in Figure 1.6. The Pt particles are in perfect contact with the carbon support which provides the electronic conductivity and the Nafion ionomer which provides the ionic conduction. Here, Pt particles, protons and gas-reactant give origin to the three-phase boundary were the ORR takes place.

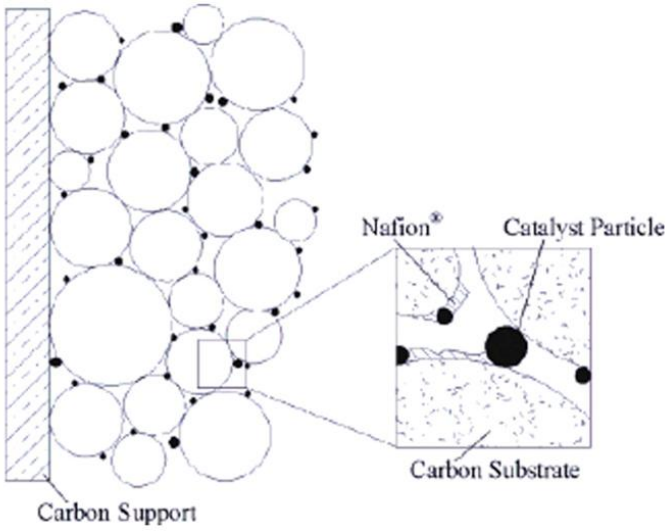

Figure 1.6 : DMFC cathode catalyst layer and three-phase boundary (29).

In the first generation of catalyst layer, the unsupported Pt particles were bounded by the resilient PTFE polymer (31) whereas the impregnation of the catalyst layer with Nafion ensured the proton conductivity. Despite the excellent long-term performance of the PTFE bound catalyst layer, the required amount of Pt catalyst and the associated cost were extremely high. In the next generation of catalyst layer for PEMFC, the Nafion thin-film design (30) was privileged to enhance the proton conductivity inside the pores, to increase the catalyst active area (and the catalyst utilization), to reduce the supported Pt loading, and to make more affordable the commercialization of the fuel cells. The Nafion loaded catalyst layers showed a higher performance (30; 32), however an excessive amount of ionomer can block the porous structure leading to limited mass transfer (gas diffusion and water removal) (30; 32; 33).

Over the years, different studies have been dedicated to the optimization of the composition of the DMFC cathode catalyst layer (34; 35; 36; 37; 38; 39; 40). The Nafion content was found to affect the catalyst utilization and the catalyst layer resistivity(34; 35; 36) and for optimized Nafion content, reduced catalyst layer resistance and higher performance were observed. However, an excess of ionomer in the catalyst layer can isolate the catalyst particles, obstruct the gas diffusion to the reaction sites (35; 36; 41; 39) and promote the flooding of the cathode(42; 43).

It has been demonstrated for PEMFC that hydrophobic gas diffusion layers increase the hydraulic pressure in the cathode microporous layer, which in turn creates a pressure differential across the membrane and a water backflow from the cathode to the anode (18; 44; 45). Such approach would provide a simple way to remove water from the cathode without using auxiliaries. Two recent studies have reported the use of PTFE in DMFC cathode' catalyst layers in counteracting the flooding of the catalyst layer(46; 47). The authors found that the higher hydrophobicity of the cathode catalyst layer reduces its wettability and the Pt poisoning from methanol cross-over. However, the impact of the PTFE binder on the overall performance of the MEAs varies between the works and probably due to the different PTFE content, catalyst layer composition and fabrication methods.

In the present study, we explore the partial substitution of Nafion by PTFE and the simultaneous deposition of the two binders with the Pt catalyst as a strategy to improve the water removal, and to guarantee the continuous supply of oxygen to the catalyst sites during the DMFC operation,

without reducing, or minimizing the losses on the proton conductivity and extent of the triple-phase boundary in the catalyst layer. In practice, series of Pt-based cathodes where I) the relative Nafion and PTFE content was varied between 0 and 15 % but the total amount of binder was maintained constant; II) the Pt distribution of a Nafion/PTFE-based cathode was varied; III) the morphology of a PTFE-based cathode was varied by sintering the cathode at 350 °C, spraying the cathode with Nafion or by preparing the cathode on a wet-proofed support were prepared and characterized by physicochemical, ex-situ electrochemical and in-situ fuel cell techniques.

In this work, no gas diffusion layer was used in the preparation of the DMFC cathodes. This choice was based on two different reasons. From one side, the DMFC cathodes require high catalyst loading so the resulting cathodes are relatively thick. Therefore, this choice aimed to minimize the serial resistance in the fuel cell, and indeed has been adopted by other researchers for this specific application(48; 49; 50; 51). On the other side, as mentioned above, this work is focused on the flooding of the cathode catalyst layer. Therefore, it was purposely chosen to avoid the GDL utilization also to induce an excessive accumulation of water in the cathode.

In addition, the use of Nafion/PTFE cathodes was also meant for establishing a simple protocol for the investigation of the cathodes' flooding (next paragraph) and to set a baseline for a future work concerning the preparation of cathodes using other co-polymers than Nafion and PTFE.

B. Development of an electrochemical strategy for the investigation of flooding in DMFC cathodes

Over the last two decades the water flooding in hydrogen PEMFCs has been extensively studied (52). Several experimental methods based on the combination of impedance spectroscopy measurements, variation of the experimental parameters (cell temperature, anode and cathode flow humidity, reactant pressure) and observation of cell voltage or pressure drops have been proposed as diagnostic tools for detection of water flooding (53; 54; 55; 56). By a model-based approach coupled with EIS, it was shown that the flooding occurs in two steps (56). During the first steps, water accumulates in the gas diffusion layer while the cell voltage drops slowly. During the second step, the water droplets block the gas channels. This produces an increase of the local pressure that quickly flushes out the excess liquid water and restores the current density. However, once the accumulated water cannot be evacuated efficiently, the water flooding brings

to an increase of the reactant diffusion resistance and induces a rapid cell voltage drop, as shown in Figure 1.7 for PEMFC fuel cells.

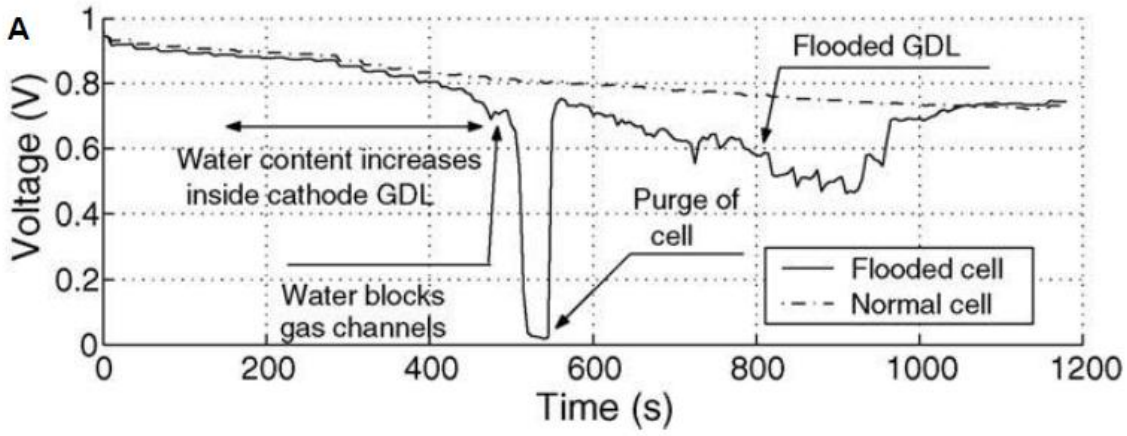

Figure 1.7 : Flooding in a PEMFC(56).

The pressure drop between the inlet and outlet channels has been used as well as diagnostic tool to monitor the water content in gas diffusion layers (57). From the pressure drop, the water saturation which corresponds to the extent of flooding was estimated. A non-invasive method based on two sensing electrodes (SE) placed at the fuel inlet and outlet was also proposed for the early diagnosis of the flooding (58). The failure mechanism was identified by the characteristic response of the SEs occurring before any variation of the cell potential.

Visual methods have been used to look inside an operational fuel cell and visualizing the distribution of liquid water. These methods are based on direct visualization, nuclear magnetic resonance (NMR) imaging, beam interrogation and fluorescence microscopy. The direct visualization technique provide information about the water transport in gas flow channels, GDL pores and catalyst layer (59; 60; 61; 62; 63; 64; 65; 66; 67). This technique requires a transparent cell plate that allows access to the channels for optical devices, including digital or infrared cameras. It is particularly useful to provide information on water droplet formation, growth and movement or to investigate the effect of hydrophobicity, channel geometry, and air flow rate on droplet formation and instability. However, this method only provides qualitative data because of limited depth perception from the transparent window.

The NMR imaging technique enables the in situ measurement of liquid water distribution through materials that would be opaque to optical access (68; 69; 70; 71; 72). It provides valuable

information about the water content in gas channels and membranes but it cannot be used to investigate the GDLs due to the rapid attenuation of the signal in the carbon layer.

The beam interrogation involves neutron imaging (73; 74; 75), electron microscopy (76; 77; 78) and X-rays (79; 80) techniques. The neutron imaging technique is used because on the sensitive response of neutrons to water and their insensitivity to common fuel cell materials. It is the only diagnostic tool that can be applied in situ with minimal invasiveness and maxima ability to provide information, however, because of the high cost and rare availability of radioactive radiation equipments it has limited application. Vapor condensation, liquid water morphology and breakthrough in the porous layers of PEMFC can be observed by environmental scanning electron microscopy (ESEM) technique.

Besides visual methods, computational fluid dynamics (CFD) theoretical models have been used to describe the water management in PEMFC and the water transport mechanisms inside the fuel cell (81; 82). Three-dimensional CFD simulations were reported to investigate the effect of GDL flooding on cell performance (83), the effect of flow rate, inlet humidity and temperature on the liquid water flooding in the cathode (84) and the effect of water flooding in the GDL and catalyst layer on the fuel cell performance (85).

As shown above, several techniques are available for the investigation of flooding. However, no established, unique and simple methodology exists as yet for the determination of the flooding under any operative condition. For this reason a strategy for the investigation of the flooding of a DMFC cathode was proposed in this work. It was believed that the electrochemical characterization of the cathodes in 0.5 M sulphuric acid solution can be representative of the flooding condition encountered in a fuel cell, therefore the ex-situ electrochemical characterization was proposed for a pre-screening of the cathodes before their test in fuel cell. This procedure is less-time consuming and less expensive since it does not require the preparation of the electrode-membrane assemblies (MEA) and the use anode catalysts is not required. Then the cathodes were tested in a DMFC system. After activation in temperature, polarization curves and impedance spectra were recorded under fully humidified air and oxygen to investigate the cathode performance. The response of the MEAs to the water content in the air stream was also studied by varying the relative humidity at the cathode (50% RH and >100% RH).

1.5. Summary of the thesis

This chapter has been an introduction to the energy revolution and the main alternative energies under development. The focused has been pointed towards fuel cells and in particular to direct methanol fuel cells. The high energy density of the liquid fuel makes methanol fuel cell of easy applicability in portable devices and best candidate to replace Li-ion batteries. However, at the state of the art the commercial availability of DMFCs is still limited by its low performance and the flooding of the cathode is one of the causes. The flooding phenomena and the main diagnostic technique have been explained. The interest in improving the water removal in the cathode by investigation of Nafion/PTFE-based cathodes and in developing a strategy for the investigation of flooding has been reported. All the experimental details and techniques used in this work are reported in the next chapter.

The third and four chapters are devoted to the use of the electrochemical impedance spectroscopy technique and fitting procedure to characterize cathodes immersed in sulphuric acid solution (chapter 3) and in a membrane-electrode-assembly in fuel cell (chapter 4). On the importance of chapter 4 the analysis of the complete DMFC impedance spectra and the attribution of the low frequency semicircle to the cathode behaviour. The experimental results of different series of Nafion/PTFE-based cathodes are reported in chapters 5 and 6. The chapter 5 concerns the investigation of Nafion/PTFE-based cathodes, and as it will be shown the simultaneous deposition of Nafion and Teflon in a specific ratio improves the performance of the cathodes in terms of flooding. In addition, it will be shown that the PTFE-based cathode had a very low resistance for the transport of protons through the catalyst layer. The chapter 6 concerns a further investigation of PTFE-based cathode which underwent to morphological variations. Finally, the last chapter contains the conclusions of this work and the future perspectives as well.

1.6. References

1. **(IEA), International Energy Agency.** *CO2 emissions from fuel combustion - Highlights.* 2011.

2. **Greenpeace, European Renewable Energy Council -.** *Energy Revolution - A sustainable world energy lookout.* June 2010.

3. **X.-Z. Yuan, H. Wang.** PEM Fuel Cell Fundamentals. [book auth.] J. Zhang. *PEM Fuel Cell Electrocatalysts and Catalyst Layers: Fundamental and Applications.* s.l. : Springer, 2008, pp. 1-31.

4. **EG&G Technical Services, Inc.** *Fuel Cell Handbook.* 7th. 2004. pp. 1-2.

5. http://www.green-planet-solar-energy.com/fuel-cells.html. [Online]

6. **R. O'Hayre, S.-W. Cha, W. Colella, F.B. Prinz.** *Fuel Cell Fundamentals (2nd edition).* s.l. : Wiley&sons, 2009. p. 283.

7. **Agnolucci, P.** Economics and market prospects of portable fuel cells. *International Journal of Hydrogen Energy .* 2007, Vol. 32, pp. 4319 – 4328.

8. **Hoogers, G.** Portable Applications. *Fuel Cell Handbook Technology.* 9.

9. **Panasonic.** Overview of Lithium ion batteries. *http://www.panasonic.com/industrial/includes/pdf/Panasonic_LiIon_Overview.pdf.* [Online] 2007.

10. **Dyer, C.K.** Fuel cells and portable electronics. *VLSI Circuits, 2004. Digest of Technical Papers. 2004 Symposium on.* 2004, pp. 124 - 127.

11. **J. Larminie, A. Dicks.** Direct Methanol Fuel Cell Applications. *Fuel cell system explained.* 2nd. s.l. : John Wiley & Sons Ltd, 2003, 6.6, pp. 157-160.

12. **M. Winter, R.J. Brodd.** What are Batteries, Fuel Cells, and Supercapacitors? *Chemical Reviews.* 2004, Vol. 104, pp. 4245-4269.

13. **I. Hadjipaschalis, A. Poullikkas, V. Efthimiou.** Overview of current and future energy storage technologies for electric power applications. *Renewable and Sustainable Energy Reviews.* 2009, Vol. 13, pp. 1513-1522.

14. **A.S. Aricò, S. Srinivasan, V. Antonucci.** DMFCs: From Fundamental Aspects to Technology Development. *Fuel Cells.* 2001, Vol. 1, 2, p. 133.

15. **S.K. Kamarudin, W.R.W. Daud, S.L. Ho, U.A. Hasran.** Overview on the challenges and developments of micro-direct methanol fuel cells (DMFC). *Journal of Power Sources.* 2007, Vol. 163, pp. 743–754.

16. **C.Y. Du, T.S. Zhao, W.W. Yang.** Effect of methanol crossover on the cathode behavior of a DMFC: A half-cell investigation. *Electrochimica Acta.* 2007, Vol. 52, p. 5266.

17. **S.K. Kamarudin, F. Achmad, W.R.W. Daud.** Overview on the application of direct methanol fuel cell (DMFC) for portable electronic devices. *International Journal of Hydrogen Energy .* 2009, Vol. 34, pp. 6902-6916.

18. **G.Q. Lu, F.Q. Liu, C.-Y. Wang.** Water Transport Through Nafion 112 Membrane in DMFCs. *Electrochemical and Solid-State Letters.* 2005, Vol. 8, 1, p. A1.

19. **V.B. Oliveira, C.M. Rangel, A.M.F.R. Pinto.** Water management in direct methanol fuel cells. *International Journal of Hydrogen Energy.* 2009, Vol. 34, pp. 8245-8256.

20. **G. Jewett, Z. Guo, A. Faghri.** Water and air management systems for a passive direct methanol fuel cell. *Journal of Power Sources.* 2007, Vol. 168, pp. 434-446.

21. **T.S. Zhao, C. Xu, R. Chen, W.W. Yang.** Mass transport phenomena in direct methanol fuel cells. *Progress in Energy and Combustion Science.* 2009, Vol. 35, pp. 275–292.

22. **S Gottesfeld, T. Zawodzinski.** Polymer Electrolyte Fuel Cells. *Advances in Electrochemical Sciences and Engineering.* 1997, Vol. 5, 4, pp. 195-301.

23. **C.Y. Chen, P. Yang.** Performance of an air-breathing direct methanol fuel cell. *Journal of Power Sources.* 2003, Vol. 123, pp. 37-42.

24. **K.-Y. Song, H.-K. Lee, H.-T. Kim.** MEA design for low water crossover in air-breathing DMFC. *Electrochimica Acta.* 2007, Vol. 53, pp. 637–643.

25. **C. Xu, T.S. Zhao, Y.L. He.** Effect of cathode gas diffusion layer on water transport and cell performance in direct methanol fuel cells. *Journal of Power Sources.* 2007, Vol. 171, pp. 268–274.

26. **C. Xu, T.S. Zhao.** In situ measurements of water crossover through the membrane for direct methanol fuel cells. *Journal of Power Sources.* 2007, Vol. 168, pp. 143–153.

27. **Pan, Y.H.** Advanced air-breathing direct methanol fuel cells for portable applications. *Journal of Power Sources.* 2006, pp. 282-289.

28. **F.Q. Liu, G.Q. Lu, C.Y. Wang.** Low crossover of methanol and water through thin membranes in direct methanol fuel cells. *Journal of Electrochemical Society.* 2006, Vol. 153, pp. A543-A553.

29. **A.M. Zainoodin, S.K. Kamarudin, W.R.W. Daud.** Electrode in direct methanol fuel cells. *2010.* Vol. 35, pp. 4606-4621.

30. **S. Litster, G. McLean.** PEM fuel cell electrodes. *Journal of Power Sources .* 2004, Vol. 130, pp. 61-76.

31. **M.S. Wilson, J.A. Valerio and S.Gottesfeld.** Low Platinum loading electrodes for polymer electrolyte fuel cells fabricated using thermoplastic ionomers. *Electrochimica Acta.* 1995, Vol. 40, 3, pp. 355-363.

32. **E. Antolini, L. Giorgi, A. Pozio, E. Passalacqua.** Influence of Nafion loading in the catalyst layer of gas-diffusion electrodes for PEFC. *Journal of Power Sources.* 1999, Vol. 77, pp. 136–142.

33. **G. Li, P.G. Pickup.** Ionic Conductivity of PEMFC Electrodes. *Journal of The Electrochemical Society.* 2003, Vol. 150, 11, p. C745.

34. **B. Krishnamurthy, S. Deepalochani, K.S. Dhathathreyan.** Effect of Ionomer Content in Anode and Cathode Catalyst Layers on Direct Methanol Fuel Cell Performance. *Fuel Cells.* 2008, Vol. 8, p. 404.

35. **K. Furukawa, K. Okajima, M. Sudoh.** Structural control and impedance analysis of cathode for direct methanol fuel cell. *Journal of Power Sources.* 2005, Vol. 139, p. 9.

36. **S.C. Thomas, X. Ren, S. Gottesfeld.** Influence of Ionomer Content in Catalyst Layers on Direct Methanol Fuel Cell Performance. *Journal of The Electrochemical Society.* 1999, Vol. 146, 12, p. 4354.

37. **T.V. Reshetenko, H.-T. Kim, H. Lee, M. Jang, H.-J. Kweon.** Performance of a direct methanol fuel cell (DMFC) at low temperature: Cathode optimization. *Journal of Power Sources.* 2006, Vol. 160, pp. 925–932.

38. **F. Liu, C.-Y. Wang.** Optimization of cathode catalyst layer for direct methanol fuel cells Part I. Experimental investigation. *Electorchimica Acta.* 2006, Vol. 52, p. 1417.

39. **X. Zhao, W. Li, Y. Fu, A. Manthiram.** Influence of ionomer content on the proton conduction and oxygen transport in the carbon-supported catalyst layers in DMFC. *International Journal of Hydrogen Energy.* 2012, Vol. 37, pp. 9845-9852.

40. **M.A. Abdelkareema, T. Tsujiguchi, N. Nakagawa.** Effect of black catalyst ionomer content on the performance of passive DMFC. *Journal of Power Sources.* 2010, Vol. 195, pp. 6287–6293.

41. **B. Krishnamurthy, S. Deepalochani.** Experimental analysis of platinum utilization in a DMFC cathode. *Journal of Applied Electrochemistry.* 2009, Vol. 39, p. 1003.

42. **M. Eikerling, A.A. Kornyshev, A.R. Kucernak.** Water in polymer electrolyte fuel cells: friend or foe? *Physic Today.* 2006, Vol. 59, p. 38.

43. **X. Ren, M.S. Wilson, S. Gottesfeld.** High Performance Direct Methanol Polymer Electrolyte Fuel Cells. *Journal of Electrocchemical Society.* 1996, Vol. 143, 1, p. L12.

44. **E. Peled, A. Blum, A. Aharon, M. Philosoph, Y. Lavi.** *Electrochem. Solid-State Lett.* 2003, Vol. 6, p. A268.

45. **U. Pasaogullari, C.Y. Wang.** Liquid Water Transport in Gas Diffusion Layer of Polymer Electrolyte Fuel Cells. *Journal of The Electrochemical Society.* 2004, Vol. 151, 3, p. A399.

46. **V. Baglio, A. Stassi, F.V. Matera, H. Kim, V. Antonucci, A.S. Aricò.** AC-Impedance Investigation of Different MEA Configurations for Passive-Mode DMFC Mini-Stack Applications. *Fuel Cells.* 2010, Vol. 10, p. 124.

47. **A. Di Blasi, V. Baglio, T. Denaro, V. Antonucci, A.S. Aricò.** Optimization of Electrode Properties for Low Temperature DMFC Applications. *Journal of New Materials for Electrochemical Systems.* 2008, 11, p. 165.

48. **A.S. Aricò, V. Antonucci, V. Alderucci, E. Modica, N. Giordano.** A.c.-impedance spectroscopy study of oxygen reduction at Nation coated gas-diffusion electrodes in sulphuric acid: Teflon loading and methanol cross-over effects. *Journal of Applied Electrochemistry.* 1993, Vol. 23, p. 1107.

49. **C.Y. Chen, C.S. Tsao.** Characterization of electrode structures and the related performance of direct methanol fuel cells. *International Journal of Hydrogen Energy.* 2006, Vol. 31, p. 391.

50. **C. Song, P.G. Pickup.** Effect of hot pressing on the performance of direct methanol fuel cells. *Journal of Applied Electrochemistry.* 2004, Vol. 34, p. 1065.

51. **A.S. Aricò, V. Alderucci, V. Antonucci, S. Ferrara, V. Recupero, N. Giordano, K. Kinoshita.** ac Impedance spectroscopy of porous gas diffusion electrode in sulphuric acid. *Electrochimica Acta.* 1992, Vol. 37, 3, pp. 523-529.

52. **M. Ji, Z. Wei.** A review of water management in polymer electrolyte membrane fuel cells. *Energies.* 2009, Vol. 2, pp. 1057-1106.

53. **J.M.L. Canut, R.M. Abouatallah, D.A. Harrington.** Detection of membrane drying, fuel cell flooding, and anode catalyst poisoning on PEMFC stacks by electrochemical impedance spectroscopy. *Journal of Electrochemcal Society.* 2006, Vol. 153, pp. A857-A864.

54. **F. Barbir, H. Gorgun, X. Wang.** Relationship between pressure drop and cell resistance as a diagnostic tool for PEM fuel cells. *Journal of Power Sources.* 2005, Vol. 141, pp. 96-101.

55. **A. Hakenjos, H. Muenter, U. Wittstadt, C. Hebling.** A PEM fuel cell for combined measurement of current and temperature distribution, and flow field flooding. *Journal of Power Sources .* 2004, Vol. 131, pp. 213–216.

56. **N. Fouquet, C. Doulet, C. Nouillant, G. Dauphin-Tanguy, B. Ould-Bouamama.** Model based PEM fuel cell state-of-health monitoring via ac impedance measurements. *Journal of Power Sources.* 2006, Vol. 159, pp. 905–913.

57. **K. Ito, K. Ashikaga, H. Masuda, T. Oshima,Y. Kakimoto, K. Sasaki.** Estimation of flooding in PEMFC gas diffusion layer by differential pressure measurement. *Journal of Power Sources.* 2008, Vol. 175, pp. 732–738.

58. **O. Herrera, W. Mérida, D.P.Wilkinson.** Sensing electrodes for failure diagnostics in fuel cells. *Journal of Power Sources.* 2009, Vol. 190, pp. 103–109.

59. **X. Liu, H. Guo, C.F. Ma.** Water flooding and two-phase flow in cathode channels of proton exchange membrane fuel cells. *Journal of Power Sources.* 2006, Vol. 156, pp. 267-280.

60. **X. Liu, H. Guo, F. Ye, C.F. Ma.** Water flooding and pressure drop characteristics in flow channels of proton exchange membrane fuel cells. *Electrochimica Acta.* 2007, Vol. 52, pp. 3607-3614.

61. **A.M. Lopez, F. Barreras, A. Lozano, J.A. Garcia, L. Valino, R. Mustata.** Comparison of water management between two bipolar plate flow-field geometries in proton exchange membrane fuel cells at low-density current range. *Journal of Power Sources.* 2009, Vol. 192, pp. 94-99.

62. **I.S. Hussaini, C.Y. Wang.** Visualization and quantification of cathode channel flooding in PEM fuel cells. *Journal of Power Sources.* 2009, Vol. 187, pp. 444-451.

63. **H.P. Ma, H.M. Zhang, J. Hu, Y.H. Cai, B.I. Yi.** Diagnostic tool to detect liquid water removal in the cathode channels of proton exchange membarne fuel cells. *Journal of Power Sources.* 2006, Vol. 162, pp. 469-473.

64. **K. Tuber, D. Pocza, C. Hebling.** Visualization of water buildup in the cathode of a transparent PEM fuel cell. *Journal of Power Sources.* 2003, Vol. 124, pp. 403-414.

65. **D. Spernjak, S. Advani, A. Prasad.** Experiemntal investigation of liquid water formation and transport in a transparent single-serpentine PEM fuel cell. *Journal of Power Sources.* 2007, Vol. 170, pp. 334-344.

66. **F.B. Weng, A. Su. C.Y. Hsu, C.Y. Lee.** Study of water-flooding behaviour in cathode channel of a transparent proton exchange membrane fuel cell. *Journal of Power Sources.* 2006, Vol. 157, pp. 674-680.

67. **X.G. Yang, F.Y. Zhang, A. Lubawy, C.Y. Wang.** Visualization of liquid water transport in a PEFC. *Electrochemical Solid-State Letters.* 2004, Vol. 7, pp. A408-A411.

68. **Z.H. Zhang, J. Martin, J.F. Wu, H.J. Wang, K. Promislow, B.J. Balcom.** Magnetic resonance imaging of water content across the Nafion membrane in an operation PEM fuel cell. *Journal of Magnetic Resonance.* 2008, Vol. 193, pp. 259-266.

69. **Z. Dunbar, R. Masel.** Quantitative MRI study of water distribution during operation of a PEM fuel cell using Teflon flow fields. *Journal of Power Sources.* 2007, Vol. 171, pp. 678-687.

70. **K.W. Feindel, S.H. Bergens, R.E. Wasylishen.** The influence of membarne electrode assembly water content on the performance of a polymer electrolyte membarne fuel cell as investiagted by H NMR microscopy. *Physical Chemistry Chemical Physic.* 2007, Vol. 9, pp. 1850-1857.

71. —. The use of H NMR microscopy to study proton-exchange membrane fuel cells. *Physical Chemistry Chemical Physic.* 2006, Vol. 7, pp. 67-75.

72. —. Insights into the distribution of water in a self-humidifying H2/O2 proton-exchange membrane fuel cell using H NMR microscopy. *Journal of American Chemical Society.* 2006, Vol. 128, pp. 14192-14199.

73. **T.J. Kim, J.R. Kim, C.M. Sim, S.W. Lee, M. Kaviany, S.Y. Son, M.H. Kim.** Experimental approaches for distribution and behaviour of water in PEMFC under flow direction and differential pressure using neutron imaging technique. *Nuclear Instr. and Meth.Phys.Res.Sec.A.* 2009, Vol. 600, pp. 325-327.

74. **G.Gebel, O.Diat.** Neutron and X-ray scattering suitable tools for studying ionomer membranes. *Fuel Cells.* 2005, Vol. 5, pp. 261-276.

75. **J.J. Gagliardo, J.P. Owejan, T.A. Trabold, T.W. Tighe.** Neutron radiography characterization of an operating proton exchange membrane fuel cell with localized current distribution measurements. *Nucl. Instr. Meth. Phy. Res. Sec. A.* 2009, Vol. 605, pp. 115-118.

76. **L.-J. Yu, W.-C. Chen, M.-J. Qin, G.-P. Ren.** Experimental research on water management in proton exchange membrane fuel cells. *Journal of Power Sources.* 2009, Vol. 189, pp. 882-887.

77. **J.-H. Nam, K.J. Lee, G.S. Hwang, C.J. Kim, M. Kaviany.** Microporous layer for water morphology control in PEMFC. *Int. J. Heat Mass Transfer.* 2009, Vol. 52, pp. 2779-2791.

78. **C. Lim, C.Y. Wang.** Effects of hydrophobic polymer content in GDL in power performance of a PEM fuel cell. *Electrochimica Acta.* 2004, Vol. 49, pp. 4149-4156.

79. **S.J. Lee, N.Y. Lim, S. Kim, G.G. Park, C.S. Kim.** X-ray imaging of water distribution in a polymer electrolyte fuel cell. *Journal of Power Sources.* 2008, Vol. 185, pp. 867-870.

80. **P. Sinha, P. Halleck, C.Y. Wang.** Quantification of liquid water saturation in a PEM fuel cell diffusion medium using X-ray microtomography. *Electrochemical Solid-State Letters.* 2006, Vol. 9, pp. A244-A248.

81. **H. Ju, G. Luo, C.Y. Wang.** Probing liquid water saturation in diffusion media of polymer electrolyte fuel cells. *Journal of Electrochemical Society.* 2007, Vol. 154, pp. B218-B228.

82. **S. Shimpalee, S. Greenway, D. Spuckler, J.W. Van Zee.** Predicting water and current distributions in a commercial-size PEMFC. *Journal of Power Sources.* 2004, Vol. 135, pp. 79-87.

83. **S. Shimpalee, U. Beuscher, J.W. Van Zee.** Analysis of GDL flooding effect on PEMFC performance. *Electrochimica Acta.* 2077, Vol. 52, pp. 6748-6754.

84. **D. Natarajan, T.V. Nguyen.** Three-dimensional effects of liquid water flooding in the cathode of a PEM fuel cell. *Journal of Power Sources.* 2003, Vol. 115, pp. 66-80.

85. **G.Y. Lin, W.S. He, T.V. Nguyen.** Modeling liquid water effects in the gas diffusion and catalyst layers of the cathode of a PEM fuel cell. *Journal of Electrochemical Society.* 2004, Vol. 151, pp. A1999-A2006.

CHAPTER 2 : EXPERIMENTAL METHODS

2.1. Preparation of DMFC cathodes

A. Techniques of preparation

The cathode preparation is one of the most important and challenging steps involved in the membrane - electrodes assembly (MEA) manufacture. The cathode should be designed to generate high reaction rate and power output by using the minimum amount of catalyst. In addition, for a proper functioning it is required:

a) Extended interface between the cathode and the electrolyte membrane,
b) Efficient proton transport through the catalyst layer,
c) Easy transport of oxygen and removal of condensed water,
d) Continuous electronic conduction between the three-phase boundaries and the current collectors,
e) For the specific case of DMFC, low concentration polarization caused by the liquid sealing effect.

The cathode performance depends on these physical characteristics which are affected by the technique involved in the preparation of the catalyst layer (CL). Traditionally, a catalyst slurry is applied on a porous support by various coating methods such as screen printing, knife-coating, slot-coating, brushing, spraying and painting, (1; 2; 3; 4).

Screen printing is one of the most popular methods used for the fabrication of CLs due to its convenience and adaptability. In this technique the catalyst slurry is directly printed onto the support by using a screen which determines the amount of catalyst ink applied to the substrate. Knife coating and slot coating are also well-know methods especially in the production of commercial fuel cell electrodes. In the knife coating, the amount of applied ink is controlled by the distance knife-substrate, even if a certain amount of ink that penetrates in the pores of the substrate. In the slot coating, the amount of applied catalyst is controlled by a metering pump. In spraying, as described from Srinivasan (5), the catalyst ink is prepared by mixing the catalyst, the solvent and the ionomer and it is repeatedly sprayed, in presence of air or nitrogen, onto a sheet of carbon cloth or carbon paper. Between each spraying, the support is heated to evaporate the

solvent, in order to prevent the components from re-dissolving during the next spraying. Because of its simplicity and low-cost, and the possibility to prepare thinner samples (6), the spray technique is a promising method for the fabrication of commercial electrodes. Indeed a production line can be fully automated and therefore the electrode fabrication can be readily scaled up.

In addition to the conventional methods, novel advanced methods such as electrospray, vapor deposition and sputtering, electro-deposition and electrophoretic deposition techniques have been developed (1; 7; 8). The electrospray method shows both morphological and structural improvements that contribute to better catalyst utilization in comparison with conventional methods. The physical, thermal or chemical vapor deposition (CVD) methods are based on the advantageous deposition of low-loading Pt nanoparticles on gas diffusion electrodes. The sputtering provides a method of depositing a thin catalyst layer that delivers high performance combined with a low Pt loading. In pulse electro-deposition, it is ensured that most of the deposited Pt catalyst is in close contact with the membrane. In electrophoretic deposition (EPD) a suspension consisting of ethanol, carbon powders with Pt catalyst, and ionomer is used to obtain a stable dispersed solution; the thickness of the prepared CL is controlled by the EPD duration or concentration of the suspension.

At the state of the art, some technical aspects of the catalyst layer for DMFC still need to be improved. In particular, it is necessary to:

- *Maximize the three-phase interface of the CL*. The performance of a CL depends on its electrochemical active surface area. High catalyst loading are generally required to counteract the poisoning effect of methanol (9) and consequently thick catalyst layers are prepared. The thickness of the CL increases the tortuosity of oxygen diffusion and the pathway of proton conduction, leading to low catalyst utilization and mass transport limitations. Optimizing the ratios of the components, the structure, the thickness and the hydrophobicity or hydrophilicity is necessary.
- *Stabilize the metal particle on the support*. The metal particles on supports, like carbon powder or carbon nanotubes, undergo agglomeration or detach from the support. This is because there are no chemical bonds between the particles and the support and the nanoparticles are active and mobile and they have the tendency to agglomerate together. It

is necessary to structure the support in such a way that allows the metal particles to anchor tightly on the surface of the support.

- *Reduce the degradation of the CLs' components*. The catalyst particles, binder and carbon support degrade during the operation due to chemical and electrochemical corrosion. It is necessary to find ways to stabilize the components such as the graphitization used to increase the stability and conductivity of the support.
- *Accelerate the activation of the CL*. To make the fuel cell work it is necessary to activate the MEA. This process makes the CL reaches its maximum activity. Depending on the used method, the activation of the MEA can take time therefore it is necessary to find ways for an easier start up.

B. Instrumentation and experimental parameters

In this work, different DMFC composite Pt-based cathodes were realized by spray technique. All cathodes were prepared by deposition of the catalyst layer on a porous carbon cloth supports (Ballard 1071 HCB, ElectroChem Inc. EC-CC1-060-T) to form the so called Gas Diffusion Electrodes (GDE). Since high catalyst loadings were used, it was chosen to minimize the thickness of the cathodes by not using any microporous gas diffusion layer in between the carbon support and the catalyst layer. Indeed, this approach has already been adopted in the preparation of electrodes for DMFCs (10; 11; 12; 13). The catalyst layer were formed using catalyst inks which were prepared by mixing the required amounts of

- Catalyst: 60 wt % Pt/Vulcan catalyst (BASF)
- Binder: 5 wt % Nafion solution (Ion Power)
- Binder: 60 wt % Teflon suspension (Sigma-Aldrich)
- Solvents: water and isopropyl alcohol

The inks were prepared in two steps. In the first step the Pt/C catalyst powder was dispersed in the solvents. In the second step the Nafion solution and/or the Teflon suspension were added to the mixture. Each step was followed by 15 min of homogenization in an ultrasonic water bath at 40 °C. The catalyst inks were then sprayed under air onto 36 cm^2 carbon supports on a hot plate at 80 °C, as shown in Figure 2.1. From the 36 cm^2 samples, several cathodes were derived and used for the ex-situ electrochemical and in-situ fuel cell characterization. A spray-gun or an

airbrush were used to prepared the cathodes and their specifications are presented below. The final composition of the DMFC cathodes is reported in Table 2.1.

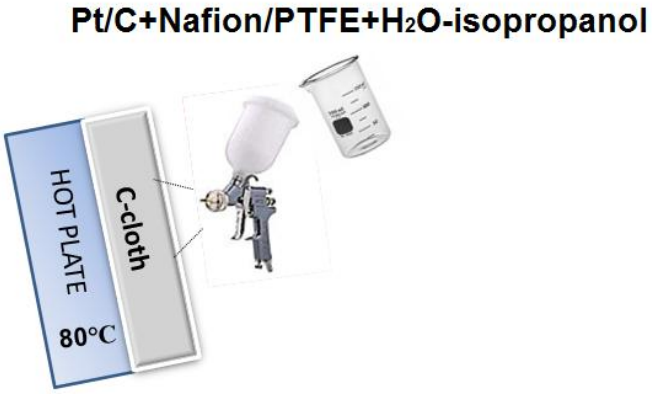

Figure 2.1: Deposition of the catalyst layer by spray technique.

Table 2.1: Description of the parameters related to the preparation of the cathodes.

	Spray gun / Airbrush	*Name*	*Pt loading mgcm^{-2}*	*wt% Nafion*	*wt% PTFE*	*Support*
Series I	TJR spray gun (HVLP)	N15/T00	2.94	15	0	Carbon cloth
		N10/T05	2.82	10	5	Carbon cloth
		N05/T10	2.86	5	10	Carbon cloth
		N00/T15	2.87	0	15	Carbon cloth
Series II	Paasche airbrush (VL)	N10/T05-P	2.84	10	5	Carbon cloth
Series	TJR spray gun (HVLP)	N00/T15-350	2.87	0	15	Carbon cloth
		N00/T15-N05	2.87	5	15	Carbon cloth
		N00/T15-TFE	3.3	0	15	TFE-treated Carbon cloth

✓ *Series I: Nafion-PTFE-based cathodes*

Four different cathodes with 2.82 ± 0.12 mgcm^{-2} Pt loading and 15 wt% binder with respect to Pt were prepared by spraying the catalyst layer on untreated C-cloth support. The relative amount of Nafion and PTFE binders were varied as follows:

- 15 wt % Nafion and 0 wt % PTFE
- 10 wt% Nafion and 5 wt % PTFE

- 5 wt% Nafion and 10 wt % PTFE
- 0 wt% Nafion and 15 wt % PTFE

The cathodes were identified as N XX / T YY, where XX is the wt% of Nafion and YY the wt% of PTFE. The cathodes were not subjected to the usual thermal treatment at 350 °C required for sintering the PTFE because Nafion's sulfonic acid groups undergo degradation at this temperature. The cathodes were prepared by using a TJR spray gun from C.A. Technologies (see below).

- ✓ *Series II: N 10 / T 05 - P cathode*

A cathode with the same chemical composition of the N 10 / T 05 (Table 2.1) was prepared by using a Paasche Airbrush. The Pt loading of the cathode is 2.84 ± 0.03 $mgcm^{-2}$. The cathode was identified as N 10 / T 05 - P where P is the acronym of Paasche Airbrush. Again, no thermal treatment was applied to the cathode.

- ✓ *Series III: N 00 / T 15-based cathodes*

Three additional cathodes, with similar composition as the N 00 / T 15 cathode (Table 2.1), were prepared.

The first cathode (2.87 $mgcm^{-2}$ Pt loading and 15 wt% PTFE with respect to Pt) was subjected to the thermal treatment at 350 °C to sintering the PTFE. An oven was used for this purpose. The cathode was inserted in the oven at room temperature and heated up to 350 °C; it was maintained at this temperature for 30 min and it was slowly cooled down to 25 °C for 21 h.

The second cathode (2.87 $mgcm^{-2}$ Pt loading and 15 wt% PTFE with respect to Pt) was sprayed with the 5 wt % Nafion.

The third cathode (3.3 $mgcm^{-2}$ Pt loading and 15 wt% PTFE with respect to Pt) was prepared by spraying the catalyst layer on TFE-treated C-cloth support (ElectroChem Inc. EC-CC1-060-T).

The cathodes were identified as N 00 / T 15 - Z, where Z is the temperature of sintering (350) or the percentage of Nafion coating (N 05) or the treatment of the support (TFE). The cathodes were prepared by using a TJR spray gun from C.A. Technologies (see below).

C.A. Technologies TJR Spray gun – model HVLP

Spray guns are commercial tools typically used for painting/covering large surface areas with high volume of paint (14; 15; 16). Hand-held or automated, spray guns conventionally work at pressures between 15 psi and 60 psi; however, the specific models "High Volume Low Pressure (HVLP)" are designed to apply large quantities of paint at very low pressure (7.5 psi). This is useful to prevent waste of paint (17). One feature of spray guns not available in airbrushes is the fan control (see picture). This option allows air to be directed at the sides of the pain coin as it leaves the nozzle, this has the effect of turning the coin into a fan. The ring that controls this function can be rotated so that the fan can be horizontal, vertical or any angle in between.

In this work, a TJR spray gun (C.A. Technologies) model HVLP with gravity feed and tip size 0.8 mm was used to prepare the first and third series of cathodes (18). As shown in Figure 2.2, the spray gun has two controllable knobs: the material knob and the air volume knob. The material knob was unscrewed about $2_{1/2}$ turns whereas the air volume knob was opened to the point where the air volume started to stay the same. The cigar shaped pattern produced with horizontal fun is also shown in Figure 2.2.

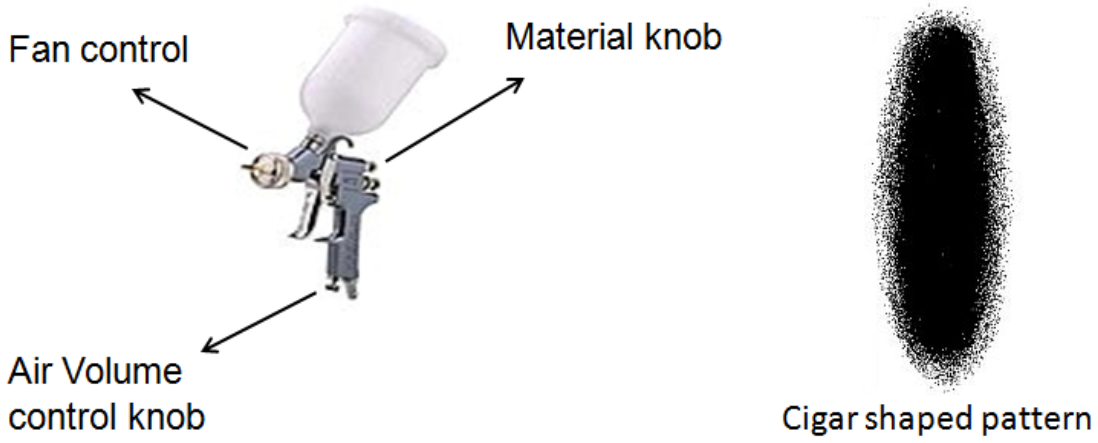

Figure 2.2 : TJR-HVLP Spray gun (C.A.Technologies), cigar shaped pattern from horizontal fun (19).

Paasche Airbrush – model VL

Airbrushes are small precision tools that combine inks with compressed air to create a fine mist or spray. They are hand-held and used instead of a brush for detailed work such as photo retouching, painting nails, fine art (20; 21). All airbrushes have an inlet for compressed air, a nozzle through which paint is sprayed under pressure and a release valve (finger lever) that

enables the operator to use air to propel the paint and to control the amount of air and paint that comes out the nozzle. The specific model "double-action" airbrush allows the control and variation of the spray pattern during each stroke. Two separate finger actions control the spray pattern: the first action is to depress the finger lever releasing air only. The second action is to pull the finger lever back releasing pigment. Pulling the lever further back releases more ink and enlarges the spray pattern.

In this work, a double-action airbrush (Paasche) model VL, Figure 2.3, was used to prepare the N 10 / T 05 – P cathode (22). The airbrush was chosen to change the catalyst distribution within the catalyst layer and to concentrate it more on the surface of the cathode. A head size 3 with a tip size 0.73 mm was chosen to reproduce the same condition of the previous spray gun. With the support of an air regulator, the airbrush was operated at 20 psi pressure. The finger lever was pulled back completely to produce the most enlarged pattern which is shown as well in Figure 2.3.

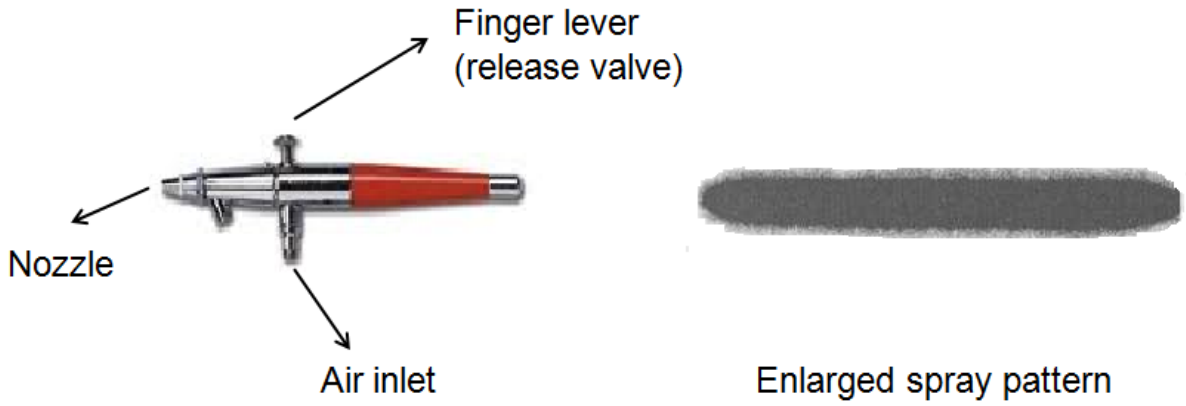

Figure 2.3: Double-action-VL Airbrush (Paasche), enlarged spray pattern (23).

- ✓ *Commercial – Pt/KB-based and Pt_3Co/KB-based cathodes*

A commercial cathode from the ElectroChem. Inc. company, a Pt/KB–based cathode and a Pt_3Co/KB-based cathode were used in this work for the study of the DMFC total impedance (Chapter 4). The commercial cathode was prepared by spreading the PTFE-catalyst ink on the TFE-treated carbon support (25 ± 5 % wet-proofing). 60 wt % Pt/Vulcan XC-72 catalyst and 20 wt % Teflon suspension were used for a final 3 $mgcm^{-2}$ Pt loading and unknown amount of PTFE. The cathode was coated with a 5 wt % Nafion solution (Ion Power) to a final 33 wt % Nafion content (with respect to Pt loading). No microporous GDL was used in this cathode.

The Pt/KB–based and Pt_3Co/KB-based cathodes were prepared from 50 wt% Pt/KB (Ketjenblack) and 50 wt% Pt_3Co/KB catalysts which were synthesised in the CNR-ITAE laboratory in Messina, following the procedure reported in our work (24). The catalysts were mixed with 15 wt % Nafion ionomer (Ion Power, Nafion solution) and deposited on by a doctor blade technique onto LT-ELAT gas diffusion layers (E-TEK). The final Pt loading was 3 $mgcm^{-2}$. The final composition of the cathodes is reported in Table 2.2.

Table 2.2 : Description of the parameters for commercial, Pt/KB-based and Pt_3Co/KB-based cathodes.

Name	*Catalyst*	*Pt loading ($mgcm^{-2}$)*	*wt% Nafion*	*Support*
Commercial	60 wt% Pt/Vulcan	3	33	TFE-treated carbon cloth
Pt/KB-based	50 wt % Pt/KB	3	15	LT-ELAT
Pt_3Co-based	50 wt % Pt_3Co/KB	3	15	LT-ELAT

2.2. Preparation of MEAs

In this work, the MEAs were prepared by applying the gas diffusion electrodes to the sides of the membrane. A commercial PtRu-based electrode from ElectroChem. Inc. company (40 wt % Pt - 20 wt% Ru /Vulcan XC-72 catalysts, 3 $mgcm^{-2}$ Pt loading, unknown amount of PTFE, 33 wt% Nafion ionomer coating, TFE-treated carbon support (25 ± 5 % wet-proofing)) was used as anode. A pre-treated Nafion 117 membrane (DuPont) was used as electrolyte. The pre-treatment consisted in boiling the membrane for 1 h in 3 % vol. H_2O_2 (Fisher Scientific, 30 % vol.), for 1 h in deionized water, for 1 h in 1.2 M H_2SO_4 (Fisher Scientific, Puriss. 95-98%), and finally washing it in deionized water. The membrane-electrodes assemblies were formed by hot-pressing procedure. The cathode-membrane-anode sandwiches were disposed between two copper plates, covered with 0.25 mm thick PTFE sheets (GoodFellow). They were placed in a Carver press, pre-heated at 143 °C, for 1 min and then pressed for 40 s at the standard pressure 500 lbs. Since this work contains an investigation of the effect of the assembly pressure, a couple of MEAs were pressed at the lower values 375 and 250 lbs. In relation to the nomenclature used for the cathodes, the prepared MEAs were identified as MEA-T where T is the name of the cathode. The extension -500, -375 and -250 was finally added to MEA-T to identify the MEAs prepared at different pressures.

Concerning the MEAs containing the Pt/KB–based and Pt_3Co/KB-based cathodes (Chapter 4), they were prepared following the same procedure, with a Nafion 117 membrane but with another type of anode (unsupported Pt-Ru catalyst (Johnson-Matthey), 3 $mgcm^{-2}$ Pt loading, 15 wt % Nafion ionomer, HT-ELAT gas diffusion layer).

A list of the MEAs investigated in this thesis is reported in Table 2.3.

Table 2.3: List of MEAs investigated in this thesis.

MEA	*Cathode*	*Type of investigation*	*Chapter*
MEA - N15/T00	N15/T00 (Table 2.1)	Effect Nafion/PTFE binders	5
MEA - N10/T05	N10/T05 (Table 2.1)	Effect Nafion/PTFE binders	5
MEA - N05/T10	N05/T10 (Table 2.1)	Effect Nafion/PTFE binders	5
MEA - N00/T15	N00/T15 (Table 2.1)	Effect Nafion/PTFE binders	5
MEA - N10/T05-P	N10/T05-P (Table 2.1)	Effect of Pt distribution	5
MEA - N00/T15 - 500	N00/T15 (Table 2.1)	Effect assembly pressure	6
MEA - N00/T15 - 375	N00/T15 (Table 2.1)	Effect assembly pressure	6
MEA - N00/T15 - 250	N00/T15 (Table 2.1)	Effect assembly pressure	6
MEA -N00/T15-N05	N00/T15-N05 (Table 2.1)	Effect morphology cathode	6
MEA -N00/T15-TFE	N00/T15-TFE (Table 2.1)	Effect morphology cathode	6
MEA – Pt/KB	Pt/KB-based cathode (Table 2.2)	EIS - Fitting	3
MEA – Pt_3Co/KB	Pt_3Co/KB-based cathode (Table 2.2)	EIS - Fitting	3
MEA – Pt/XC72	Commercial cathode (Table 2.2)	EIS - Fitting	3

2.3. Cathode Characterization

All the techniques used in this work to characterize the cathodes are presented in Table 2.4. The experimental description and the principle of each technique are reported in the corresponding section.

Table 2.4 : List of techniques used to characterize cathodes and MEAs.

	Technique	*Objective*	*Paragraph/Chapter*
Cathodes ex-situ	SEM / EDS	➢ Images of surface and cross-section ➢ Cartography of the surface (mapping) and cross-section (linear-scan) ➢ Quantitative chemical analysis	2.3.1.1
	RBS	Quantification of the Pt and S composition in the first 200 nm of the cross-section	2.3.1.2
	DVS / H_2O – Hexane uptake	Effect of Nafion/PTFE content on the hydrophilicity/hydrophobicity of the cathodes	2.3.1.3 2.3.1.4
	Sessile-drop contact angle	Wettability of the cathode surface	2.3.1.5
	N_2 adsorption	Total micro, meso and macro-pore volume (up to 200 nm)	2.3.1.6
	Cyclic Voltammetry	➢ Under N_2: electrochemical surface area, catalyst utilization, potential range for double-layer capacity ➢ Under O_2: performance towards ORR, half-wave potential and limiting-current	2.3.2.2
	Chronoamperometry	➢ Thin-film mechanism on N 00 / T 15 cathode and flooding for N 15 / T 00 cathode	2.3.2.3
	EIS	Fully investigation of the cathode in 0.5 M H_2SO_4 solution	Chapter 3
Cathodes in DMFC	EIS (high frequency)	Cell resistance	2.3.3.4
	E-j curves	Fuel cell performance (OCV and current density at 0.1 V)	2.3.3.5
	O_2 gain	Voltage loss related to mass-transport limitations	2.3.3.6
	EIS	Fully investigation of the cathode in DMFC	Chapter 3

For this work the mercury porosimetry technique would be required to measure the macro-porosity of the cathodes (25; 26; 27; 9). However, up to now, we did not find any facility able to do this type of measurements on our samples. We have been searching for this instrument in the main local universities (Concordia University, McGill University, Université de Sherbrooke, Université de Trois-Rivieres) but either they didn`t have the instrument either it was not in function from many years, either we didn't get any response. Concerning companies, we have contacted for example Quantachrome company but they requested samples of 1.2 cm^2 with a mass of 2-5 g, and the weight of our samples with those dimensions is typically 0.1 g.

2.3.1. Physicochemical characterization

Scanning Electron Microscopy – Energy Dispersive Spectrometry

In this work the SEM technique was used to acquire images of the surfaces and cross-sections of the cathodes as well as to reproduce the cartography of surface areas (mapping) and cross-sections (linear-scan), as exemplified in Figure 2.4. The JSM-6300F microscope (JEOL Company) was used for the purpose. In all the measurements, the working distance was 15 mm and the tensions of 5 kV and 20 kV were used as necessary. An X-rays energy-dispersive detector (Oxford instrument, Link ISIS) was used for the elemental analysis. From the images of the cross-sections, the total thickness (support and catalyst layer) was measured using the Semaphore software. The thickness was measured in different points of the cathode' cross-section and an average value were calculated.

The Scanning Electron Microscopy (SEM) is a method for high-resolution imaging of surfaces (28; 29; 30). This technique is based on the electron-sample interaction and it gives information on the morphology, topography and composition of the sample. The source, an electron gun, generates a beam of incident electrons which cause an emission of electrons from the sample. The type of information that can be achieved depends on the nature of the detected electrons. An inelastic collision of the incident beam causes the emission of the low-energy secondary electrons. These electrons are emitted from the sample surface therefore the contrast in the acquired image depends on the surface morphology. An image contrast as a function of the

composition can be provided by the backscattered electrons which are high-energy electrons, ejected by an elastic collision of the incident beam with a much deeper area of the sample.

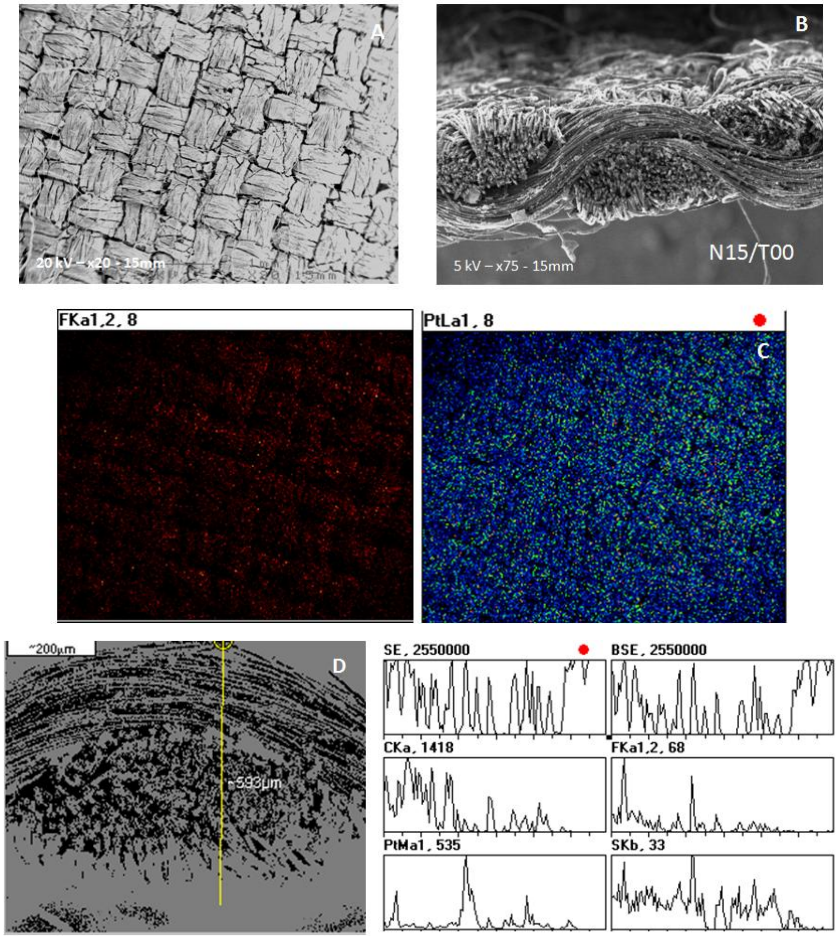

Figure 2.4 : a) Surface, b) cross-section, c) mapping, d) linear-scan for N 15 / T 00 cathode.

The interaction of an incident beam with the sample target causes also the emission of X-rays which can be used to obtain a chemical analysis of the sample (31). The Figure 2.5 reports an example of ED spectrum for a N 15 / T 00 cathode with the x-axis reporting the X-ray energy (keV) and the y-axis the intensity. The spectrum shows the peaks of C, F and Pt. The peak of S (not shown) appears at 2.2 keV, partially overlapping with the Pt peak. Because of the irresolution of the two peaks, in this work EDS could not be used to quantify the Pt and S composition in the sample. In addition, the ZAF correction failed in the quantitative analysis. Therefore, the C and F compositions were not trustable as well.

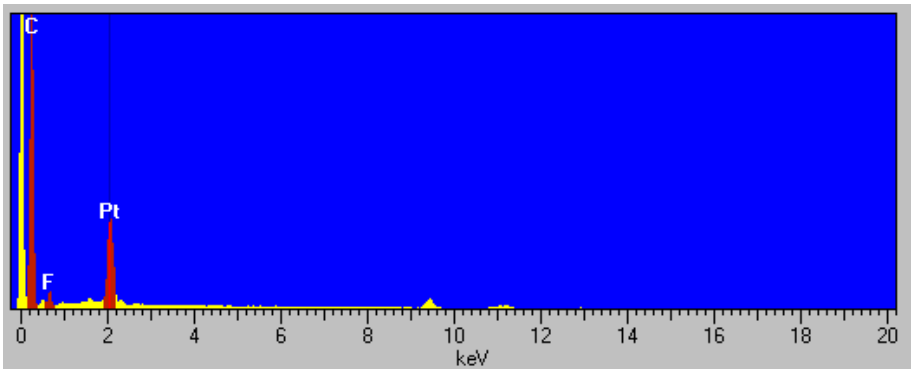

Figure 2.5 : ED spectrum of N 15 / T 00 cathode with peaks of C, F and Pt.

Rutherford Backscattering Spectroscopy

As shown above, the quantification of Pt and S by EDS analysis was not possible because of the irresolution of the two peaks. In this work the RBS technique was used to try to investigate the distribution of Pt and S in the first 200 nm of cathode thickness. Variations in the S composition were expected because of the different Nafion content in the samples. Since the cathodes have the same catalyst loading, no differences were expected in the Pt quantification. However, it was suspected that the different type and ratio of binders could affect the Pt distribution within the catalyst layer and therefore its quantification. The RBS spectrum (count rate vs. energy) of I series of cathodes and N 10 / T 05 – P cathode is reported in Figure 2.6. As shown, the peak of Pt is well resolved; however, the S peaks is elongated towards lower energies and not resolved. For this reason, the quantification of S composition was not possible and the RBS technique was not considered useful for our studies.

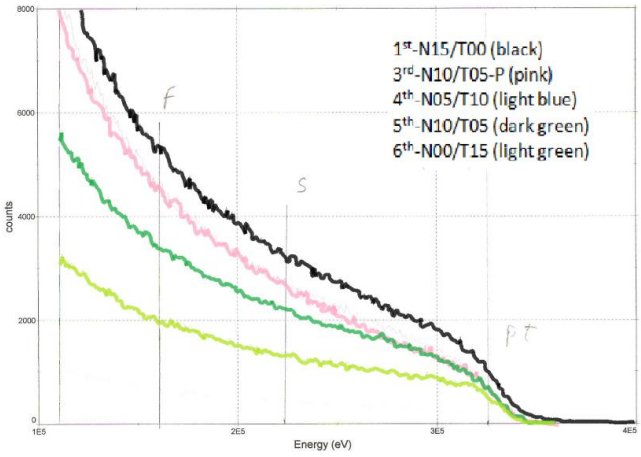

Figure 2.6 : RBS spectrum for cathodes with peaks of S and Pt.

The RBS measurements were performed with a beam of mono-energetic ^{4}He particles of low energy 350 keV collimated onto the sample positioned in a vacuum chamber at 10^{-9} torr. The backscattered ions were detected at a scattering angle of 145° by a solid state detector with energy resolution of 22 keV.

Rutherford Backscattering Spectroscopy (RBS) is an ion scattering technique used for quantitative compositional analysis and depth profiling of individual elements of thin film samples (32; 33). During a RBS measurement, high-energy ions (H^{+}, He^{++}) are collimated onto the sample positioned in a vacuum chamber (10^{-6} – 10^{-9} torr) and the backscattered ions are detected. The energy of the backscattered ions gives information about the type of atoms encountered and the length of the path traveled, whereas the number is directly proportional to the concentration of a given element in sample.

Dynamic Vapor Sorption

In this work the water vapor sorption isotherms were recorded to explore the effect of Nafion/PTFE content on the hydrophilic character of the cathodes. Since we were particularly interested in the W_{up} at high relative humidity, sorption isotherms were recorded by increasing the relative humidity (RH%) with step of 30% RH and 30 min up to 90% RH and a step to 97% RH for 48 h. The experimental profile is shown in Figure 2.7a. The experiments were performed with a DVS – High Throughput apparatus (Surface Measurement Systems) equipped with a Cahn ultra microbalance with a mass resolution of 10 μg. Sample of 0.16 mm^2 area were placed in the DVS – HT pans and dried under a stream of dry nitrogen (5.0) at 25 °C for 6 h. The total gas flow used was 400 sccm.

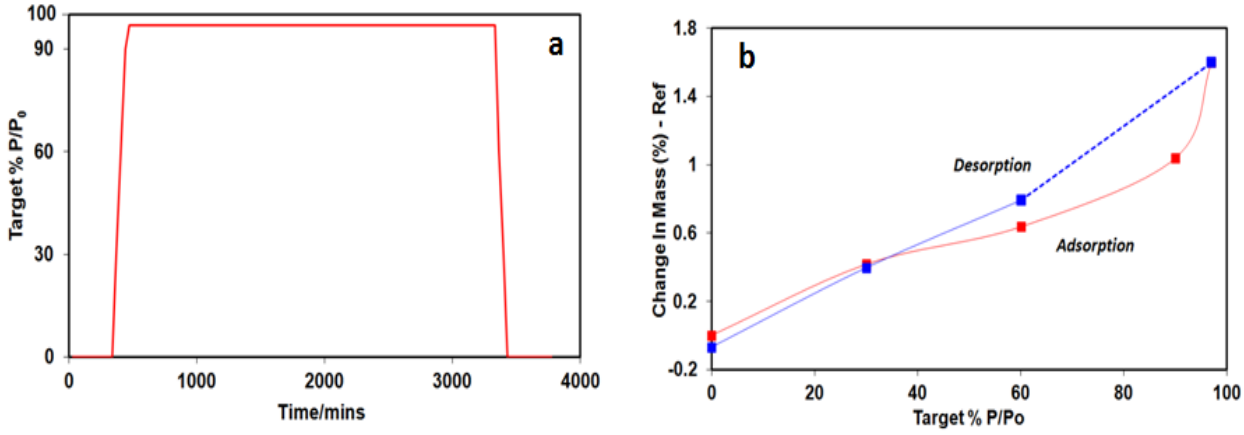

Figure 2.7: a) Water sorption profile, b) adsorption and desorption isotherms for N 15 / T 00 cathode.

The Dynamic Vapor Sorption (DVS) is a gravimetric technique that measures the rate at which a vapour solvent is absorbed by the sample (34; 35). The sample is exposed to a series of step changes in relative humidity and the mass change is monitored as a function of time. The equilibrium mass values at each relative humidity step are used to generate isotherms. Isotherms are typically divided in two components: adsorption for increasing humidity steps and desorption for decreasing humidity steps. The difference in water vapor uptake between the two isotherms is called hysteresis. The shape of the isotherm hysteresis gives information about the sorption mechanism and sample porosity. The Figure 2.7b shows the shape of typical water adsorption/desorption isotherms recorded for N 15 / T 00 cathode.

Liquid water and hexane uptake

In this work the liquid water and hexane uptake were measured to investigate the hydrophilic and hydrophobic character of the cathodes. Samples of 4 cm^2 area were dried for 3 h in the oven at 50 °C and weighted. The samples were then immersed for 48 h in 50 ml of liquid water/hexane and weighted again. For each sample, the weight after the uptake was measured 3 times and an average value was calculated. Measurements of water uptake were performed on all the cathodes. Hexane absorption measurements were attempted on the series I of Nafion/PTFE cathodes; however no relevant uptake was observed.

The solvent uptake is a method to measure the solvent absorption capacity of a sample. The technique consists in immersing the sample in a solvent (generally, water, methanol, toluene and hydrocarbons) and in calculating the solvent uptake by the weight difference between the wet electrode and the dry electrode as follow:

$$\%wt_{solvent} = \frac{\left(wt_{wet} - wt_{dry}\right)}{wt_{dry}} \times 100 \qquad \textbf{Equation 2.1}$$

The time of immersion of the sample is related to the type of sample and it can go from some minutes to many hours.

Sessile drop contact angle

In this work the sessile drop contact angle was used to evaluate the wetting of the cathodes' surface. The apparatus for the contact angle measurements consisted in a programmable pump, that pushed and withdrawn with constant rate (2.5 $\mu l min^{-1}$) the specified volume of deionized

water (5 μl) through a micro-capillary tube and formed a growing drop (~ 0.35 mm in diameter) on the 1 cm^2 sample surface. The evolution of the drop (advancing and receding contact angles) was observed using a camera and the recorded images were analyzed using the Acquidam 2.2 software. Figure 2.8 shows the water drop at maximum evolution on the surface of the N 15 / T 00 cathode.

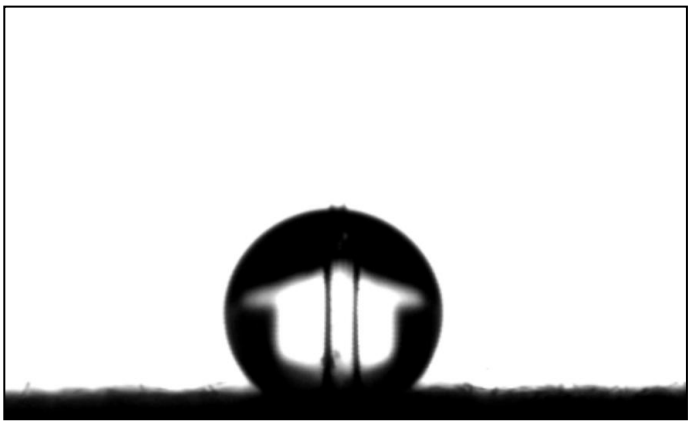

Figure 2.8 : Water drop on the surface of N 15 / T 00 cathode.

The contact angle measurement is a method to characterize the interfacial properties of a liquid in contact with a solid substrate (36; 37; 38; 39) and an important tool in the investigation of non-homogeneous, porous, hydrophilic/hydrophobic surfaces (40; 41; 42).

The contact angle describes the shape of a liquid droplet resting on a solid surface. Generally the Young's equation is used to explain the balance of forces of the liquid drop on the surface:

$$\gamma^{sv} = \gamma^{sl} + \gamma^{lv} \cos\theta \qquad \textbf{Equation 2.2}$$

where γ^{sv} is the solid surface free energy, γ^{lv} the liquid surface free energy, γ^{sl} the solid/liquid interfacial free energy and θ the contact angle. When drawing a tangent line from the droplet to the touch of the solid surface, the contact angle is the angle between the tangent line and the solid surface. The contact angle measurement gives information on:

a) The nature of the solid, if a liquid with well-know properties is used.
b) The affinity of the liquid to the solid: one can deduce the hydrophobic (large angle) or hydrophilic (small angle) character of the surface.
c) The roughness of the surface (hysteresis between advancing and recessing angles).

The sessile drop method is the most common method to measure the contact angle. Typically, a liquid droplet is deposited using a syringe and its evolution is observed by adding more liquid to it. Depending on the adhesive forces between the solid and the liquid, the drop can spread out over the surface and wet more the surface. As the tendency of the drop to spread out over the surface increases, the contact angle decreases. Thus, as shown in Table 2.5, the contact angle provides a measure of the wettability.

Table 2.5 : Contact angle and wetting process.

Contact angle	***Degree of wetting***
$\theta = 0°$	Perfect wetting
$0° < \theta < 90°$	High wettability
$90° \leq \theta < 180°$	Low wettability
$\theta = 180°$	Non - wetting

Unlike ideal surfaces, the real surfaces show roughness which affects the position of the drop over the surface. The expansion and retraction of the droplet produces two contact angles, the advancing contact angle (ACA) which is the maximum stable angle, and the recessing contact angle (RCA) which is the minimum stable angle. The hysteresis provides information on the roughness of the surface.

Nitrogen adsorption

In this work the nitrogen sorption isotherms were recorded to measure the total micro, meso and macro (up to 200 nm) pore volume of the cathodes. The experiments were performed using a Quantachrome Instrument Autosorb-1. The samples were weighted, placed on the analysis port and pre-treated at 80 °C for 4 h under vacuum. The adsorption and desorption isotherms were measured at 100 °C using nitrogen as adsorbate down to relative pressure 10^{-6}. The Figure 2.9 shows the shape of typical nitrogen adsorption/desorption isotherms recorded for N 15 / T 00 cathode. For the analysis of the results, it was considered that the porosity of the carbon cloth support (macro-porosity) is not negligible since it contributes 2/3 of the total electrodes' weight. For this reason, no computational or statistical methods could be used for the calculations and the total pore volume was measured directly from the adsorption/desorption isotherms at $P/P_0 = 1$.

The total porosity was then converted from cc/g of gas nitrogen adsorbed to cc/g of liquid nitrogen adsorbed.

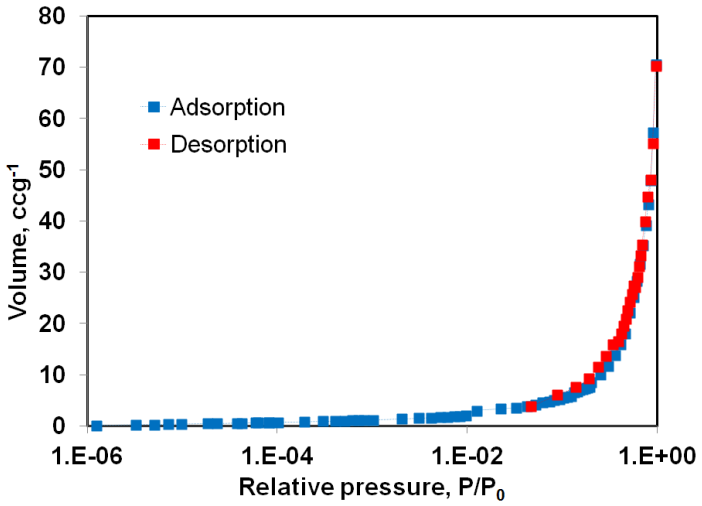

Figure 2.9 : Nitrogen sorption isotherms for N 15 / T 00 cathode.

The gas adsorption is a technique used for the characterization of porous samples presenting micro and meso-porosity, in the range 0.35 – 100 nm (43; 44; 45; 46). This technique consists in the adsorption of gas molecules (adsorbate) on a solid surface (adsorbent). During an experiment, the sample is pre-treated by heating it under vacuum or flowing gas to remove adsorbed contaminants acquired from atmospheric exposure (degassing). Once cleaned, the sample is brought to a constant temperature and small amount of gas (normally nitrogen) is sent to the sample to be adsorbed and form a thin monolayer that covers the surface. Further increasing of the gas pressure leads to a multilayer coverage and capillary condensation. As the equilibrium pressure approaches the saturation, the surface is completely covered and the pores totally filled. If at this stage the adsorption process is reversed, desorption isotherms are generated.

2.3.2. Electrochemical characterization

Electrochemical cell

The electrochemical characterization occurred in a conventional three-electrode cell (Metrohm) as the one reported in Figure 2.10a. The cell was equipped with a Pt wire as counter electrode (black), an Ag/AgCl reference electrode (Metrohm) (blue) and a gas inlet/outlet (Metrohm). The

working electrode (red) was set in the middle of the cell, near the reference electrode to reduce the ohmic drop and facing the counter electrode to maximize the output current. A 0.5 moldm^{-3} sulphuric acid solution (Fisher, Puriss. 95-98 %) saturated with nitrogen or oxygen was used as electrolyte. A PGSTAT30 potentiostat/galvanostat (Autolab), Figure 2.10b, equipped with GPES software and FRA2 module was used to run the experiments.

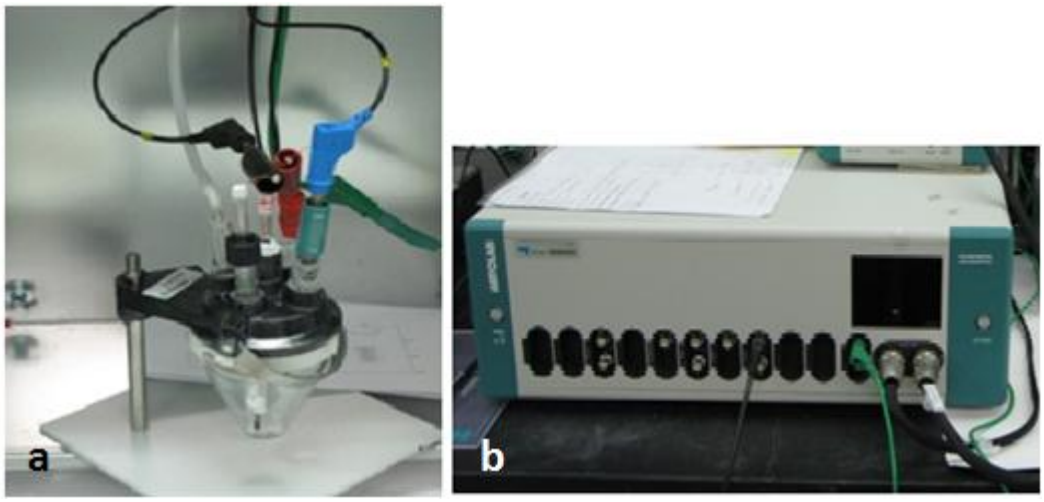

Figure 2.10: a) Electrochemical cell (Metrohm) and b) PGSTAT30 potentiostat (Autolab).

The study of an electrochemical system is focused on the processes and factors that affect the transport of charge across the interface between the electronic conductor (electrode) and the ionic conductor (electrolyte) and in understanding the events that occur when an electric potential is applied and current passes (47). Generally, the interest is on the chemical reaction that occurs on the main electrode called working electrode. The evolution of the interfacial potential related to the reaction is followed by using a reference electrode such as standard hydrogen electrode (SHE), the saturated calomel electrode (SCE) or silver-silver chloride electrode (Ag/AgCl). The current flow produced by the chemical reaction is observed by using an auxiliary electrode (or counter electrode) which is usually chosen to be an electrode that does not cause interfering reactions and is frequently positioned in a compartment separated from the working electrode. Typically, Pt electrodes are used as counter electrodes. The plot of the current as a function of the potential gives a current-potential curve which contain important information about the nature of the electrode/solution interface and the reactions occurring in the system.

Cyclic Voltammetry

In this work, the cyclic voltammetry technique in nitrogen saturated sulphuric acid solution (Fisher, Puriss. 95-98 %) was used to determine the electrochemical surface area (ESA), the catalyst utilization and the potential range for the double-layer capacity. The cathodes were first activated in the wide range of potential - 0.4 V – 1.4 V (vs. Ag/AgCl), recording 20 cycles at 50 mVs^{-1} and 3 cycles at 20 mVs^{-1}. A massive evolution of hydrogen and oxygen, necessary for the activation of the Pt catalyst, occurred in this wide range of potential. The cyclic voltammograms (10 cycles) were then recorded at 20 mVs^{-1}, in the range - 0.28 V - 1.3 V (vs. Ag/AgCl). The last cycle was saved and used for analysis. The cyclic voltammetry technique was also used in oxygen saturated sulphuric acid solution (Fisher, Puriss. 95-98 %) to study the cathodes' performance towards the oxygen reduction reaction and to determine the half-wave potential and the limiting-current. After a pre-conditioning of 30 min (degassing), the 2 cycles were recorded at 5 mVs^{-1}, in the range of potential 1 V – 0 V (vs. Ag/AgCl).

The Cyclic Voltammetry (CV) is a potentiodynamic technique largely used to obtain qualitative and quantative information of the phenomena occurring in the electrochemical system (48; 49). In a CV experiment, the working electrode potential is swept linearly in time until a set point where it is inverted. This process happens multiple times during the experiment, as shown in Figure 2.11a. The typical voltammogram for a Pt-based electrode in H_2SO_4 is reported in Figure 2.11b.

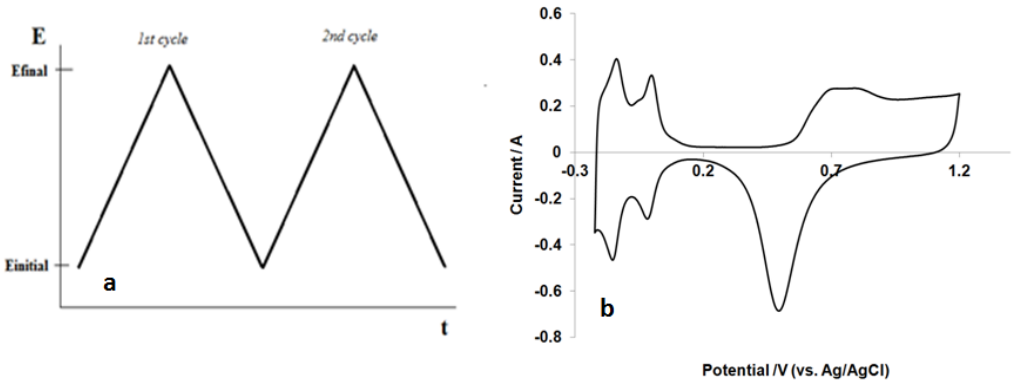

Figure 2.11: a) Cyclic voltammetry wave form, b) voltammogram of a Pt electrode.

Chronoamperometry

In this work, the chronoamperometry was used as a complementary method for the investigation

of the performance of the gas diffusion electrodes towards the oxygen reduction reaction. The capacitive and steady-state currents were determined to evaluate the thin-film mechanism or the flooding condition occurring in the porous cathodes. For the purpose, the sulphuric acid solution (Fisher, Puriss. 95-98 %) was saturated with oxygen for 30 min. The experiments were performed maintaining the system for 10 sec at the rest potential (equilibration time) and then applying a step of potential from the OCV value (~ 0.78 V) to a lower potential. Each time the potential was stepped to a value 20 mV lower than the potential used in the previous experiment and the curves were recorded until 0.3 V. After the 10 sec of equilibration time, the chronoamperograms were recorded for 120 min.

The chronoamperometry is a pulsed electrochemical technique applied for measuring the electrode surface areas, diffusion coefficients, adsorption of electroactive species, and the mechanism and rate constants for chemical reactions coupled to electron transfer reactions (50; 51). It has also been used to obtain qualitative information on the nature of the electrode structures (52; 53) and to determine the thickness of the diffusion layer (δ) formed at the electrode/solution interface. In a chronoamperometric experiment, the potential of the working electrode is stepped from a value at which no faradaic current occurs ($E_{initial}$) to a potential (E_{final}) at which a chemical reaction takes place, as shown in Figure 2.12a. The potential step causes the consumption of reagent near the electrode surface and leads to the diffusion of the reactant from a region of high concentration (bulk solution) to a region of low concentration (electrode surface). The magnitude of the region depleted in reactant (diffusion zone) increases with the time of the reaction and it can be graphically illustrated in a concentration-distance profile. The exponentially decay of the resulting current from the faradic processes occurring at the electrode (caused by the potential step) is monitored over time. After an initial peak due to the electrolysis of the molecules adjacent to the electrode surface, the current decreases slightly as shown in Figure 2.12b.

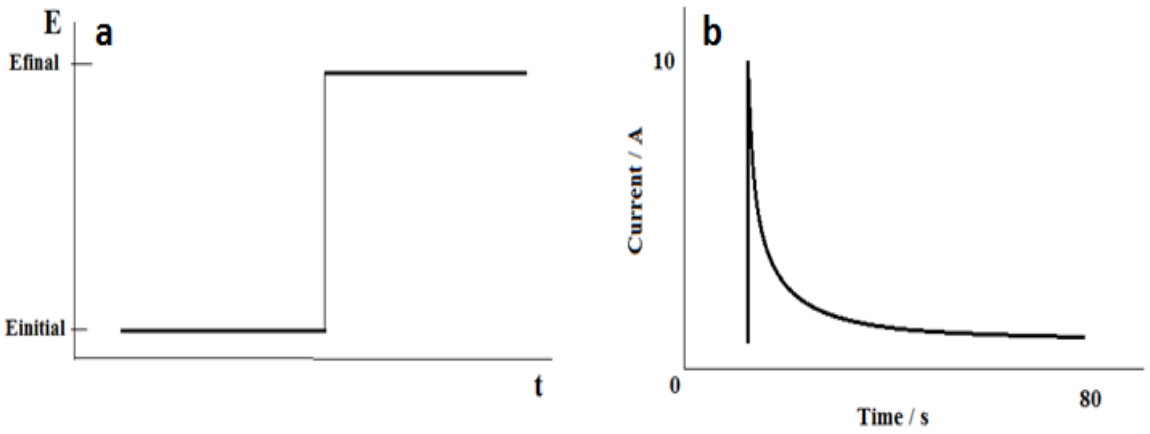

Figure 2.12: a) Potential excitation signal, b) Transient current response (53).

Electrochemical Impedance Spectroscopy

In this work, the cathodes were fully investigated by impedance spectroscopy technique. All the experimental and theoretical details of this technique are reported in the chapter 3.

2.3.3. Fuel cell characterization

Fuel cell

The DMFC tests were carried out in the fuel cell test station (850C, Scribner Associates) reported in Figure 2.13. The station was equipped with a FRA unit for impedance and a fuel cell test fixture of 5 cm^2 active area (Fuel cell Technologies), containing Au-covered current collector plates and graphite blocks with serpentine gas flow channels. The minimum suggested pressure of 10.8 Nm was used to close the fixture. The experiments were run under oxygen (purity 5.2) and air conditioned by an external type humidifier contained into the fuel cell system. The methanol solution was driven into the fuel cell test fixture by a peristaltic pump (Gilson) using a calibrated tube of size 1.02 mm (internal diameter). A 1 M aqueous methanol solution (Fisher, Puriss. > 95 %) at a flow rate of 2.5 $mlmin^{-1}$ (stoichiometry 5.0) was used for all the experiences which were performed under atmospheric pressure on both anode and cathode compartments. The experiments were followed on a computer equipped with the FuelCell software that was used

to control all the experimental parameters. The FCview and Zview programs were used for the data analysis.

Figure 2.13: Fuel cell station and fuel cell test fixture.

Each MEA was firstly conditioned with the methanol solution and humidified air (100% RH – 220 $mlmin^{-1}$ – stoichiometry 2.4) at room temperature for at least 1 h hour. The cell resistance was measured at open circuit potential, using an external potentiostat (VersaSTAT 3, Princeton Applied Research) operated in potentiostatic mode. The impedance spectrum (Nyquist plot) was recorded in the high frequency range 100 kHz – 1 Hz and the resistance value was extrapolated for -Im(Z) = 0 as interception of the curve with the x-axis. Subsequently, under the same air conditions, the MEAs were activated by two cycles of galvanostatic polarizations recorded between 25 °C and 80 °C.

The polarization curves were recorded at 40 °C with fully humidified air (220 $mlmin^{-1}$ - stoichiometry 2.4) and oxygen (51 $mlmin^{-1}$ – stoichiometry 2.7) and the oxygen gain was calculated. In additional experiments, the air was preheated to a different temperature to vary the relative humidity at the cathode (50% RH and >100% RH) and test the response of the MEAs to the water content into the air stream.

The complete impedance spectra of the single DMFCs were recorded in the galvanostatic mode, applying a sinusoidal signal with amplitude of 10 mA and in a frequency range from 100 kHz to 1 mHz. The spectra were recorded at different current density values under humidified air (220 $mlmin^{-1}$, stoichiometry 2.4, 100% RH) and humidified oxygen (51 $mlmin^{-1}$, stoichiometry 2.7, 100% RH).

Stoichiometry for methanol – oxygen – air

In this work, the fuel cell was always operated with an excess of methanol, oxygen and air to guarantee the presence of reactants to complete the oxide-reduction reactions. The abundance or lack of reactant is determined by the stoichiometry factor which is defined as the ratio between the amount of reactant present and the amount of the reactant needed to complete the reaction (theoretical). A stoichiometry factor of 1.0 means that the amount of reactant provided corresponds to the theoretical amount. The methanol/oxygen/air flow rates were calculated at stoichiometry 1.0 and then increased to have the stoichiometry factor of 5.0, 2.7 and 2.4, respectively. The calculations for the stoichiometry factor of 1.0 are reported below.

MEA size	5 cm^2
Current density used for calculations	1 Acm^{-2}
[MeOH]	1 M
Total equation	$CH_3OH + (3/2)\ O_2 \rightarrow CO_2 + 2H_2O$
Faraday's law	$N = I/nF$

Methanol flow rate (at stoichiometry 1.0)

$$N_{MeOH} = 5/(6 \cdot 96485) = 8.64 \cdot 10^{-6}\ mol/s$$

$$8.64 \cdot 10^{-6}\ mol/s \div 1\ mol/l = 8.64 \cdot 10^{-6}\ l/s$$

$$8.64 \cdot 10^{-6}\ l/s \cdot 60\ s/min \cdot 1000\ ml/l = \mathbf{0.52\ ml/min}$$

Oxygen flow rate (at stoichiometry 1.0)

Molecular weight	32 $gmol^{-1}$
Density (25 ° C – 1.013 bar)	1.309 gl^{-1}

$$1\ mol\ MeOH \rightarrow 3/2\ mol\ O_2$$

$$N_{O_2} = 8.64 \cdot 10^{-6}\ mol/s \cdot 3/2 = 12.96 \cdot 10^{-6}\ mol/s$$

$$12.96 \cdot 10^{-6}\ mol/s \cdot 32\ g/mol = 414.57 \cdot 10^{-6}\ g/s$$

$$414.57 \cdot 10^{-6}\ g/s \div 1.309\ g/l = 3.16 \cdot 10^{-4}\ l/s = 0.316\ ml/s = \mathbf{19\ ml/min}$$

Air flow rate (at stoichiometry 1.0)

Percentage of O_2 in air	20.95 %

$$N_{air} = 19 \cdot 100/20.95 = \mathbf{91\ ml/min}$$

Humidification of the cathode

In this work the fuel cell was always operated with humidified gas stream either because we investigated the ability of the cathodes for water removing, either because of the fuel cell manufacturing. As mentioned before, the gas was conditioned by an external type humidifier as the one shown in Figure 2.14. The external humidifier required that the inlet gas was conditioned before being introduced into the fuel cell. The gas was bubbled through heated water, humidified and sent into the system through a gas piping that was heated to prevent condensation phenomena.

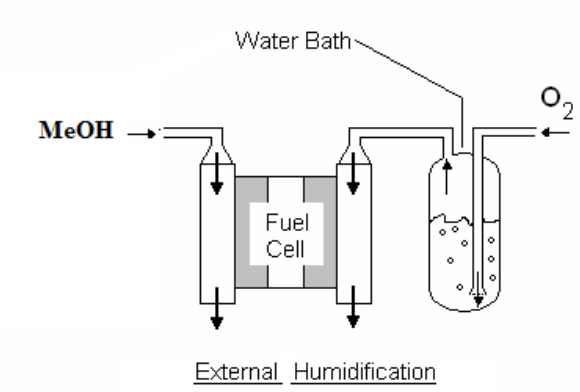

Figure 2.14: External humidifier (54).

The humidity is typically measure as "relative humidity" (RH) and was calculated by:

$$RH = \frac{p_{wv,humidifier}}{p_{wv,fuel\ cell}} \times 100 \qquad \textbf{Equation 2.3}$$

where $p_{wv,humidifier}$ is the water vapor pressure for the humidifier temperature and $p_{wv,fuelcell}$ is the water vapor pressure for the cell temperature. Knowing the temperature of the humidifier and cell, the water vapor pressures were easily determined by using the Antoine's equation and

tabulated data. The relative humidity of 100% was determined for a water-saturated gas, whereas relative humidity over 100% was determined for a water-saturated gas with the occurring of condensation phenomena at the gas inlet of the cathode.

Cell resistance

The total cell resistance (R_{cell}) includes the ionic resistance, the electronic resistance and the contact resistances between the fuel cell components. A high fuel cell resistance may result in a low fuel cell performance.

The ionic resistance represents the proton transfer within the fuel cell membrane and indirectly reflects the membrane conductivity. Aside from their transport in the membrane, protons need to be transferred to the active sides of the catalyst layer and this may be another source of proton resistance. Generally, the proton conductivity of the catalyst layer is strongly dependent of the electrolyte materials, electrolyte loadings, components and structure, as well as the ratio of the electrolyte to carbon (Nafion loading), the temperature and the water activity. In addition, the conditions used to operate the fuel cell system, such as relative humidity of the reactants, may affect the proton conductivity of the catalyst layer and consequently its performance.

The electronic resistance is related to the flow of electrons through the catalyst layers. The electronic conductivity also depends on the used materials, the carbon loading, the components and the structure of the electrodes and it was found decreasing at the increase of the Nafion loading.

The total cell resistance may be reduced using extremely high conductive materials, minimizing the thickness of the electrodes and using well-designed bipolar plates, which have high conductivities and short lengths.

Polarization curves

In this work the performance of the MEAs equipped with the Nafion/PTFE-based cathodes was measured by recording polarization curves at different temperature, under air and oxygen and at different cathode relative humidity. The typical polarization curve recorded for MEA – N 15 / T 00 at 40 °C in presence of air is reported in Figure 2.15. The E-j plot shows that the fuel cell achieves highest voltage at open circuit potential when there is no current load. Then the cell reports a drop of potential at the increasing of the applied current density. The main sources of

losses (55; 56; 57) responsible of the potential decrease are:

a) *Activation losses* due to the slow kinetics and poor electro-catalytic activity of the catalysts towards the methanol oxidation and the oxygen reduction. The effects of these losses are most pronounced at the low current densities (~1 to 50 $mAcm^{-2}$).

b) *Ohmic losses* due to resistive losses in the electrolyte, in the electrodes and in the terminal connections. The effects of these losses are more pronounced at intermediate current densities (~50 to 200 $mAcm^{-2}$).

c) *Concentration losses* due to parasitic reactions that tend to lower the equilibrium potential. One particularly important source of concentration losses in methanol fuel cells is the fuel cross-over from anode to cathode. The methanol cross-over is the dominant source of losses at open circuit.

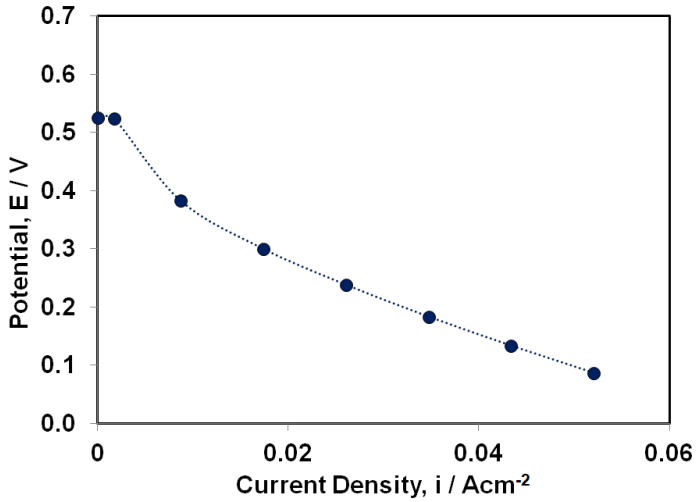

Figure 2.15: Polarization curve for MEA – N 15 / T 00 recorded at 40 °C under air.

The shape of the polarization curve depends on the operating temperature and from the feeding at the cathode (air or oxygen). The polarization curve moves towards higher values at the increasing of the operating temperature and when the cathode is fed with oxygen. Generally, the variation of one parameter that causes the polarization curve to go up is beneficial because greater power and higher efficiency can be achieved. The polarization curve increases with the increasing of the operating temperature because of the higher open circuit voltage, higher catalyst utilization and rate of the chemical reactions, improved mass-transport and lowered cell resistance. However, the methanol cross-over and the swallowing of the Nafion membrane increase also with the operating temperature. As a consequence, the optimum temperature to operate a direct methanol fuel cell

system is 60 °C. As mentioned previously, these studies are focused on the lower operating temperature of 40 °C. The choice of investigating the performance of our cathodes under this condition is related to the final applications, the portable devices for which the operating temperature cannot exceed the 50°C.

The polarization curve increases also when the cathode is fed with oxygen. The higher oxygen partial pressure allows an higher catalyst utilization, open circuit potential and improved mass-transport. Therefore, the optimal condition to achieve higher performance is to operate the fuel cell with oxygen. In this study the emphasis is given to DMFCs operated with air. Again, since the portable devices are the final applications it is expected to obtain high performance with air-breathing DMFCs.

Oxygen gain

In this work the difference in cell potential between polarization curves recorded under air and oxygen feed, named oxygen gain (58; 59) was calculated to estimate the voltage loss associated with mass transport in cathodes operating with air. The typical oxygen gain curve recorded for MEA – N 15 / T 00 is reported in Figure 2.16. A small oxygen gain is desired, especially in the case of air-breathing fuel cells in which the cathode is feed with atmospheric air and losses due to mass transport can be very high. Usually, a large oxygen gain indicates that the cathode suffers from a high transport resistance when air is used as oxidant, although higher oxygen reduction charge transfer resistance and lower thermodynamic voltage can also contribute to the O_2 gain.

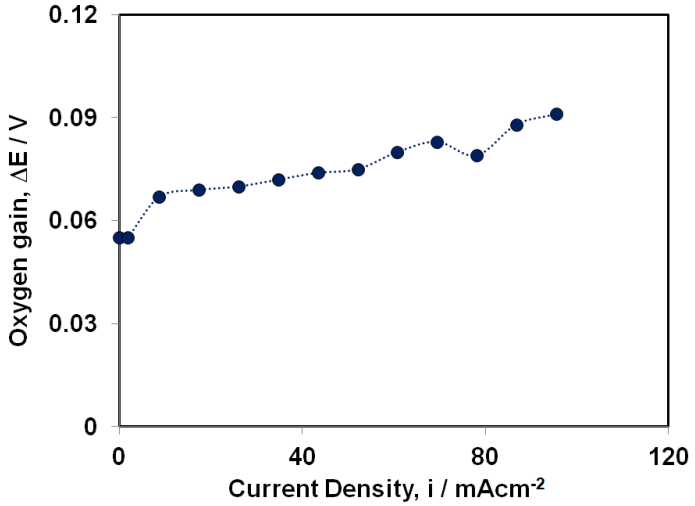

Figure 2.16: Oxygen gain for MEA – N 15 / T 00 at 40 °C.

The theoretical voltage drop that occurs when oxygen is switched to air can be calculated from the thermodynamic equations:

$$\Delta G = \Delta G^0 - RTln\left(\frac{a^{3/2}{}_{O_2}}{a_{CO_2} \cdot a^2{}_{H2O}}\right) \qquad \textbf{Equation 2.4}$$

$$E = E^0 + \frac{RT}{nF} ln\left(\frac{\alpha^{3/2}}{\beta^2 \cdot \gamma}\right) + \frac{RT}{nF} ln\left(P^{-3/2}\right) \qquad \textbf{Equation 2.5}$$

$$\Delta E = \frac{RT}{4F} ln\left(\frac{\alpha_{O_2}}{\alpha_{H2O}}\right) \qquad \textbf{Equation 2.6}$$

The drop is function of the temperature; a loss of 10 mV can be supposed at 25 °C and of 11.5 mV at 60 °C. In the specific case of methanol fuel cells, another parameter, the methanol crossover, should be taken in consideration in the determination of the oxygen gain. As indicated by the OCV values, the permeation of methanol from anode to cathode cannot be neglected and, therefore, the oxygen gain may overestimate the loss in the cathode catalyst layer during air operation. Since the rate of methanol crossover decreases with the current density (60), the problem may be overcome by considering the variation of the oxygen gain in an interval of high current density values.

Electrochemical impedance spectroscopy

Complete fuel cell spectra were recorded under operating fuel cell conditions. More detailed information about this technique is provided in the Chapter 3.

2.4. References

1. **Zhang, J.** *PEM fuel cell electrocatalysts and catalyst layers: fundamentals and applications.* s.l. : Springers, 2008. p. 895.

2. **N. Rajalakshmi, K.S. Dhathathreyan.** Catalyst layer in PEMFC electrodes - Fabrication, characterization and analysis. *Chemical Engineering Journal.* 2007, 129, p. 31.

3. **A.Glüsen, M.Müller, N.Kimiaie, I.Konradi, J.Mergel, D.Stolten.** Manufacturing Technologies for Direct Methanol Fuel Cells (DMFCs). Proceedings 18th World Hydrogen Energy Conference, 2010 May 16-21, Essen.

4. **Basu, Suddhasatwa.** *Recent trends in fuel cell science and technology.* s.l. : Springer, 2007. p. 61.

5. **R. Mosdale, M. Wakizoe, S. Srinivasan.** Fabrication of electrodes for proton exchange membrane fuel cells using a spraying method and their performance evaluation. *The Electrochemical Society.* 1994, p. 179. Proceedings of the symposium on electrode materials and processes for energy conversion and storage.

6. **Roller, Justin.** *Low platinum electrodes for proton exchange fuel cells manufactured by reactive spray deposition technology.* p. 10. Mechanical engineering, University of British Columbia, Vancouver 2009.

7. **R. Benitez, J.Soler, L.Daza.** Novel method for preparation of PEMFC electrodes by the electrospray technique. *Journal of Power Sources.* 2005, Vol. 151, p. 108.

8. **J-H. Wee, K-Y. Lee, S.H. Kim.** Fabrication methods of low-P- loading electrocatalysts in proton exchange membrane fuel cell systems. *Journal of Power Sources.* 2007, Vol. 165, p. 667.

9. **X. Zhao, W. Li, Y. Fu, A. Manthiram.** Influence of ionomer content on the proton conduction and oxygen transport in the carbon-supported catalyst layers in DMFC. *International Journal of Hydrogen Energy.* 2012, Vol. 37, pp. 9845-9852.

10. **A.S. Aricò, V. Alderucci, V. Antonucci, S. Ferrara, V. Recupero, N. Giordano, K. Kinoshita.** ac Impedance spectroscopy of porous gas diffusion electrode in sulphuric acid. *Electrochimica Acta.* 1992, Vol. 37, 3, pp. 523-529.

11. **A.S. Aricò, V. Antonucci, V. Alderucci, E. Modica, N. Giordano.** A.c.-impedance spectroscopy study of oxygen reduction at Nation coated gas-diffusion electrodes in sulphuric acid: Teflon loading and methanol cross-over effects. *Journal of Applied Electrochemistry.* 1993, Vol. 23, pp. 1107-1116.

12. **C. Song, P.G. Pickup.** Effect of hot pressing on the performance of direct methanol fuel cells. *Journal of Applied Electrochemistry.* 2004, Vol. 34, pp. 1065-1070.

13. **C.Y. Chen, C.S. Tsao.** Characterization of electrode structures and the related performance of direct methanol fuel cells. *International Journal of Hydrogen Energy.* 2006, Vol. 31, p. 391.

14. http://en.wikipedia.org/wiki/Spray_gun. [Online]

15. http://www.phoenix-paints.co.uk/about-us/hints-tips/choosing-an-airbrush-or-spraygun.html. [Online]

16. http://www.diy-compressors.com/spraying-basics.htm#mechanics. [Online]

17. http://www.how-to-build-hotrods.com/set-up-hvlp.html. [Online]

18. **C.A.Technologies.** TJR. *Techline JR - Gravity Feed Spray Gun - Product Information.*

19. http://www.spraycat.com. [Online]

20. http://en.wikipedia.org/wikiAirbrush. [Online]

21. http://draftingmanuals.tpub.com/14262/css/14262_290.htm. [Online]

22. **Paasche.** VL & VLS – Airbrushes Double Action - Internal Mix - Siphon Feed - PTFE Packings. *INSTRUCTIONS AND PARTS LIST VL/VLS-8/31/2011.*

23. http://www.paascheairbrush.com. [Online]

24. **S. Siracusano, A. Stassi, V. Baglio, A.S. Aricò, F. Capitanio, A.C. Tavares.** Investigation of carbon-supported Pt and PtCo catalysts for oxygen reduction in direct methanol fuel cells. *Electrochimica Acta.* 2009, Vol. 54, p. 4844.

25. **J.Xie, K.L. More, T.A. Zawodzinski, W.H. Smith.** Porosimetry of MEAs Made by ''Thin Film Decal'' Method and Its Effect on Performance of PEFCs. *Journal of The Electrochemical Society.* 2004, Vol. 151, 11, pp. A1841-A1846.

26. **T.V. Reshetenko, H.-T. Kim, H.-J. Kweon.** Cathode structure optimization for air-breathing DMFC by application of pore-forming agents. *Journal of Power Sources.* 2007, Vol. 171, p. 433.

27. **J. Lobato, P. Canizares, M.A. Rodrigo, C.R.-Lopez, J.J. Linares.** Influence of the Teflon loading in the gas diffusion layer of PBI-based PEM fuel cells. *Journal of Applied Electrochemistry.* 2008, Vol. 38, p. 793.

28. http://en.wikipedia.org/wiki/Scanning_electron_microscope. [Online]

29. http://serc.carleton.edu/research_education/geochemsheets/techniques/SEM.html. [Online]

30. http://mee-inc.com/sem.html. [Online]

31. Introduction to Energy Dispersive X-ray Spectrometry (EDS). *http://micron.ucr.edu/public/manuals/EDS-intro.pdf.* [Online]

32. **M.Mayer.** Rutherford Backscattering Spectroscopy. Lecture given at the Workshop on Nuclear Data for Science and Technology: Materials Analysis. Trieste, 2003 May 19-30.

33. **Ernst, F.** *Rutherford Backscattering Spectroscopy.* [EMSE-515] Fall-2005.

34. http://en.wikipedia.org/wiki/Dynamic_vapor_sorption. [Online]

35. http://www.thesorptionsolution.com/. [Online]

36. **P.C.Hiemenz, R.Rajagopalan 3rd ed.** *Principle of colloids and surface chemistry.* New York : Marcel Dekker, 1997. pp. 265-276.

37. http://en.wikipedia.org/wiki/Contact_angle. [Online]

38. **B.Bhushan, Y.C. Jung, K. Koch.** Micro-, nano- and hierarchical structures for superhydrophobicity, self-cleaning and low adhesion. *Philosophical Transactions of The Royal Society A.* 2009, Vol. 367, pp. 1631-1672.

39. **Y.C. Jung, B. Bhushan.** Contact angle, adhesion and friction properties of micro- and nanopatterned polymers for superhydrophobicity. *Nanotechnology.* 2006, Vol. 17, pp. 4970-4980.

40. **H.M. Yu, C. Ziegler, M. Oszcipok, M. Zobel, C. Hebling.** Hydrophilicity and hydrophobicity study of catalyst layers in proton exchange membrane fuel cells. *Electrochimica Acta.* 2006, 51, pp. 1199–1207.

41. **Jari Ihonen, Mikko Mikkola, Göran Lindbergh.** Flooding of Gas Diffusion Backing in PEFCs. *Journal of Electrochemical Society.* 2004, Vol. 151, 8, pp. A1152-A1161.

42. **D.L. Wood III, C. Rulison, R.L. Borup.** Surface properties of PEMFC gas diffusion layers. *Journal of Electrochemical Society.* 2010, Vol. 157, 2, pp. B195-B206.

43. **S. Lowell, J.E. Shields, M.A. Thomas, M. Thommes.** *Characterization of porous solids and powders: surface area, pore size and density.* s.l. : Kluwer Academic Publishers. p. 5.

44. **Westermarck, Sari.** *Use of mercury porosimetry and nitrogen adsorption in characterization of the pore structure of mannitol and microcrystalline cellulose powders, granules and tablets.* Academic dissertation, Faculty of Science, Department of Pharmacy, University of Helsinki, 2000.

45. http://www.micromeritics.com/Repository/Files/Gas_Sorption.pdf. [Online]

46. **Yeung, Dr. KingLun.** Adsorption and Catalysis. Department of Chemical Engineering - Hong Kong University of Science and Technology : s.n.

47. **A.J. Bard, L.R. Faulkner.** *Electrochemical Methods, Fundamentals and Applications, 2nd ed.* s.l. : John Wiley & sons Inc. p. 2.

48. —. *Electrochemical Methods, Fundamentals and Applications, 2nd ed.* s.l. : John Wiley & sons, Inc. p. 226.

49. **P.T. Kissinger, W.R. Heineman.** *Laboratory Techniques in Electroanalytical Chemistry, 2nd ed.* s.l. : Marcel Dekker Inc. p. 84.

50. **A.J. Bard, L.R. Faulkner.** *Electrochemical Methods, Fundamentals and Applications, 2nd ed.* s.l. : John Wiley & sons, Inc.

51. **P.T. Kissinger, W.R. Heineman.** *Laboratory Techniques in Electroanalytical Chemistry, 2nd.* s.l. : Marcel Dekker Inc.

52. **D.B. Zhou, H.V. Poorten.** Electrochemical characterization of oxygen reduction on teflon-bonded gas diffusion electrodes. *Electrochimica Acta.* 1995, Vol. 40, 12, p. 1819.

53. **A. Kamat, A. Huth, O. Klein, S. Scholl.** Chronoamperometric investigations of the electrode-electrolyte interface of a commercial high temperature PEM fuel cell. *Fuel cells.* 2010, Vol. 00, 0, p. 1.

54. **Evans, J.P.** *Experimental Evaluation of the Effect of Inlet Gas Humidification on Fuel Cell Performance.* Blacksburg, Virginia : s.n., 2003. Master of Science in Mechanical Engineering.

55. **EG&G Technical services, Inc.** *Fuel cell Handbook (7th edition).* 2004. U.S. Department of Energy, National Energy Technology Laboratory.

56. **Rayment, C.** Introduction to fuel cell technology. 2003. Department of aerospace and mechanical engineering, Univerity of Notre Dame, USA.

57. **Ramani, V.** Fuel Cells. The Electrochemical society interface - Spring 2006.

58. **Zhang, J.** *PEM Fuel Cell electrocatalysts and catalyst layers.* p. 599. Springer, London 2008.

59. **M. Prasanna, H.Y. Ha, E.A. Cho, S.-A. Hong, I.-H. Oh.** *Journal of Power Sources.* 2004, Vol. 137, p. 1.

60. **A.S. Aricò, S. Srinivasan, V. Antonucci.** DMFCs: From Fundamental Aspects to Technology Development. *Fuel Cells.* 2001, Vol. 1, 2, p. 133.

CHAPTER 2 : EXPERIMENTAL METHODS

2.1. Preparation of DMFC cathodes

A. Techniques of preparation

The cathode preparation is one of the most important and challenging steps involved in the membrane - electrodes assembly (MEA) manufacture. The cathode should be designed to generate high reaction rate and power output by using the minimum amount of catalyst. In addition, for a proper functioning it is required:

a) Extended interface between the cathode and the electrolyte membrane,
b) Efficient proton transport through the catalyst layer,
c) Easy transport of oxygen and removal of condensed water,
d) Continuous electronic conduction between the three-phase boundaries and the current collectors,
e) For the specific case of DMFC, low concentration polarization caused by the liquid sealing effect.

The cathode performance depends on these physical characteristics which are affected by the technique involved in the preparation of the catalyst layer (CL). Traditionally, a catalyst slurry is applied on a porous support by various coating methods such as screen printing, knife-coating, slot-coating, brushing, spraying and painting, (1; 2; 3; 4).

Screen printing is one of the most popular methods used for the fabrication of CLs due to its convenience and adaptability. In this technique the catalyst slurry is directly printed onto the support by using a screen which determines the amount of catalyst ink applied to the substrate. Knife coating and slot coating are also well-know methods especially in the production of commercial fuel cell electrodes. In the knife coating, the amount of applied ink is controlled by the distance knife-substrate, even if a certain amount of ink that penetrates in the pores of the substrate. In the slot coating, the amount of applied catalyst is controlled by a metering pump. In spraying, as described from Srinivasan (5), the catalyst ink is prepared by mixing the catalyst, the solvent and the ionomer and it is repeatedly sprayed, in presence of air or nitrogen, onto a sheet of carbon cloth or carbon paper. Between each spraying, the support is heated to evaporate the

solvent, in order to prevent the components from re-dissolving during the next spraying. Because of its simplicity and low-cost, and the possibility to prepare thinner samples (6), the spray technique is a promising method for the fabrication of commercial electrodes. Indeed a production line can be fully automated and therefore the electrode fabrication can be readily scaled up.

In addition to the conventional methods, novel advanced methods such as electrospray, vapor deposition and sputtering, electro-deposition and electrophoretic deposition techniques have been developed (1; 7; 8). The electrospray method shows both morphological and structural improvements that contribute to better catalyst utilization in comparison with conventional methods. The physical, thermal or chemical vapor deposition (CVD) methods are based on the advantageous deposition of low-loading Pt nanoparticles on gas diffusion electrodes. The sputtering provides a method of depositing a thin catalyst layer that delivers high performance combined with a low Pt loading. In pulse electro-deposition, it is ensured that most of the deposited Pt catalyst is in close contact with the membrane. In electrophoretic deposition (EPD) a suspension consisting of ethanol, carbon powders with Pt catalyst, and ionomer is used to obtain a stable dispersed solution; the thickness of the prepared CL is controlled by the EPD duration or concentration of the suspension.

At the state of the art, some technical aspects of the catalyst layer for DMFC still need to be improved. In particular, it is necessary to:

- *Maximize the three-phase interface of the CL*. The performance of a CL depends on its electrochemical active surface area. High catalyst loading are generally required to counteract the poisoning effect of methanol (9) and consequently thick catalyst layers are prepared. The thickness of the CL increases the tortuosity of oxygen diffusion and the pathway of proton conduction, leading to low catalyst utilization and mass transport limitations. Optimizing the ratios of the components, the structure, the thickness and the hydrophobicity or hydrophilicity is necessary.
- *Stabilize the metal particle on the support*. The metal particles on supports, like carbon powder or carbon nanotubes, undergo agglomeration or detach from the support. This is because there are no chemical bonds between the particles and the support and the nanoparticles are active and mobile and they have the tendency to agglomerate together. It

is necessary to structure the support in such a way that allows the metal particles to anchor tightly on the surface of the support.

- *Reduce the degradation of the CLs' components*. The catalyst particles, binder and carbon support degrade during the operation due to chemical and electrochemical corrosion. It is necessary to find ways to stabilize the components such as the graphitization used to increase the stability and conductivity of the support.
- *Accelerate the activation of the CL*. To make the fuel cell work it is necessary to activate the MEA. This process makes the CL reaches its maximum activity. Depending on the used method, the activation of the MEA can take time therefore it is necessary to find ways for an easier start up.

B. Instrumentation and experimental parameters

In this work, different DMFC composite Pt-based cathodes were realized by spray technique. All cathodes were prepared by deposition of the catalyst layer on a porous carbon cloth supports (Ballard 1071 HCB, ElectroChem Inc. EC-CC1-060-T) to form the so called Gas Diffusion Electrodes (GDE). Since high catalyst loadings were used, it was chosen to minimize the thickness of the cathodes by not using any microporous gas diffusion layer in between the carbon support and the catalyst layer. Indeed, this approach has already been adopted in the preparation of electrodes for DMFCs (10; 11; 12; 13). The catalyst layer were formed using catalyst inks which were prepared by mixing the required amounts of

- Catalyst: 60 wt % Pt/Vulcan catalyst (BASF)
- Binder: 5 wt % Nafion solution (Ion Power)
- Binder: 60 wt % Teflon suspension (Sigma-Aldrich)
- Solvents: water and isopropyl alcohol

The inks were prepared in two steps. In the first step the Pt/C catalyst powder was dispersed in the solvents. In the second step the Nafion solution and/or the Teflon suspension were added to the mixture. Each step was followed by 15 min of homogenization in an ultrasonic water bath at 40 °C. The catalyst inks were then sprayed under air onto 36 cm^2 carbon supports on a hot plate at 80 °C, as shown in Figure 2.1. From the 36 cm^2 samples, several cathodes were derived and used for the ex-situ electrochemical and in-situ fuel cell characterization. A spray-gun or an

airbrush were used to prepared the cathodes and their specifications are presented below. The final composition of the DMFC cathodes is reported in Table 2.1.

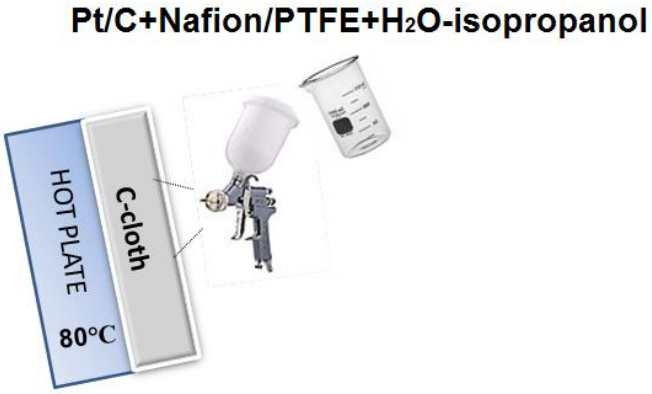

Figure 2.1: Deposition of the catalyst layer by spray technique.

Table 2.1: Description of the parameters related to the preparation of the cathodes.

	Spray gun / Airbrush	*Name*	*Pt loading mgcm^{-2}*	*wt% Nafion*	*wt% PTFE*	*Support*
Series I	TJR spray gun (HVLP)	N15/T00	2.94	15	0	Carbon cloth
		N10/T05	2.82	10	5	Carbon cloth
		N05/T10	2.86	5	10	Carbon cloth
		N00/T15	2.87	0	15	Carbon cloth
Series II	Paasche airbrush (VL)	N10/T05-P	2.84	10	5	Carbon cloth
Series	TJR spray gun (HVLP)	N00/T15-350	2.87	0	15	Carbon cloth
		N00/T15-N05	2.87	5	15	Carbon cloth
		N00/T15-TFE	3.3	0	15	TFE-treated Carbon cloth

✓ *Series I: Nafion-PTFE-based cathodes*

Four different cathodes with 2.82 ± 0.12 mgcm^{-2} Pt loading and 15 wt% binder with respect to Pt were prepared by spraying the catalyst layer on untreated C-cloth support. The relative amount of Nafion and PTFE binders were varied as follows:

- 15 wt % Nafion and 0 wt % PTFE
- 10 wt% Nafion and 5 wt % PTFE

- 5 wt% Nafion and 10 wt % PTFE
- 0 wt% Nafion and 15 wt % PTFE

The cathodes were identified as N XX / T YY, where XX is the wt% of Nafion and YY the wt% of PTFE. The cathodes were not subjected to the usual thermal treatment at 350 °C required for sintering the PTFE because Nafion's sulfonic acid groups undergo degradation at this temperature. The cathodes were prepared by using a TJR spray gun from C.A. Technologies (see below).

- ✓ *Series II: N 10 / T 05 - P cathode*

A cathode with the same chemical composition of the N 10 / T 05 (Table 2.1) was prepared by using a Paasche Airbrush. The Pt loading of the cathode is 2.84 ± 0.03 $mgcm^{-2}$. The cathode was identified as N 10 / T 05 - P where P is the acronym of Paasche Airbrush. Again, no thermal treatment was applied to the cathode.

- ✓ *Series III: N 00 / T 15-based cathodes*

Three additional cathodes, with similar composition as the N 00 / T 15 cathode (Table 2.1), were prepared.

The first cathode (2.87 $mgcm^{-2}$ Pt loading and 15 wt% PTFE with respect to Pt) was subjected to the thermal treatment at 350 °C to sintering the PTFE. An oven was used for this purpose. The cathode was inserted in the oven at room temperature and heated up to 350 °C; it was maintained at this temperature for 30 min and it was slowly cooled down to 25 °C for 21 h.

The second cathode (2.87 $mgcm^{-2}$ Pt loading and 15 wt% PTFE with respect to Pt) was sprayed with the 5 wt % Nafion.

The third cathode (3.3 $mgcm^{-2}$ Pt loading and 15 wt% PTFE with respect to Pt) was prepared by spraying the catalyst layer on TFE-treated C-cloth support (ElectroChem Inc. EC-CC1-060-T).

The cathodes were identified as N 00 / T 15 - Z, where Z is the temperature of sintering (350) or the percentage of Nafion coating (N 05) or the treatment of the support (TFE). The cathodes were prepared by using a TJR spray gun from C.A. Technologies (see below).

C.A. Technologies TJR Spray gun – model HVLP

Spray guns are commercial tools typically used for painting/covering large surface areas with high volume of paint (14; 15; 16). Hand-held or automated, spray guns conventionally work at pressures between 15 psi and 60 psi; however, the specific models "High Volume Low Pressure (HVLP)" are designed to apply large quantities of paint at very low pressure (7.5 psi). This is useful to prevent waste of paint (17). One feature of spray guns not available in airbrushes is the fan control (see picture). This option allows air to be directed at the sides of the pain coin as it leaves the nozzle, this has the effect of turning the coin into a fan. The ring that controls this function can be rotated so that the fan can be horizontal, vertical or any angle in between.

In this work, a TJR spray gun (C.A. Technologies) model HVLP with gravity feed and tip size 0.8 mm was used to prepare the first and third series of cathodes (18). As shown in Figure 2.2, the spray gun has two controllable knobs: the material knob and the air volume knob. The material knob was unscrewed about $2_{1/2}$ turns whereas the air volume knob was opened to the point where the air volume started to stay the same. The cigar shaped pattern produced with horizontal fun is also shown in Figure 2.2.

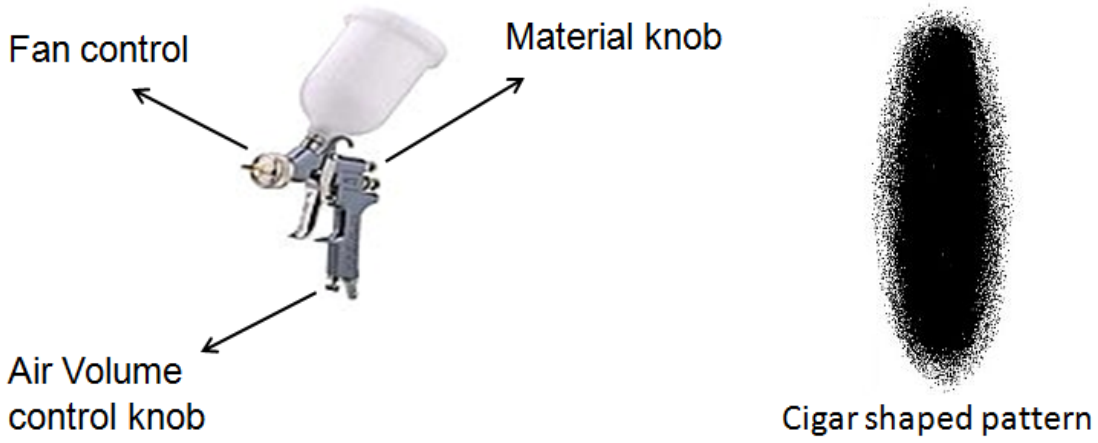

Figure 2.2 : TJR-HVLP Spray gun (C.A.Technologies), cigar shaped pattern from horizontal fun (19).

Paasche Airbrush – model VL

Airbrushes are small precision tools that combine inks with compressed air to create a fine mist or spray. They are hand-held and used instead of a brush for detailed work such as photo retouching, painting nails, fine art (20; 21). All airbrushes have an inlet for compressed air, a nozzle through which paint is sprayed under pressure and a release valve (finger lever) that

enables the operator to use air to propel the paint and to control the amount of air and paint that comes out the nozzle. The specific model "double-action" airbrush allows the control and variation of the spray pattern during each stroke. Two separate finger actions control the spray pattern: the first action is to depress the finger lever releasing air only. The second action is to pull the finger lever back releasing pigment. Pulling the lever further back releases more ink and enlarges the spray pattern.

In this work, a double-action airbrush (Paasche) model VL, Figure 2.3, was used to prepare the N 10 / T 05 – P cathode (22). The airbrush was chosen to change the catalyst distribution within the catalyst layer and to concentrate it more on the surface of the cathode. A head size 3 with a tip size 0.73 mm was chosen to reproduce the same condition of the previous spray gun. With the support of an air regulator, the airbrush was operated at 20 psi pressure. The finger lever was pulled back completely to produce the most enlarged pattern which is shown as well in Figure 2.3.

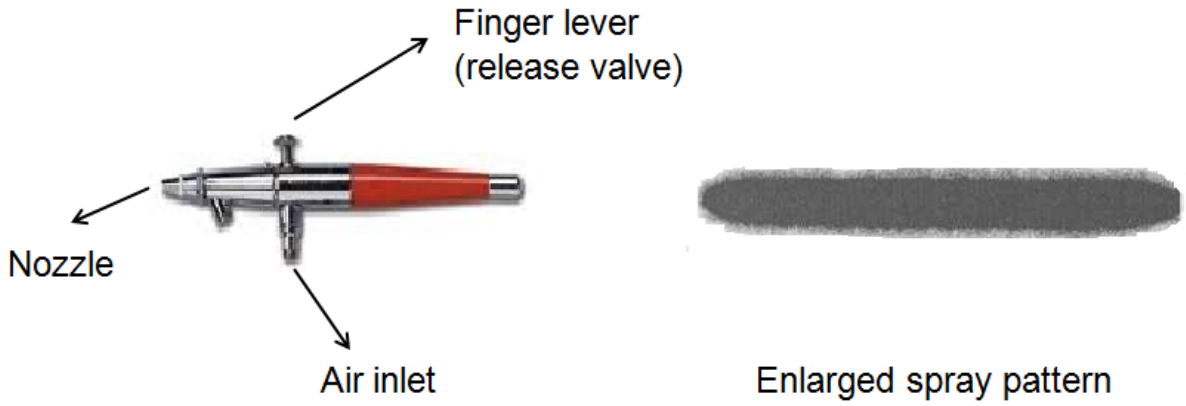

Figure 2.3: Double-action-VL Airbrush (Paasche), enlarged spray pattern (23).

- ✓ *Commercial – Pt/KB-based and Pt_3Co/KB-based cathodes*

A commercial cathode from the ElectroChem. Inc. company, a Pt/KB–based cathode and a Pt_3Co/KB-based cathode were used in this work for the study of the DMFC total impedance (Chapter 4). The commercial cathode was prepared by spreading the PTFE-catalyst ink on the TFE-treated carbon support (25 ± 5 % wet-proofing). 60 wt % Pt/Vulcan XC-72 catalyst and 20 wt % Teflon suspension were used for a final 3 $mgcm^{-2}$ Pt loading and unknown amount of PTFE. The cathode was coated with a 5 wt % Nafion solution (Ion Power) to a final 33 wt % Nafion content (with respect to Pt loading). No microporous GDL was used in this cathode.

The Pt/KB–based and Pt_3Co/KB-based cathodes were prepared from 50 wt% Pt/KB (Ketjenblack) and 50 wt% Pt_3Co/KB catalysts which were synthesised in the CNR-ITAE laboratory in Messina, following the procedure reported in our work (24). The catalysts were mixed with 15 wt % Nafion ionomer (Ion Power, Nafion solution) and deposited on by a doctor blade technique onto LT-ELAT gas diffusion layers (E-TEK). The final Pt loading was 3 $mgcm^{-2}$. The final composition of the cathodes is reported in Table 2.2.

Table 2.2 : Description of the parameters for commercial, Pt/KB-based and Pt_3Co/KB-based cathodes.

Name	*Catalyst*	*Pt loading ($mgcm^{-2}$)*	*wt% Nafion*	*Support*
Commercial	60 wt% Pt/Vulcan	3	33	TFE-treated carbon cloth
Pt/KB-based	50 wt % Pt/KB	3	15	LT-ELAT
Pt_3Co-based	50 wt % Pt_3Co/KB	3	15	LT-ELAT

2.2. Preparation of MEAs

In this work, the MEAs were prepared by applying the gas diffusion electrodes to the sides of the membrane. A commercial PtRu-based electrode from ElectroChem. Inc. company (40 wt % Pt - 20 wt% Ru /Vulcan XC-72 catalysts, 3 $mgcm^{-2}$ Pt loading, unknown amount of PTFE, 33 wt% Nafion ionomer coating, TFE-treated carbon support (25 ± 5 % wet-proofing)) was used as anode. A pre-treated Nafion 117 membrane (DuPont) was used as electrolyte. The pre-treatment consisted in boiling the membrane for 1 h in 3 % vol. H_2O_2 (Fisher Scientific, 30 % vol.), for 1 h in deionized water, for 1 h in 1.2 M H_2SO_4 (Fisher Scientific, Puriss. 95-98%), and finally washing it in deionized water. The membrane-electrodes assemblies were formed by hot-pressing procedure. The cathode-membrane-anode sandwiches were disposed between two copper plates, covered with 0.25 mm thick PTFE sheets (GoodFellow). They were placed in a Carver press, pre-heated at 143 °C, for 1 min and then pressed for 40 s at the standard pressure 500 lbs. Since this work contains an investigation of the effect of the assembly pressure, a couple of MEAs were pressed at the lower values 375 and 250 lbs. In relation to the nomenclature used for the cathodes, the prepared MEAs were identified as MEA-T where T is the name of the cathode. The extension -500, -375 and -250 was finally added to MEA-T to identify the MEAs prepared at different pressures.

Concerning the MEAs containing the Pt/KB–based and Pt_3Co/KB-based cathodes (Chapter 4), they were prepared following the same procedure, with a Nafion 117 membrane but with another type of anode (unsupported Pt-Ru catalyst (Johnson-Matthey), 3 $mgcm^{-2}$ Pt loading, 15 wt % Nafion ionomer, HT-ELAT gas diffusion layer).

A list of the MEAs investigated in this thesis is reported in Table 2.3.

Table 2.3: List of MEAs investigated in this thesis.

MEA	*Cathode*	*Type of investigation*	*Chapter*
MEA - N15/T00	N15/T00 (Table 2.1)	Effect Nafion/PTFE binders	5
MEA - N10/T05	N10/T05 (Table 2.1)	Effect Nafion/PTFE binders	5
MEA - N05/T10	N05/T10 (Table 2.1)	Effect Nafion/PTFE binders	5
MEA - N00/T15	N00/T15 (Table 2.1)	Effect Nafion/PTFE binders	5
MEA - N10/T05-P	N10/T05-P (Table 2.1)	Effect of Pt distribution	5
MEA - N00/T15 - 500	N00/T15 (Table 2.1)	Effect assembly pressure	6
MEA - N00/T15 - 375	N00/T15 (Table 2.1)	Effect assembly pressure	6
MEA - N00/T15 - 250	N00/T15 (Table 2.1)	Effect assembly pressure	6
MEA -N00/T15-N05	N00/T15-N05 (Table 2.1)	Effect morphology cathode	6
MEA -N00/T15-TFE	N00/T15-TFE (Table 2.1)	Effect morphology cathode	6
MEA – Pt/KB	Pt/KB-based cathode (Table 2.2)	EIS - Fitting	3
MEA – Pt_3Co/KB	Pt_3Co/KB-based cathode (Table 2.2)	EIS - Fitting	3
MEA – Pt/XC72	Commercial cathode (Table 2.2)	EIS - Fitting	3

2.3. Cathode Characterization

All the techniques used in this work to characterize the cathodes are presented in Table 2.4. The experimental description and the principle of each technique are reported in the corresponding section.

Table 2.4 : List of techniques used to characterize cathodes and MEAs.

	Technique	*Objective*	*Paragraph/Chapter*
Cathodes ex-situ	SEM / EDS	➢ Images of surface and cross-section ➢ Cartography of the surface (mapping) and cross-section (linear-scan) ➢ Quantitative chemical analysis	2.3.1.1
	RBS	Quantification of the Pt and S composition in the first 200 nm of the cross-section	2.3.1.2
	DVS / H_2O – Hexane uptake	Effect of Nafion/PTFE content on the hydrophilicity/hydrophobicity of the cathodes	2.3.1.3 2.3.1.4
	Sessile-drop contact angle	Wettability of the cathode surface	2.3.1.5
	N_2 adsorption	Total micro, meso and macro-pore volume (up to 200 nm)	2.3.1.6
	Cyclic Voltammetry	➢ Under N_2: electrochemical surface area, catalyst utilization, potential range for double-layer capacity ➢ Under O_2: performance towards ORR, half-wave potential and limiting-current	2.3.2.2
	Chronoamperometry	➢ Thin-film mechanism on N 00 / T 15 cathode and flooding for N 15 / T 00 cathode	2.3.2.3
	EIS	Fully investigation of the cathode in 0.5 M H_2SO_4 solution	Chapter 3
Cathodes in DMFC	EIS (high frequency)	Cell resistance	2.3.3.4
	E-j curves	Fuel cell performance (OCV and current density at 0.1 V)	2.3.3.5
	O_2 gain	Voltage loss related to mass-transport limitations	2.3.3.6
	EIS	Fully investigation of the cathode in DMFC	Chapter 3

For this work the mercury porosimetry technique would be required to measure the macro-porosity of the cathodes (25; 26; 27; 9). However, up to now, we did not find any facility able to do this type of measurements on our samples. We have been searching for this instrument in the main local universities (Concordia University, McGill University, Université de Sherbrooke, Université de Trois-Rivieres) but either they didn`t have the instrument either it was not in function from many years, either we didn't get any response. Concerning companies, we have contacted for example Quantachrome company but they requested samples of 1.2 cm^2 with a mass of 2-5 g, and the weight of our samples with those dimensions is typically 0.1 g.

2.3.1. Physicochemical characterization

Scanning Electron Microscopy – Energy Dispersive Spectrometry

In this work the SEM technique was used to acquire images of the surfaces and cross-sections of the cathodes as well as to reproduce the cartography of surface areas (mapping) and cross-sections (linear-scan), as exemplified in Figure 2.4. The JSM-6300F microscope (JEOL Company) was used for the purpose. In all the measurements, the working distance was 15 mm and the tensions of 5 kV and 20 kV were used as necessary. An X-rays energy-dispersive detector (Oxford instrument, Link ISIS) was used for the elemental analysis. From the images of the cross-sections, the total thickness (support and catalyst layer) was measured using the Semaphore software. The thickness was measured in different points of the cathode' cross-section and an average value were calculated.

The Scanning Electron Microscopy (SEM) is a method for high-resolution imaging of surfaces (28; 29; 30). This technique is based on the electron-sample interaction and it gives information on the morphology, topography and composition of the sample. The source, an electron gun, generates a beam of incident electrons which cause an emission of electrons from the sample. The type of information that can be achieved depends on the nature of the detected electrons. An inelastic collision of the incident beam causes the emission of the low-energy secondary electrons. These electrons are emitted from the sample surface therefore the contrast in the acquired image depends on the surface morphology. An image contrast as a function of the

composition can be provided by the backscattered electrons which are high-energy electrons, ejected by an elastic collision of the incident beam with a much deeper area of the sample.

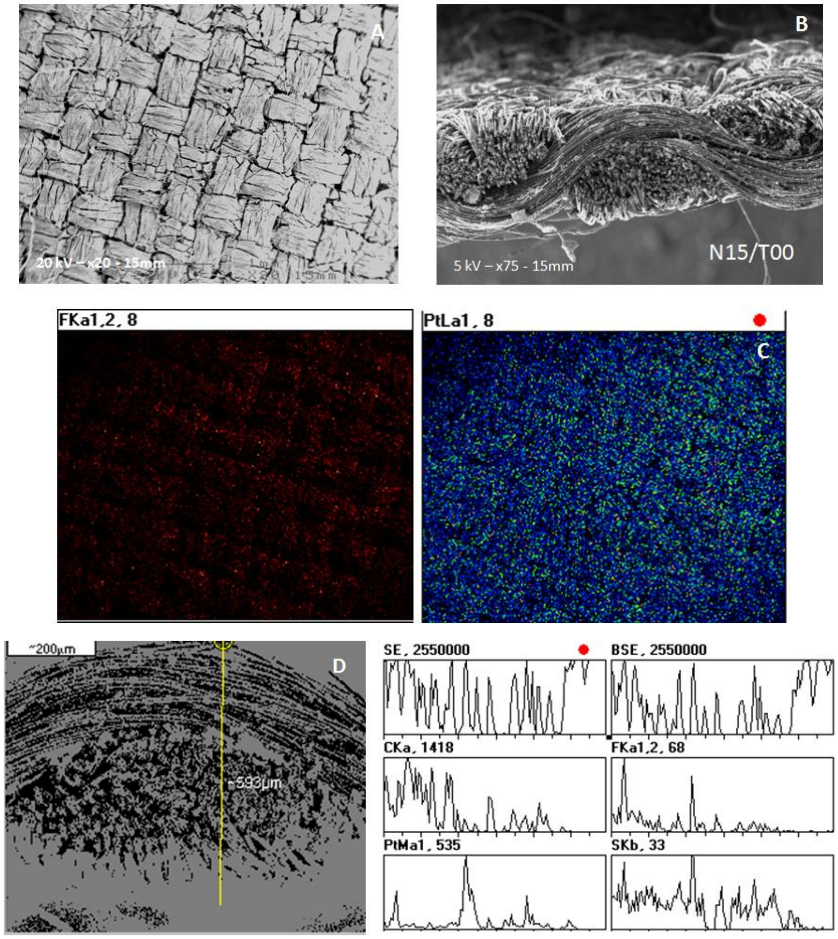

Figure 2.4 : a) Surface, b) cross-section, c) mapping, d) linear-scan for N 15 / T 00 cathode.

The interaction of an incident beam with the sample target causes also the emission of X-rays which can be used to obtain a chemical analysis of the sample (31). The Figure 2.5 reports an example of ED spectrum for a N 15 / T 00 cathode with the x-axis reporting the X-ray energy (keV) and the y-axis the intensity. The spectrum shows the peaks of C, F and Pt. The peak of S (not shown) appears at 2.2 keV, partially overlapping with the Pt peak. Because of the irresolution of the two peaks, in this work EDS could not be used to quantify the Pt and S composition in the sample. In addition, the ZAF correction failed in the quantitative analysis. Therefore, the C and F compositions were not trustable as well.

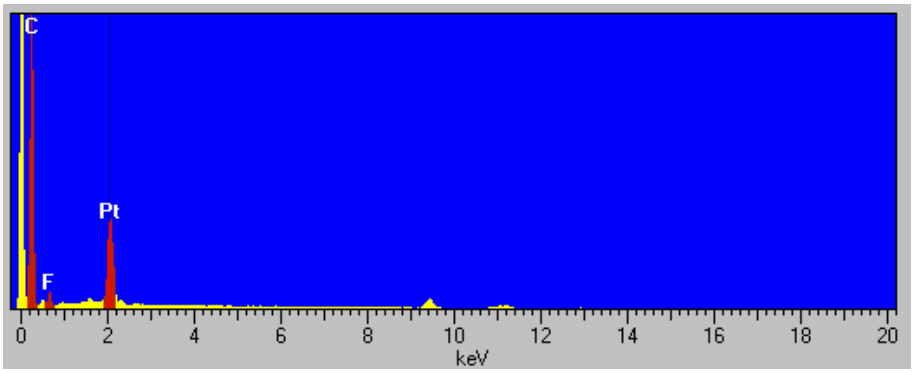

Figure 2.5 : ED spectrum of N 15 / T 00 cathode with peaks of C, F and Pt.

Rutherford Backscattering Spectroscopy

As shown above, the quantification of Pt and S by EDS analysis was not possible because of the irresolution of the two peaks. In this work the RBS technique was used to try to investigate the distribution of Pt and S in the first 200 nm of cathode thickness. Variations in the S composition were expected because of the different Nafion content in the samples. Since the cathodes have the same catalyst loading, no differences were expected in the Pt quantification. However, it was suspected that the different type and ratio of binders could affect the Pt distribution within the catalyst layer and therefore its quantification. The RBS spectrum (count rate vs. energy) of I series of cathodes and N 10 / T 05 – P cathode is reported in Figure 2.6. As shown, the peak of Pt is well resolved; however, the S peaks is elongated towards lower energies and not resolved. For this reason, the quantification of S composition was not possible and the RBS technique was not considered useful for our studies.

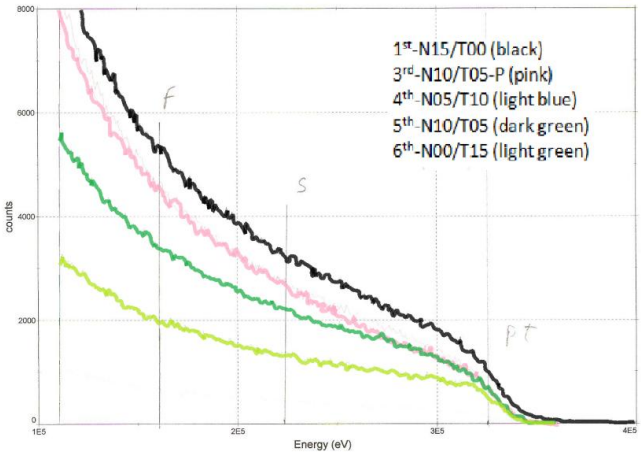

Figure 2.6 : RBS spectrum for cathodes with peaks of S and Pt.

The RBS measurements were performed with a beam of mono-energetic ^{4}He particles of low energy 350 keV collimated onto the sample positioned in a vacuum chamber at 10^{-9} torr. The backscattered ions were detected at a scattering angle of 145° by a solid state detector with energy resolution of 22 keV.

Rutherford Backscattering Spectroscopy (RBS) is an ion scattering technique used for quantitative compositional analysis and depth profiling of individual elements of thin film samples (32; 33). During a RBS measurement, high-energy ions (H^{+}, He^{++}) are collimated onto the sample positioned in a vacuum chamber (10^{-6} – 10^{-9} torr) and the backscattered ions are detected. The energy of the backscattered ions gives information about the type of atoms encountered and the length of the path traveled, whereas the number is directly proportional to the concentration of a given element in sample.

Dynamic Vapor Sorption

In this work the water vapor sorption isotherms were recorded to explore the effect of Nafion/PTFE content on the hydrophilic character of the cathodes. Since we were particularly interested in the W_{up} at high relative humidity, sorption isotherms were recorded by increasing the relative humidity (RH%) with step of 30% RH and 30 min up to 90% RH and a step to 97% RH for 48 h. The experimental profile is shown in Figure 2.7a. The experiments were performed with a DVS – High Throughput apparatus (Surface Measurement Systems) equipped with a Cahn ultra microbalance with a mass resolution of 10 μg. Sample of 0.16 mm^2 area were placed in the DVS – HT pans and dried under a stream of dry nitrogen (5.0) at 25 °C for 6 h. The total gas flow used was 400 sccm.

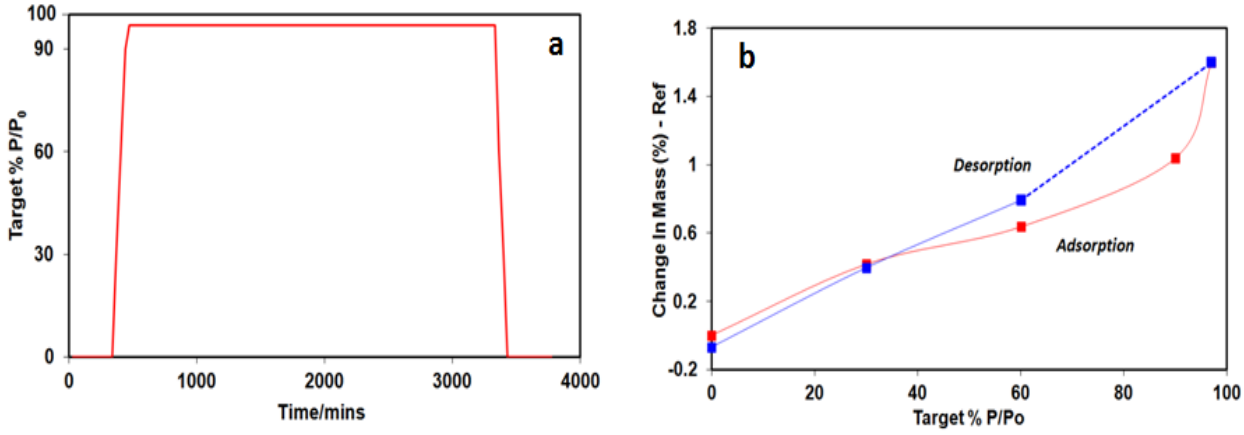

Figure 2.7: a) Water sorption profile, b) adsorption and desorption isotherms for N 15 / T 00 cathode.

The Dynamic Vapor Sorption (DVS) is a gravimetric technique that measures the rate at which a vapour solvent is absorbed by the sample (34; 35). The sample is exposed to a series of step changes in relative humidity and the mass change is monitored as a function of time. The equilibrium mass values at each relative humidity step are used to generate isotherms. Isotherms are typically divided in two components: adsorption for increasing humidity steps and desorption for decreasing humidity steps. The difference in water vapor uptake between the two isotherms is called hysteresis. The shape of the isotherm hysteresis gives information about the sorption mechanism and sample porosity. The Figure 2.7b shows the shape of typical water adsorption/desorption isotherms recorded for N 15 / T 00 cathode.

Liquid water and hexane uptake

In this work the liquid water and hexane uptake were measured to investigate the hydrophilic and hydrophobic character of the cathodes. Samples of 4 cm^2 area were dried for 3 h in the oven at 50 °C and weighted. The samples were then immersed for 48 h in 50 ml of liquid water/hexane and weighted again. For each sample, the weight after the uptake was measured 3 times and an average value was calculated. Measurements of water uptake were performed on all the cathodes. Hexane absorption measurements were attempted on the series I of Nafion/PTFE cathodes; however no relevant uptake was observed.

The solvent uptake is a method to measure the solvent absorption capacity of a sample. The technique consists in immersing the sample in a solvent (generally, water, methanol, toluene and hydrocarbons) and in calculating the solvent uptake by the weight difference between the wet electrode and the dry electrode as follow:

$$\%wt_{solvent} = \frac{\left(wt_{wet} - wt_{dry}\right)}{wt_{dry}} \times 100 \qquad \textbf{Equation 2.1}$$

The time of immersion of the sample is related to the type of sample and it can go from some minutes to many hours.

Sessile drop contact angle

In this work the sessile drop contact angle was used to evaluate the wetting of the cathodes' surface. The apparatus for the contact angle measurements consisted in a programmable pump, that pushed and withdrawn with constant rate (2.5 $\mu l min^{-1}$) the specified volume of deionized

water (5 μl) through a micro-capillary tube and formed a growing drop (~ 0.35 mm in diameter) on the 1 cm^2 sample surface. The evolution of the drop (advancing and receding contact angles) was observed using a camera and the recorded images were analyzed using the Acquidam 2.2 software. Figure 2.8 shows the water drop at maximum evolution on the surface of the N 15 / T 00 cathode.

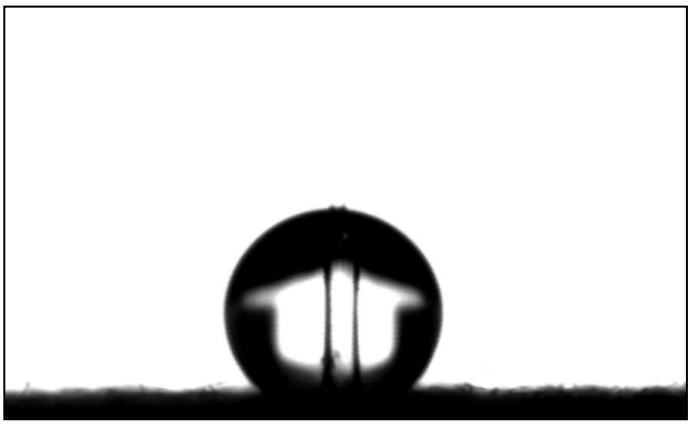

Figure 2.8 : Water drop on the surface of N 15 / T 00 cathode.

The contact angle measurement is a method to characterize the interfacial properties of a liquid in contact with a solid substrate (36; 37; 38; 39) and an important tool in the investigation of non-homogeneous, porous, hydrophilic/hydrophobic surfaces (40; 41; 42).

The contact angle describes the shape of a liquid droplet resting on a solid surface. Generally the Young's equation is used to explain the balance of forces of the liquid drop on the surface:

$$\gamma^{sv} = \gamma^{sl} + \gamma^{lv} \cos\theta \qquad \textbf{Equation 2.2}$$

where γ^{sv} is the solid surface free energy, γ^{lv} the liquid surface free energy, γ^{sl} the solid/liquid interfacial free energy and θ the contact angle. When drawing a tangent line from the droplet to the touch of the solid surface, the contact angle is the angle between the tangent line and the solid surface. The contact angle measurement gives information on:

a) The nature of the solid, if a liquid with well-know properties is used.
b) The affinity of the liquid to the solid: one can deduce the hydrophobic (large angle) or hydrophilic (small angle) character of the surface.
c) The roughness of the surface (hysteresis between advancing and recessing angles).

The sessile drop method is the most common method to measure the contact angle. Typically, a liquid droplet is deposited using a syringe and its evolution is observed by adding more liquid to it. Depending on the adhesive forces between the solid and the liquid, the drop can spread out over the surface and wet more the surface. As the tendency of the drop to spread out over the surface increases, the contact angle decreases. Thus, as shown in Table 2.5, the contact angle provides a measure of the wettability.

Table 2.5 : Contact angle and wetting process.

Contact angle	***Degree of wetting***
$\theta = 0°$	Perfect wetting
$0° < \theta < 90°$	High wettability
$90° \leq \theta < 180°$	Low wettability
$\theta = 180°$	Non - wetting

Unlike ideal surfaces, the real surfaces show roughness which affects the position of the drop over the surface. The expansion and retraction of the droplet produces two contact angles, the advancing contact angle (ACA) which is the maximum stable angle, and the recessing contact angle (RCA) which is the minimum stable angle. The hysteresis provides information on the roughness of the surface.

Nitrogen adsorption

In this work the nitrogen sorption isotherms were recorded to measure the total micro, meso and macro (up to 200 nm) pore volume of the cathodes. The experiments were performed using a Quantachrome Instrument Autosorb-1. The samples were weighted, placed on the analysis port and pre-treated at 80 °C for 4 h under vacuum. The adsorption and desorption isotherms were measured at 100 °C using nitrogen as adsorbate down to relative pressure 10^{-6}. The Figure 2.9 shows the shape of typical nitrogen adsorption/desorption isotherms recorded for N 15 / T 00 cathode. For the analysis of the results, it was considered that the porosity of the carbon cloth support (macro-porosity) is not negligible since it contributes 2/3 of the total electrodes' weight. For this reason, no computational or statistical methods could be used for the calculations and the total pore volume was measured directly from the adsorption/desorption isotherms at $P/P_0 = 1$.

The total porosity was then converted from cc/g of gas nitrogen adsorbed to cc/g of liquid nitrogen adsorbed.

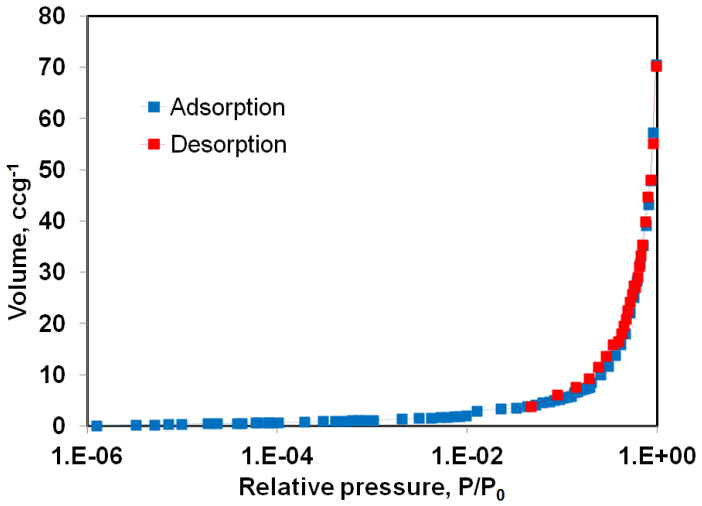

Figure 2.9 : Nitrogen sorption isotherms for N 15 / T 00 cathode.

The gas adsorption is a technique used for the characterization of porous samples presenting micro and meso-porosity, in the range 0.35 – 100 nm (43; 44; 45; 46). This technique consists in the adsorption of gas molecules (adsorbate) on a solid surface (adsorbent). During an experiment, the sample is pre-treated by heating it under vacuum or flowing gas to remove adsorbed contaminants acquired from atmospheric exposure (degassing). Once cleaned, the sample is brought to a constant temperature and small amount of gas (normally nitrogen) is sent to the sample to be adsorbed and form a thin monolayer that covers the surface. Further increasing of the gas pressure leads to a multilayer coverage and capillary condensation. As the equilibrium pressure approaches the saturation, the surface is completely covered and the pores totally filled. If at this stage the adsorption process is reversed, desorption isotherms are generated.

2.3.2. Electrochemical characterization

Electrochemical cell

The electrochemical characterization occurred in a conventional three-electrode cell (Metrohm) as the one reported in Figure 2.10a. The cell was equipped with a Pt wire as counter electrode (black), an Ag/AgCl reference electrode (Metrohm) (blue) and a gas inlet/outlet (Metrohm). The

working electrode (red) was set in the middle of the cell, near the reference electrode to reduce the ohmic drop and facing the counter electrode to maximize the output current. A 0.5 moldm^{-3} sulphuric acid solution (Fisher, Puriss. 95-98 %) saturated with nitrogen or oxygen was used as electrolyte. A PGSTAT30 potentiostat/galvanostat (Autolab), Figure 2.10b, equipped with GPES software and FRA2 module was used to run the experiments.

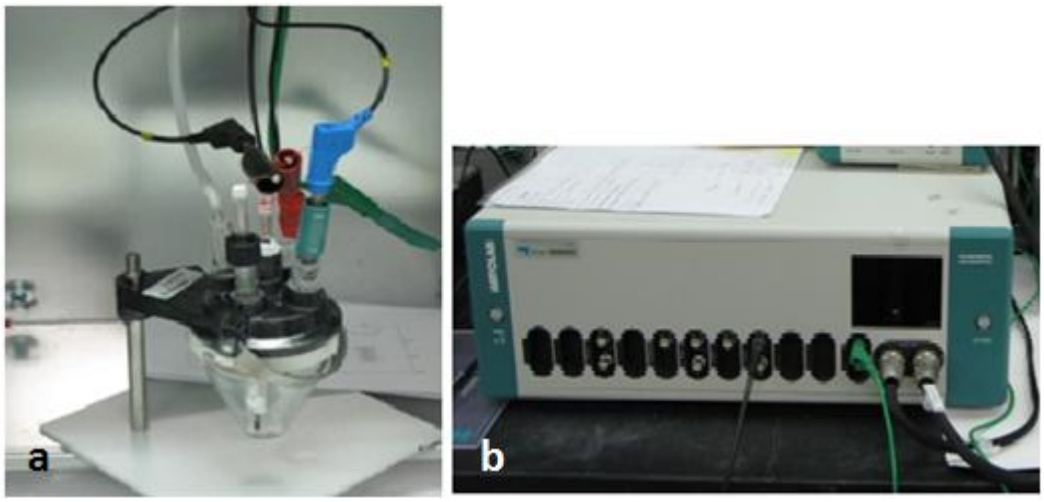

Figure 2.10: a) Electrochemical cell (Metrohm) and b) PGSTAT30 potentiostat (Autolab).

The study of an electrochemical system is focused on the processes and factors that affect the transport of charge across the interface between the electronic conductor (electrode) and the ionic conductor (electrolyte) and in understanding the events that occur when an electric potential is applied and current passes (47). Generally, the interest is on the chemical reaction that occurs on the main electrode called working electrode. The evolution of the interfacial potential related to the reaction is followed by using a reference electrode such as standard hydrogen electrode (SHE), the saturated calomel electrode (SCE) or silver-silver chloride electrode (Ag/AgCl). The current flow produced by the chemical reaction is observed by using an auxiliary electrode (or counter electrode) which is usually chosen to be an electrode that does not cause interfering reactions and is frequently positioned in a compartment separated from the working electrode. Typically, Pt electrodes are used as counter electrodes. The plot of the current as a function of the potential gives a current-potential curve which contain important information about the nature of the electrode/solution interface and the reactions occurring in the system.

Cyclic Voltammetry

In this work, the cyclic voltammetry technique in nitrogen saturated sulphuric acid solution (Fisher, Puriss. 95-98 %) was used to determine the electrochemical surface area (ESA), the catalyst utilization and the potential range for the double-layer capacity. The cathodes were first activated in the wide range of potential - 0.4 V – 1.4 V (vs. Ag/AgCl), recording 20 cycles at 50 mVs^{-1} and 3 cycles at 20 mVs^{-1}. A massive evolution of hydrogen and oxygen, necessary for the activation of the Pt catalyst, occurred in this wide range of potential. The cyclic voltammograms (10 cycles) were then recorded at 20 mVs^{-1}, in the range - 0.28 V - 1.3 V (vs. Ag/AgCl). The last cycle was saved and used for analysis. The cyclic voltammetry technique was also used in oxygen saturated sulphuric acid solution (Fisher, Puriss. 95-98 %) to study the cathodes' performance towards the oxygen reduction reaction and to determine the half-wave potential and the limiting-current. After a pre-conditioning of 30 min (degassing), the 2 cycles were recorded at 5 mVs^{-1}, in the range of potential 1 V – 0 V (vs. Ag/AgCl).

The Cyclic Voltammetry (CV) is a potentiodynamic technique largely used to obtain qualitative and quantative information of the phenomena occurring in the electrochemical system (48; 49). In a CV experiment, the working electrode potential is swept linearly in time until a set point where it is inverted. This process happens multiple times during the experiment, as shown in Figure 2.11a. The typical voltammogram for a Pt-based electrode in H_2SO_4 is reported in Figure 2.11b.

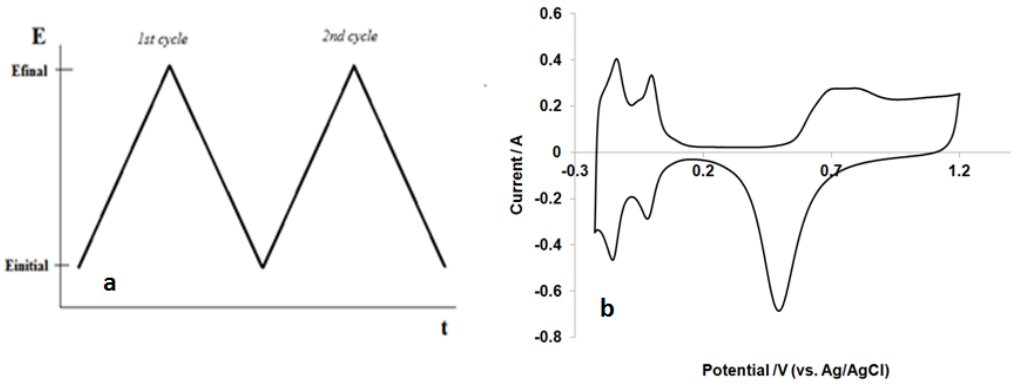

Figure 2.11: a) Cyclic voltammetry wave form, b) voltammogram of a Pt electrode.

Chronoamperometry

In this work, the chronoamperometry was used as a complementary method for the investigation

of the performance of the gas diffusion electrodes towards the oxygen reduction reaction. The capacitive and steady-state currents were determined to evaluate the thin-film mechanism or the flooding condition occurring in the porous cathodes. For the purpose, the sulphuric acid solution (Fisher, Puriss. 95-98 %) was saturated with oxygen for 30 min. The experiments were performed maintaining the system for 10 sec at the rest potential (equilibration time) and then applying a step of potential from the OCV value (~ 0.78 V) to a lower potential. Each time the potential was stepped to a value 20 mV lower than the potential used in the previous experiment and the curves were recorded until 0.3 V. After the 10 sec of equilibration time, the chronoamperograms were recorded for 120 min.

The chronoamperometry is a pulsed electrochemical technique applied for measuring the electrode surface areas, diffusion coefficients, adsorption of electroactive species, and the mechanism and rate constants for chemical reactions coupled to electron transfer reactions (50; 51). It has also been used to obtain qualitative information on the nature of the electrode structures (52; 53) and to determine the thickness of the diffusion layer (δ) formed at the electrode/solution interface. In a chronoamperometric experiment, the potential of the working electrode is stepped from a value at which no faradaic current occurs ($E_{initial}$) to a potential (E_{final}) at which a chemical reaction takes place, as shown in Figure 2.12a. The potential step causes the consumption of reagent near the electrode surface and leads to the diffusion of the reactant from a region of high concentration (bulk solution) to a region of low concentration (electrode surface). The magnitude of the region depleted in reactant (diffusion zone) increases with the time of the reaction and it can be graphically illustrated in a concentration-distance profile. The exponentially decay of the resulting current from the faradic processes occurring at the electrode (caused by the potential step) is monitored over time. After an initial peak due to the electrolysis of the molecules adjacent to the electrode surface, the current decreases slightly as shown in Figure 2.12b.

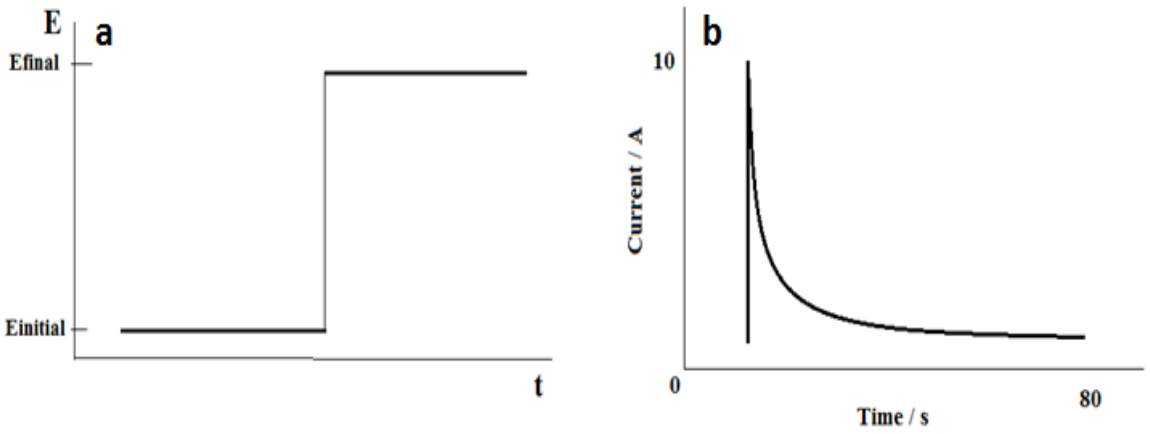

Figure 2.12: a) Potential excitation signal, b) Transient current response (53).

Electrochemical Impedance Spectroscopy

In this work, the cathodes were fully investigated by impedance spectroscopy technique. All the experimental and theoretical details of this technique are reported in the chapter 3.

2.3.3. Fuel cell characterization

Fuel cell

The DMFC tests were carried out in the fuel cell test station (850C, Scribner Associates) reported in Figure 2.13. The station was equipped with a FRA unit for impedance and a fuel cell test fixture of 5 cm^2 active area (Fuel cell Technologies), containing Au-covered current collector plates and graphite blocks with serpentine gas flow channels. The minimum suggested pressure of 10.8 Nm was used to close the fixture. The experiments were run under oxygen (purity 5.2) and air conditioned by an external type humidifier contained into the fuel cell system. The methanol solution was driven into the fuel cell test fixture by a peristaltic pump (Gilson) using a calibrated tube of size 1.02 mm (internal diameter). A 1 M aqueous methanol solution (Fisher, Puriss. > 95 %) at a flow rate of 2.5 $mlmin^{-1}$ (stoichiometry 5.0) was used for all the experiences which were performed under atmospheric pressure on both anode and cathode compartments. The experiments were followed on a computer equipped with the FuelCell software that was used

to control all the experimental parameters. The FCview and Zview programs were used for the data analysis.

Figure 2.13: Fuel cell station and fuel cell test fixture.

Each MEA was firstly conditioned with the methanol solution and humidified air (100% RH – 220 $mlmin^{-1}$ – stoichiometry 2.4) at room temperature for at least 1 h hour. The cell resistance was measured at open circuit potential, using an external potentiostat (VersaSTAT 3, Princeton Applied Research) operated in potentiostatic mode. The impedance spectrum (Nyquist plot) was recorded in the high frequency range 100 kHz – 1 Hz and the resistance value was extrapolated for -Im(Z) = 0 as interception of the curve with the x-axis. Subsequently, under the same air conditions, the MEAs were activated by two cycles of galvanostatic polarizations recorded between 25 °C and 80 °C.

The polarization curves were recorded at 40 °C with fully humidified air (220 $mlmin^{-1}$ - stoichiometry 2.4) and oxygen (51 $mlmin^{-1}$ – stoichiometry 2.7) and the oxygen gain was calculated. In additional experiments, the air was preheated to a different temperature to vary the relative humidity at the cathode (50% RH and >100% RH) and test the response of the MEAs to the water content into the air stream.

The complete impedance spectra of the single DMFCs were recorded in the galvanostatic mode, applying a sinusoidal signal with amplitude of 10 mA and in a frequency range from 100 kHz to 1 mHz. The spectra were recorded at different current density values under humidified air (220 $mlmin^{-1}$, stoichiometry 2.4, 100% RH) and humidified oxygen (51 $mlmin^{-1}$, stoichiometry 2.7, 100% RH).

Stoichiometry for methanol – oxygen – air

In this work, the fuel cell was always operated with an excess of methanol, oxygen and air to guarantee the presence of reactants to complete the oxide-reduction reactions. The abundance or lack of reactant is determined by the stoichiometry factor which is defined as the ratio between the amount of reactant present and the amount of the reactant needed to complete the reaction (theoretical). A stoichiometry factor of 1.0 means that the amount of reactant provided corresponds to the theoretical amount. The methanol/oxygen/air flow rates were calculated at stoichiometry 1.0 and then increased to have the stoichiometry factor of 5.0, 2.7 and 2.4, respectively. The calculations for the stoichiometry factor of 1.0 are reported below.

MEA size	5 cm^2
Current density used for calculations	1 Acm^{-2}
[MeOH]	1 M
Total equation	$CH_3OH + (3/2)\ O_2 \rightarrow CO_2 + 2H_2O$
Faraday's law	$N = I/nF$

Methanol flow rate (at stoichiometry 1.0)

$$N_{MeOH} = 5/(6 \cdot 96485) = 8.64 \cdot 10^{-6}\ mol/s$$

$$8.64 \cdot 10^{-6}\ mol/s \div 1\ mol/l = 8.64 \cdot 10^{-6}\ l/s$$

$$8.64 \cdot 10^{-6}\ l/s \cdot 60\ s/min \cdot 1000\ ml/l = \mathbf{0.52\ ml/min}$$

Oxygen flow rate (at stoichiometry 1.0)

Molecular weight	32 $gmol^{-1}$
Density (25 ° C – 1.013 bar)	1.309 gl^{-1}

$$1\ mol\ MeOH \rightarrow 3/2\ mol\ O_2$$

$$N_{O_2} = 8.64 \cdot 10^{-6}\ mol/s \cdot 3/2 = 12.96 \cdot 10^{-6}\ mol/s$$

$$12.96 \cdot 10^{-6}\ mol/s \cdot 32\ g/mol = 414.57 \cdot 10^{-6}\ g/s$$

$$414.57 \cdot 10^{-6}\ g/s \div 1.309\ g/l = 3.16 \cdot 10^{-4}\ l/s = 0.316\ ml/s = \mathbf{19\ ml/min}$$

Air flow rate (at stoichiometry 1.0)

Percentage of O_2 in air	20.95 %

$$N_{air} = 19 \cdot 100/20.95 = \mathbf{91\ ml/min}$$

Humidification of the cathode

In this work the fuel cell was always operated with humidified gas stream either because we investigated the ability of the cathodes for water removing, either because of the fuel cell manufacturing. As mentioned before, the gas was conditioned by an external type humidifier as the one shown in Figure 2.14. The external humidifier required that the inlet gas was conditioned before being introduced into the fuel cell. The gas was bubbled through heated water, humidified and sent into the system through a gas piping that was heated to prevent condensation phenomena.

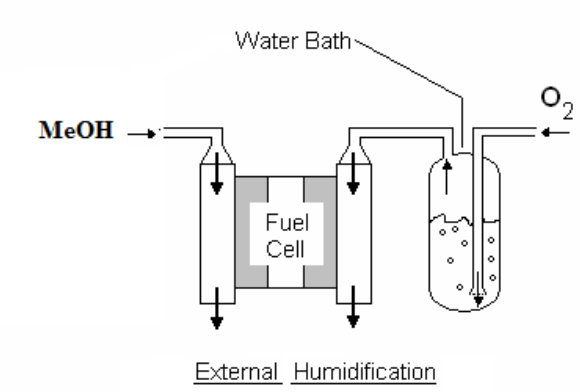

Figure 2.14: External humidifier (54).

The humidity is typically measure as "relative humidity" (RH) and was calculated by:

$$RH = \frac{p_{wv,humidifier}}{p_{wv,fuel\ cell}} \times 100 \qquad \textbf{Equation 2.3}$$

where $p_{wv,humidifier}$ is the water vapor pressure for the humidifier temperature and $p_{wv,fuelcell}$ is the water vapor pressure for the cell temperature. Knowing the temperature of the humidifier and cell, the water vapor pressures were easily determined by using the Antoine's equation and

tabulated data. The relative humidity of 100% was determined for a water-saturated gas, whereas relative humidity over 100% was determined for a water-saturated gas with the occurring of condensation phenomena at the gas inlet of the cathode.

Cell resistance

The total cell resistance (R_{cell}) includes the ionic resistance, the electronic resistance and the contact resistances between the fuel cell components. A high fuel cell resistance may result in a low fuel cell performance.

The ionic resistance represents the proton transfer within the fuel cell membrane and indirectly reflects the membrane conductivity. Aside from their transport in the membrane, protons need to be transferred to the active sides of the catalyst layer and this may be another source of proton resistance. Generally, the proton conductivity of the catalyst layer is strongly dependent of the electrolyte materials, electrolyte loadings, components and structure, as well as the ratio of the electrolyte to carbon (Nafion loading), the temperature and the water activity. In addition, the conditions used to operate the fuel cell system, such as relative humidity of the reactants, may affect the proton conductivity of the catalyst layer and consequently its performance.

The electronic resistance is related to the flow of electrons through the catalyst layers. The electronic conductivity also depends on the used materials, the carbon loading, the components and the structure of the electrodes and it was found decreasing at the increase of the Nafion loading.

The total cell resistance may be reduced using extremely high conductive materials, minimizing the thickness of the electrodes and using well-designed bipolar plates, which have high conductivities and short lengths.

Polarization curves

In this work the performance of the MEAs equipped with the Nafion/PTFE-based cathodes was measured by recording polarization curves at different temperature, under air and oxygen and at different cathode relative humidity. The typical polarization curve recorded for MEA – N 15 / T 00 at 40 °C in presence of air is reported in Figure 2.15. The E-j plot shows that the fuel cell achieves highest voltage at open circuit potential when there is no current load. Then the cell reports a drop of potential at the increasing of the applied current density. The main sources of

losses (55; 56; 57) responsible of the potential decrease are:

a) *Activation losses* due to the slow kinetics and poor electro-catalytic activity of the catalysts towards the methanol oxidation and the oxygen reduction. The effects of these losses are most pronounced at the low current densities (~1 to 50 $mAcm^{-2}$).

b) *Ohmic losses* due to resistive losses in the electrolyte, in the electrodes and in the terminal connections. The effects of these losses are more pronounced at intermediate current densities (~50 to 200 $mAcm^{-2}$).

c) *Concentration losses* due to parasitic reactions that tend to lower the equilibrium potential. One particularly important source of concentration losses in methanol fuel cells is the fuel cross-over from anode to cathode. The methanol cross-over is the dominant source of losses at open circuit.

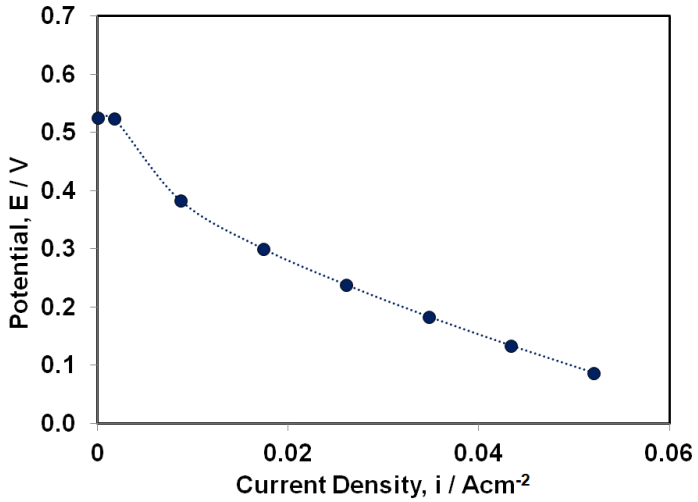

Figure 2.15: Polarization curve for MEA – N 15 / T 00 recorded at 40 °C under air.

The shape of the polarization curve depends on the operating temperature and from the feeding at the cathode (air or oxygen). The polarization curve moves towards higher values at the increasing of the operating temperature and when the cathode is fed with oxygen. Generally, the variation of one parameter that causes the polarization curve to go up is beneficial because greater power and higher efficiency can be achieved. The polarization curve increases with the increasing of the operating temperature because of the higher open circuit voltage, higher catalyst utilization and rate of the chemical reactions, improved mass-transport and lowered cell resistance. However, the methanol cross-over and the swallowing of the Nafion membrane increase also with the operating temperature. As a consequence, the optimum temperature to operate a direct methanol fuel cell

system is 60 °C. As mentioned previously, these studies are focused on the lower operating temperature of 40 °C. The choice of investigating the performance of our cathodes under this condition is related to the final applications, the portable devices for which the operating temperature cannot exceed the 50°C.

The polarization curve increases also when the cathode is fed with oxygen. The higher oxygen partial pressure allows an higher catalyst utilization, open circuit potential and improved mass-transport. Therefore, the optimal condition to achieve higher performance is to operate the fuel cell with oxygen. In this study the emphasis is given to DMFCs operated with air. Again, since the portable devices are the final applications it is expected to obtain high performance with air-breathing DMFCs.

Oxygen gain

In this work the difference in cell potential between polarization curves recorded under air and oxygen feed, named oxygen gain (58; 59) was calculated to estimate the voltage loss associated with mass transport in cathodes operating with air. The typical oxygen gain curve recorded for MEA – N 15 / T 00 is reported in Figure 2.16. A small oxygen gain is desired, especially in the case of air-breathing fuel cells in which the cathode is feed with atmospheric air and losses due to mass transport can be very high. Usually, a large oxygen gain indicates that the cathode suffers from a high transport resistance when air is used as oxidant, although higher oxygen reduction charge transfer resistance and lower thermodynamic voltage can also contribute to the O_2 gain.

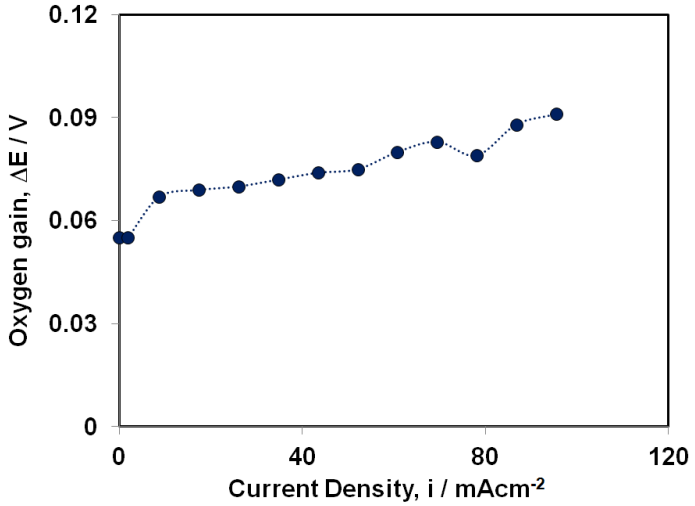

Figure 2.16: Oxygen gain for MEA – N 15 / T 00 at 40 °C.

The theoretical voltage drop that occurs when oxygen is switched to air can be calculated from the thermodynamic equations:

$$\Delta G = \Delta G^0 - RTln\left(\frac{a^{3/2}{}_{O_2}}{a_{CO_2} \cdot a^2{}_{H2O}}\right) \qquad \textbf{Equation 2.4}$$

$$E = E^0 + \frac{RT}{nF} ln\left(\frac{\alpha^{3/2}}{\beta^2 \cdot \gamma}\right) + \frac{RT}{nF} ln\left(P^{-3/2}\right) \qquad \textbf{Equation 2.5}$$

$$\Delta E = \frac{RT}{4F} ln\left(\frac{\alpha_{O_2}}{\alpha_{H2O}}\right) \qquad \textbf{Equation 2.6}$$

The drop is function of the temperature; a loss of 10 mV can be supposed at 25 °C and of 11.5 mV at 60 °C. In the specific case of methanol fuel cells, another parameter, the methanol crossover, should be taken in consideration in the determination of the oxygen gain. As indicated by the OCV values, the permeation of methanol from anode to cathode cannot be neglected and, therefore, the oxygen gain may overestimate the loss in the cathode catalyst layer during air operation. Since the rate of methanol crossover decreases with the current density (60), the problem may be overcome by considering the variation of the oxygen gain in an interval of high current density values.

Electrochemical impedance spectroscopy

Complete fuel cell spectra were recorded under operating fuel cell conditions. More detailed information about this technique is provided in the Chapter 3.

2.4. References

1. **Zhang, J.** *PEM fuel cell electrocatalysts and catalyst layers: fundamentals and applications.* s.l. : Springers, 2008. p. 895.

2. **N. Rajalakshmi, K.S. Dhathathreyan.** Catalyst layer in PEMFC electrodes - Fabrication, characterization and analysis. *Chemical Engineering Journal.* 2007, 129, p. 31.

3. **A.Glüsen, M.Müller, N.Kimiaie, I.Konradi, J.Mergel, D.Stolten.** Manufacturing Technologies for Direct Methanol Fuel Cells (DMFCs). Proceedings 18th World Hydrogen Energy Conference, 2010 May 16-21, Essen.

4. **Basu, Suddhasatwa.** *Recent trends in fuel cell science and technology.* s.l. : Springer, 2007. p. 61.

5. **R. Mosdale, M. Wakizoe, S. Srinivasan.** Fabrication of electrodes for proton exchange membrane fuel cells using a spraying method and their performance evaluation. *The Electrochemical Society.* 1994, p. 179. Proceedings of the symposium on electrode materials and processes for energy conversion and storage.

6. **Roller, Justin.** *Low platinum electrodes for proton exchange fuel cells manufactured by reactive spray deposition technology.* p. 10. Mechanical engineering, University of British Columbia, Vancouver 2009.

7. **R. Benitez, J.Soler, L.Daza.** Novel method for preparation of PEMFC electrodes by the electrospray technique. *Journal of Power Sources.* 2005, Vol. 151, p. 108.

8. **J-H. Wee, K-Y. Lee, S.H. Kim.** Fabrication methods of low-P- loading electrocatalysts in proton exchange membrane fuel cell systems. *Journal of Power Sources.* 2007, Vol. 165, p. 667.

9. **X. Zhao, W. Li, Y. Fu, A. Manthiram.** Influence of ionomer content on the proton conduction and oxygen transport in the carbon-supported catalyst layers in DMFC. *International Journal of Hydrogen Energy.* 2012, Vol. 37, pp. 9845-9852.

10. **A.S. Aricò, V. Alderucci, V. Antonucci, S. Ferrara, V. Recupero, N. Giordano, K. Kinoshita.** ac Impedance spectroscopy of porous gas diffusion electrode in sulphuric acid. *Electrochimica Acta.* 1992, Vol. 37, 3, pp. 523-529.

11. **A.S. Aricò, V. Antonucci, V. Alderucci, E. Modica, N. Giordano.** A.c.-impedance spectroscopy study of oxygen reduction at Nation coated gas-diffusion electrodes in sulphuric acid: Teflon loading and methanol cross-over effects. *Journal of Applied Electrochemistry.* 1993, Vol. 23, pp. 1107-1116.

12. **C. Song, P.G. Pickup.** Effect of hot pressing on the performance of direct methanol fuel cells. *Journal of Applied Electrochemistry.* 2004, Vol. 34, pp. 1065-1070.

13. **C.Y. Chen, C.S. Tsao.** Characterization of electrode structures and the related performance of direct methanol fuel cells. *International Journal of Hydrogen Energy.* 2006, Vol. 31, p. 391.

14. http://en.wikipedia.org/wiki/Spray_gun. [Online]

15. http://www.phoenix-paints.co.uk/about-us/hints-tips/choosing-an-airbrush-or-spraygun.html. [Online]

16. http://www.diy-compressors.com/spraying-basics.htm#mechanics. [Online]

17. http://www.how-to-build-hotrods.com/set-up-hvlp.html. [Online]

18. **C.A.Technologies.** TJR. *Techline JR - Gravity Feed Spray Gun - Product Information.*

19. http://www.spraycat.com. [Online]

20. http://en.wikipedia.org/wikiAirbrush. [Online]

21. http://draftingmanuals.tpub.com/14262/css/14262_290.htm. [Online]

22. **Paasche.** VL & VLS – Airbrushes Double Action - Internal Mix - Siphon Feed - PTFE Packings. *INSTRUCTIONS AND PARTS LIST VL/VLS-8/31/2011.*

23. http://www.paascheairbrush.com. [Online]

24. **S. Siracusano, A. Stassi, V. Baglio, A.S. Aricò, F. Capitanio, A.C. Tavares.** Investigation of carbon-supported Pt and PtCo catalysts for oxygen reduction in direct methanol fuel cells. *Electrochimica Acta.* 2009, Vol. 54, p. 4844.

25. **J.Xie, K.L. More, T.A. Zawodzinski, W.H. Smith.** Porosimetry of MEAs Made by ''Thin Film Decal'' Method and Its Effect on Performance of PEFCs. *Journal of The Electrochemical Society.* 2004, Vol. 151, 11, pp. A1841-A1846.

26. **T.V. Reshetenko, H.-T. Kim, H.-J. Kweon.** Cathode structure optimization for air-breathing DMFC by application of pore-forming agents. *Journal of Power Sources.* 2007, Vol. 171, p. 433.

27. **J. Lobato, P. Canizares, M.A. Rodrigo, C.R.-Lopez, J.J. Linares.** Influence of the Teflon loading in the gas diffusion layer of PBI-based PEM fuel cells. *Journal of Applied Electrochemistry.* 2008, Vol. 38, p. 793.

28. http://en.wikipedia.org/wiki/Scanning_electron_microscope. [Online]

29. http://serc.carleton.edu/research_education/geochemsheets/techniques/SEM.html. [Online]

30. http://mee-inc.com/sem.html. [Online]

31. Introduction to Energy Dispersive X-ray Spectrometry (EDS). *http://micron.ucr.edu/public/manuals/EDS-intro.pdf.* [Online]

32. **M.Mayer.** Rutherford Backscattering Spectroscopy. Lecture given at the Workshop on Nuclear Data for Science and Technology: Materials Analysis. Trieste, 2003 May 19-30.

33. **Ernst, F.** *Rutherford Backscattering Spectroscopy.* [EMSE-515] Fall-2005.

34. http://en.wikipedia.org/wiki/Dynamic_vapor_sorption. [Online]

35. http://www.thesorptionsolution.com/. [Online]

36. **P.C.Hiemenz, R.Rajagopalan 3rd ed.** *Principle of colloids and surface chemistry.* New York : Marcel Dekker, 1997. pp. 265-276.

37. http://en.wikipedia.org/wiki/Contact_angle. [Online]

38. **B.Bhushan, Y.C. Jung, K. Koch.** Micro-, nano- and hierarchical structures for superhydrophobicity, self-cleaning and low adhesion. *Philosophical Transactions of The Royal Society A.* 2009, Vol. 367, pp. 1631-1672.

39. **Y.C. Jung, B. Bhushan.** Contact angle, adhesion and friction properties of micro- and nanopatterned polymers for superhydrophobicity. *Nanotechnology.* 2006, Vol. 17, pp. 4970-4980.

40. **H.M. Yu, C. Ziegler, M. Oszcipok, M. Zobel, C. Hebling.** Hydrophilicity and hydrophobicity study of catalyst layers in proton exchange membrane fuel cells. *Electrochimica Acta.* 2006, 51, pp. 1199–1207.

41. **Jari Ihonen, Mikko Mikkola, Göran Lindbergh.** Flooding of Gas Diffusion Backing in PEFCs. *Journal of Electrochemical Society.* 2004, Vol. 151, 8, pp. A1152-A1161.

42. **D.L. Wood III, C. Rulison, R.L. Borup.** Surface properties of PEMFC gas diffusion layers. *Journal of Electrochemical Society.* 2010, Vol. 157, 2, pp. B195-B206.

43. **S. Lowell, J.E. Shields, M.A. Thomas, M. Thommes.** *Characterization of porous solids and powders: surface area, pore size and density.* s.l. : Kluwer Academic Publishers. p. 5.

44. **Westermarck, Sari.** *Use of mercury porosimetry and nitrogen adsorption in characterization of the pore structure of mannitol and microcrystalline cellulose powders, granules and tablets.* Academic dissertation, Faculty of Science, Department of Pharmacy, University of Helsinki, 2000.

45. http://www.micromeritics.com/Repository/Files/Gas_Sorption.pdf. [Online]

46. **Yeung, Dr. KingLun.** Adsorption and Catalysis. Department of Chemical Engineering - Hong Kong University of Science and Technology : s.n.

47. **A.J. Bard, L.R. Faulkner.** *Electrochemical Methods, Fundamentals and Applications, 2nd ed.* s.l. : John Wiley & sons Inc. p. 2.

48. —. *Electrochemical Methods, Fundamentals and Applications, 2nd ed.* s.l. : John Wiley & sons, Inc. p. 226.

49. **P.T. Kissinger, W.R. Heineman.** *Laboratory Techniques in Electroanalytical Chemistry, 2nd ed.* s.l. : Marcel Dekker Inc. p. 84.

50. **A.J. Bard, L.R. Faulkner.** *Electrochemical Methods, Fundamentals and Applications, 2nd ed.* s.l. : John Wiley & sons, Inc.

51. **P.T. Kissinger, W.R. Heineman.** *Laboratory Techniques in Electroanalytical Chemistry, 2nd.* s.l. : Marcel Dekker Inc.

52. **D.B. Zhou, H.V. Poorten.** Electrochemical characterization of oxygen reduction on teflon-bonded gas diffusion electrodes. *Electrochimica Acta.* 1995, Vol. 40, 12, p. 1819.

53. **A. Kamat, A. Huth, O. Klein, S. Scholl.** Chronoamperometric investigations of the electrode-electrolyte interface of a commercial high temperature PEM fuel cell. *Fuel cells.* 2010, Vol. 00, 0, p. 1.

54. **Evans, J.P.** *Experimental Evaluation of the Effect of Inlet Gas Humidification on Fuel Cell Performance.* Blacksburg, Virginia : s.n., 2003. Master of Science in Mechanical Engineering.

55. **EG&G Technical services, Inc.** *Fuel cell Handbook (7th edition).* 2004. U.S. Department of Energy, National Energy Technology Laboratory.

56. **Rayment, C.** Introduction to fuel cell technology. 2003. Department of aerospace and mechanical engineering, Univerity of Notre Dame, USA.

57. **Ramani, V.** Fuel Cells. The Electrochemical society interface - Spring 2006.

58. **Zhang, J.** *PEM Fuel Cell electrocatalysts and catalyst layers.* p. 599. Springer, London 2008.

59. **M. Prasanna, H.Y. Ha, E.A. Cho, S.-A. Hong, I.-H. Oh.** *Journal of Power Sources.* 2004, Vol. 137, p. 1.

60. **A.S. Aricò, S. Srinivasan, V. Antonucci.** DMFCs: From Fundamental Aspects to Technology Development. *Fuel Cells.* 2001, Vol. 1, 2, p. 133.

CHAPTER 3 : ELECTROCHEMICAL IMPEDANCE SPECTROSCOPY

3.1 Introduction

The Electrochemical Impedance Spectroscopy (EIS) is one of the main in-situ diagnostic techniques and is used in many fields of the electrochemical research. It is a powerful tool for investigating systems governed by coupled reactions occurring at different rates, for measuring transport properties of porous materials and for providing a better insight on the interfacial processes in electrochemical systems (1; 2; 3; 4). In EIS a periodic small-amplitude ac signal (voltage or current) is applied and the associated response (current or voltage) coming from the investigated system is measured (5; 6). As shown in Figure 3.1, the voltage response to a sinusoidal current signal $i_t = i_0 \sin(\omega t)$ is a sinusoid $E_t = E_0 \sin(\omega t + \varphi)$, at the same frequency (ωt) but shifted in phase (φ).

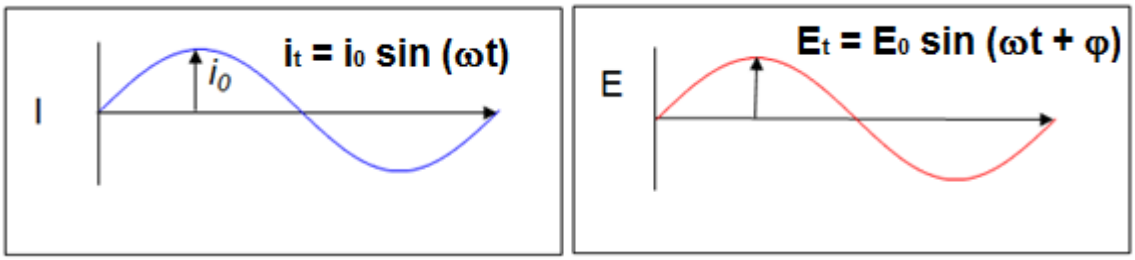

Figure 3.1: Applied and measured ac signals during an EIS experiment.

With an expression analogous to the Ohm's law, the impedance of the analyzed system can be defined as:

$$Z = \frac{E_t}{i_t} = \frac{E_0 \sin(\omega t + \varphi)}{i_0 \sin(\omega t)} = Z_0 \frac{\sin(\omega t + \varphi)}{\sin(\omega t)} \qquad \textbf{Equation 3.1}$$

Or by Euler's relationship it can be expressed as a complex function:

$$Z = \frac{E_t}{i_t} = \frac{E_0 \exp(j\omega t)}{i_0 \exp(j\omega t - \varphi)} = Z_0 \exp(j\varphi) = Z_0(\cos\varphi + j \sin\varphi) \qquad \textbf{Equation 3.2}$$

which is composed of a real and an imaginary part. In an electrochemical system, slow kinetics reactions and diffusion can all impede the electron flow, and this can be considered analogous to the resistors, capacitors, and inductors that impede the flow of electrons in an ac circuit. In the case of a resistor, the impedance is independent of the frequency and has no imaginary component. The phase shift is zero degrees and the current is in phase with the voltage. For a

capacitor, the impedance has no real component. The imaginary component is function of the frequency, and the current is always 90 degree shifted with the voltage. Since the impedance of a capacitor varies inversely with the frequency, at high frequencies the impedance tends to zero, whereas at low frequencies it tends towards infinite. Like for a capacitor, the current through an inductor is 90 degree shifted with the voltage. However, the shift is in the opposite direction and the impedance increases with the frequency.

The impedance of a system can be represented by plotting the real and the complex parts on the x-axis and y-axis to obtain the so called Nyquist plot, Figure 3.2a. Each point of the Nyquist plot corresponds to the impedance of the system at one frequency; on the left side of the plot are the points at high frequencies whereas on the right side are the points at low frequencies. On the Nyquist plot, the impedance can be represented as a vector of length |Z|. The angle between this vector and the x-axis is the phase angle φ (argZ). The Nyquist plot representation has the advantage of an easy identification of the frequency-independent parameters of the system such as the ohmic resistance. Indeed, this parameter can be easily extrapolated from the interception of the graph with the x-axis in the high frequency region. However, the frequencies do not appear explicitly in this type of plot. Therefore, calculations are required for the determination of the capacitance and inductance.

The impedance data can also be represented by plotting the absolute impedance |Z| and the phase angle φ as a function of the frequency ω to obtain the so called Bode plots, Figure 3.2b. From this type of plots it is easy to understand how the impedance behaves with the frequency and it is possible a more effective extrapolation of the data in the high frequency region. The logarithm of the frequency is often used to allow a wide frequency range to be plotted and this is of particular advantage for the determination of the frequency-dependent parameters.

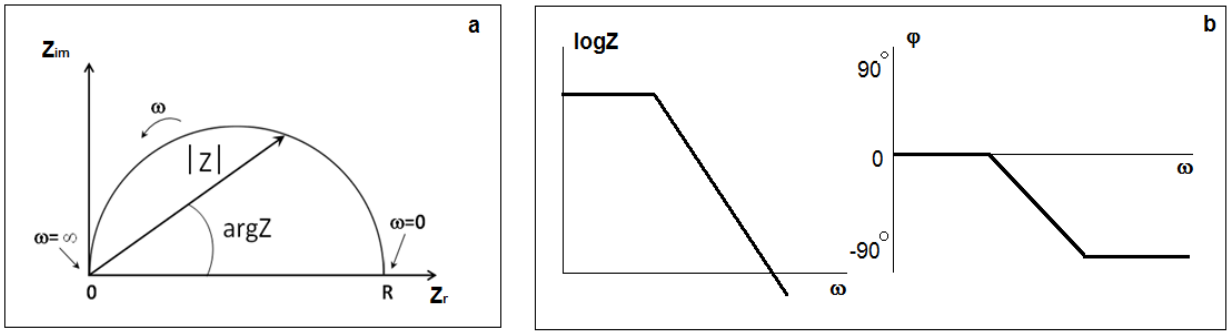

Figure 3.2: Impedance representations: a) Nyquist plot and b) Bode plots.

3.2 Electrochemical Impedance Spectroscopy in 0.5 M H_2SO_4

Since the end of the 1980s, EIS has been employed in fuel cell studies, starting with the characterization of porous gas diffusion electrodes (GDE) (7; 8; 9; 10; 11; 12; 13; 14; 15). Springer and Raistrick (7; 8) introduced theoretical models which describe the structure of a porous electrode (simple pore model) and represent the phenomena occurring in the pores in presence of electrochemical reactions (thin-film model and agglomerate model). Based on these models, experimental approaches were proposed by other authors afterwards (10; 11; 12; 13). In these works, the electrochemical spectra were recorded in sulphuric acid solution (or in potassium hydroxide solution) to investigate the proton conduction through the porous structure of the electrode catalyst layer (10) and to characterize the behaviour of porous electrodes with different hydrophobicity (11; 12; 13).

The typical impedance spectrum of a porous gas diffusion electrode, recorded in a nitrogen saturated sulphuric acid solution, is reported in the form of Nyquist plot in Figure 3.3 (8). The complex plot is similar to the one reported by Pickup and co-worker in their work (10). The impedance spectrum can be divided in two frequency regions which are characterized by different features. At high frequencies, the complex plot shows a straight line with 45 degree angle. This part of the plot, which is named Warburg region, corresponds to the ion diffusion through the porous catalyst layer. At low frequencies, the plot shows a straight line corresponding to the total capacitance at the interface pore - solution and to the total resistance of the pore.

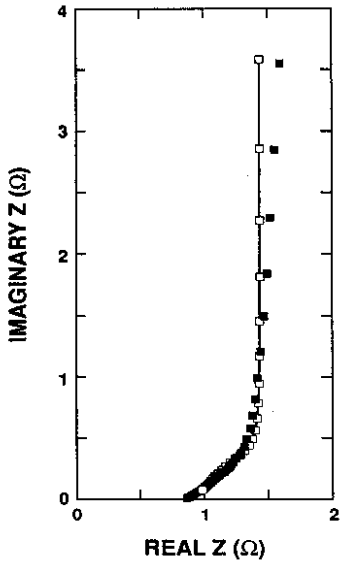

Figure 3.3: Complex impedance of a porous electrode in nitrogen saturated H_2SO_4 solution (8).

The shape of the complex plot at high frequency depends on the porosity of the electrode and changes in the 45 degree zone may occur because of the pore geometry. Figure 3.4 shows examples of impedance plots for different pore geometries. In some cases, the high frequency impedance assumes the shape of a distorted semicircle.

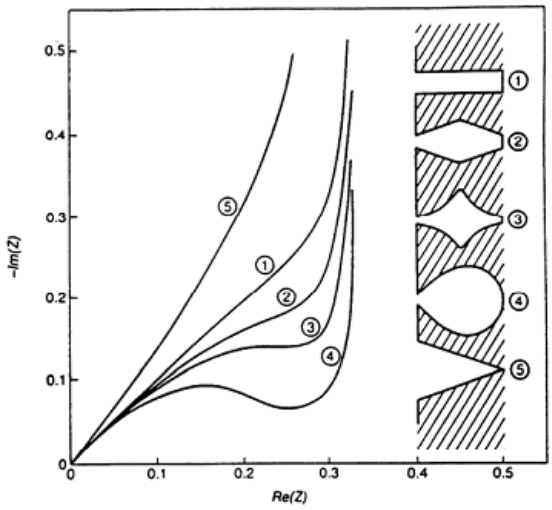

Figure 3.4: Complex impedance plot for different pore geometries (16).

Important studies on porous gas diffusion electrodes immersed in an oxygen saturated sulphuric acid solution were done by Aricò and co-workers (11; 12). The typical impedance spectrum is reported in Figure 3.5. At high frequencies, the plot tends to a linear dependence which modifies to a depressed semicircle going towards lower frequencies. Again, the behaviour at 45 degree (Warburg region) is related to the diffusion in the porous structure. The semicircle at low frequencies is related to the electrochemical oxygen reduction reaction occurring in the porous structure at the interface electrode-electrolyte. The distortion and depression of the semicircle has been attributed to the heterogeneity of the porous electrode.

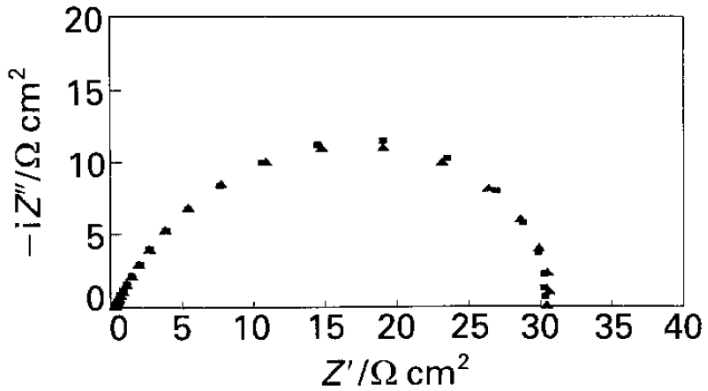

Figure 3.5: Complex impedance plot of a porous electrode in oxygen sat. H_2SO_4 solution (12).

The complex impedance spectra of the porous gas diffusion electrodes are generally resolved by using one of the two approaches: the transmission-line approach (10) or the equivalent circuit approach (11; 12). In the transmission-line approach, the porous structure is represented by a circuit, as the one reported in Figure 3.6. Commonly, on the base of de Levie assumption (16), the pores are considered of cylindrical shape and the solution to be homogeneously distributed along the length of the pore. The circuit is built with two parallel resistive rails, one for the electron transport through the conducting carbon particles (R_e) and another for the ion transport in the electrode catalyst layer (R_i). The rails are connected by capacitors (C) representing the double-layer capacitance at the interface electrolyte-catalyst (Pt and carbon). Since the carbon particles are good electronic conductors, the R_e are usually neglected. In the presence of Faradaic processes another resistance related to the charge-transfer occurring in the electrode – solution interface (R_{ct}) is added to the circuit. In this case, the R_{ct} and C are disposed in a parallel circuit.

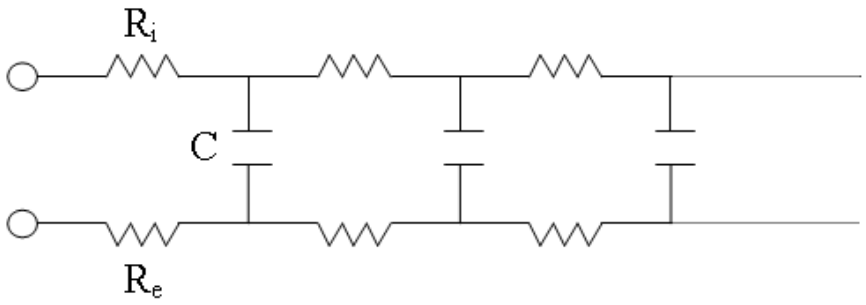

Figure 3.6: Simple transmission-line circuit for a uniformly distributed porous electrode (17).

In the equivalent circuit approach, the lumped circuit is defined in terms of combinations of electrical elements which values and arrangements represent the physical properties or the phenomena occurring in the porous gas diffusion electrode. Resistors, capacitors and Warburg elements are used to simulate the electrochemical system as explained above.

In this paragraph we introduce the methodology used for the analysis of impedance spectra recorded in nitrogen saturated and oxygen saturated sulphuric acid solutions. N 15 / T 00 and N 00 / T 15 cathodes (Table 3.1) were chosen. The spectra acquired in nitrogen saturated solution, Figure 3.7a, were used to determine the ionic resistance and the double-layer capacitance of the cathode in contact with the electrolyte solution. For the spectra recorded in oxygen saturated solution, Figure 3.7b, the kinetic parameters for ORR were determined by fitting the results with equivalent circuits.

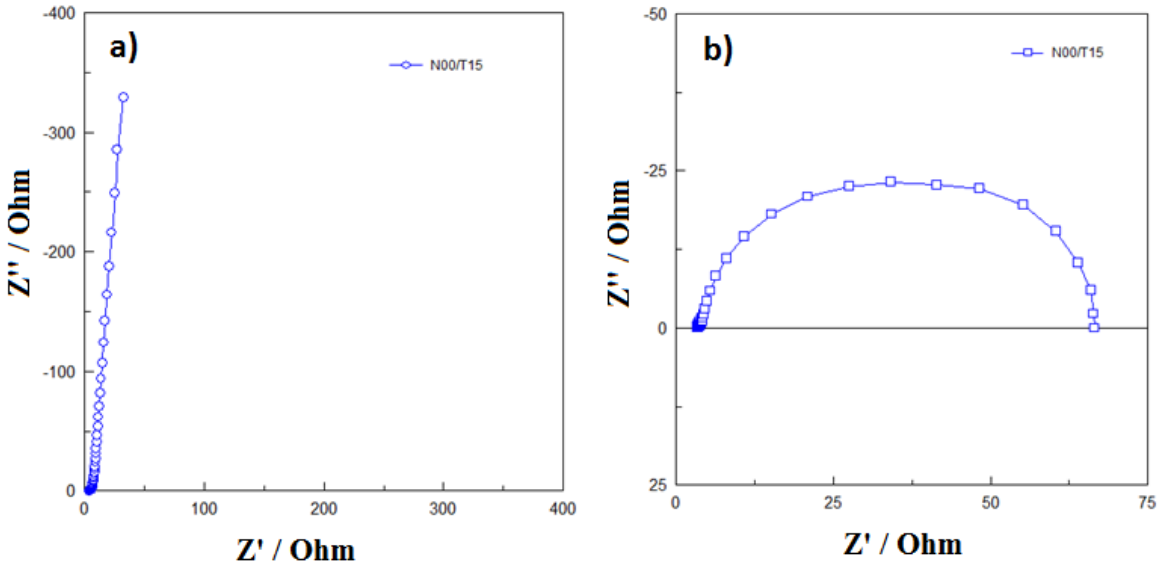

Figure 3.7: Impedance spectra for a N00/T15 cathode recorded in a) N_2 sat. and b) O_2 sat. 0.5 M H_2SO_4.

Table 3.1: Composition of the cathodes.

	Pt loading ($mgcm^{-2}$)	**wt% Nafion**	**wt% PTFE**	**Support**
N15/T00	2.94	15	0	C-cloth
N00/T15	2.87	0	15	C-cloth

3.2.1. Analysis impedance spectra in N_2 saturated 0.5 M H_2SO_4

In this work, the impedance spectrum of the N 15 / T 00 cathode was recorded in a nitrogen saturated sulphuric acid solution at the potential 0.2 V (vs. Ag/AgCl) which corresponds to the center of the capacitance zone of the cyclic voltammogram (Chapter 5 – Figure 5.6). In this way, only proton transport through the catalyst layer and the double-layer capacitance formed between the porous electrode and the electrolyte should be considered. The Nyquist and Bode plots are shown in Figure 3.8. The impedance spectrum in the Nyquist plot form, Figure 3.8a, shows similar profile to the one reported by Pickup and co-worker (10) for gas diffusion electrodes in contact with a liquid electrolyte.

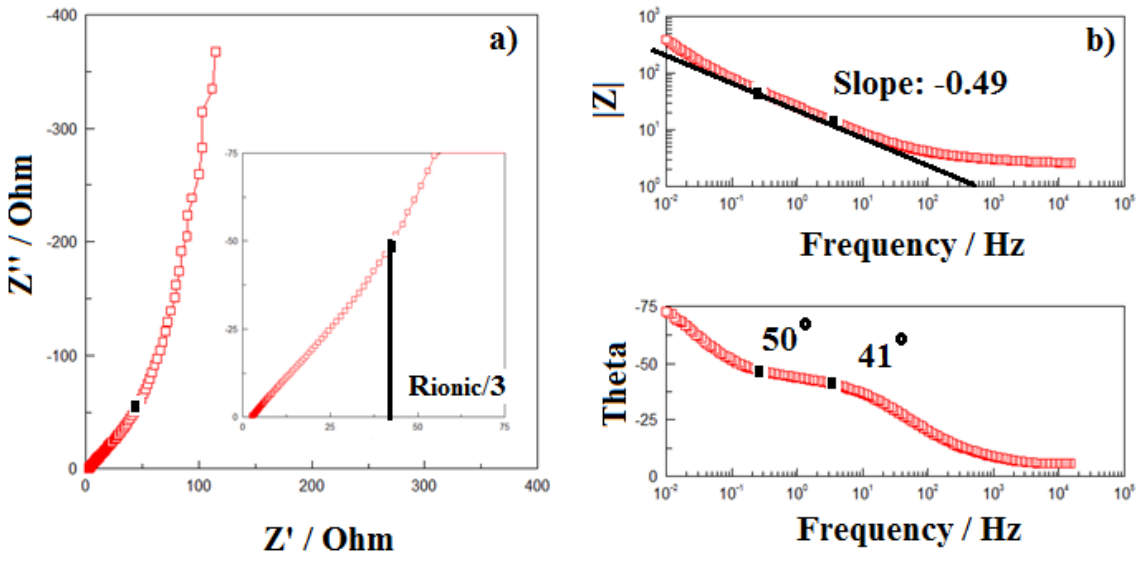

Figure 3.8: Impedance spectra for N15/T00 cathode at 0.2 V in N_2 sat. H_2SO_4 a) Nyquist, b) Bode plots.

The ionic resistance is obtained from the projection of the Warburg-like region onto the real impedance axis, and is defined as (10; 18):

$$Z' = \frac{R_{ionic}}{3} \qquad \textbf{\textit{Equation}}\ \mathbf{3.3}$$

Where 1/3 comes from the low-frequency behaviour of the coth function that describes the transmission-line circuit used by Pickup and co-workers to fit the impedance spectrum. The extension of the Warburg region was determined by identifying the frequency interval with a slope of -1/2 in the module and a phase angle of 45 degree in the Bode diagrams (6). Since the pores have not perfect cylindrical shape, a variation of the phase angle between 41 and 50 degree was observed. On the contrary, the slope in the module Bode plot did not show a significant variation from the theoretical -1/2 value in this range of phase angles.

A capacitance plot, as the one reported in Figure 3.9, was used to determine the double-layer capacitance, using the following relation:

$$C = -\frac{1}{Z''\omega} \qquad \textbf{\textit{Equation}}\ \mathbf{3.4}$$

The capacitance of the interface formed between the cathode and the electrolyte solution was determined from the plateau.

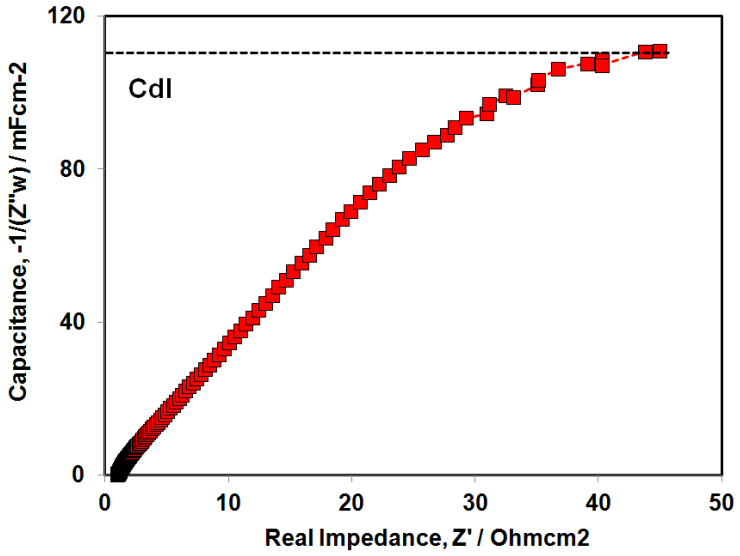

Figure 3.9 Capacitance plot for N15/T00 cathode (N_2 sat. H_2SO_4 - 0.2 V).

3.2.2. Analysis impedance spectra in O_2 saturated 0.5 M H_2SO_4

For the spectra recorded in oxygen saturated solution, the equivalent circuit (EC) approach was chosen for the fitting of the experimental results. The impedance spectra of the cathodes were recorded in the range of potential 0.3 – 0.7 V (vs. Ag/AgCl), and the typical impedance spectrum in the form of Nyquist and Bode plots for a N 00 / T 15 cathode is reported in Figure 3.10. The spectrum was recorded at 0.6 V.

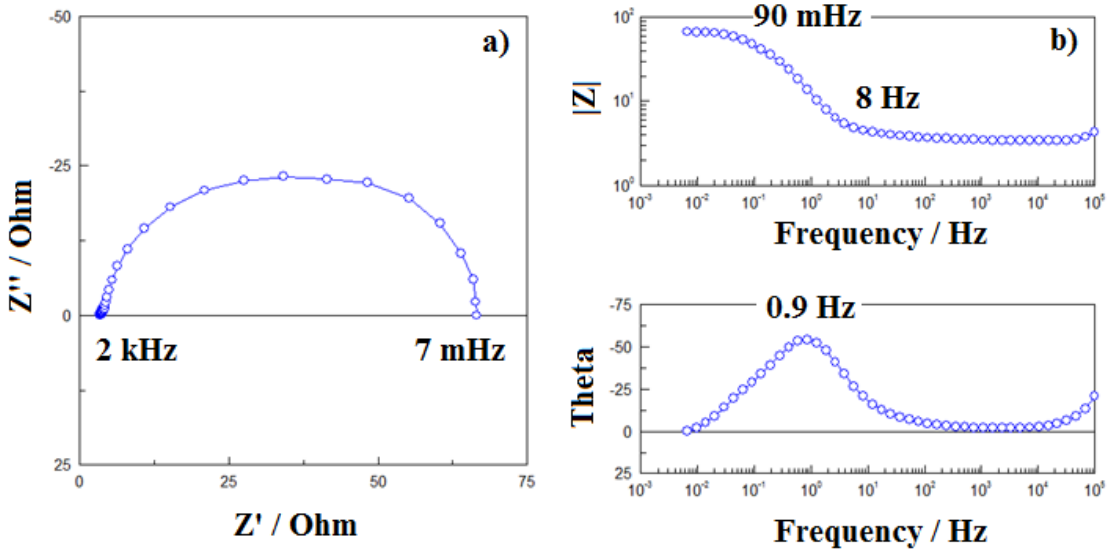

Figure 3.10: Typical impedance spectra recorded in O_2 sat. H_2SO_4 at 0.6 V.

The Nyquist plot, Figure 3.10a, shows a depressed semicircle in the frequency range 2 kHz – 7 mHz. The plot can be analyzed as follow: in the high frequency region, the interception of the spectrum with the real impedance axis (Z') represents the series resistance. A limited-extended Warburg zone related to the diffusion of the species in the porous structure is present in the high frequency region and it is followed by a depressed semicircle related to the electrochemical oxygen reduction reaction.

The Bode plot phase-angle shows a phase-shift maximum at the frequencies of 0.9 Hz which is related to the charge-transfer resistance and double-layer capacitance of the electrochemical processes by (3):

$$\omega_{max} = \frac{1}{R_{CT} \cdot C_{dl}} \cdot \sqrt{\frac{R_s + R_{CT}}{R_s}} \qquad \textbf{Equation 3.5}$$

Concerning the Bode plot, the asymptotic behaviour of the module impedance is interrupted by two breaking point frequencies, ω_1 and ω_2, at 8 Hz and 90 mHz. The breaking point frequencies allow the determination of the characteristic Bode time constants, $\tau_1 = 1/\omega_1$ and $\tau_2 = 1/\omega_2$.

The equivalent circuit used to fit our experimental data is reported in Figure 3.11, and was built by using the Zview program. It contains the series resistance, R_s, for the electrolyte solution, the charge-transfer resistance, R_{CT}, for the electrochemical oxygen reduction reaction, the constant phase element, CPE, representing the double-layer capacitance and the finite Warburg element, W_N, related to the diffusion of the species in the electrode porous structure.

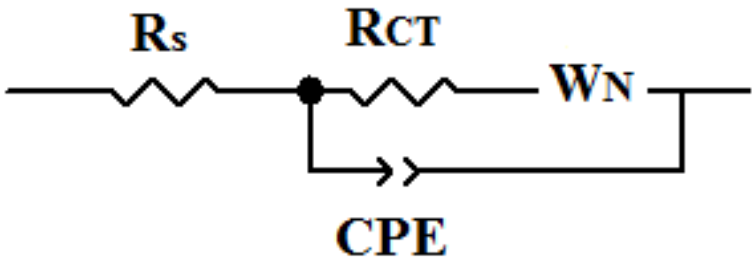

Figure 3.11: Equivalent circuit used to fit the impedance spectra recorded in O_2 sat. H_2SO_4.

The Constant Phase Element (CPE)

The constant phase element (CPE) is used to describe the double-layer capacitance of rough irregular electrode surfaces and inhomogeneous surfaces characterized by adsorption phenomena. The impedance of a constant phase element is defined as:

$$\boldsymbol{Z_{CPE} = \left(T(i\omega)^{\phi}\right)^{-1}\omega L} \qquad \textbf{Equation 3.6}$$

where T is a constant ($Fcm^{-2}s^{\phi-1}$) and ϕ the CPE exponent that characterized the phase shift. The CPE can be used to describe pure resistor (ϕ=0, $T=R^{-1}$), a pure capacitor (ϕ=1, T=C), or a pure inductor (ϕ=-1, $T=L^{-1}$). For very rough surfaces, ϕ=0.5 and the CPE is associated with the Warburg element.

The Warburg Element (W)

The electrochemical processes are often performed under diffusion-limited conditions. This mass-transport limitations create another additional resistive term, named Warburg impedance, Z_w, that appears in series with the previously mentioned charge-transfer resistance.

For case of a gas diffusion electrode, the electrochemical reaction occurs in the porous structure of the electrode. Generally, the inner surface of the pores is wetted by a thin layer of electrolyte of thickness δ. The diffusion occurs through the finite layer, known as Nernst diffusion layer and the Nernst impedance, Z_N (finite Warburg impedance) is:

$$\boldsymbol{Z_N = \frac{\sigma_a}{\sqrt{\omega}}\tanh\left(\sqrt{\frac{j\omega}{D_a}}\delta\right)(1-j)} \qquad \textbf{Equation 3.7}$$

Where σ_a is the Warburg coefficient related to the diffusivity of the species 'a', the reaction rate, the concentration of species 'a', the current density, the potential and D_a the diffusion coefficient. This impedance shows in the complex plot as a linear tendency (45 degree) at high frequencies which modifies to a depressed semicircle going towards lower frequencies. The semicircle intercepts the x-axis at:

$$\boldsymbol{Z' = R_S + R_{CT} + \frac{\sqrt{2}\sigma_a\delta}{\sqrt{D_a}}} \qquad \textbf{Equation 3.8}$$

Complex Non-Linear Least Square Fitting (CNLS) procedure

Generally, the value of the parameters of the equivalent circuits is determined by a complex non-linear least square fitting procedure (CNLS) employed in commercial fitting programs like ZView or LEVM. CNLS is used to fit the real and imaginary parts or the magnitude and phase parts of the experimental impedance data to an equivalent circuit and it is quite used to fit circuits containing up to 10 parameters. CNLS is very sensitive to the inserted value of the initial parameters and the choice of the number of free parameters. Because of the iterative nature of the program, the choice of the initial values determines the quality of the fitting, whereas the choice of the number of free parameters determines the convergence to a local minimum. For circuits containing few elements, the initial values can be determined by trial, using different initial sets of values in attempt to reach the convergence, or building a simpler circuit and adding more elements until a model with good initial values is built.

Chi-Squared (χ^2)Test

The Chi-Squared Test (χ^2) is used to measure the goodness of the fitting. It is defined as:

$$\boldsymbol{\chi^2 \equiv \sum_{i=1}^{2N} \left\{ \frac{1}{\sigma_i^2} [y_i - y(x_i)]^2 \right\}} \qquad \textbf{Equation 3.9}$$

Where i is the index of the individual data points, σ_i^2 the variance, y_i the data, $y(x_i)$ the fitted values and N the number of frequencies at which the impedance is measured. For the case of the commercial program ZView, the χ^2 values are provided within the fitting results.

F-Ratio

The F-Ratio is generally used to understand if the addition of another parameter to the equivalent circuit is useful to improve the fitting of the experimental results. In addition, this test can be used to compare fittings of a spectrum deriving from different models and to understand which model is better. The F-Ratio is defined as:

$$\boldsymbol{F = \frac{\chi^2(n-1) - \chi^2(n)}{\chi^2(n)/(2N-n)}} \qquad \textbf{Equation 3.10}$$

Where n is the number of the parameters in the model and 2N is the number of experimental data points.

Because of the importance of having good initial parameters, at first, the Warburg impedance and the R_{CT}-C_{dl} circuit were fitted individually. The option "instant fit" of the Zview program was used to facilitate the determination of these parameters. Next, the values of the partial fitting were used as initial parameters in the fitting of the complete spectrum. The result of the fitting procedure on the impedance spectrum recorded at 0.6 V is shown in Figure 3.12.

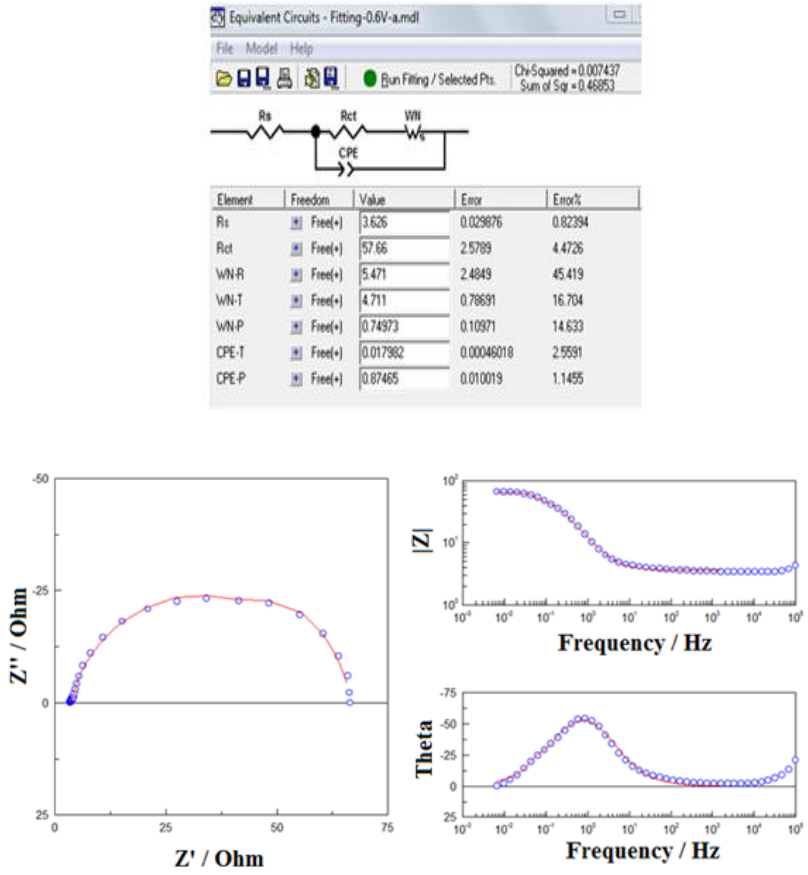

Figure 3.12: Fitting of impedance spectrum of N00/T15 in O_2 sat. H_2SO_4 at 0.6 V.

The Chi-square value is of the order 10^{-3} and the errors associated with the parameters are generally within the 15%, made the exception for the Warburg resistance parameter which shows an error of the 45%. In general, errors within the 10-15% are desirable, however it was reported that the kinetic data obtained from fitting a model to the experimental data can carry a large positive error of up to 100% (19). Based on this statement, we consider the 45% error acceptable.

Results

The experimental and fitted spectra of the N 00 / T 15 cathode recorded in the range of potential 0.3 – 0.7 V (vs. Ag/AgCl) are reported in Figure 3.13. The spectra in the Nyquist plot, Figures 3.13a and 3.13c show single semicircles whose form and amplitude depend on the applied potential. At 0.7 V the arc extends until very low frequencies without reaching finite amplitude. Complete semicircles appear in the 0.65 - 0.3 V potential range. The amplitude of the arc decreases with the applied potential and therefore this arc is related to the charge transfer resistance for the ORR (12), but it is also affected by the mass-transport. Indeed, at high overpotentials, 0.4 and 0.3 V, the amplitude of the arc increases again due to limited support of reactant. In the Bode plot, Figures 3.13b and 3.13d, it is observed a shift of the phase-maximum towards higher frequencies when the potential is decreased from 0.7 V to 0.5 V, and it displaces back to lower frequencies at 0.4 V and 0.3 V. Concerning the module Bode plot, a significant decrease of the impedance is observed between 0.7 and 0.5, whereas no significant variations are noticed below 0.5 V.

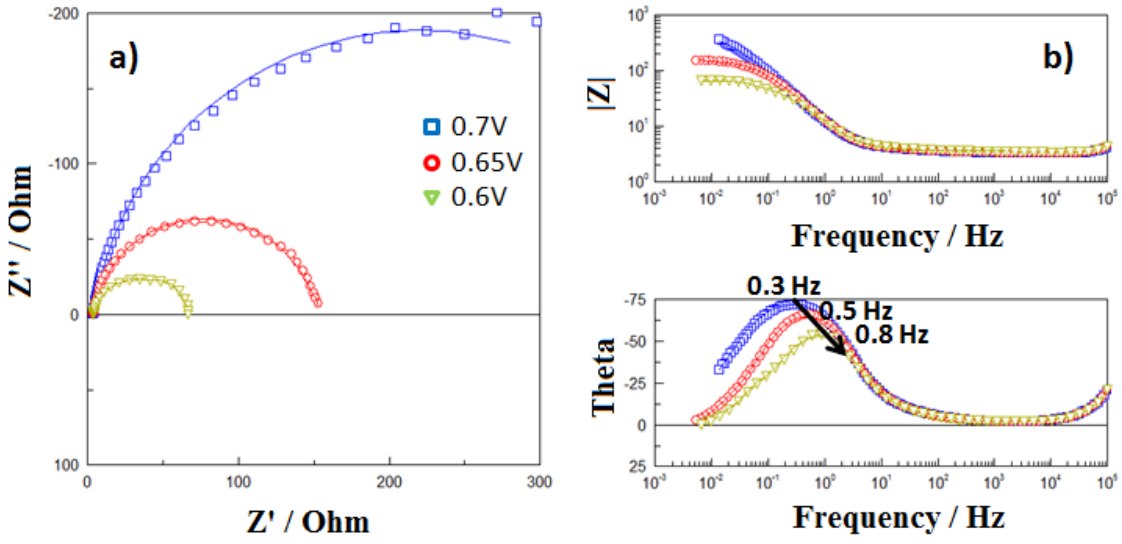

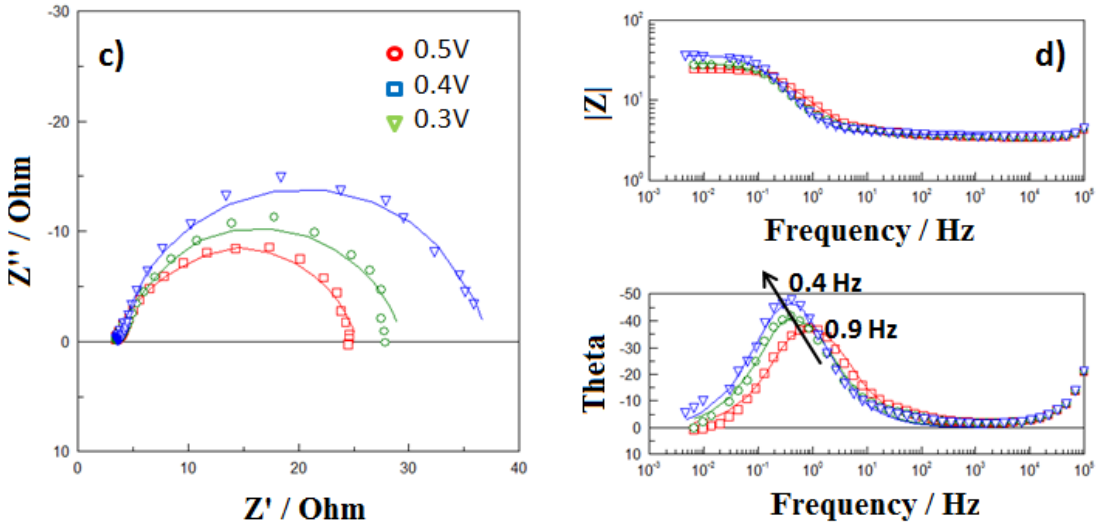

Figure 3.13: Experimental/fitted spectra for N00/T15 cathode in O_2 sat. H_2SO_4 in the range 0.3 - 0.7 V.

The kinetic parameters for the N 00 / T 15 cathode ($R_{CT\text{-}ORR}$, C_{dl}) as a function of the applied potential are reported in Figure 3.14. The analysis of the graphs allows the following observations:

a) The serial resistance, related to the ionic resistance of the electrolyte and the electronic resistance of the electrode, is constant during the EIS experiments and equal to 1.20 ± 0.01 Ωcm^2. But since the cathode has a low electronic resistance, the serial resistance may be assumed as the ionic resistance of the electrolyte (10).

b) The charge-transfer resistance behaves coherently; it shows a drastic decrease from 0.7 V to 0.65 V (147.64 ± 2.77 Ωcm^2 to 49.44 ± 0.56 Ωcm^2), it continues to decrease up to 0.5 V (6.78 ± 0.10 Ωcm^2) and shows a slight increase at the lower potentials 0.4 and 0.3 V (8.00 ± 0.17 Ωcm^2 to 10.54 ± 0.20 Ωcm^2). A linear relationship between the logarithm of the $R_{CT\text{-}ORR}$ and the potential is reported at low overpotentials and with a slope of 66 $mVdec^{-1}$.

c) The double-layer capacitance increases with the overpotential (from 35.79 ± 0.29 $mFcm^{-2}$ to 96.29 ± 0.23 $mFcm^{-2}$) showing that the catalyst utilization is not limited by the produced water and that the cathode is not flooded.

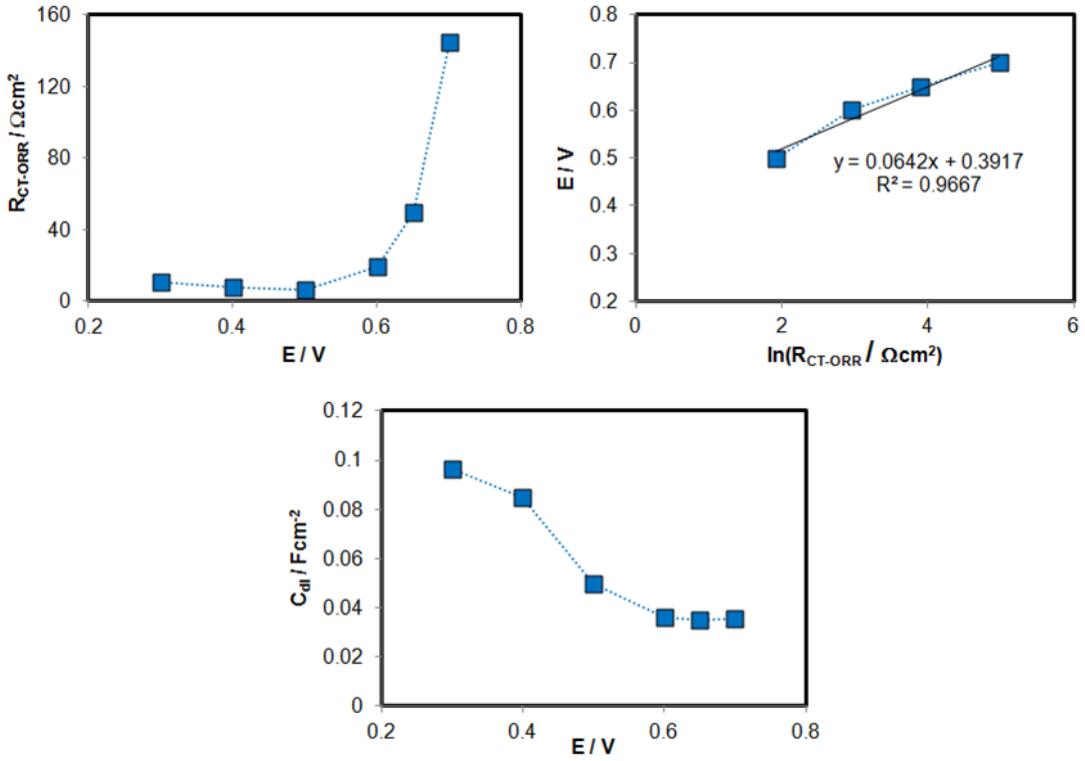

Figure 3.14: Kinetic parameters as a function of the cell potential for N00/T15 cathode (O_2 sat. H_2SO_4).

3.2.3. Conclusions

In this paragraph we explained the procedures followed in the analysis of the impedance spectra recorded in sulphuric acid solution.

For the spectra recorded in N_2 saturated solution, the analysis and elaboration of the Nyquist plot allowed the determination of the ionic resistance and double-layer capacitance.

For the spectra recorded in O_2 saturated solution, the fitting of the experimental data with an equivalent circuit was required for the determination of the kinetic parameters. The coherence of the results shows that the equivalent circuit was chosen properly to model this electrochemical system.

These approaches will be systematically used in Chapters 5 and 6.

3.3 Electrochemical Impedance Spectroscopy in Direct Methanol Fuel Cell

Since its application in fuel cell studies, the Electrochemical Impedance Spectroscopy technique (EIS) has been mainly concentrated on hydrogen proton exchange membrane fuel cells (PEMFCs), with a remarkable number of publications on different aspects of PEMFCs (20; 21; 22; 23; 24; 9; 25; 26; 27) to cite a few examples. EIS has been largely used to measure the electrolyte resistance within the catalyst layer (20; 22; 9), and to investigate the dehydration and the effect of the cell compression on the membrane resistance as well (27). Impedance spectra were typically recorded under H_2/O_2 or H_2/N_2 operating conditions. The rapid H_2 kinetic resulted in negligible impedance contribution from the anode, therefore the final spectra were representative of the cathode behaviour.

Up to now, the application of the EIS technique to the direct methanol fuel cells (DMFCs) has received less attention. Compared to the hydrogen oxidation, the rate of methanol oxidation is not negligible and both anodic and cathodic reactions contribute to the EIS spectrum. Moreover, the methanol oxidation is a multi-step reaction occurring through the formation of a CO intermediate which easily poisons the Pt-based catalysts and limits their activities (28). In addition, methanol crosses the permeable Nafion membrane (cross-over), and affects drastically the performance of the cathode (overpotential and Pt poisoning) (29). As the result of all these simultaneous processes the DMFC investigation by impedance is not straightforward.

The pioneers of the impedance spectroscopy applied to DMFC are Müller and Urban (30). They have introduced a method of separating the anode and cathode impedance spectra based on the PEMFC-assumption that the hydrogen reaction can be neglected when compared to oxygen reaction (31). The method consists into recording firstly the entire DMFC spectrum (under normal anode/cathode operative conditions), secondly the anode spectrum (the cathode is set as a dynamic hydrogen reference electrode (DHRE)), followed by calculating the cathode spectrum by difference (30). The example of measured anodic spectrum and calculated cathodic spectrum is shown in Figure 3.15. Müller and Urban have analyzed these spectra in the low, intermediate and high frequencies regions and investigated the effect of the operating conditions on the electrochemical parameters and electrode performance (30). The spectrum of the anode, Figure 3.15a, shows three distinct arcs in the high, intermediate and low frequency zones. Each of these arcs was related to a different process: the high frequencies arc was related to the ionic transport

through the membrane, the arc at intermediate frequencies was attributed to the methanol electro-oxidation reaction, and the arc at low frequencies was associated with the methanol mass-transfer in the anode. Concerning the cathode, Figure 3.15b, the subtraction process eliminates the high frequencies arc, therefore two arcs are observed in the spectrum recorded in presence of air, whereas one single semicircle appears in the spectrum acquired under oxygen. The arc at intermediate frequencies was attributed to the oxygen reduction reaction, whereas the arc at low frequencies was related to the oxygen mass-transfer in the cathode backing. In this approach, the oxidation of crossed-over methanol at the cathode was not taken in consideration.

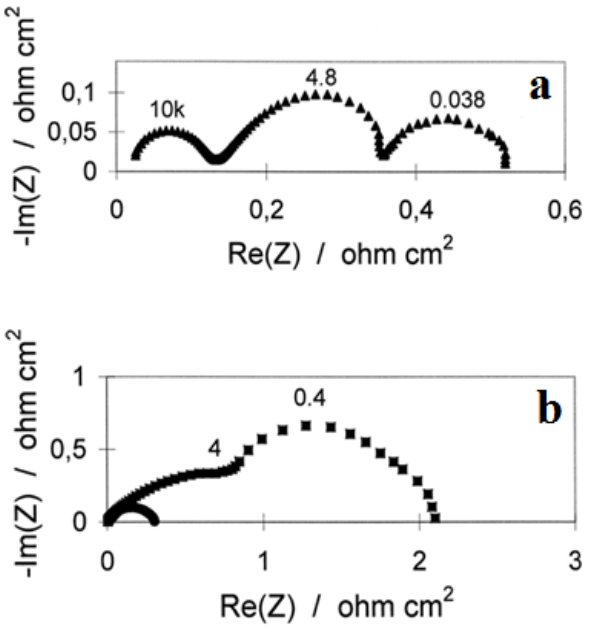

Figure 3.15: DMFC a) anode b) cathode impedance spectra (30).

Remarkable DMFC studies on the investigation of the anode (32; 33; 19; 34; 35; 36; 37) and cathode (19; 38) behaviours by electrochemical impedance spectroscopy found their inspiration in Müller and Urban's method. A complete study on DMFC anode and cathode impedance spectra was reported by Piela and co-workers (19); in this work the spectra were recorded and interpreted assuming porous electrode models. At the anode, the methanol electro-oxidation reaction was investigated with no evidence of mass-transport problems and considering the CO poisoning of the Pt-Ru catalyst. At the cathode, both the crossed-over methanol electro-oxidation and the oxygen electro-reduction reactions were investigated with evidence of mass-transport problems in the backing layer. The high sensitivity of impedance method allowed the authors to investigate separately the flooding of the cathode gas diffusion layer from the flooding/dry out of

the cathode catalyst layer. The determination of the electrochemical parameters was accurate, however this approach may be quite deceptive because the fuel cell is monitored under pseudo-DMFC configuration rather than during MeOH/air operating condition and the mutual dependence of the methanol oxidation reaction at the anode and the oxygen reduction reaction at the cathode is not taken into account.

Most recently, Diard and co-workers have introduced an alternative way of measuring separately the cathode and anode contributions, based on the use of an external reference electrode (39). The results seemed to be reproducible (40; 41), however the utilization of a reference may introduce significant problems related to the packaging, the correct placement of the electrode and its utilization in micro-fuel cells. The complete DMFC spectrum and the resolved anodic and cathodic spectra (vs. Ag/AgCl reference electrode) presented by Yang and co-workers in their works are reported in the Figure 3.16 (41).

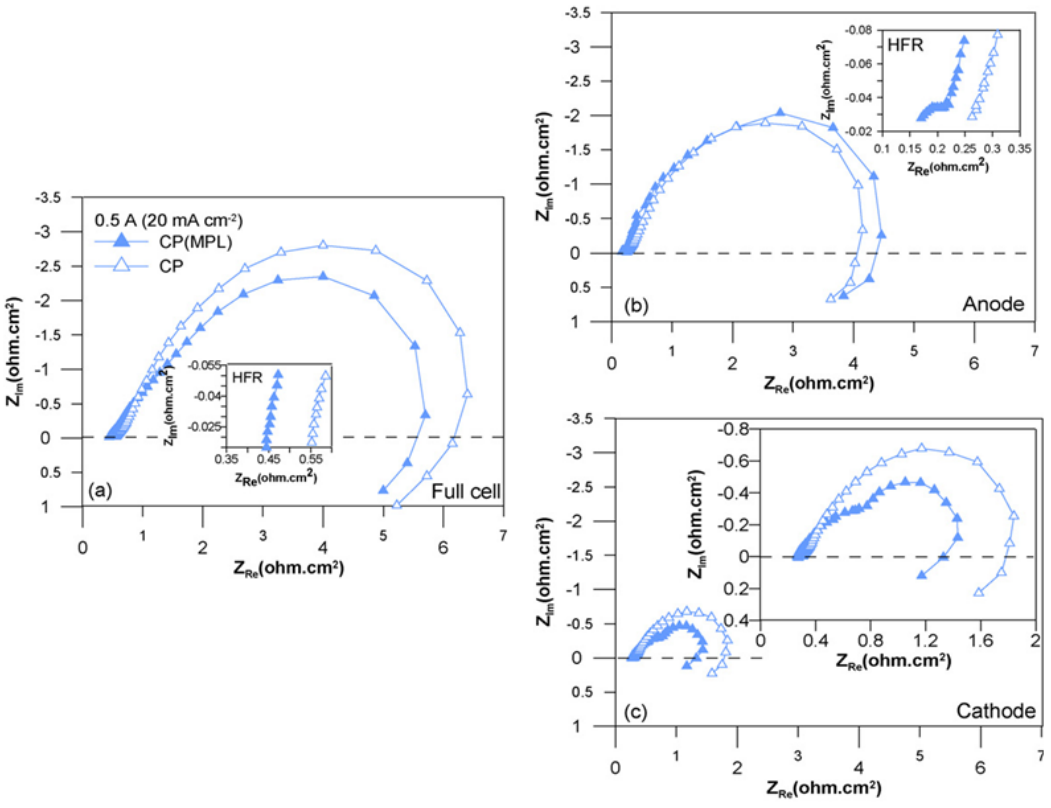

Figure 3.16: Complete DMFC spectrum and resolved anodic and cathodic impedance spectra (41).

Besides Müller and Urban's approach, the literature reports few recent EIS studies on DMFC under operative conditions (42; 43; 44; 45; 46; 47). In these works the complete fuel cell spectra

were recorded and interpreted and the contributions of the anode –and the cathode to the total spectra were identified . In their work, Mohan and Shrestha (45), employed impedance to differentiate and determinate the losses in a passively operated fuel cell. The complete spectra in the Nyquist plot form, Figure 3.17, were recorded at different current values and methanol concentrations and the ohmic losses (R_O), the cathode and anode activation losses (R_a and R_c), the mass transport losses (R_m) were estimated.

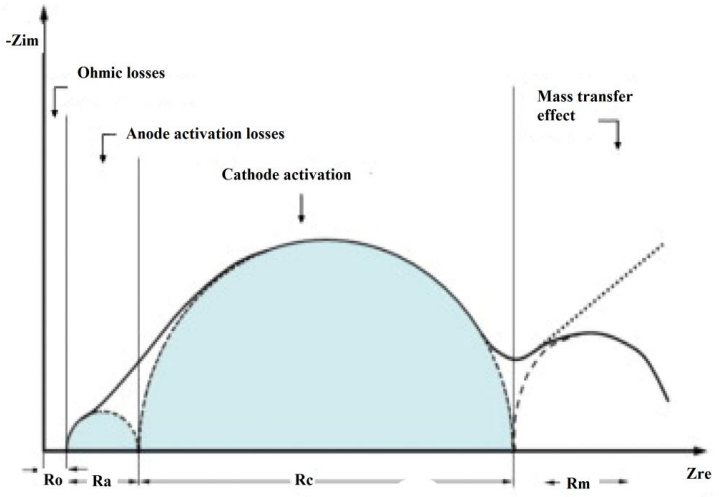

Figure 3.17: Complete spectrum for a passive DMFC (45) .

In their work, Lai and co-workers (44), used impedance to understand the reaction mechanisms occurring in the MEA. The complete spectra in the form of Nyquist and Bode plots were recorded and presented as in Figure 3.18. The impedance of the system was divided in three components: the one at high frequency was attributed to the interfacial behaviour membrane-electrodes, the medium-frequency component was assigned to the anodic and cathodic electrochemical reactions, and the low-frequency impedance was related to the adsorption/relaxation of the CO. Particular emphasis was given to the utilization of the Bode plots because no magnifications are necessary to analyze the individual loops.

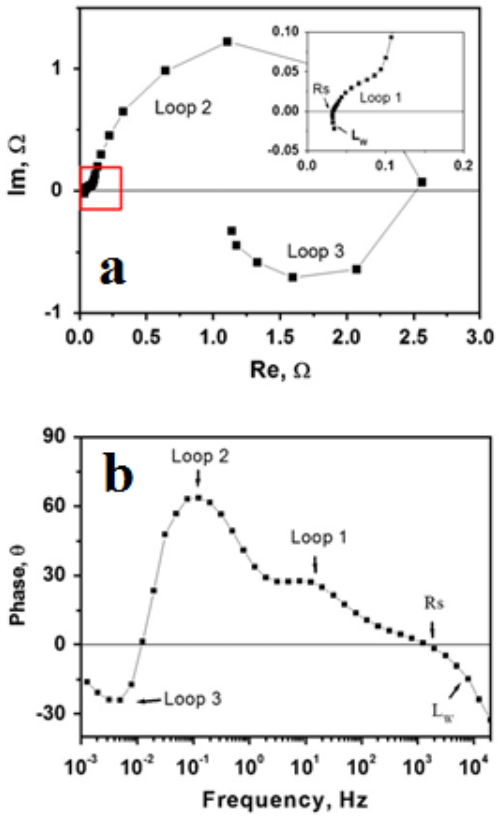

Figure 3.18: a) Nyquist and b) Bode plots for a DMFC (44).

In his work, Oedegaard investigated the performance of a DMFC system operated under near-ambient conditions (42). The fuel cell impedance spectra and half-cell impedance spectra (cathode set as DHRE), Figure 3.19, were recorded at different methanol flow rate, methanol concentrations and temperature. Two overlapping semicircles concerning the anode and the cathode appeared in the complete spectrum, whereas one single semicircle corresponding to the anode was present in the half-cell spectrum. The comparison between the complete and half-cell spectra allowed the interpretation of the semicircles in the complete spectrum. Since the semicircle at low frequency resembled the one for half-cell operation, this semicircle was associated with the anodic processes, whereas the semicircle at high frequency was related to the cathodic processes.

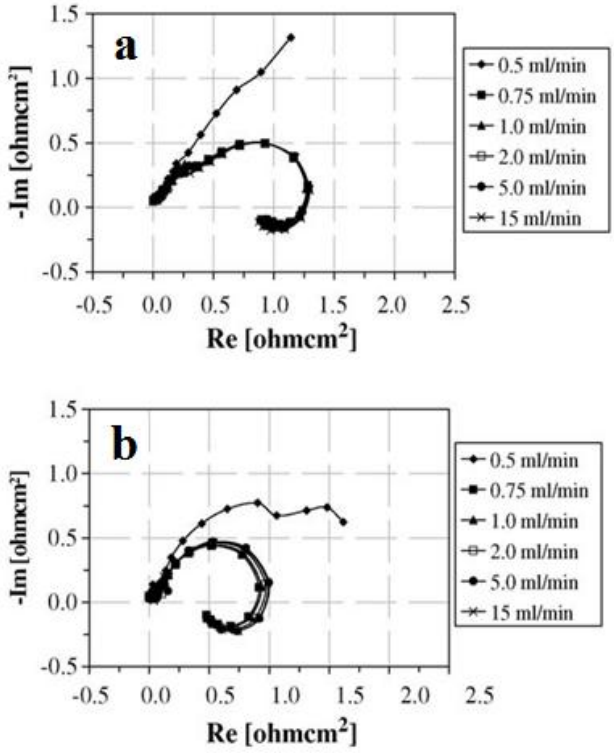

Figure 3.19: a) Fuel cell and b) half-cell DMFC impedance spectra (42).

In their work, Aricò and co-workers used impedance to investigate the effect of the MEA configuration on the performance of an air-breathing DMFC mini-stack (46). The hydrophobic-hydrophilic properties of the anode and cathode catalyst layers were varied and three different MEAs were prepared. The complete spectra were recorded under DMFC operative conditions; the spectra, similar in shape to the ones reported by Oedegaard, showed two overlapping semicircles, one small semicircle at high frequency and a large one at low frequency. The authors noticed that the amplitude of the semicircle at low frequency responds to the variations of potential and methanol concentration and to the type of reactant (air/oxygen). It was concluded that the semicircle at low frequency is representative of the cathode behaviour and, at high methanol concentration, the limiting process concerns the cathode because of the high rate of methanol cross-over.

In the work developed as collaboration between Aricò and our group (47), we reported the complete investigation of two DMFCs monitored during their operation under methanol and air. Two MEAs, containing the same anode, Nafion 117 membrane but different cathodes (Pt-based and Pt_3Co-based cathodes) were prepared and investigated under varying operative conditions

(cell voltage, reactant, and fuel concentration) and with excess of methanol. The recorded DMFC spectra show two overlapping and distorted semicircles, distributed in the frequency range 10 kHz – 10 mHz, Figure 3.20. The comparison of the spectra shows that only the amplitude of the semicircle at the low frequencies responds to the different MEAs composition (cathode), the variation of cell voltage and to the reactant type (air and oxygen), so the authors agreed in featuring it as representative of the cathode behaviour. As previously reported by Müller, when fed with an excess of methanol, the anode does not respond to the variation of the cell parameters (32).

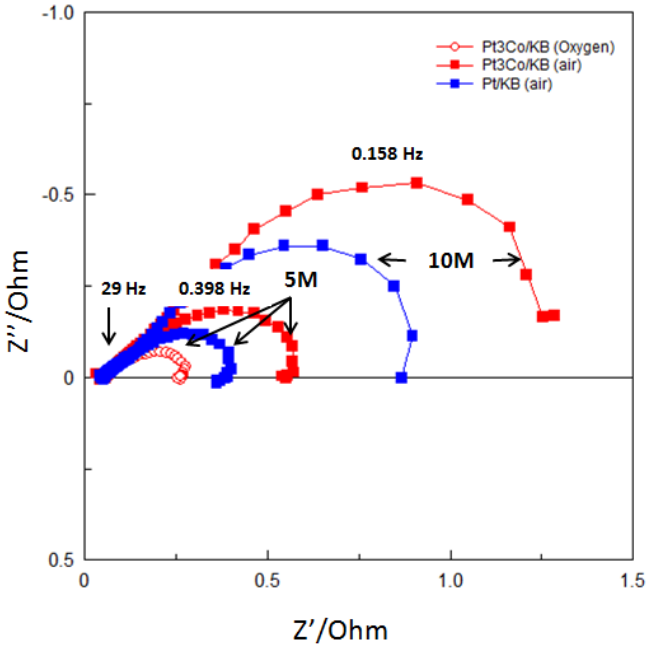

Figure 3.20: Complete impedance spectra of single DMFCs (47).

The variety of approaches reported above shows that an unique and simple method for the analysis of the DMFC impedance spectra does not exist as yet. Consequently, the objective of this study is to find an easy and not time dispending approach for the investigation of the total DMFC spectra. Based on the argument proposed in our work (47), this paragraph is meant to the analysis of impedance spectra recorded in (47) by fitting them with appropriate equivalent circuits and determining the electrochemical parameters. This study is expedient to extend the fitting process to the MEAs that are specific subject of this thesis and to validate our conclusion/hypothesis that for these MEAs operated under excess of methanol, the semicircle at low frequency is representative of the cathode behaviour. For this purpose, this paragraph

includes as well the investigation of two other MEAs, the first one containing a commercial PtRu-based anode (Electrochem. Inc.), Nafion 117 membrane and commercial Pt-based cathode (Electrochem. Inc.), and the second one with a commercial PtRu-based anode (Electrochem. Inc.), Nafion 117 membrane and homemade Pt-based cathode). The spectra of the DMFCs containing these MEAs were recorded under various cell potentials, and in presence of air/oxygen, as shown in Figure 3.21.

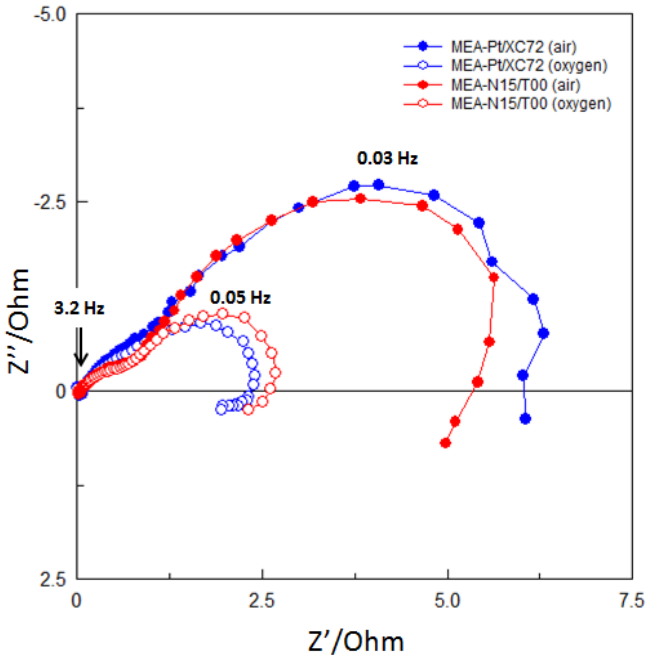

Figure 3.21: Complete impedance spectra of single DMFCs analyzed in this paragraph.

3.3.1. Equivalent Circuits from the literature

Several groups have developed equivalent circuits to fit the total impedance of PEMFCs and DMFCs. The main works are attributed to:

Andreaus (48; 49)

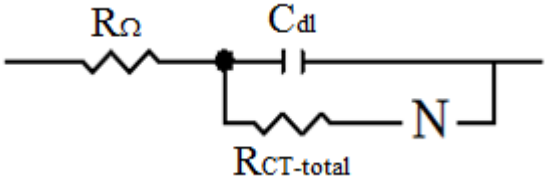

Andreaus proposed an idealized model to describe the impedance of a polymer electrolyte fuel cell operated at high current density. The model was used to study the water balance in the membrane and its effect on the performance of the fuel cell. This model is simple, does not consider the porous structure of the electrodes and the cathodic and anodic contributions are not distinguished. The circuit contains the membrane resistance, R_{Ω}, the double-layer capacitance for the entire cell, C_{dl}, the total charge-transfer resistance, $R_{CT\text{-}total,}$ and the Nernstian element N which is related to the mass transport limitations occurring at low frequency, and specifically to the water back-transport from the cathode to the anode.

Schiller – Wagner (50; 51; 52; 53)

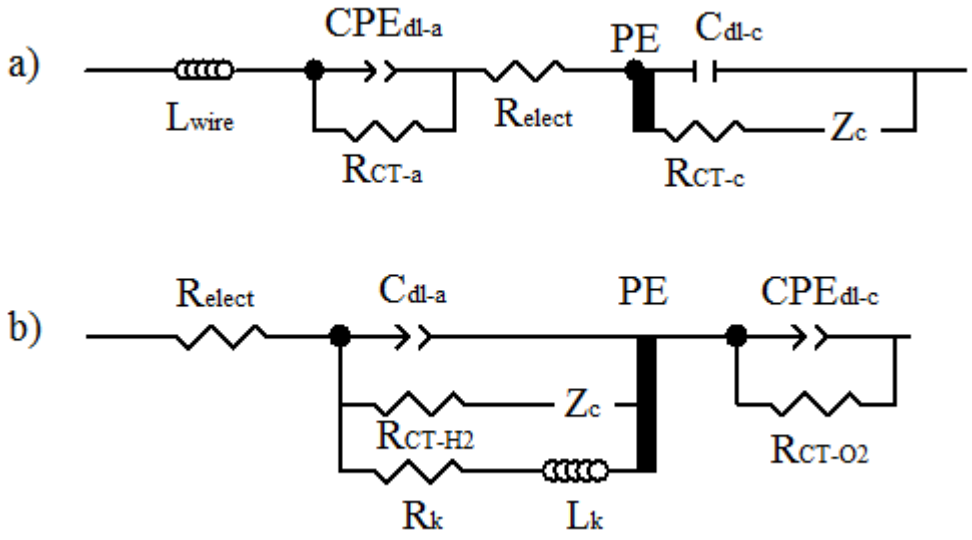

Schiller and Wagner proposed two models to describe the impedance of a polymer electrolyte fuel cell a) during normal operative conditions (51) and b) during CO poisoning (50; 52; 53).

In the first case, EIS was used to investigate the fuel cell performance after the cathode gas outlet was closed and the water was prevented from being removed. The fuel cell was operated at low current density so that the diffusion contributions to the total impedance could be minimized. The diffusion contribution at the anode was neglected, whereas the one at the cathode was considered because of the water accumulation in the electrode porous structure. The built circuit contains the wiring inductance, L_{wire}, the electrolyte resistance, R_{elect}, the anodic branch with the charge-transfer resistance, $R_{CT\text{-}a,}$ and the constant phase element, $CPE_{dl\text{-}a}$, approximating the anodic porous structure and the complex cathodic branch concerning the oxygen diffusion through the

flooded cathodic porous structure. This branch contains the model for a porous electrode, PE, in series with the double-layer capacitance, C_{ld}, the charge-transfer resistance, R_{CT-c} and the finite diffusion impedance, Z_c.

In the second case, EIS was used to investigate the progressive CO poisoning of the anodic Pt catalyst. For the purpose, the anode was fed with a hydrogen/carbon monoxide mixture and the anode gas outlet was closed. High oxygen stoichiometry was used to prevent the occurrence of mass-transport problems in the cathode. The circuit was built simplifying the cathodic branch to the constant phase element, CPE_{dl-c} and the charge-transfer resistance R_{CT-O2}. The anodic branch was modelled using the porous electrode, PE, in series with the double-layer capacitance, C_{dl-a}, which is in parallel with the Faradaic impedance (Z_F). The Faradaic impedance is a surface relaxation impedance; it contains the charge-transfer resistance for the hydrogen oxidation, R_{CT-H2}, the finite diffusion impedance Z_c, and the relaxation resistance, R_k, and the pseudo-inductance L_k as well which are related to the CO poisoning of the catalyst surface.

Ciureanu (54; 55; 56)

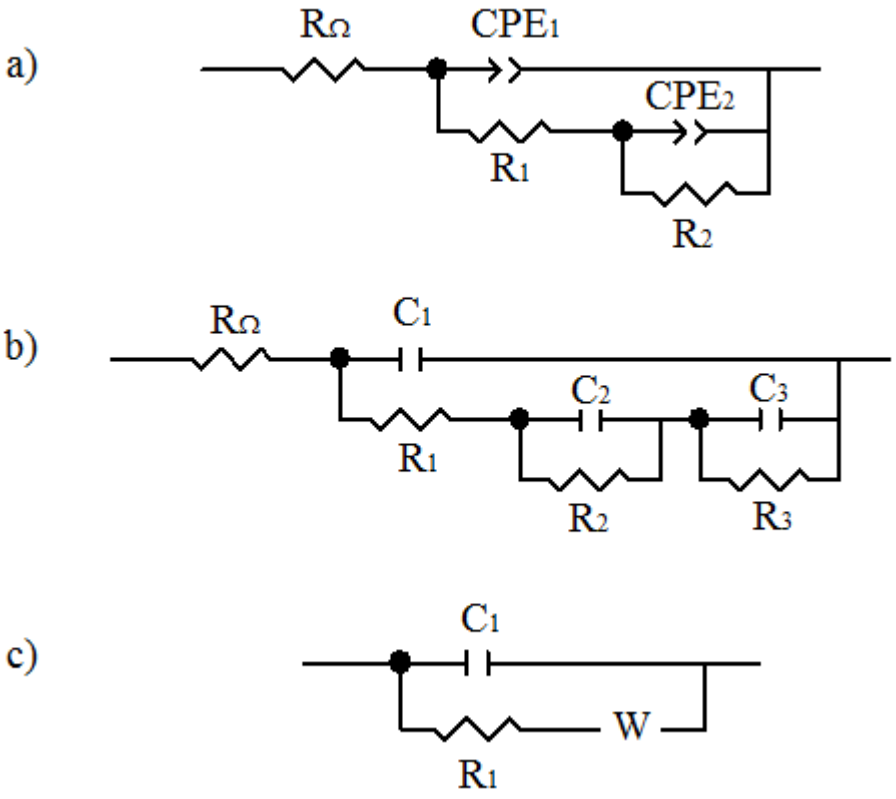

Ciureanu proposed several models to investigate fuel cells, with a particular interest in the anodic behaviour. The first and second circuits were proposed to fit the impedance of a cell fed with H_2/H_2+CO to model the effect of CO poisoning. In the first model, CPE_1 is the double-layer capacitance, R_1 the charge-transfer resistance, CPE_2 and R_2 the capacitance and resistance of the adsorbed species. In the second model, C_3 and R_3 are associated with the process of oxidative removal CO. The third model was used to fit a humidified PEM fuel cell; R_1 is the bulk resistance, C_1 the cell capacitance and W the finite Warburg element related with the diffusion of protons within the membrane.

Latham (57)

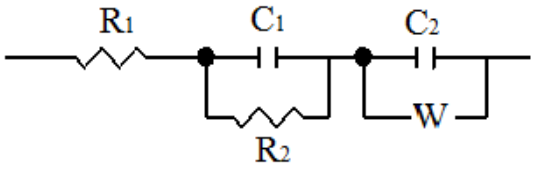

In his work Latham developed an equivalent circuit to fit the impedance spectra of a PEM fuel cell during flooding, drying and CO poisoning conditions. The circuit contains the resistance R_1 to represent the contact resistances (membrane, electrodes, GDLs and current collector plates), the resistor-capacitor parallel circuit (R_2-C_1) to represent the resistivity and the geometric capacitance of the membrane, and another parallel circuit with the double-layer capacitance C_2 and the Warburg element W_1 to describe the diffusion.

Lai (44)

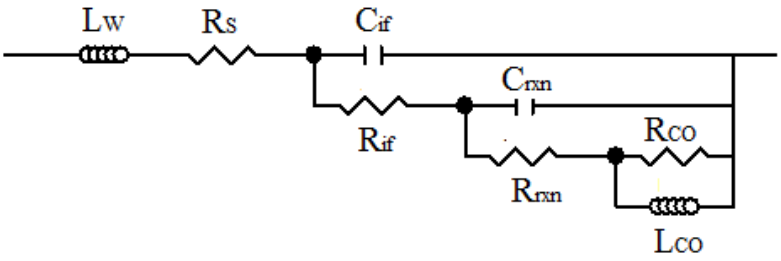

Lai proposed a model to fit the total impedance spectrum of a DMFC run under normal operative conditions. The parallel circuit with C_{if} and R_{if} describes the interfacial impedance, the parallel circuit with C_{rxn} and R_{rxn} corresponds to the impedance resulting from the electrochemical

reactions and the circuit with R_{CO} and L_{CO} is related to the impedance caused by relaxation/adsorption of intermediate species CO, produced by methanol oxidation.

Oedegaard (42)

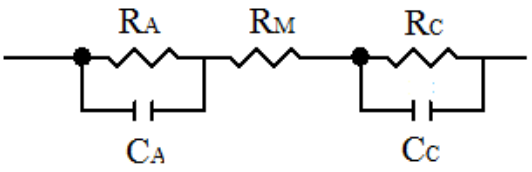

Oedegaard used this model to characterize the total impedance of a DMFC operated under near-ambient conditions. The R_A and C_A parallel circuit is related to the anode impedance, R_M to the membrane resistance and the R_C and C_C parallel circuit to the cathode impedance.

3.3.2. Equivalent Circuits Fitting for our MEAs

Analyzed MEAs

In this work, the total impedance spectra of single DMFCs containing four different MEAs were recorded under normal operative conditions (anode fed with methanol and cathode fed with air/oxygen). The impedance spectra were fitted with equivalent circuits and the resulting parameters analyzed. The MEAs were labeled according to the cathode composition as MEA-Pt/KB, MEA-Pt_3Co/KB, MEA-Pt/XC72 and MEA-N15/T00, Table 3.2. Detailed information about the cathodes' preparation and the assembling procedure are reported in Chapter 2.

The impedance spectra were recorded in the frequency range 100 kHz – 1 mHz, at the cell temperature of 40 °C, under various operative conditions listed in Table 3.3. To validate the hypothesis that the semicircle at low frequencies is representative of the cathodic behaviour, the impedance spectra were recorded in presence of excess of methanol (2 – 2.5 $mlmin^{-1}$) at different cell potentials (0.1 – 0.5 V), methanol concentration (1, 2, 5, 10 M), air flow rate (220, 350, 420 $mlmin^{-1}$) and under air/oxygen (51, 81 $mlmin^{-1}$) feed.

Table 3.2: Composition of the analyzed MEAs.

	ANODE	MEMBRANE	CATHODE
MEA-Pt/KB	Unsupported PtRu 3mg/cm^2 15 wt% Nafion HT-ELAT	Nafion117	Pt/KB 3mg/cm^2 15 wt% Nafion LT-ELAT
MEA-Pt_3Co/KB	Unsupported PtRu 3mg/cm^2 15 wt% Nafion HT-ELAT	Nafion117	Pt_3Co/KB 3mg/cm^2 15 wt% Nafion LT-ELAT
MEA-Pt/XC72	60 wt% PtRu/VulcanXC-72 3mg/cm^2 33 wt% Nafion coating TFE-treated Carbon cloth	Nafion117	60 wt% Pt/VulcanXC-72 3mg/cm^2 33 wt% Nafion coating TFE-treated Carbon cloth
MEA-N15/T00	60 wt% PtRu/VulcanXC-72 3mg/cm^2 33 wt% Nafion coating TFE-treated Carbon cloth	Nafion117	60 wt% Pt/VulcanXC-72 2.94mg/cm^2 15 wt% Nafion Carbon cloth

Table 3.3: Operative conditions for impedance measurements.

	MEA-Pt/KB	MEA-Pt_3Co/KB	MEA-Pt/XC72	MEA-N15/T00
E (V)	0.3	0.2–0.3–0.4–0.5	0.1–0.2–0.3–0.4–0.5	0.1–0.2–0.5
MeOH stoich.	4–8–20–40	4–8–20–40	5	5
Air stoich.	3.8	2.4 – 3.8 – 4.6	2.4	2.4
O_2 stoich.	4.3	4.3	2.7	2.7

Typical impedance spectra

Typical examples of Nyquist and Bode plots of the analyzed MEAs are reported in Figure 3.22. The experimental spectrum in the Nyquist plot of Figure 3.22a, recorded at 0.4 V, shows two overlapping and distorted semicircles distributed in the 10 kHz – 100 Hz and 100 Hz – 40 mHz frequencies ranges and a negative loop up to 10 mHz. The Nyquist plot can be analyzed as follow: the interception of the spectrum with the real impedance axis (Z') represents the serial resistance in which the membrane resistance is the dominating component. The small arc in the high frequencies region is representative of the anode behaviour, whereas the wide arc in the low frequencies region is representative of the cathode behaviour. The negative inductive loop at low frequencies concerns the adsorption/desorption of the CO which is an intermediate of the multi-step methanol oxidation reaction. Concerning the experimental spectrum recorded at 0.2 V, Figure 3.22b, two overlapping and distorted semicircles are shown in the region of frequencies 10 kHz – 20 mHz, however no inductive loop is present at lower frequencies. Again, the small arc in the high frequencies region is representative of the anode behaviour, whereas the one at low frequencies in related to the cathode.

The analysis of the Bode plot phase-angle allow the observation of two phase-shift maxima at the frequencies of 1.6 kHz, 0.3 Hz in the plot of Figure 3.22a, and at 2 kHz and 4 Hz in the plot of Figure 3.22b. The cathodic and anodic maxima of the phase angle can be related to the charge-transfer resistances and double-layer capacitances of the cathodic and anodic processes (Equation 3.5).

Concerning the Bode magnitude plot, the asymptotic behaviour of the module impedance is interrupted by two breaking point frequencies, 1.3 kHz and 79 mHz in the plot of Figure 3.22a, and 1.3 kHz and 400 mHz in the plot of Figure 3.22b.

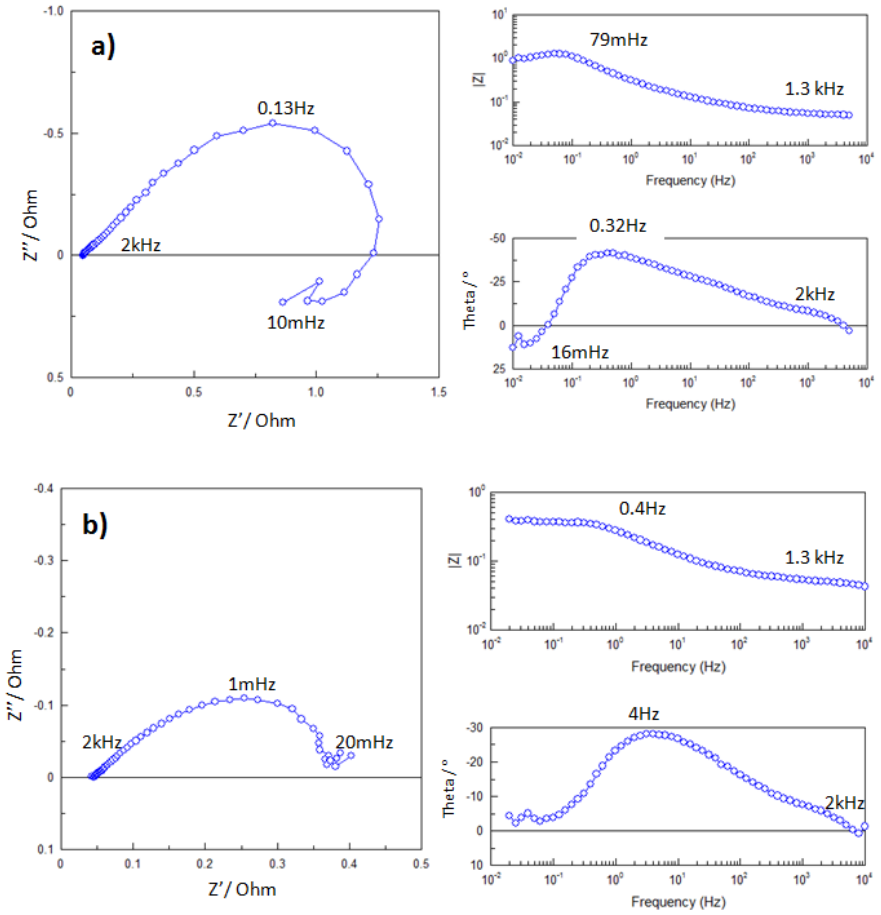

Figure 3.22: Typical Nyquist and Bode plots for DMFC impedance spectra at a) 0.4 V, b) 0.2 V (350 cc/min air flow – 5M methanol).

Building the Equivalent Circuits

The total impedance spectra were fitted by modelled equivalent circuits which were built to consider the electrochemical processes occurring at the cathode, the anode and the electrolyte membrane. Since the electrical inductance of the wires appears in a region of the spectrum out of investigation (over 10 kHz), it was not considered as part of the circuit. The Figure 3.23 shows the equivalent circuits used to fit the DMFC impedance spectra, built by using the Zview program.

The circuits are composed of the serial resistance (R_s), the anodic circuit and the cathodic circuit. Given that the main objective of this thesis concerns the study of cathodes for DMFCs, in a first approach the anode circuit was built with the charge-transfer resistance ($R_{ct\text{-}MOR}$) for the methanol oxidation reaction (MOR) and the constant phase element (CPE_{anode}) for the anodic

porous electrode. The relaxation impedance related to CO adsorption on the PtRu catalyst was not considered in the anodic circuit.

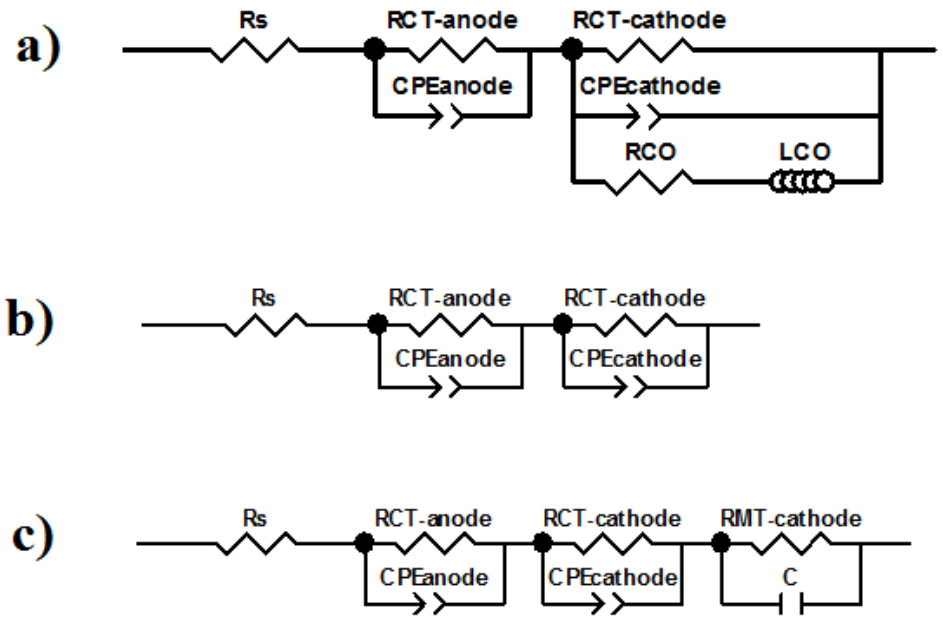

Figure 3.23: Equivalent circuits used to fit the EIS spectra of DMFCs.

The first cathodic circuit, Figure 3.23a, was built considering that two reactions occur simultaneously at the cathode: the oxygen reduction reaction (ORR) and the parasitic methanol oxidation reaction (MOR) due to the methanol cross-over from the anode to the cathode. Since the adsorption of the CO intermediate affects drastically the performance of the Pt cathode catalyst, the relaxation impedance was added in parallel to the ($R_{ct\text{-}ORR\&MOR}$) - ($CPE_{cathode}$) circuit. As reported in the literature (32; 53), the relaxation impedance is represented by the serial branch (R_{CO}) - (L_{CO}).

The second cathodic circuit, Figure 3.23b, was built considering that low methanol cross-over from anode to cathode occurs at high overpotential. Under this condition the poisoning of the Pt cathode catalyst can be neglected and the cathodic branch was built with the parallel circuit ($R_{ct\text{-}ORR\&MOR}$) - ($CPE_{cathode}$).

The third cathodic circuit, Figure 3.23c, was built taking in consideration the diffusion limitations occurring at the cathode at high overpotential. Under these conditions, a third semicircle appears

in the lower frequency region of the impedance spectrum and it can be fitted with a parallel R_{MT} – C circuit.

Fitting of the spectra

The experimental spectrum of the MEA-Pt_3Co/KB recorded at 0.5 V, feeding the anode with a 5M MeOH solution (2 ml/min – stoichiometry 20) and the cathode with air (220 ml/min – stoichiometry 2.4) was fitted first, using the equivalent circuit of Figure 3.23a. At first, anode and cathode were fitted individually using the "instant fit" option of the Zview program. The anode was fitted in the range of frequencies 2.5 kHz – 400 Hz, whereas the cathode was fitted in the range 400 Hz – 10 mHz. Next, the values of the partial fitting were used as initial parameters in the fitting of the complete spectrum; at the beginning, maintaining them fixed and then releasing them one by one. The results of the fitting are reported in Figure 3.24.

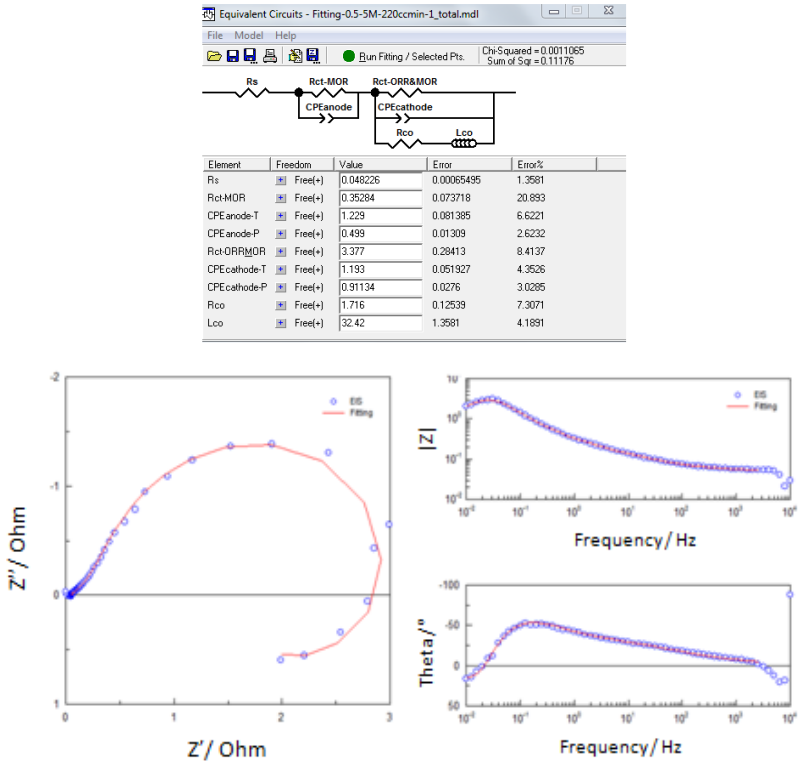

Figure 3.24: Fitting of impedance spectrum of MEA-Pt_3Co/KB (0.5 V - 5M MeOH solution (2 ml/min – stoich. 20) - air (220 ml/min – stoich. 2.4)).

The values coming from the fitting of the total spectrum recorded at 0.5 V (MeOH conc. 5M, air flow rate 220 ml/min (stoich. 2.4)) were used to fit the series of spectra for which a parameter

such as the potential, air flow rate or methanol concentration, was varied. The outcome of this procedure is represented in Figure 3.25, which shows the spectra recorded in the range 0.5 - 0.2 V, in 5M MeOH solution (2 ml/min – stoichiometry 20) and under 420 ml/min air flow rate (stoichiometry 4.6).

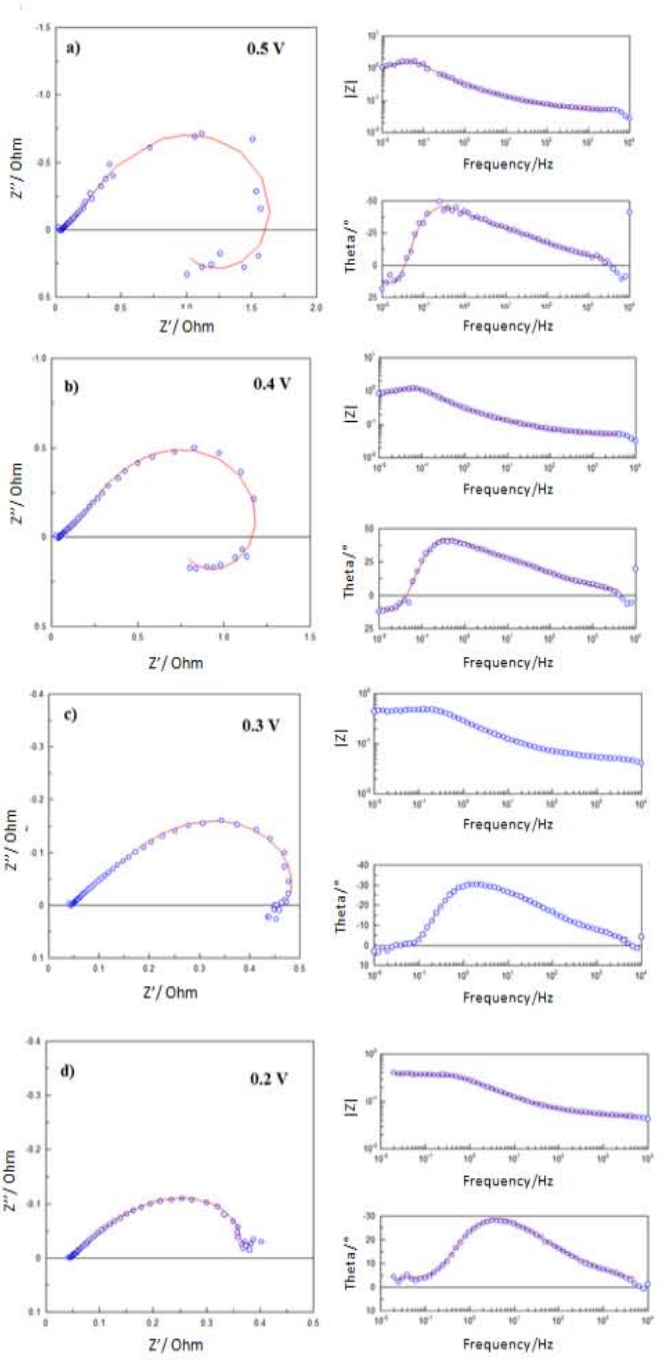

Figure 3.25: Fitting of impedance spectrum of MEA-Pt_3Co/KB at a) 0.5 V, b) 0.4 V, c) 0.3 V and d) 0.2 V (5M MeOH solution (2 ml/min – stoich. 20) - air (420 ml/min – stoich. 4.6)).

The fitting model reproduced quite well the experimental data and with Chi-square values of the order 10^{-3} - 10^{-4}. However, the errors associated with the parameters increased, especially the ones related to the R_{CO} and L_{CO} parameters, as shown in Figure 3.26.

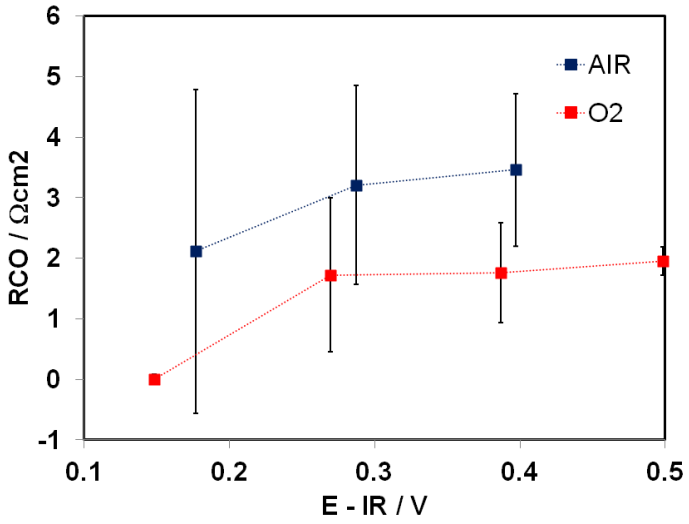

Figure 3.26: Values and errors of the $R_{CO\text{-}cathode}$ determined by fitting of MEA-Pt_3Co/KB using the equivalent circuit of Figure 3.23a.

Different approaches were attempted to reduce the magnitude of the errors. Firstly, it was observed that the spectra recorded at 0.2 V, Figure 3.25d, did not show any inductive loops. Consequently, these spectra were re-fitted by using the circuit presented in Figure 3.23b which allowed a good reproduction of the experimental data and low errors on all parameters.

Concerning the spectra recorded in the range of potentials 0.5 – 0.3 V, it was attempted to re-fit them starting from the individual fittings of the anode and the cathode. Even if different initial values were used, this approach did not bring any improvement to the final result because the fittings were still converging to the same local minima. However, by doing so we could verify that the fitting technique was not producing a systematic propagation of the error.

As mentioned above, the anodic branch was simplified as much as possible, although a more precise scenario should consider the CO-poisoning effect on the PtRu catalyst as well. The effect of the poisoning on the PtRu may be relevant at high cell potentials where the oxidation of the fuel occurs at low rate. For this reason, the spectra recorded at 0.5 V were re-fitted after including the anodic inductance in the equivalent circuit. At first, the anodic R_{CO} and L_{CO} values were set equal to the cathodic R_{CO} and L_{CO} parameters and maintained fixed during the fitting. Then, the

two parameters were released and the fitting was repeated. The final result of this process is reported in Figure 3.27.

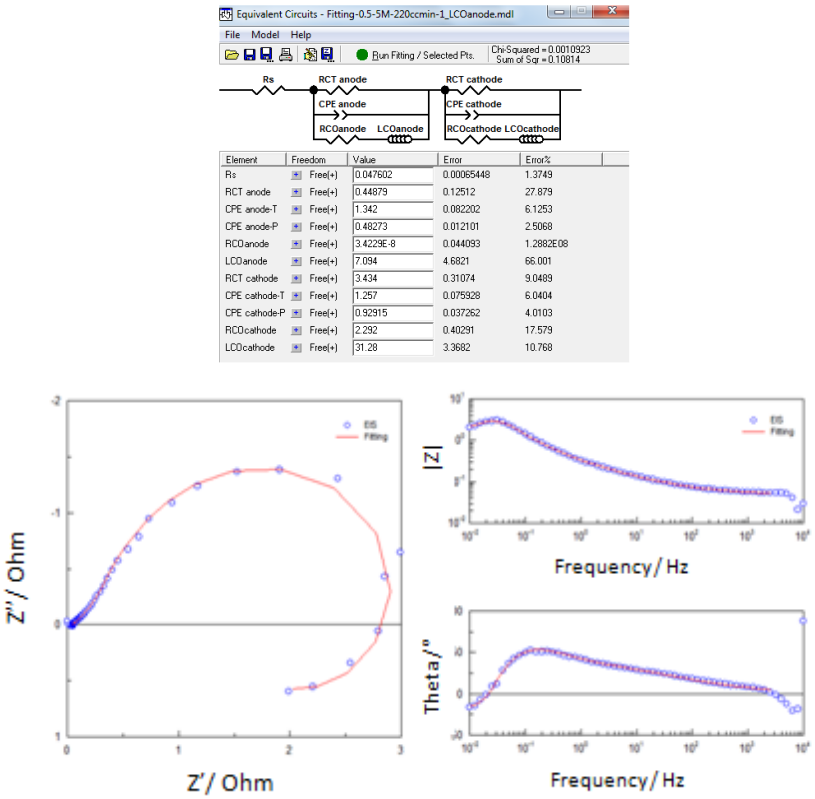

Figure 3.27: Fitting of impedance spectrum of MEA-Pt_3Co/KB (0.5 V - 5M MeOH solution (2 ml/min – stoich. 20) - air (220 ml/min – stoich. 2.4)) by a circuit provided with anodic inductance.

Compared to the previous modelling (circuit without anodic inductance), this fitting does not seem to have better quality and the Chi-square value has the same order of magnitude (10^{-3}). In terms of error, the $R_{CO\text{-}anode}$ and $L_{CO\text{-}anode}$ parameters show large errors, especially R_{CO}, and the insertion of the anodic inductance in the total circuit seems to have worsened the errors related to the anodic charge-transfer resistance and the cathodic parameters. No better results were obtained by doubling and halving the initial values of the anodic R_{CO} and L_{CO}.

Since the contribution of the anodic inductance did not give any improvement in the fitting of the spectra, the poisoning of the anode was not further considered. It was concluded that all the experimental results could be analyzed using the two "simplified circuits" of Figure 3.23.

Concerning the spectra recorded at different methanol concentrations, the spectra were fitted starting from the spectrum recorded at 0.3 V, in presence of 5 M methanol solution and during

the fitting procedure the anodic parameters were maintained fixed. This allowed a correct comparison of the results between MEAs containing the same type of anode. In addition, the spectra recorded with 1 M methanol solution, which did not show any inductive loop, were fitted using the circuit of Figure 3.23b.

Concerning the fittings and results presented in the Chapters 5 and 6, the spectra were fitting by using the equivalent circuits of Figure 3.23 as well.

3.3.3. Results

MEA-Pt_3Co/KB and MEA-Pt/KB

As reported in Table 3.3, the impedance spectra of MEA-Pt_3Co/KB were recorded under varying operative conditions, whereas MEA-Pt/KB was only investigated as a function of the methanol concentration. For this reason, the results of MEA-Pt_3Co/KB and MEA-Pt/KB are presented as follow:

Section A) for MEA-Pt_3Co/KB: Effect of the cell voltage

Section B) for MEA-Pt_3Co/KB: Effect of the air stoichiometry

Section C) for MEA-Pt_3Co/KB and MEA-Pt/KB: Effect of the methanol concentration

Section A) for MEA-Pt_3Co/KB: Effect of the cell voltage

The Figure 3.28 shows the experimental and fitted spectra as a function of the potential which was varied between 0.5 V and 0.1 V, in presence of air (350 ml/min – stoichiometry 3.8) and oxygen (81 ml/min – stoichiometry 4.3), with a 5 M methanol solution (2 ml/min – stoichiometry 20). The cathodic and anodic parameters derived from the fittings are presented in Figure 3.29.

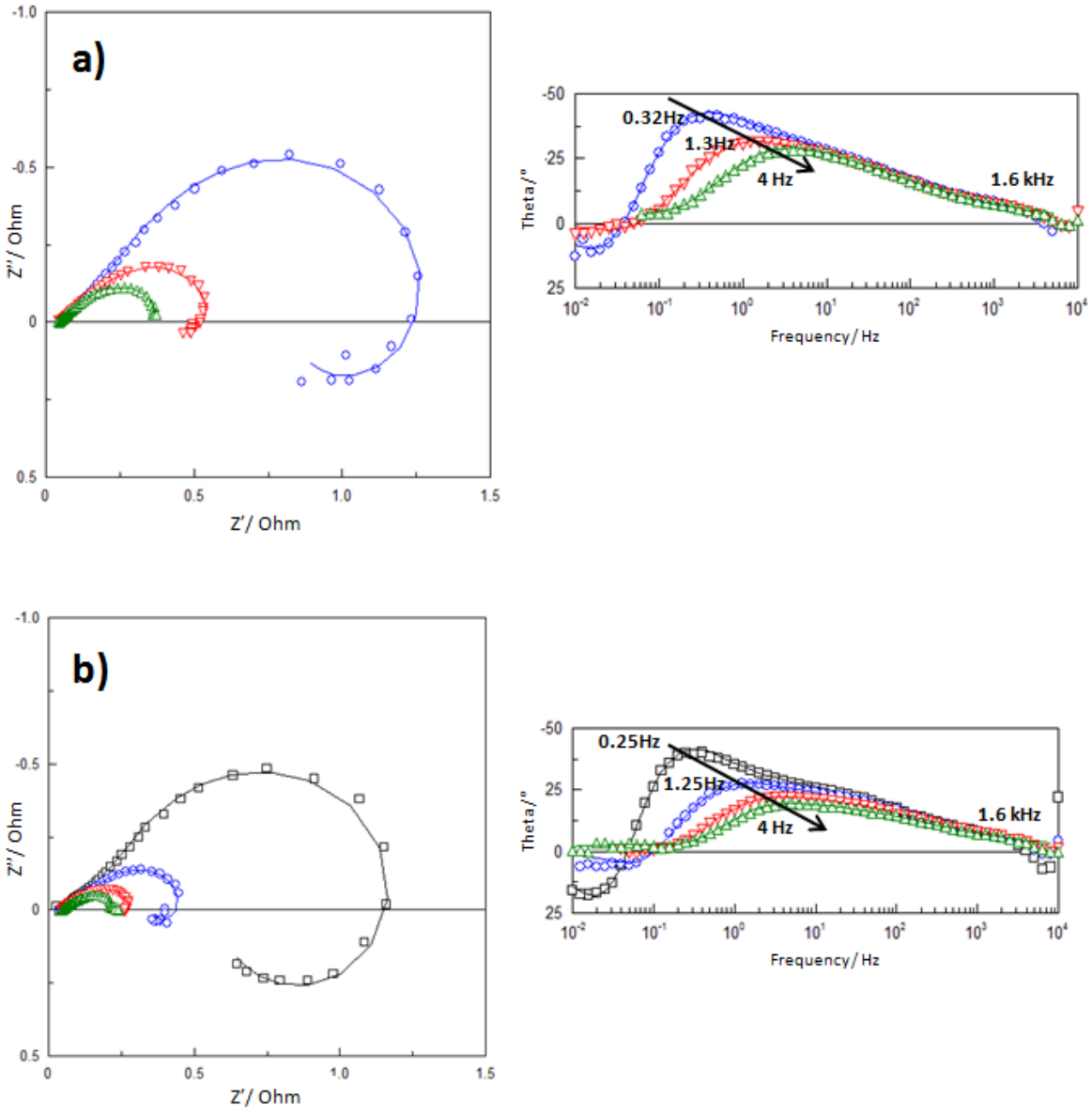

Figure 3.28: Experimental and fitted spectra for MEA-Pt_3Co/KB recorded at different E_{cell} in 5 M MeOH solution (2 ml/min – stoich. 20) under a) air (350 ml/min – stoich. 3.8) and b) O_2 (81 ml/min – stoich. 4.3).

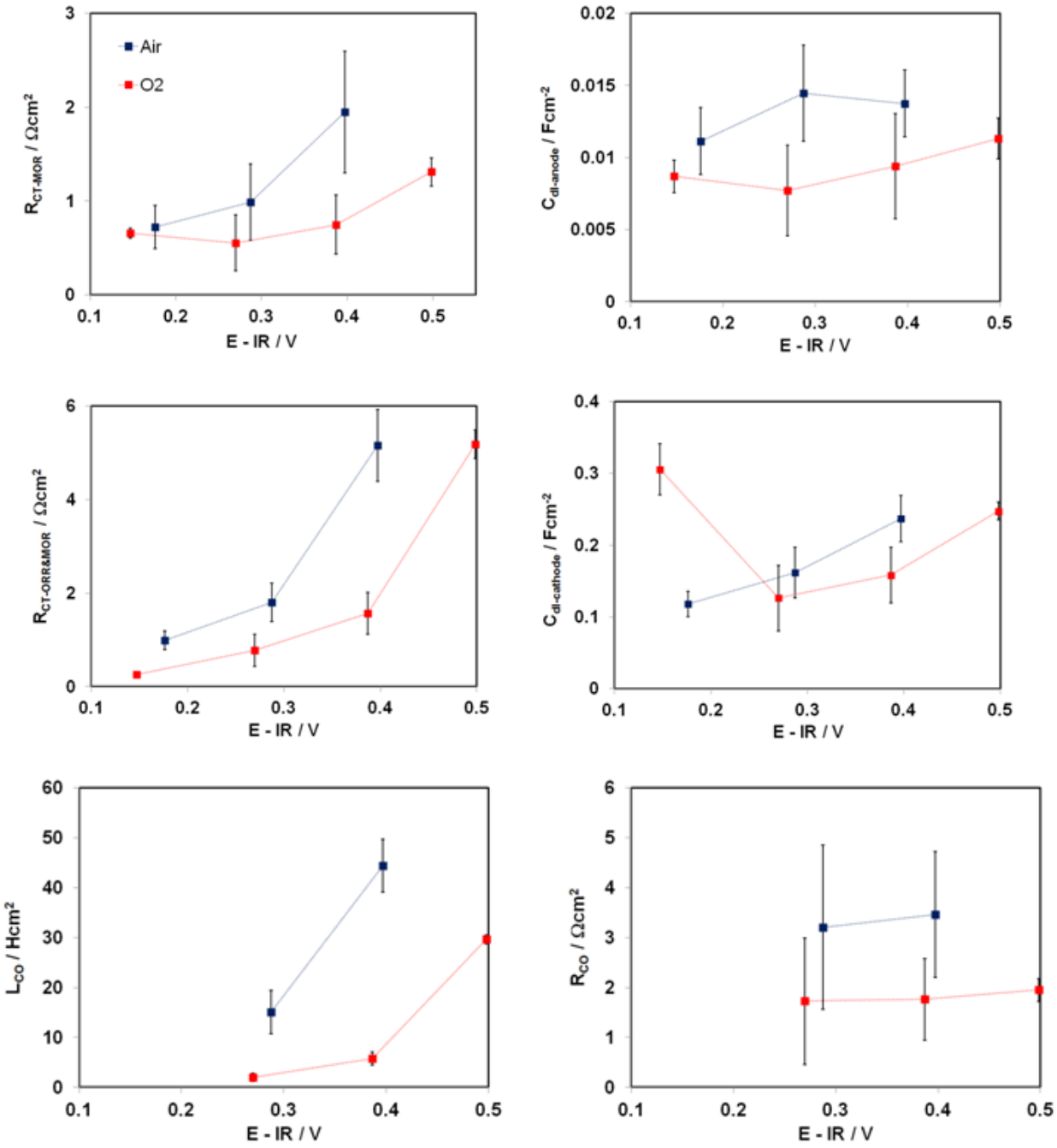

Figure 3.29: Kinetic parameters for the anode ($R_{ct\text{-}MOR}$ and $C_{dl\text{-}anode}$) and the cathode ($R_{ct\text{-}ORR\&MOR}$, $C_{dl\text{-}cathode}$, R_{CO} and L_{CO}) as a function of the IR-corrected cell potential, under air (350 ml/min – stoich. 3.8) and O_2 (81 ml/min – stoich. 4.3) in 5 M MeOH solution (2 ml/min – stoich. 20).

The analysis of the spectra and graphs allows the following observations:

a) Since two reactions (oxygen reduction and methanol oxidation) occur at the cathode, the values of charge transfer resistance and double-layer capacitance are naturally higher than for the anode.

b) The charge-transfer resistance decreases with the increasing of the overpotential because the electrochemical reactions are accelerated. As expected, this effect is more marked for the cathode. Although the oxidant stoichiometry was maintained almost constant, the charge-transfer resistance is lower in presence of pure oxygen than in presence of air. In fact, the absence of nitrogen allows a faster diffusion of the reagent into the electrode porous structure and a better utilization of the catalyst.

c) The double-layer capacitances are constant with the air or oxygen feed and do not vary significantly with the potential, except for the cathode at 0.1 V where the $C_{dl\text{-}cathode}$ almost increases three times. Since the fuel stoichiometry was maintained high during the experiments, it seems reasonable to suppose that the anode and the cathode may be strongly poisoned (high CO-coverage and low Pt-OH-coverage) and that only the combination of oxygen with a high current density may improve the catalyst utilization.

d) The inductance and the resistance behave coherently and decrease with increasing overpotential. In fact, the CO oxidation becomes faster with the increasing of the current density and the coverage by CO – like residues consequently decreases. When the coverage of the active sites is very low (no inductive loop), at 0.1 V and in presence of oxygen, more of the electrode surface is available for the oxygen reduction reaction, therefore a significant increase of the double-layer capacitance is observed.

e) Consistently with the decrease of the charge-transfer resistance, the cathodic phase-shift maximum in the Bode plot (Figure 3.28) moves towards higher frequencies at the increasing of the overpotential.

Section B) for MEA-Pt_3Co/KB: Effect of the air stoichiometry

The Figure 3.30 shows the experimental and fitted spectra as a function of the air flow rate which was varied between 220 and 420 ml/min (stoichiometry between 2.4 and 4.6), recorded at different potentials (0.2 – 0.5 V). A 5 M methanol solution (2 ml/min – stoichiometry 20) was used in all cases. The cathodic and anodic parameters derived from the fitting are presented in Figure 3.31.

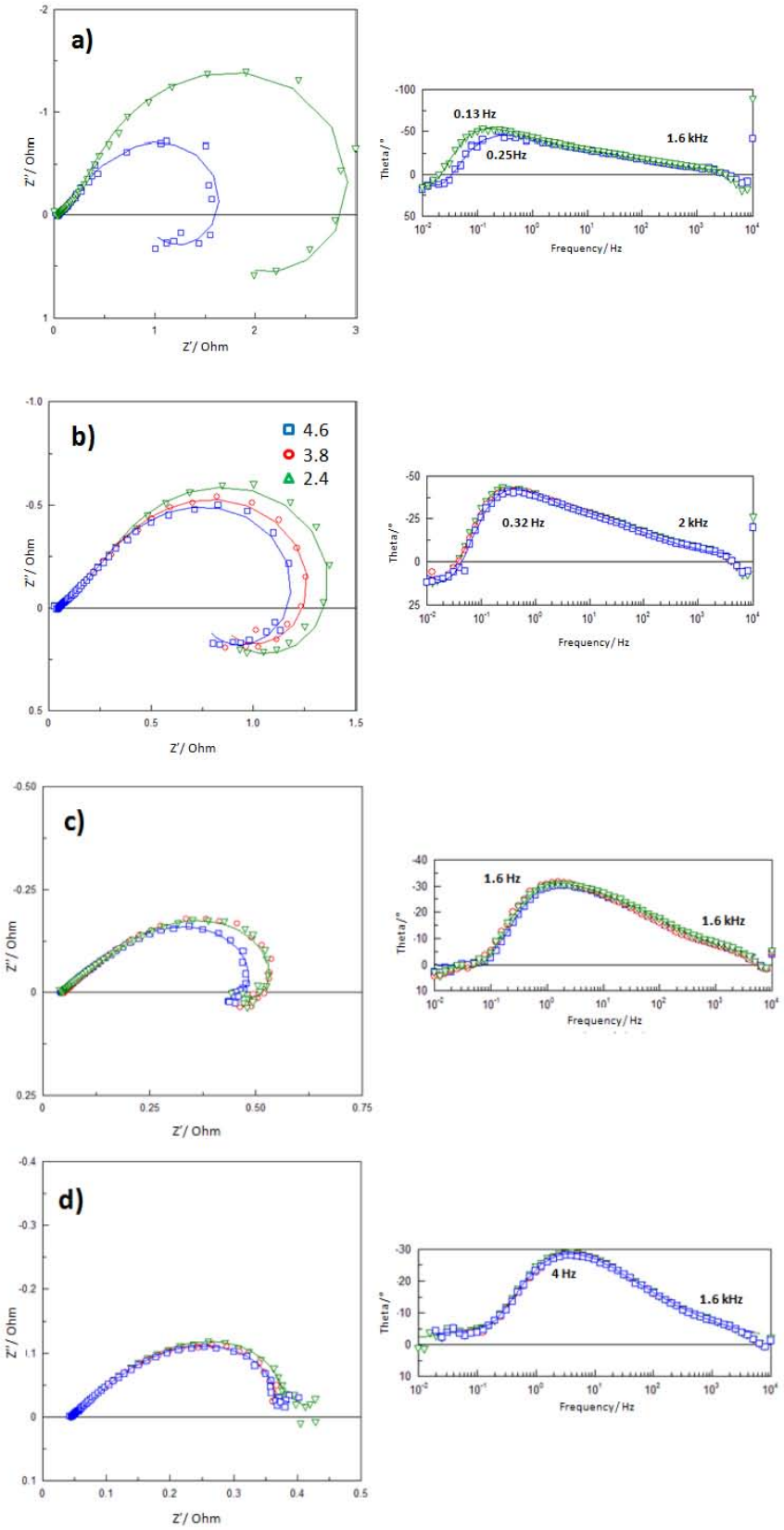

Figure 3.30: Experimental and fitted spectra for MEA-Pt_3Co/KB recorded at different air stoichiometry ratio in 5 M MeOH solution (2 ml/min – stoich. 20) at a) 0.5 V, b) 0.4 V, c) 0.3 V, d) 0.2 V.

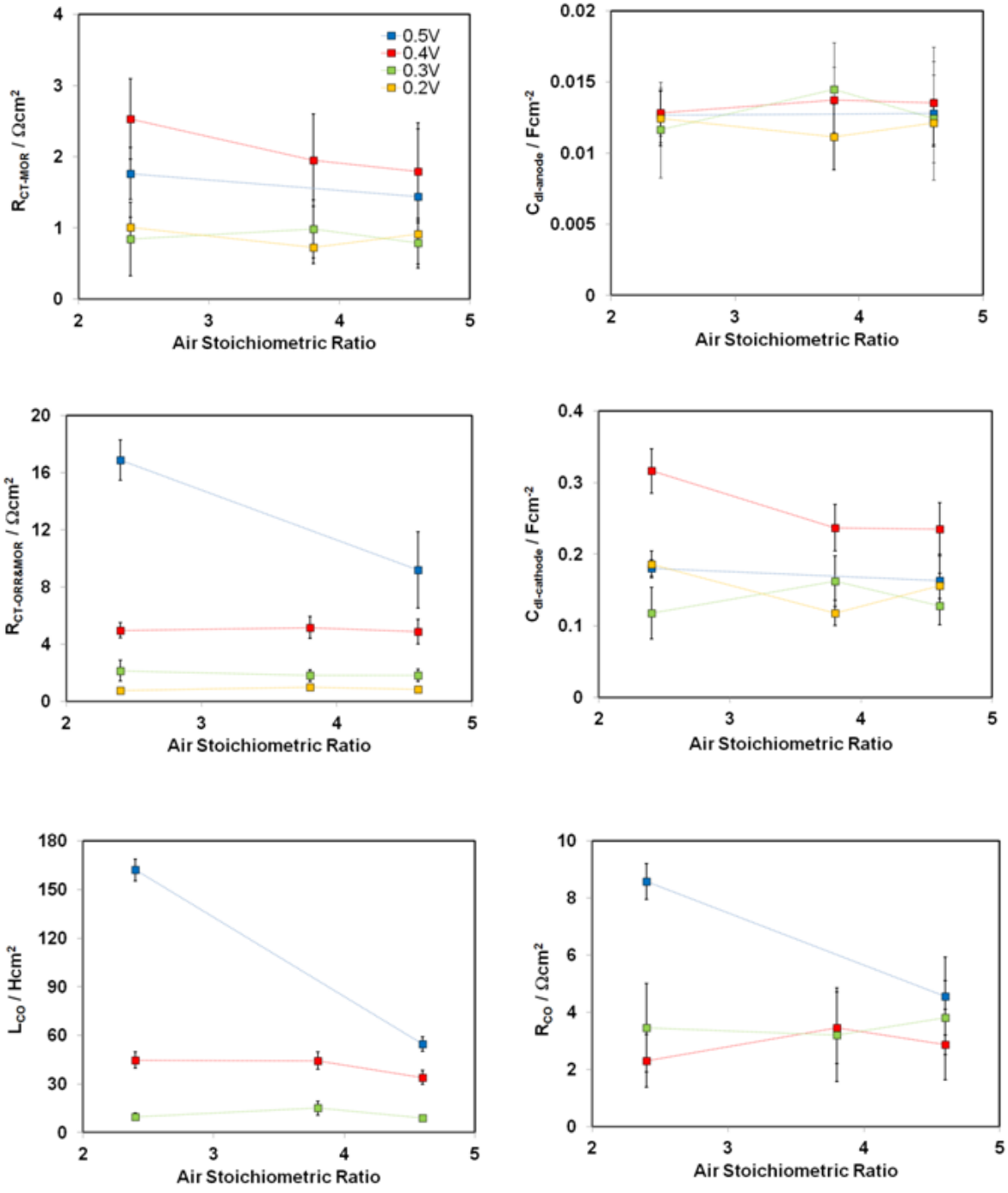

Figure 3.31: Kinetic parameters for the anode (R_{ct-MOR} and $C_{dl-anode}$) and the cathode ($R_{ct-ORR\&MOR}$, $C_{dl-cathode}$, R_{CO} and L_{CO}) at different potentials in function of the air stoichiometry ratio.

The analysis of the graphs allows the following observations:

a) The effect of the air stoichiometry on the cathodic parameters $R_{CT-ORR\&MOR}$, L_{CO} and R_{CO} is clearly visible at OCV where the reaction kinetics are slow and the methanol cross-over

is very high. The increase of the air flow rate from 220 ml/min (stoichiometry 2.4) to 420 ml/min (stoichiometry 4.6) guarantees a higher provision of reactant for the oxygen reduction reaction and explains the decrease of the charge-transfer resistance $R_{CT\text{-}ORR\&MOR}$. In addition, the higher concentration of reactant allows an easier consume of methanol (cross-over) and a faster release of CO_2 from the poisoned surface (lower L_{CO} and R_{CO}). It should be noticed that, at OCV, the air stoichiometry ratio has a stronger impact on the poisoning of the catalyst than on the kinetic of ORR. In fact, the increase of the air flow rate produces a decrease of 50% on the charge-transfer resistance and 33% on the inductance and adsorption resistance. Finally, the effect of the air stoichiometry ratio on the charge-transfer resistance becomes less relevant at the increasing of the overpotential.

b) The anodic double-layer capacitance does not vary significantly with the air stoichiometry ratio despite the magnitude of the error associated to this parameter. On the contrary, important changes occur for the cathodic double-layer capacitance. As noticed above, a remarkable increase in the capacitance is observed when the cell potential is decreased from 0.5 V to 0.4 V because the electrochemical reactions are accelerated. This increase is more notable at low air flow (220 ml/min) and less pronounced at the higher stoichiometries. Depending on the water content in the gas, the effect of a high flow rate may be the gradual dry-out (for non-humidified gas) or the flooding (for humidified gas) of the cathode. Since the air flow used in this experiments was highly humidified (RH 100%), the most probable phenomenon occurring in the system is the accumulation of water. This hypothesis seems to be validated by the further decrease of the capacitance at higher overpotentials, where the dry-out of the cathode may be excluded because of the higher rate of the oxygen reduction. It should be noticed that the flooding of the cathode was not observed in the polarization curves recorded under the same operative conditions. However, one should keep in mind the different time scale of the two experiments: during an EIS measurement, the cell is maintained at the applied potential for circa 30min, whereas 1-2 minutes are required for the acquisition of the data-potential in a polarization test. For this reason, there are more chances to see the flooding during an EIS experiment.

Section C) for MEA-Pt_3Co/KB and MEA-Pt/KB: Effect of the methanol concentration

The Figure 3.32 shows the experimental and fitted spectra for the two MEAs, MEA-Pt_3Co/KB and MEA-Pt/KB, as a function of the methanol concentration which was varied between 1 and 10 M. The results concern impedance spectra recorded at 0.3 V, under air flow rate of 220 ml/min (stoichiometry 2.4). The resulting cathodic parameters are presented in Figure 3.33.

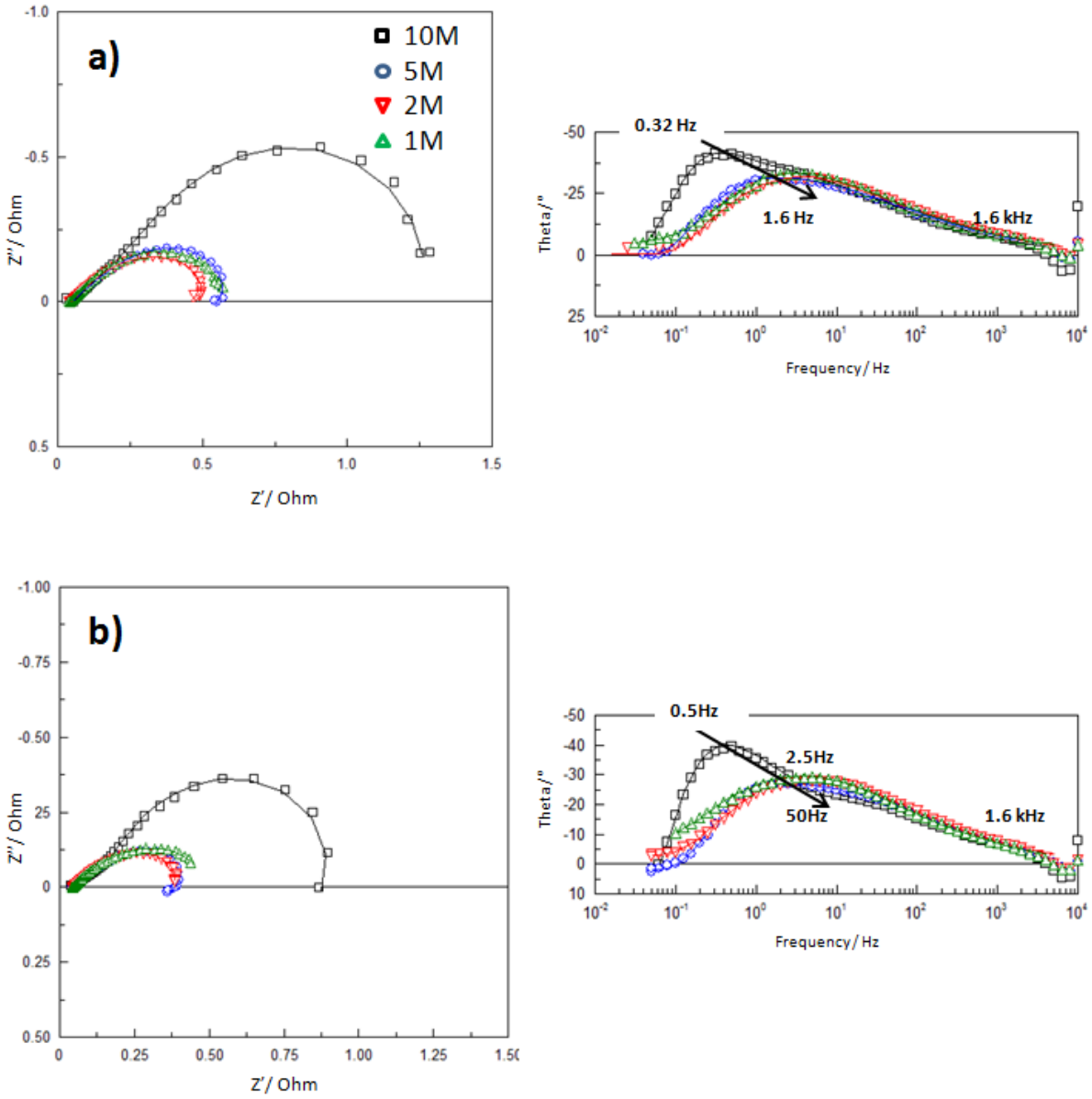

Figure 3.32: Experimental and fitted spectra for a) MEA-Pt_3Co/KB and b) MEA-Pt/KB recorded at different MeOH concentrations (at 0.3 V – air flow rate 220 ml/min – stoich. 2.4).

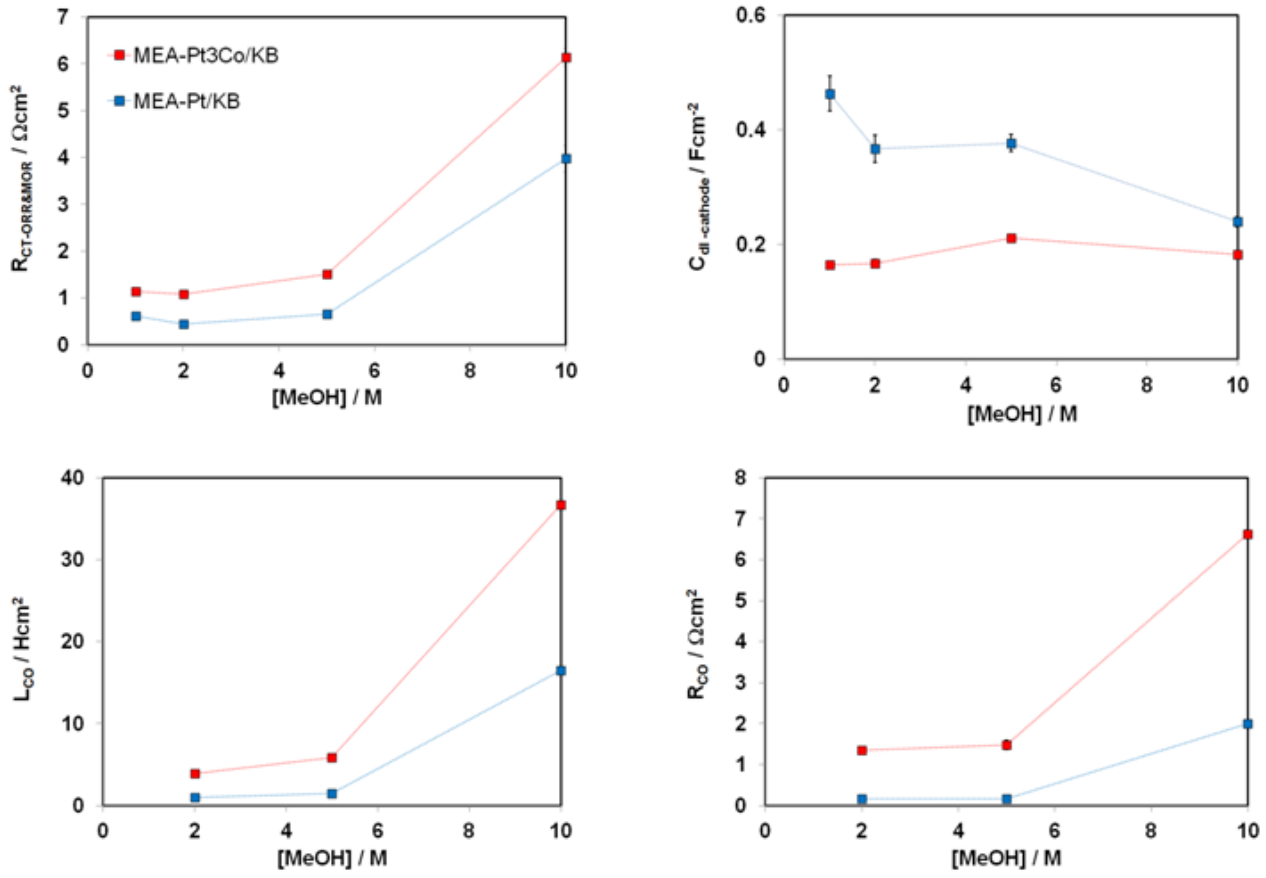

Figure 3.33: Kinetic parameters for the cathode ($R_{ct\text{-}ORR\&MOR}$, $C_{dl\text{-}cathode}$, R_{CO} and L_{CO}) of MEA-Pt_3Co/KB and MEA-Pt/KB as a function of the methanol concentration (at 0.3 V – air flow rate 220 ml/min – stoich. 2.4).

The analysis of the graphs shows that:

a) The charge-transfer resistance increases with the concentration of methanol because of the higher poisoning of the cathode catalyst due to methanol cross-over and lower Pt availability for the oxygen reduction reaction. As expected, the effect is more marked for the MEA-Pt_3Co/KB since the Pt_3Co/KB catalyst has lower methanol tolerance than the Pt/KB catalyst (47).

b) The double-layer capacitance of MEA-Pt/KB decreases at the increasing of the methanol concentration due to the increasing CO-poisoning effect of the catalyst, whereas lower and constant capacitance is observable for the MEA-Pt_3Co/KB. The high fuel stoichiometry used in the experiments and the lower tolerance to methanol of the

Pt_3Co/KB catalyst affect strongly the performance of the MEA- Pt_3Co/KB, even at low MeOH concentration (1M).

c) The relaxation inductance and resistance behave coherently and increase with the methanol concentration.

Conclusions

The fitting of the impedance spectra of MEA-Pt_3Co/KB and MEA-Pt/KB by using the equivalent circuits of Figures 3.23 allowed the determination of the anodic and cathodic kinetic parameters. The results are coherent and can be well-explained.

The model used for the fitting properly attribute the cathodic impedance to the semi-circle at low frequencies and the anodic impedance to the semi-circle at high frequencies. The cathodic parameters respond coherently to the variation of cell potential, type of reactant (air/O_2), air flow rate and cathode composition. On the contrary, the anodic parameters did not show significant variation with the operative conditions, as expected from the high fuel stoichiometry used in these experiments (32).

MEA-Pt/XC72 and MEA-N15/T00

This section contains the investigation of the two other MEAs, MEA-Pt/XC72 and MEA-N00/T15, which impedance spectra were recorded at varying cell potentials, under air and oxygen, Table 3.3. The experimental spectra are analyzed to confirm once again the validity of our hypothesis that the semicircle appearing in the low frequency region is representative of the cathode behaviour.

The spectra recorded at 0.5 V are reported in Figure 3.34. The spectra show the two overlapping anodic and cathodic semicircles and the inductive loop relative to the CO-poisoning. As above, the amplitude of the cathodic semicircle at low frequencies responds to the variation of type of reactant (air/oxygen), whereas the anodic semicircle at high frequencies is unvaried, as shown in the Nyquist plot, Figure 3.34a-c. The cathodic phase-shift maximum, Figure 3.34b-d, moves towards higher frequencies (from 0.05 Hz to 0.1 Hz for MEA-N15/T00, from 0.1 Hz to 0.25 Hz for MEA-Pt/XC72) when the reactant is switched from air to oxygen. On the contrary, the anodic phase-shift maximum is unchanged to the variation of reactant.

As observed in the Bode plot, the anodic phase-shift maximum of the two MEAs appears at different frequencies (16 Hz for MEA-N15/T00 and 5 Hz for MEA-Pt/XC72). It may seem unusual since the MEAs are composed of the same type of anode, however, as reported in the Table 3.2, the cathodes are different in terms of support (carbon cloth vs. TFE-treated carbon cloth) and catalyst layer (15 wt% Nafion in the C.L. vs. 33 wt% Nafion coating). These differences might influence the transport of reagent in the support and the ionic conductivity in the catalyst layer, affecting the performance of the cathode and of the anode as well.

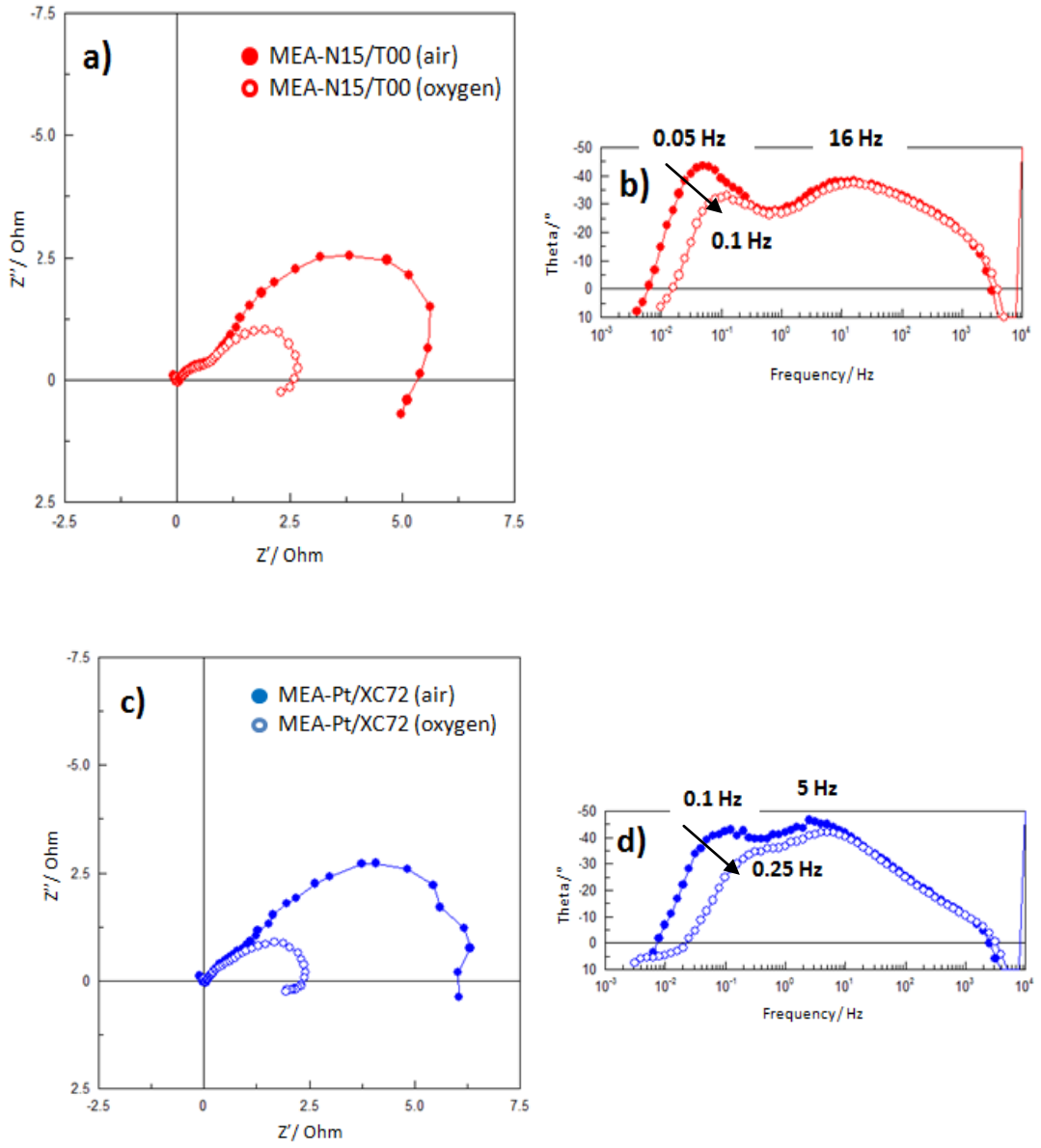

Figure 3.34: Nyquist and Bode plots for a-b) MEA-N15/T00 and c-d) MEA-Pt/XC72. Spectra recorded at 0.5 V, under air (220 ml/min – stoich. 2.4) and O_2 (51 ml/min – stoich. 2.7) with 1 M MeOH solution (2.5 ml/min – stoich. 5).

The Figure 3.35 reports the spectra of the MEA-Pt/XC72 recorded in presence of air in the range of potential 0.15 – 0.5 V. The amplitude of the semicircle decreases with the potential and consistently the cathode phase-shift maximum moves towards higher frequencies. Overlapped single semicircles are observed at 0.4 and 0.3 V, whereas another small semicircle appears in the low frequencies region in the spectrum recorded at 0.15 V, Figure 3.35a.

Mass-transport diffusion problems can be identified by the presence of arc in the low frequency region of the impedance spectrum (45; 30; 32) and by the increase of the cell impedance in the module Bode plot as well (58). However, it may be difficult to observe differences between single phenomena (infinite and finite diffusion) in the module Bode plot due to the logarithmic scale. The Figure 3.35b reports the module Bode plot of the MEA-Pt/XC72 spectra. The impedance has an exponential decrease from 100 Ω to 10 Ω with the applied potential, however the curves are not distinguishable below 0.4 V. On the contrary, mass-transport limitations can be observed in the phase-shift Bode plot of Figure 3.35b. Indeed, another phase-shift maximum is observed at 25 mHz in the spectra recorded at 0.15 V. This maximum may be related to the flooding of the cathode.

The flooding of the cathode can be related to catalyst flooding and backing flooding. The former concerns the catalyst layer structure (pore size, C.L. thickness, number of the active sites), the second is related to the hydrophobicity and porosity of the backing layer. In DMFC impedance spectra, the cathode' flooding has been observed as a semicircle in the lowest frequency region (31; 30; 38). Concerning the investigation of the mass-transport limitations for MEA-Pt/XC72, the experimental conditions at which the spectra were recorded (high overpotential and high air flow rate) and the specific cathode' structure (no GDL and high amount of Nafion coating) would suggest the occurrence of flooding.

Concerning this work and the spectra reported in Chapters 5 and 6, the amount of points recorded in the spectra at low overpotentials did not allow the complete observation of the third semicircle. Consequently, the spectra were fitted using the equivalent circuit of Figure 3.23b. However, in some cases the behaviour of the phase angle showed the need to discuss qualitatively the diffusion limitations.

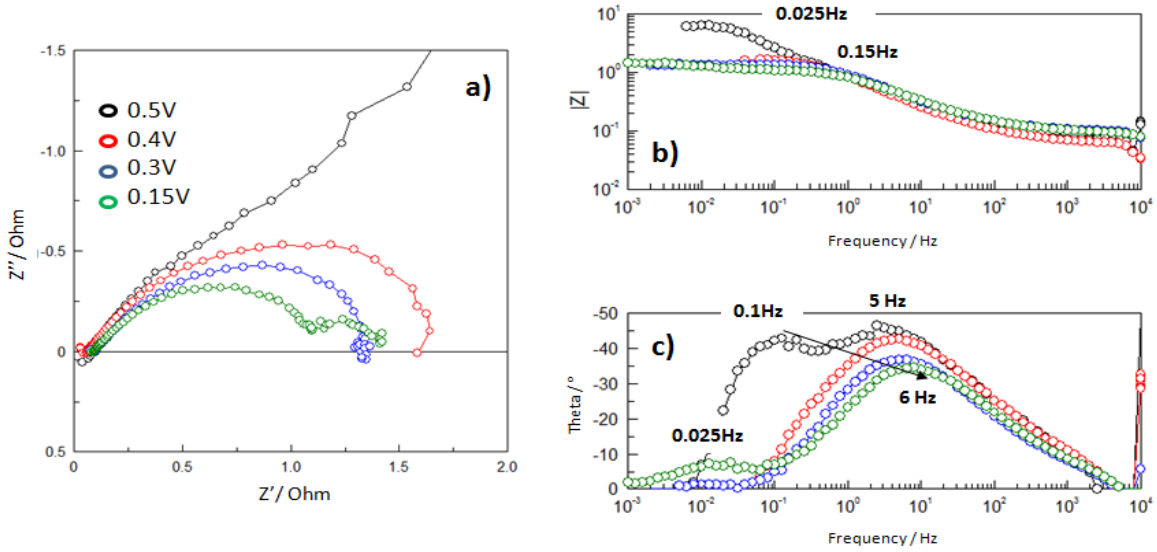

Figure 3.35: a) Nyquist and b-c) Bode plots of MEA-Pt/XC72 for spectra recorded under air (220 ml/min – stoich. 2.4), 1 M MeOH solution (2.5 ml/min – stoich. 5) in the range 0.15 – 0.5 V.

Conclusions

The analysis of the impedance spectra of MEA-N15/T00 and MEA-Pt/XC72 confirmed the validity of our hypothesis that the semicircle appearing in the low frequency region is representative of the cathode behaviour. Indeed the analysis of the Bode plot showed that the cathodic phase-shift maximum responds to the type of reactant (air/oxygen) and to the variation of cell potential, whereas the anodic maximum is unvaried.

This investigation showed as well that the mass-transport limitations occur at high overpotential and maybe be related to the flooding of the cathode catalyst layer.

3.4 References

1. **Macdonald, D.D.** Reflections on the history of electrochemical impedance spectroscopy. *Electrochimica Acta.* 2006, Vol. 51, p. 1376.

2. **E. Barsoukov, J. R. Macdonald.** *Impedance spectroscopy: theory, experiment, and applications, 2nd ed.* s.l. : John Wiley and sons, 2005. p. 2.

3. **Lasia, A.** *Electrochemical Impedance Spectroscopy and its Applications.* Sherbrooke : s.n. p. 156.

4. **C.Y. Du, T.S. Zhao, C. Xu.** Simultaneous oxygen-reduction and methanol-oxidation reactions at the cathode of a DMFC: A model-based electrochemical impedance spectroscopy study. *Journal of power sources.* 2007, Vol. 167, p. 265.

5. **Instruments, Gamry.** Application Notes: Basics of Electrochemical Impedance Spectroscopy. [Online]

6. **Research, Princeton Applied.** Basics of Electrochemical Impedance Spectroscopy. [Online]

7. **T. E. Springer, I. D. Raistrick.** Electrical Impedance of a Pore Wall for the Flooded-Agglomerate Model of Porous Gas-Diffusion Electrodes. *Journal of electrochemical society.* 1989, Vol. 136, 6, p. 1594.

8. **Raistrick, I.D.** Impedance studies of porous electrodes. *Electrochimica Acta.* 1990, Vol. 35, 10, pp. 1579-1586.

9. **M. C. Lefebvre, R. B. Martin, P. G. Pickup.** Characterization of Ionic Conductivity Profiles within Proton Exchange Membrane Fuel Cell Gas Diffusion Electrodes by Impedance Spectroscopy. *Electrochemical and solid-state letters.* 1999, Vol. 2, 6, p. 259.

10. **E. B. Easton, P. G. Pickup.** An electrochemical impedance spectroscopy study of fuel cell electrodes. *Electrochimica Acta.* 2005, Vol. 50, p. 2469.

11. **A.S. Aricò, V. Alderucci, V. Antonucci, S. Ferrara, V. Recupero, N. Giordano, K. Kinoshita.** ac Impedance spectroscopy of porous gas diffusion electrode in sulphuric acid. *Electrochimica Acta.* 1992, Vol. 37, 3, pp. 523-529.

12. **A.S. Aricò, V. Antonucci, V. Alderucci, E. Modica, N. Giordano.** A.c.-impedance spectroscopy study of oxygen reduction at Nation coated gas-diffusion electrodes in sulphuric acid: Teflon loading and methanol cross-over effects. *Journal of Applied Electrochemistry.* 1993, Vol. 23, pp. 1107-1116.

13. **D.B. Zhou, H.V. Poorten.** Electrochemical characterisation of oxygen reduction on teflon-bonded gas diffusion electrodes. *Electrochimica Acta.* 1995, Vol. 40, 12, pp. 1819-1826.

14. **S.L.A. da Silva, E.A. Ticianelli.** Studies of the limiting polarization behavior of gas diffusion electrodes with different platinum distributions and hydrophobic properties. *Journal of electroanalytical chemistry.* 1995, Vol. 391, pp. 101-109.

15. **S.-J. Lee, S.-I. Pyun.** Oxygen reduction kinetics in Nafion-impregnated gas diffsuion electrode under mixed contol using EIS and PCT. *Journal of Electrochemical Society.* 2008, Vol. 155, 12, pp. B1274-B1280.

16. **Lasia, A.** Impedance of Porous Electrodes. *ECS Transactions.* 2008, Vol. 13, 13, pp. 1-18.

17. **Wagner, N.** *Theory and Application of Porous Electrodes in Fuel Cell Characterization.* DLR, Institut für Technische Thermodynamik, Stuttgart. Kloster Banz : s.n., 2009. KronachImpedance Days 2009 "Hermann Göhr".

18. **M. Lefebvre, Z. Qi, D.Rana, P.G. Pickup.** Chemical Synthesis, Characterization, and Electrochemical Studies of Poly(3,4-ethylenedioxythiophene)/Poly(styrene-4-sulfonate) Composites. *Chemical Materials.* 1999, Vol. 11, pp. 262-268.

19. **P. Piela, R. Fields, P. Zelenay.** Electrochemical Impedance Spectroscopy for Direct Methanol Fuel Cell Diagnostics. *Journal of The Electrochemical Society.* 2006, Vol. 153, 10, p. A1902.

20. **R. Makharia, M. F. Mathias, D. R. Baker.** Measurement of catalyst layer electrolyte resistance in PEFCs using electrochemical impedance spectroscopy. *Journal of electrochemical society.* 2005, Vol. 152, p. A970.

21. **M. Ciureanu, R. Roberge.** Electrochemical impedance study of PEM fuel cells. Experimental diagnostics and modeling of air cathodes. *Journal of physical chemistry B.* 2001, Vol. 105, p. 3531.

22. **G. Li, P. G. Pickup.** Ionic conductivity of PEMFC electrodes. Effect of Nafion loading. *Journal of electrochemical society.* 2003, Vol. 150, p. C745.

23. —. Measurement of single electrode potentials and impedances in hydrogen and direct methanol PEM fuel cells. *Electrochimica acta.* 2004, Vol. 49, p. 4119.

24. **M. Eikerling, A. A. Kornyshev.** Electrochemical impedance of the cathode catalyst layer in polymer electrolyte fuel cells. *Journal of electroanalytical chemistry.* 1999, Vol. 475, p. 107.

25. **S.-S. Hsieh, S.-H. Yang, C.-L Feng.** Characterization of the operational parameters of a H2/air micro PEMFC with different flow fields by impedance spectroscopy. *Journal of power sources.* 2006, Vol. 162, p. 262.

26. **J. M. Song, S. Y. Cha, W. M. Lee.** Optimal composition of polymer electrolyte fuel cell electrodes determined by the AC impedance method. *Journal of power sources.* 2001, Vol. 94, p. 78.

27. **J.- M. Le Canut, R. Latham,W. Mérida, D. A. Harrington.** Impedance study of membrane dehydration and compression in proton exchange membrane fuel cells. *Journal of power sources.* 2009, Vol. 192, p. 457.

28. **A. S. Aricò, S. Srinivasan, V. Antonucci.** DMFCs: From Fundamental Aspects to Technology Development. *Fuel cells.* 2001, Vol. 1, 2, p. 133.

29. **C.Y. Du, T.S. Zhao, W.W. Yang.** Effect of methanol crossover on the cathode behavior of a DMFC: A half-cell investigation. *Electrochimica Acta.* 2007, Vol. 52, p. 5266.

30. **J.T. Mueller, P.M. Urban.** Characterization of direct methanol fuel cells by ac impedance spectroscopy. *Journal of Power Sources.* 1998, Vol. 75, p. 139.

31. **T. E. Springer, T. A. Zawodzinski, M. S. Wilson, S. Gottesfeld.** *Characterization of Polymer Electrolyte Fuel Cells Using AC Impedance Spectroscopy.* Electronic and Electrochemical Materials and Devices, Los Alamos National Laboratory. Los Alamos : s.n., 1996.

32. **J. T. Mueller, P. M. Urban, W. F. Hölderich.** Impedance studies on direct methanol fuel cell anodes. *Journal of Power Sources.* 1999, Vol. 84, p. 157.

33. **N.-Y. Hsu, S.-C. Yen, K.-T. Jeng, C.-C. Chien.** Impedance studies and modeling of direct methanol fuel cell anode with interface and porous structure perspectives. *Journal of Power Sources.* 2006, Vol. 161, p. 232.

34. **T. Schulz, C. Weinmüller, M. Nabavi, D. Poulikakos.** Electrochemical impedance spectroscopy analysis of a thin polymer film-based micro-direct methanol fuel cell. *Journal of Power Sources .* 2010, Vol. 195, p. 7548.

35. **V. B. Silva, A. Rouboa.** In situ activation procedures applied to a DMFC: Analysis and optimization study. *Fuel.* 2011, Vol. in press.

36. **X. Zhao, X. Fan, S. Wang, S. Yang, B. Yi, Q. Xi, G. Sun.** Determination of ionic resistance and optimal composition in the anodic catalyst layers of DMFC using AC impedance. *International Journal of Hydrogen Energy .* 2005, 30, p. 1003.

37. **D. Chakraborty, I. Chorkendorff, T. Johannessen.** Electrochemical impedance spectroscopy study of methanol oxidation on naoparticulate PtRu direct methanol fuel cell anodes: kinetics and performance evaluation. *Journal of Power Sources.* 2006, Vol. 162, p. 1010.

38. **H.S. Im, S-K. Kim, S. Lim, D-H. Peck, D. Jung, W.H. Hong.** Study on the Water Flooding in the Cathode of Direct Methanol Fuel Cells. *Journal of Nanoscience and Nanotechnology.* 2011, Vol. 11, p. 5788.

39. **J.-P. Diard, N. Glandut, P. Landaud, B. Le Gorrec, C. Montella.** A method for determining anode and cathode impedances of a direct methanol fuel cell running on a load. *Electrochimica Acta.* 2003, Vol. 48, p. 555.

40. **K.i Furukawa, K.i Okajima, M. Sudoh.** Structural control and impedance analysis of cathode for direct methanol fuel cell. *Journal of Power Sources.* 2005, Vol. 139, p. 9.

41. **S.-H. Yang, C.-Y. Chen, W.-J. Wang.** An impedance study for the anode micro-porous layer in an operating direct methanol fuel cell. *Journal of Power Scources.* 2010, Vol. 195, p. 3536.

42. **Oedegaard, A.** Characterization of direct methanol fuel cells under near-ambient conditions. *Journal of Power Sources.* 2006, Vol. 157, p. 244.

43. **C. Christenn, G. Steinhilber, M. Schulze, K. A. Friedrich.** Physical and electrochemical characterization of catalysts for oxygen reduction in fuel cells. *Journal of Applied Electrochemistry.* 2007, Vol. 37, p. 1463.

44. **C.-M. Lai, J.-C. Lin, K.-L. Hsueh, C.-P. Hwang, K.-C. Tsay, L.-D. Tsai,Y.-M. Peng.** On the electrochemical impedance spectroscopy of direct methanol fuel cell. *International Journal of Hydrogen Energy.* 2007, Vol. 32, p. 4381.

45. **S. Mohan, S.O. B. Shrestha.** Experimental Investigation of a Passive Direct Methanol Fuel Cell. *The Open Fuels & Energy Science Journal.* 2009, Vol. 2, p. 124.

46. **V. Baglio, A. Stassi, F.V. Matera, H. Kim, V. Antonucci, A.S. Aricò.** AC-Impedance Investigation of Different MEA Configurations for Passive-Mode DMFC Mini-Stack Applications. *Fuel Cells.* 2010, Vol. 10, p. 124.

47. **S. Siracusano, A. Stassi, V. Baglio, A.S. Aricò, F. Capitanio, A.C. Tavares.** Investigation of carbon-supported Pt and PtCo catalysts for oxygen reduction in direct methanol fuel cells. *Electrochimica Acta.* 2009, Vol. 54, p. 4844.

48. **B. Andreaus, A.J. McEvoy, G.G. Scherer.** Analysis of performance losses in polymer electrolyte fuel cells at high current densities by impedance spectroscopy. *Electrochimica Acta.* 2002, Vol. 47, p. 2223.

49. **B. Andreaus, G. G. Scherer.** Proton-conducting polymer membranes in fuel cells – humidification aspects. *Solid State Ionics.* 2004, Vol. 168, p. 311.

50. **C. A. Schiller, F. Richter, E. Gülzow, and N. Wagner.** Relaxation impedance as a model for the deactivation mechanism of fuel cells due to carbon monoxide poisoning. *Physical Chemistry Chemical Physics.* 2001, Vol. 3, p. 2113.

51. **C. A. Schiller, F. Richter, E Gülzow, and N. Wagner.** Validation and evaluation of electrochemical impedance spectra of systems with states that change with time. *Physical Chemistry Chemical Physics.* 2001, Vol. 3, p. 374.

52. **N. Wagner, M. Schulze.** Change of electrochemical impedance spectra during CO poisoning of the Pt and Pt-Ru anodes in a membrane fuel cell (PEFC). *Electrochimica Acta.* 2003, Vol. 48, p. 3899.

53. **N. Wagner, E. Gülzow.** Change of electrochemical impedance spectra (EIS) with time during CO-poisoning of the Pt-anode in membrane fuel cells. *Journal of Power Sources.* 2004, Vol. 127, p. 341.

54. **M. Ciureanu, H. Wang, Z. Qi.** Electrochemical Impedance Study of Membranes – Electrode Assemblies in PEM Fuel Cells. II. Electrooxidation of H2 and H2/CO Mixtures on Pt/Ru Based Gas Diffusion Electrodes. *Journal of Physical Chemistry B.* Vol. 103, p. 9645.

55. **M. Ciureanu, H. Wang.** Electrochemical impedance study of anode CO –poisoning in PEM fuel cells. *Journal of New Materials for Electrochemical Systems.* 2000, Vol. 3, p. 107.

56. **M. Ciureanu, S. D. Mikhailenko, S. Kaliaguine.** PEM fuel cells as membrane reactors: kinetic analysis by impedance spectroscopy. *Catalysis Today.* 2003, Vol. 82, p. 195.

57. **Latham, R. A.** *Algorithm Development for Electrochemical Impedance Spectroscopy Diagnostics in PEM Fuel Cells.* Mechanical Engineering, BSME, Lake Superior State University. 2001. M.Sc.

58. **E. Barsoukov, J.R. Macdonald.** *Impedance Spectroscopy - Theory, Experiments and Applications.* 2nd. s.l. : John Wiley & sons, 2005. p. 520.

CHAPTER 4 : SIMULTANEOUS DEPOSITION OF NAFION AND PTFE BINDERS IN Pt-BASED CATHODES

4.1. Summary

In this chapter, the physicochemical properties, the electrochemical and fuel cell performance of a series of new DMFCs cathodes with different Nafion/PTFE content in the catalyst layer are investigated. As explained in Chapter 1, we explored the partial substitution of Nafion by PTFE and the simultaneous deposition of the two binders with the Pt catalyst as a strategy to improve the water removal, and to guarantee the continuous supply of oxygen to the catalyst sites during the DMFC operation, without reducing, or minimizing the losses on the proton conductivity and extent of the triple-phase boundary in the catalyst layer. Five Nafion-PTFE based cathodes, N 15 / T 00, N 10 / T 05, N 05 / T 10, N 00 / T 15, N 10 / T 05-P were prepared following the procedure reported in Chapter 2. As a reminder, the cathode' composition is reported in Table 5.1.

Table 4.1 : Composition of the Nafion-PTFE based cathodes.

	Cathode	**% wt Nafion**	**% wt PTFE**
Series I	***N 15 / T 00***	15	0
	N 10 / T 05	10	5
	N 05 / T 10	5	10
	N 00 / T 15	0	15
Series II	***N 10 / T 05-P***	10	5

In the first part of the presented work, the cathodes underwent to physicochemical characterization. The quantification of the wetting properties of the cathode is important to anticipate the electrodes' tendency to flood. As explained in Chapter 2, an attempt to evaluate the wetting properties was done by water vapor and liquid water absorption, and sessile-drop contact angle measurements. The water vapor and liquid water absorption techniques were chosen to explore the effect of the Nafion/PTFE content on the hydrophilic character of the cathode porous structure. Hexane absorption measurements were attempted on the series I of Nafion/PTFE

cathodes; however no relevant uptake was observed. The water contact angle was used to investigate the effect of the Nafion/PTFE content on the wettability of the cathode surface.

The total micro, meso and a small part of the macro-pore volume of the cathodes (up to 200 nm) was measured by nitrogen adsorption technique. As explained in Chapter 2, we did not find any facility for the mercury porosimetry measurements but they will be required to quantify the macro-porosity of the samples (1; 2; 3; 4).

The second part of the work reports the electrochemical characterisation of the new cathodes. The cathode catalyst layers were characterized by cyclic voltammetry, chronoamperometry and impedance spectroscopy in nitrogen and oxygen saturated 0.5 moldm^{-3} sulphuric acid solution. These conditions were chosen in order to simulate the severe flooding of the cathode in the fuel cell, and to verify if this type of characterization can be used for the pre-screening of cathodes before assembling and testing them in a DMFC.

The DMFC tests of the new cathodes are presented and discussed in the third part of this chapter.

For the most promising cathode of the Nafion/PTFE series, the effect of Pt distribution was investigated. A cathode with the same chemical composition but with a different Pt distribution profile (more concentrated on the electrode's surface) was prepared and characterized. The results of the physicochemical characterization and the DMFC performance are reported in the fourth part of this chapter.

4.2. Nafion/PTFE-based cathodes

4.2.1. Physicochemical characterization

A. Thickness

The cathodes' thickness was measured by scanning electron microscopy (SEM) (Chapter 2). Figure 4.1 shows the images of cathodes' surfaces and cross-sections.

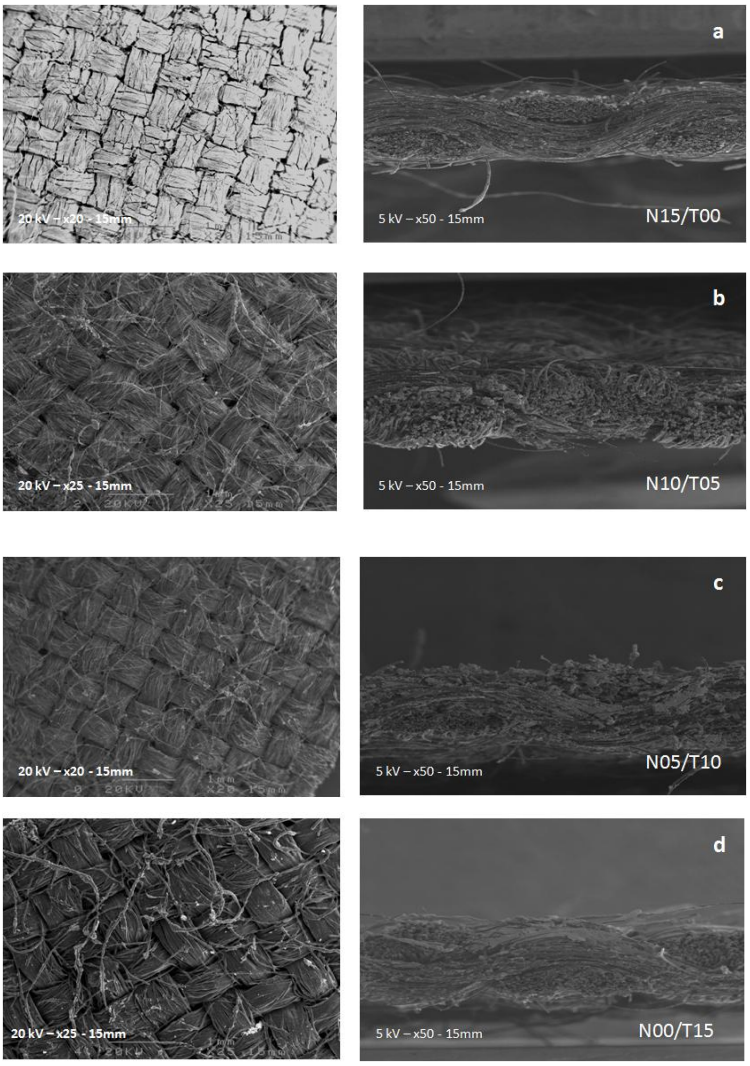

Figure 4.1 : Images of surface and cross-section of the Nafion-PTFE based cathodes.

All the PTFE-based cathodes present a non uniform distribution of the catalyst layers over the fibers, whereas for N 15 / T 00 cathode the deposit appears more dense. Concerning the cross-sections, no specific differences were observed between coatings. Because of the high porosity of the carbon cloth, the deposition occurred at both sides of the support even if the catalyst ink was sprayed only on one side of the electrode. The Figure 4.2 reports the thickness for the Nafion-PTFE based cathodes. Data for the carbon cloth are included as reference. The thickness of the cathodes varies between 425 ± 53 μm and 465 ± 32 μm. It is observed that the Nafion-based cathodes are slightly thicker than the N 00 / T 15 cathode. As explained in Chapter 2, the cartography of the surface area and cross-section was reproduced and no significant differences on the Pt and F distributions were observed between samples. The quantification of Pt and S was

attempted by EDS and RBS techniques but it was not possible because of the irresolution of the peaks.

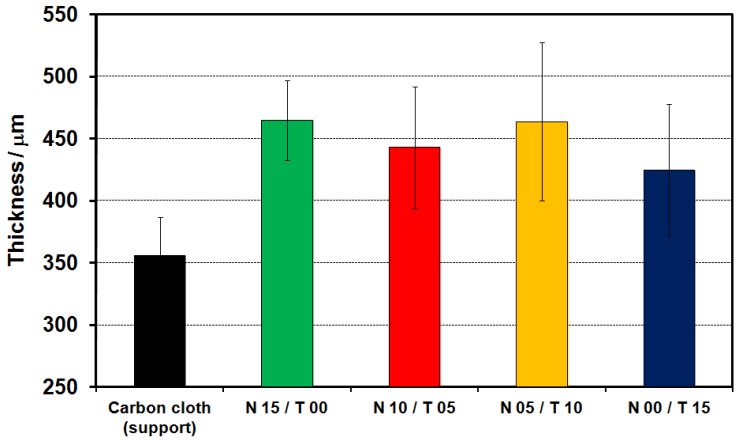

Figure 4.2 : Thickness of the N 00/ T 15 based-cathodes.

B. Water uptake

The cathodes' water vapor absorption was determined by Dynamic Vapor Sorption technique (Chapter 2) while the liquid water absorption was measured by immersion of the sample in water. Figure 4.3 reports the water uptake for the Nafion-PTFE based cathodes. Data for the carbon cloth are included as reference. The water uptake from the vapor phase is reported in the upper part of Figure 4.3, whereas the water uptake from the liquid phase is reported in the lower part of Figure 4.3. As expected, the water uptake from the liquid phase is higher than the water uptake from the vapor. And, in both cases the water uptake decrease by half and almost linearly with the PTFE content. For the water vapor uptake, the most hydrophilic cathode, N 15 / T 00, shows an absorption of 1.60 ± 0.34 wt% and the most hydrophobic cathode, N 00 / T 15, an uptake of 0.78 ± 0.31 wt%. With respect to N 15 / T 00, the cathodes with intermediates composition show a decrease in the water absorption capacity of 35 % for N 10 / T 05 and 60 % for N 05 / T 10. For the liquid water uptake, the most hydrophilic cathode, N 15 / T 00, shows an absorption of 32.46 ± 1.86 wt% and the most hydrophobic cathode, N 00 / T 15, an uptake of 16.53 ± 1.46 wt%. With respect to N 15 / T 00, the cathodes with intermediate composition show a loss of water absorption capacity of about 24 % for N 10 / T 05 and 37 % for N 05 / T 10.

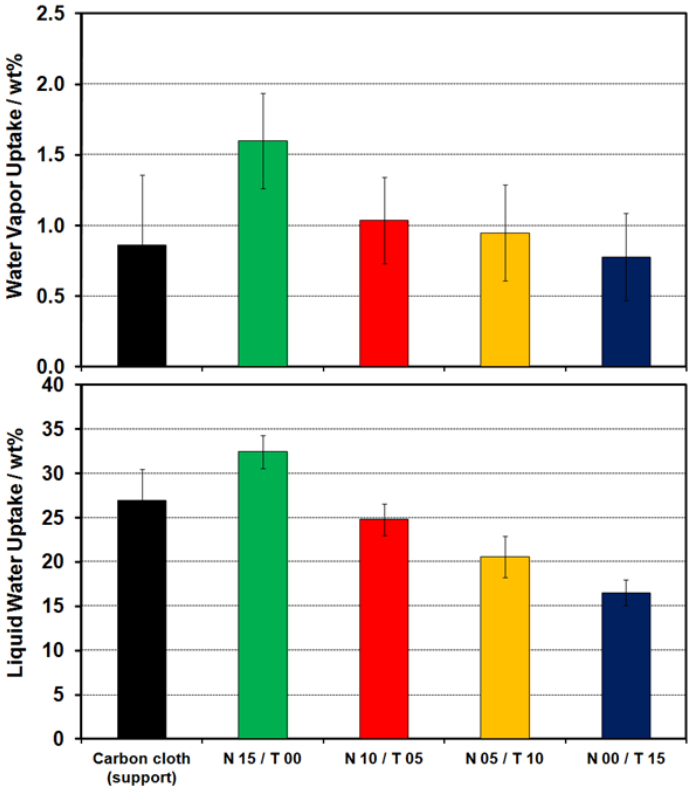

Figure 4.3 : Water uptake of the Nafion-PTFE based cathodes.

C. Sessile-drop contact angle

The wetting of the cathode catalyst layer surface was evaluated by the sessile-drop contact angle measurements (Chapter 2). Figure 4.4 reports the advancing and receding contact angles (ACA – RCA) for the Nafion-PTFE based cathodes. The results show that independently of the type and the amount of binder, the contact angle values are above 90 degree and the cathodes show low wettability. Higher values are observed for the Nafion-based cathodes (ACA: 146.91° ± 1.03° to 143.84° ± 1.47°). Despite the different Nafion content, the contact angles are identical to those measured on the carbon cloth support (ACA: 144.78° ± 1.37°). A lower contact angle is measured for the N 00 / T 15 cathode (ACA: 131.67° ± 1.30°) with a marked hysteresis between its advancing and receding values (29°), indicating that the surface is more rough than for the Nafion-based cathodes.

The results show that the wettability of the cathode surface is not determined by the binder content and type (Nafion vs. PTFE) but by their morphology of the surface. Indeed, as it was reported for porous supports (gas diffusion layers), that the measurements of sessile-drop contact

angles are influenced by the porosity and surface roughness (5). The morphology of the N 00 / T 15 cathode is distinct of the other electrodes. From the lower contact angle it may be supposed that water penetrates through some large pores. Similar hypothesis was made for an hydrophobic catalyst layer deposited on a polymer membrane (6).

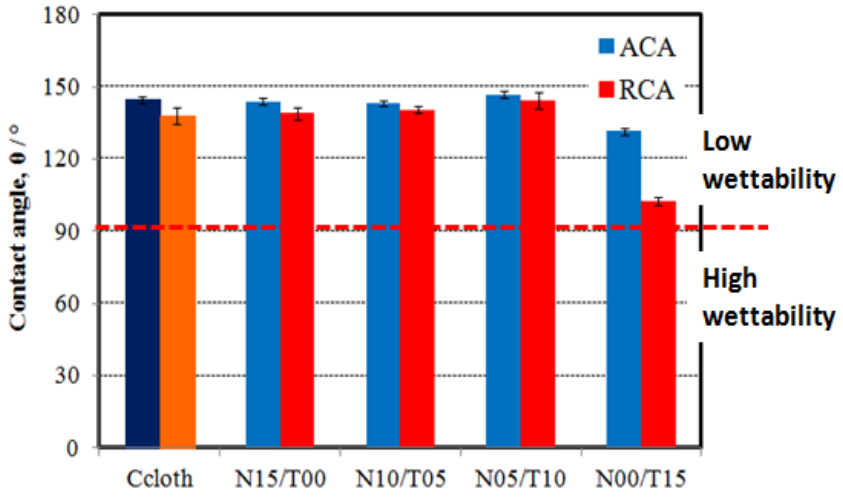

Figure 4.4 : Contact angles of the N 00/ T 15 based-cathodes.

D. Total micro- and meso-pore volume

The cathodes' total pore volume was determined from the nitrogen sorption isotherms (Chapter 2). The measured total pore volume includes the micro- and meso-pores, and a small portion (2 %) of the macro-pores (up to 200 nm). The Figure 4.5 reports the total pore volume for the Nafion-PTFE based cathodes. Carbon cloth has a low pore volume and it contributes 2/3 of the total electrodes' weight; therefore the pore volume of the catalyst layer alone should be higher than the values presented in Figure 5.5. The variation of the total pore volume with the PTFE content has a V-shape, being N 15 / T 00 the cathode with the highest total pore volume (0.109 cm^3g^{-1}) and N 10 / T 05 the cathode with lowest total pore volume (0.061 cm^3g^{-1}). The increase of the total pore volume from N 05 / T 10 to N 00 / T 15 is consistent with the contact angle measurements which anticipated a different morphology for the N 00 / T 15 cathode. Indeed, as it was reported for Nafion/PTFE–based gas diffusion electrodes, the ionomer content influences the pore size distribution in the catalyst layer and a lower fraction of micro-pores was reported for the PTFE-based cathode (7). A higher fraction of micro-pores increases the diffusive constrains

of the oxygen molecules since nitrogen is entrapped in these pores. Accordingly, the authors observed smaller diffusion constrains in the PTFE-base cathode (7).

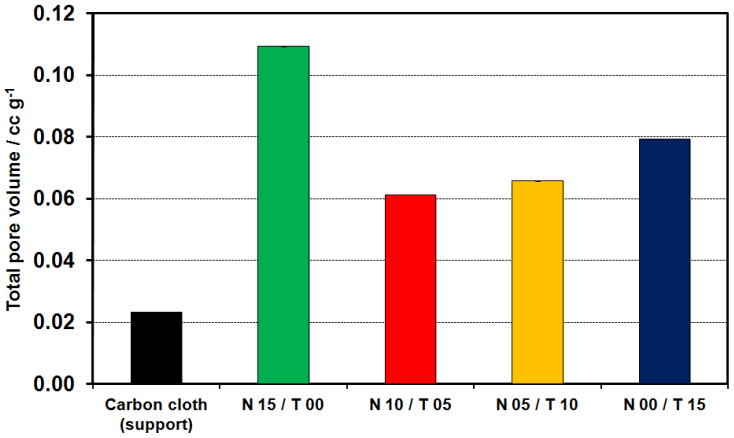

Figure 4.5 : Total pore volume of the Nafion-PTFE based cathodes.

The physicochemical characterization of the Nafion-PTFE based cathodes has showed that the systematic substitution of Nafion by PTFE in the catalyst layer affects the hydrophilicity, the morphology and the total pore volume of the cathode catalyst layers, and these parameters have to be considered in the analysis of the electrochemical and DMFC data.

4.2.2. Ex-situ electrochemical characterization

The Nafion-PTFE based cathodes were electrochemically characterized in nitrogen and oxygen saturated 0.5 moldm^{-3} sulphuric acid solutions to determine: the platinum utilization and the electrochemical surface area, the double layer capacitance, the resistance to the ionic transport through the catalyst layer, the limiting current for the oxygen reduction reaction.

A. Pt utilization and Electrochemical Surface Area

The Figure 4.6 shows the cyclic voltammogram of the N 00 / T 15 cathode. As expected, the typical shape of a polycrystalline platinum electrode was recorded: the hydrogen adsorption and desorption peaks are clearly identified in the potential interval between -0.28 V and 0 V, the oxidation peaks of platinum between 0.6 – 0.9 V, and the platinum oxide reduction peaks between 0.2 – 0.7 V.

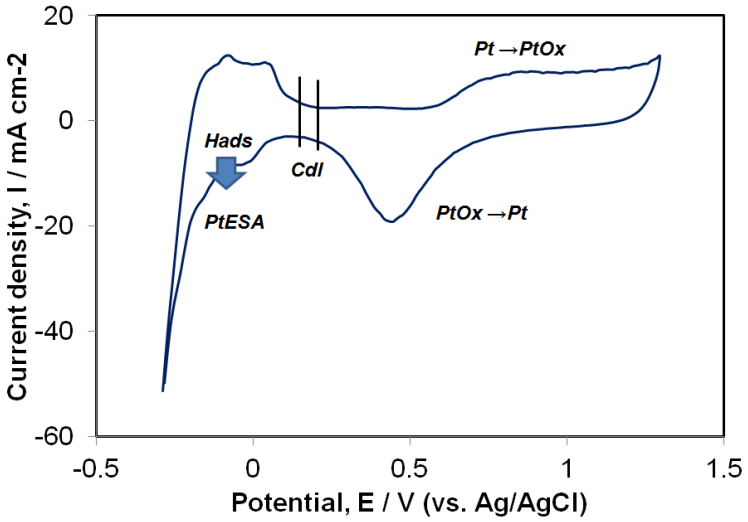

Figure 4.6 : Cyclic voltammogram (10th cycle) in N_2 sat. 0.5 moldm^{-3} H_2SO_4, recorded at 20 mV s^{-1} .

The Pt electrochemical surface areas were calculated from the charge of the hydrogen adsorption peaks developed during the cathodic sweep after correction of the double layer charging base line and using 210 μCcm^{-2} as the charge for the adsorption of a hydrogen monolayer on microcrystalline platinum. The *ESA* (m^{2}g^{-1}) values were used to determine the Pt utilization, as:

$$Pt\ utilization = \frac{ESA\ \times\ \rho\ \times d}{6\ \times 10000} \times 100 \qquad \textbf{\textit{Equation}}\ \mathbf{5.1}$$

where ρ is the density of the Pt bulk (21.4 gcm^{-3}) and *d* the diameter of the Pt particles (36 Å, according to the supplier). The average *ESA* and Pt utilization values determined for the cathodes are reported in Figure 4.7. It was found that the ESA varied between 14.60 ± 2.80 and 20.00 ± 0.80 m^{2}g^{-1} and the Pt utilization varied between 18.50 ± 3.50 and 25.50 ± 0.70 %. Similar values are observed for the PTFE-based cathodes, whereas slightly higher values are observed for the N 00 / T 15 cathode.

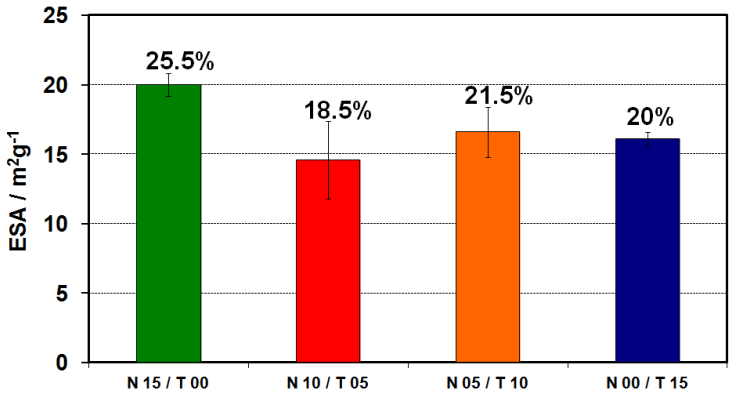

Figure 4.7 : ESA and Pt utilization estimated for the Nafion-PTFE based cathodes**.**

The Figure 4.8 reports the ESA and Pt utilization as a function of the liquid water uptake and the variation of the ESA with the BET total pore volume. The ESA and Pt utilization increase with the hydrophilicity of the cathodes, as expected from higher water uptake and total pore volume. These values are lower than those usually reported for Pt based cathodes measured in fuel cell (8; 9) and likely due to the relatively high Pt loading (3 $mgcm^{-2}$) (10; 11).

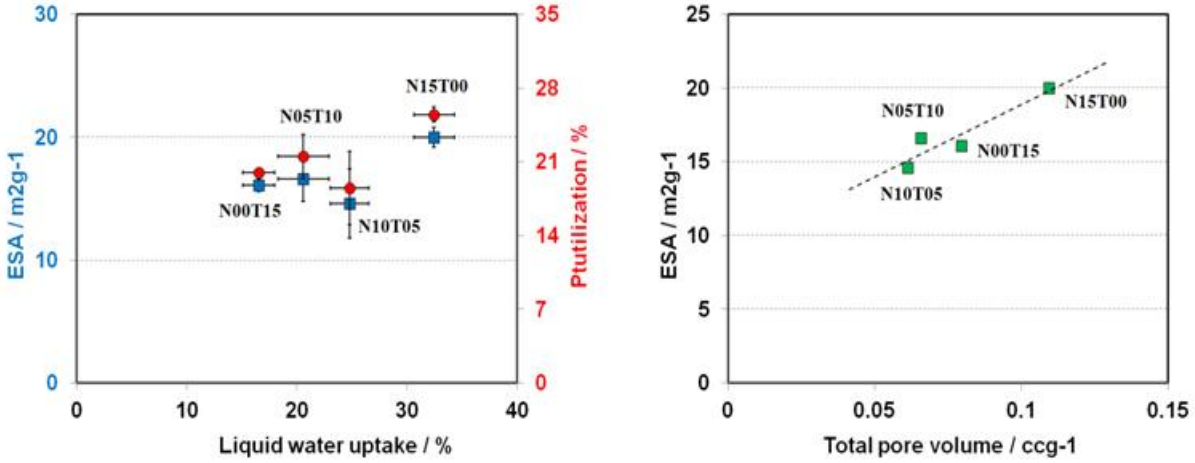

Figure 4.8 : ESA and Pt utilization vs. liquid water uptake; ESA vs. BET total pore volume.

B. Double-Layer Capacitance and Ionic Resistance

Under our experimental conditions, the extent of the double layer formed between the cathode and the electrolyte solution, and the resistance for the proton transport through the catalyst layer depend on the wettability and porosity of the cathodes. The influence of the PTFE content on the double-layer capacitance and the ionic resistance was investigated by electrochemical impedance

spectroscopy (EIS) (12). The Figure 4.9 shows the impedance spectra (Nyquist and Bode plots) of the Nafion-PTFE based cathodes recorded at 0.2 V. The lower part of Figure 4.9 shows a zoom of the high frequency region for the N 00 /T 15 cathode. The spectra show at high frequency the characteristic Warburg impedance for the ion transport through a porous electrode structure, whereas at low frequencies the spectra are dominated by the capacitive element.

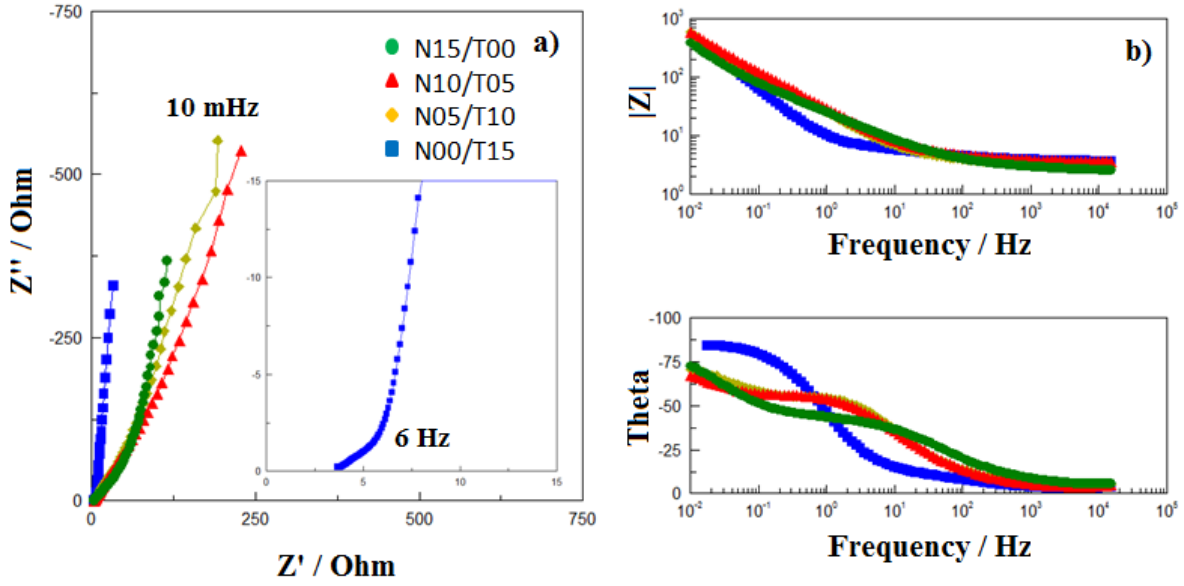

Figure 4.9 : Electrochemical impedance spectra recorded at 0.2 V (vs. Ag/AgCl), a) Nyquist b) Bode plots.

The Figure 4.10 reports the variation of the *Cdl* and the *Rionic* as a function of the PTFE content. The capacitance varies between 69.50 ± 8.20 and 104.00 ± 5.70 $mFcm^{-2}$; as expected, the capacitance follows the variation of the water up-take and is higher for the N 15 / T 00 cathode. On the other hand, the resistance for the proton transport in the cathode catalyst layer varies between 5.10 ± 0.10 and 58.90 ± 11.60 Ωcm^2; it was found to decrease with the increase of the PTFE content, and the N 00 / T 15 cathode shows an ionic resistance ten times smaller than the N 15 / T 00 cathode. This result is somewhat surprising since the N 00 / T 15 cathode absorbs less water than N 15 / T 00. The formation of a thin diffuse layer of electrolyte on the surface of the N 00 / T 15 cathode (vs. a porous structure completely filled by the electrolyte as in the N 15 / T 00 and N 10 / T 05 cathodes) is likely to account for the lower resistance for the proton transport and an impedance spectrum dominated by the capacitive element.

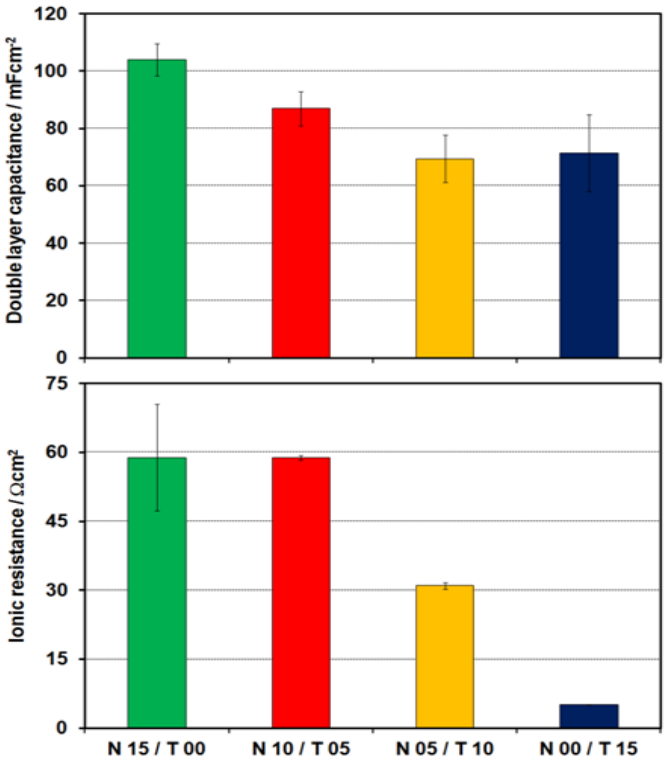

Figure 4.10 : Double layer capacitance and ionic resistance for the Nafion-PTFE based cathodes.

C. Oxygen Reduction Reaction

The activity of the cathodes towards the ORR was investigated by the meaning of linear sweep voltammetry, chronoamperometry and impedance spectroscopy. The Figure 4.11 shows the linear voltammograms of the Nafion-PTFE based cathodes in the range of potential 1 – 0 V. From these curves the onset potential (E_{ORR}) and the limiting-current (I_L) values were determined. The polarization curves of the four cathodes show the expected benefit from the presence of a hydrophilic binder on the overpotential for the ORR. Indeed, the half-wave potential is more positive for Nafion-based cathodes (in the range 0.64 – 0.67 V) with respect to the N 00 / T 15 cathode (0.54 V). However, oxygen mass-transport problems affect readily the performance of the Nafion-based cathodes and the limiting currents appear immediately (4 $mAcm^{-2}$ for N 15 / T 00 - 8 $mAcm^{-2}$ for N 10 / T 05 - 16 $mAcm^{-2}$ for N 05 / T 10). On the contrary, the polarization curve of the N 00 / T 15 cathode is characterized by the highest limiting-current clearly demonstrating the benefit of using PTFE in the cathode catalyst layer (38 $mAcm^{-2}$ for N 00 / T 15).

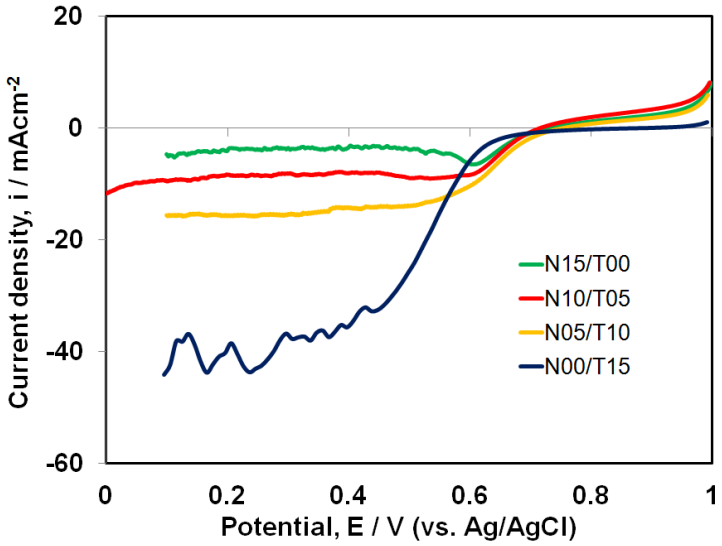

Figure 4.11 : Linear sweep voltammetry in O_2 sat. 0.5 mol dm^{-3} H_2SO_4, recorded at 5 mV s^{-1}.

The variation of the half-wave potential as a function of the liquid water uptake, and the variation of the current density at 0.2 V as a function of the ionic resistance of the cathodes are reported in Figure 4.12. As expected, the half-wave potential increases with the liquid water uptake; a drastic increase is observed from N 00 / T 15 to N 05 / T 10 (0.54 V to 0.64 V), whereas for further augments of the hydrophilic component in the cathode catalyst layer, the $E_{1/2}$ increases smoothly (0.66 V, 0.67 V). A linear relationship between the current density measured at 0.2 V and the ionic resistance can be established for the cathodes, and the larger current density is observed for the N 00 / T 15.

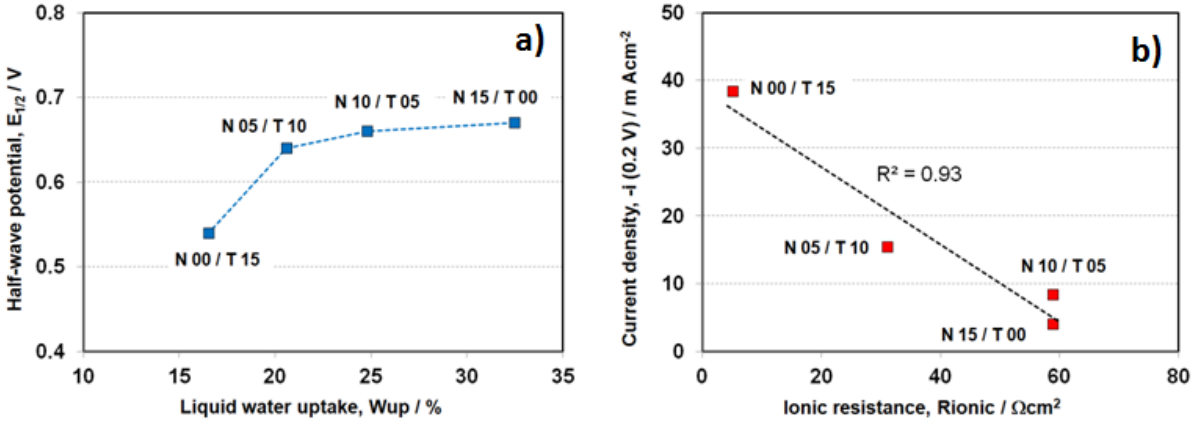

Figure 4.12 : a) Half-wave potential vs. liquid water uptake, b) current density at 0.2 V vs. ionic resistance.

A more detailed investigation on the performance of the cathodes towards the ORR was done by chronoamperometry. A similar approach was used by Kamat and co-workers to understand the mass-transport process in flooded and dried cathodes for polybenzamidazole / phosphoric acid based high temperature PEMFCs (13), and by Zhou and co-workers to investigate the electrochemical characteristics of PTFE-bonded gas diffusion electrodes with different wettability (14). The Figure 4.13 shows the evolution of the transient current recorded for the N 15 / T 00 and N 00 / T 15 cathodes at 0.7 V (activation control), 0.62 V (mixed control) and 0.4 V (mass transport control). All chronoamperograms show an initial peak due to the charging of the double-layer, followed by a current decay before reaching a steady-state current plateau. The chronoamperograms are analysed in terms of capacitive current (*icap*) and steady-state current (*iss*).

At 0.7 V the highest values of capacitive and steady-state currents were measured for the N 15 / T 00 cathode, Figure 4.13a, in accordance to the higher wettability and activity of this cathode towards the ORR with respect to the other cathodes. However, the *iss* and *icap* decrease when the applied potential is more negative than 0.7 V. In fact, at 0.4 V a very small value of *icap* and *iss* was measured for the N 15 / T 00 cathode indicating that the cathode is flooded, Figure 4.13c. On the contrary, the cathode N 00 / T 15 shows an increase of the *icap* and *iss* currents with the overpotential indicating the existence of a high number of available reactive sites, that the ORR is not controlled by the O_2 diffusion and is less affected by the flooding phenomena. Indeed, for the N 00 / T 15 cathode the limiting current density increased by a factor of 25 when the applied potential varied from 0.7 to 0.4 V. In addition, at 0.62 V the N 00 / T 15 cathode shows a slight increase of the transient current before the steady-state, Figure 4.13b. This behaviour, typical of hydrophobic cathodes, was encountered also for semi-hydrophobic electrodes (14) and dried cathodes based on polybenzamidazole / phosphoric acid for high temperature PEMFC (13). The increase of the transient current can be explained by the formation of a thin film of the electrolyte in the porous structure of cathode which extends the three-phase boundary reaction zones.

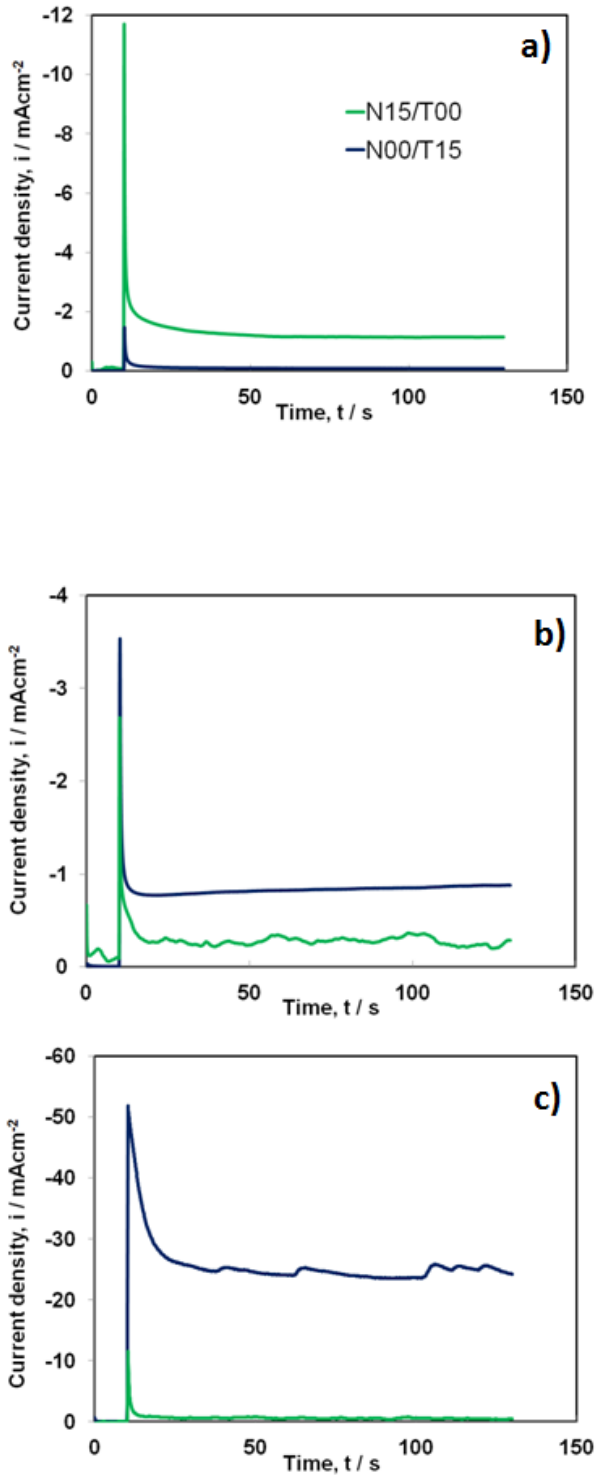

Figure 4.13 : Transient current at a) 0.7 V, b) 0.62 V, c) 0.4 V.

The variation of *icap* measured at 0.4 V as a function of the electrodes' water uptake, and the variation of *iss* as a function of the applied potential for all cathodes are reported in Figure 4.14. Figure 5.14a shows that the N 15 / T 00 cathode has the smallest *icap* value among all cathodes and confirms that at 0.4 V this cathode is flooded. In contrast, the PTFE-based cathodes show an increase of the capacitive current with the water uptake as expected for non flooded cathodes. Among the PTFE-based cathodes, the N 10 / T 05 shows the highest *icap* value. Moreover, this cathode shows the highest *iss* values among all Nafion-based cathodes, Figure 4.14b. It can be concluded, that the proper balance between the 10 wt% of the hydrophilic Nafion and the 5 wt% of the hydrophobic PTFE guarantees the right support of both protons and oxygen necessary for the ORR.

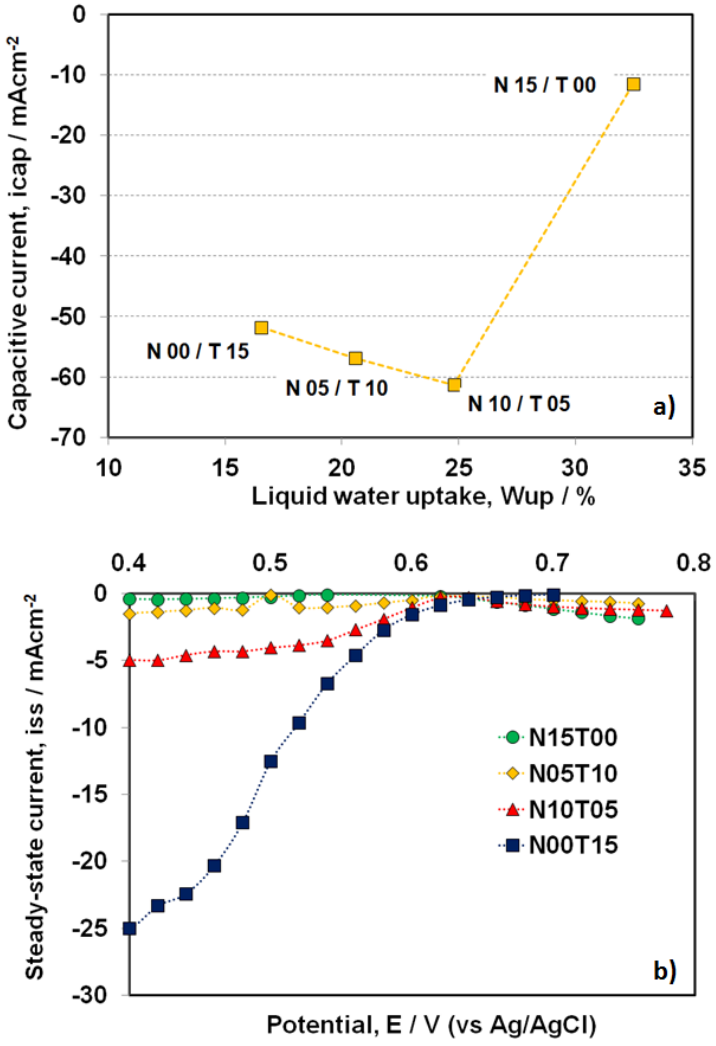

Figure 4.14 : a) Capacitive current vs. liquid water uptake, b) steady-state current vs. potential at 0.4 V.

The performance of the cathodes towards the ORR was also investigated by impedance spectroscopy. The EIS spectra of the Nafion-PTFE based cathodes, recorded at 0.65 V (activation zone of the polarization curve), are presented in Figures 4.15. For these spectra it was observed that the serial resistance slightly increase with the hydrophilicity of the cathodes, from 1.12 Ωcm^2 for N 00 / T 15 to 1.85 Ωcm^2 for N 15 / T 00. The spectra presented in the Nyquist plot show different shape. The N 15 / T 00 and N 05 / T 10 cathodes show uncompleted semicircles which extend until very low frequencies; in contrast, the N 10 / T 05 and N 00 / T 15 cathodes show complete semicircles and defined smaller charge-transfer resistances. Since the fitting of uncompleted semicircles introduces a wide error on the determined parameters, only the spectra of the N 10 / T 05 and N 00 / T 15 cathodes were fitted (Chapter 3). The values of the kinetic parameters for the two cathodes are reported below in Table 4.2. The analysis of results shows that the N 10 / T 05 cathode is characterized by the lowest charge-transfer resistance (36.86 ± 0.47 Ωcm^2) and highest capacitance (48.74 ± 0.40 $mFcm^{-2}$). This result is consistent with the chronoamperometric study and confirms that this cathode has the proper combination of Nafion and PTFE in the catalyst layer.

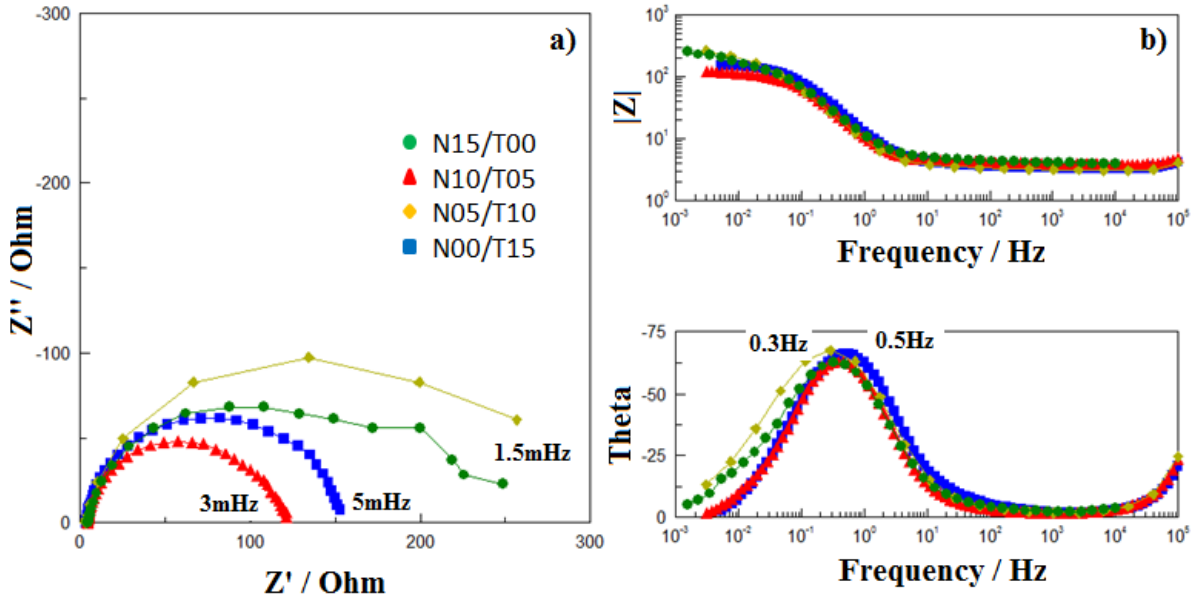

Figure 4.15 : Impedance spectra in O_2 sat. 0.5 mol dm^{-3} H_2SO_4 at 0.65 V, a) Nyquist and b) Bode plots.

Table 4.2 : EIS parameter for N 10 / T 05 and N 00 / T 15 cathodes in 0.5 moldm^{-3} H_2SO_4 at 0.65 V.

Cathode	$R_{CT\text{-}ORR}$ / Ωcm^2	C_{dl} / mFcm^{-2}
N10/T05	36.86 ± 0.47	48.74 ± 0.40
N00/T15	49.44 ± 0.56	35.06 ± 0.38

4.2.3. DMFC characterization

The DMFC performance of MEAs containing the Nafion-PTFE based cathodes was investigated to verify if the Nafion 10 wt% / PTFE 5wt% cathode is the most suitable for DMFC operation at low temperature (up to 50 °C) and if the electrochemical characterization of DMFC cathodes imbibed in H_2SO_4 solution might be a simple and efficient tool to test ex-situ the flooding phenomena.

A. Conditioning

Before performing the two cycles of polarizations curves between 25 and 80 °C, the fuel cells were conditioned with 1 moldm^{-3} methanol solution (2.5 mlmin^{-1}) and air (220 mlmin^{-1},100% RH). The open circuit voltage was monitored over time and the recorded data are reported in Figure 4.16. The DMFC equipped with the MEA - N 15 / T 00 shows a distinct behaviour with respect to the other DMFCs: the OCV increases sharply and in 10 minutes reaches 60% of its final value; then, the potential continues to increase smoothly and it stabilizes in 3 h at 0.405 V. For the DMFCs equipped with the PTFE-base cathodes the variation is less abrupt but higher OCVs (between 0.48 and 0.52 V) are reached within a shorter period of time (1 h). The higher equilibrium time required for MEA – N 15 / T 00 can be related to the higher pore volume and hydrophilicity of the N 15 / T 00 cathode with respect to the other three PTFE-based cathodes. However, the higher OCVs found for the MEAs with the PTFE-based cathodes suggest a more efficient supply of oxygen to the cathodes' catalysts sites and confirm the positive effect of the hydrophobic binder also in contrasting the methanol cross-over (15).

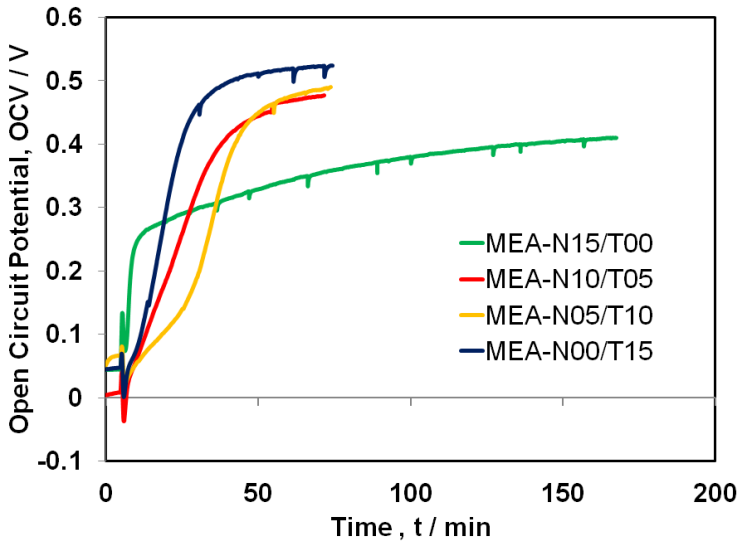

Figure 4.16 : Open circuit voltage over time for DMFCs in presence of air (220 ccmin^{-1}, atmospheric pressure) and 1 moldm^{-3} MeOH solution at 25 °C.

B. Polarization curves under air

As explained in Chapter 2, the MEAs were activated through two temperature cycles of polarization curves. During the first temperature cycle, the MEA – N 00 / T 15 performed better (higher OCV and current density) than the other MEAs up to 60 °C. But, for 70 and 80 °C the performance of all MEAs equipped with the Nafion-based cathodes improved as the result of the better hydration of the catalyst layers (data not shown). As expected, the performance of the DMFCs improved from the first to the second cycle (2).

The Figure 4.17 shows the polarization curves recorded at 25 °C, 40 °C and 80 °C during the second temperature cycle. The polarization curves show the characteristic activation zone at low overpotential (between OCV and 0.45 V), the ohmic region at higher overpotential (from 0.45 V until 0.1 V) but no limiting current due to mass transport control. As expected, the performance of all MEAs improves with the increasing of the operating temperature. At 25 °C, Figure 4.17a, the MEAs show similar OCV (0.53 – 0.55 V) and perform almost equally with slightly higher catalyst utilization (activation zone (2; 16)) for the MEA – N 15 / T 00. At 40 °C, Figure 4.17b, all MEAs with Nafion-based cathodes have higher OCV and perform better than the MEA – N 00 / T 15 (0.57 – 0.58 V vs. 0.54 V), and the catalyst utilization increases with the hydrophilicity and pore volume of the cathode catalyst layers and as in the half-cell characterization in 0.5 moldm^{-3} H_2SO_4 solution. At 60 and 80 °C, Figure 4.17c, the OCV (0.63 V) and performance of the MEA

– N 15 / T 00 is definitely higher and the MEA – N 00 / T 15 (0.54 V) is remarkably lower due to the poor hydration of the catalyst layer which aggravates with the temperature due to the natural evaporation of water.

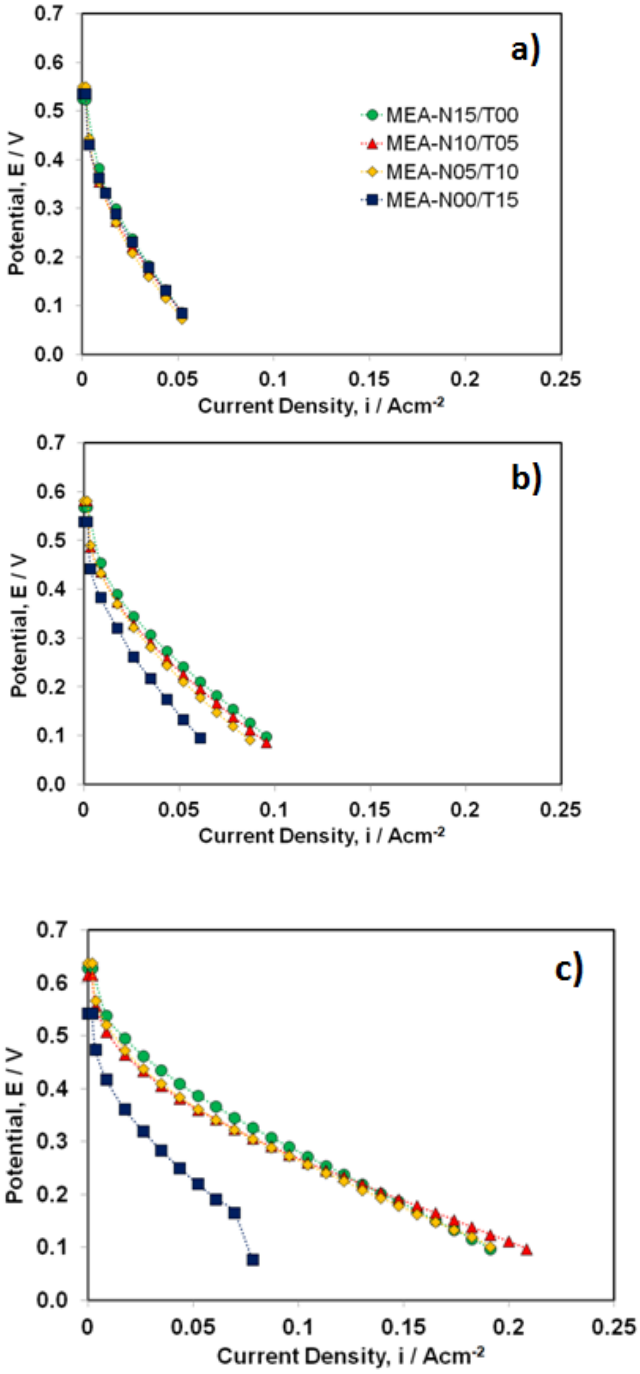

Figure 4.17 : Polarization curves recorded under air (220 $ccmin^{-1}$) at (a) 25 °C, (b) 40 °C, (c) 80 °C.

The ion conductivity of the catalyst layer is function of the volume fraction of Nafion (17) and the addition of PTFE should in principle increase the resistance (15; 9). The DMFCs resistance, Rcell, measured at 40 °C at OCV varies slightly with the cathode composition (MEA N 15 / T 00: 0.38 Ωcm^2; MEA N 10 / T 05: 0.31 Ωcm^2; MEA N 05 / T 10: 0.32 Ωcm^2; MEA N 00 / T 05: 0.37 Ωcm^2), indicating that the partial replacement of Nafion for PTFE in the catalyst layer does not affect the cathodes' and MEAs' resistances. Indeed, the EIS characterization carried out on the cathodes immersed in N_2 saturated 0.5 $moldm^{-3}$ sulphuric acid solution showed that the resistance for the proton conduction in the catalyst layer decreases with increasing PTFE content. Thus, the lower fuel cell performance of the MEA – N 00 / T 15 is likely due to the poorer hydration of the N 00 / T 15 catalyst layer.

The current density at 0.1 V and 40 °C can be correlated with the cathodes' water vapor uptake as reported in Figure 4.18. The current density increases with the water vapor uptake of the cathodes with equal and maxima values for the MEA – N 10 / T 05 and MEA – N 15 / T 00 (95 $mAcm^{-2}$). As shown in the ex-situ electrochemical characterization, the proper balance between the 10 wt% of Nafion and the 5 wt% of PTFE ensures the proton conductivity in the catalyst layer, the continuous supply of O_2 to the Pt active sites and avoids the early flooding of the cathode catalyst layer. Therefore, these results show that a N 10 / T 05 cathode has the potential to prevent the early flooding of a DMFC operating at low temperature.

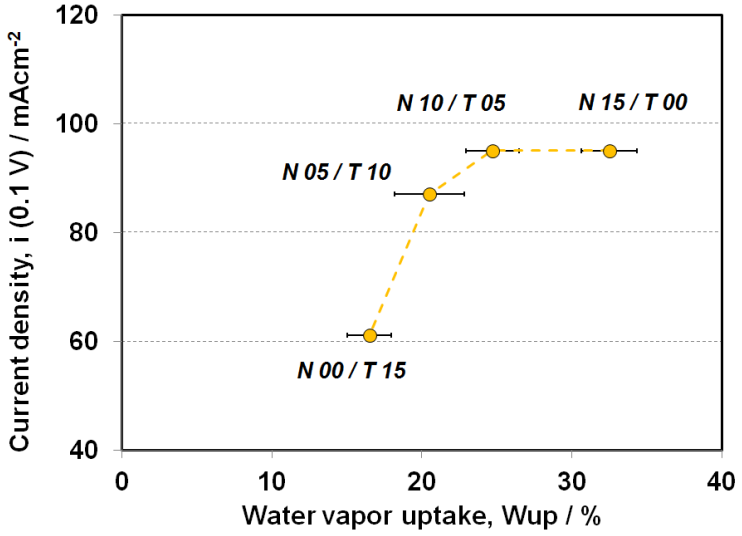

Figure 4.18 : Current density (0.1 V) at 40 °C vs. water vapor uptake cathodes.

C. Polarization curves under O_2 and oxygen gain

The performance of the MEAs was further investigated under oxygen stream at 40 °C, Figure 4.19. The oxygen stoichiometry was kept constant with respect to the tests in air; as expected, due to the higher oxygen partial pressure the performance of the fuel cells in terms of OCV, catalyst utilization and current densities improved with respect to those recorded under air stream (Figure 4.17b). However, the MEA- N 00 / T 15 performs almost as the Nafion–based MEAs: it is thought that the lower oxidant flow rate allows a better hydration of the cathode catalyst layer, resulting in an enhancement of the catalyst utilization.

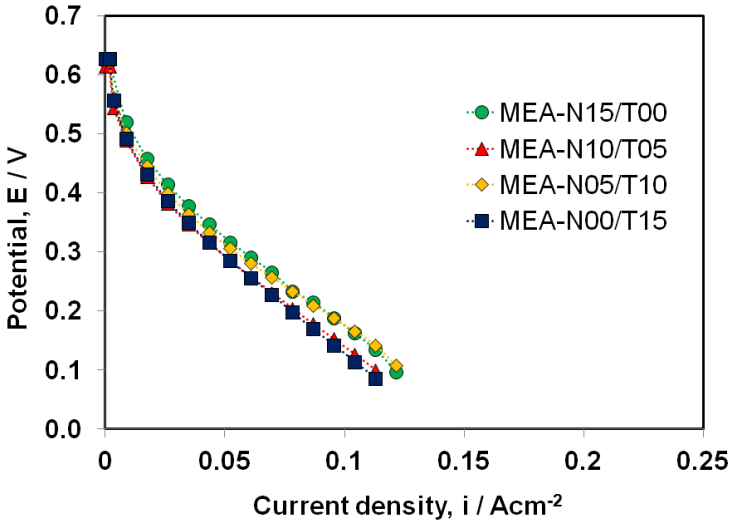

Figure 4.19 : Polarization curves recorded under O_2 (48 $ccmin^{-1}$) at 40 °C.

The difference in the cell potential between polarization curves recorded under air and oxygen feed is named oxygen gain, and it has been widely used in the literature to estimate the voltage loss associated with mass transport in cathodes operating with air for PEM fuel cells (18; 19; 3), and to our knowledge has been applied only once to DMFC systems (20). Usually, a large oxygen gain indicates that the cathode suffers from a high transport resistance when air is used as the oxidant, although higher oxygen reduction charge transfer resistance and lower thermodynamic voltage can also contribute to the oxygen gain (18; 21). A small oxygen gain is desired, especially in the case of air-breathing fuel cells in which the cathode is feed with atmospheric air and losses due to mass transport can be very high. Even if 1 $moldm^{-3}$ methanol solution was used in this work, the methanol cross-over from anode to cathode is not negligible as indicated by the OCVs, and the determination of the oxygen gain in a DMFC risks of

overestimating the loss in the cathode catalyst layer during air operation. Since the rate of methanol crossover decreases with the current density (22), in this work the variation of the oxygen gain will be considered only in the 20 – 100 $mAcm^{-2}$ current density interval, Figure 5.20. EIS measurements confirmed a negligible rate of methanol crossover in this range (see below).

As expected from the data reported in Figure 4.19 and 4.17b, the low performance of the MEA - N 00 / T 15 in air results in the highest oxygen gain of all MEAs and in its very pronounced variation with the current density (Figure 4.20). The MEA – N 10 / T 05 shows the lowest oxygen gain (60 mV which indicates an adequate supply of oxygen through the porous structure of its catalyst layer. This result is consistent with the ORR studies done ex-situ by chronoamperometry and EIS.

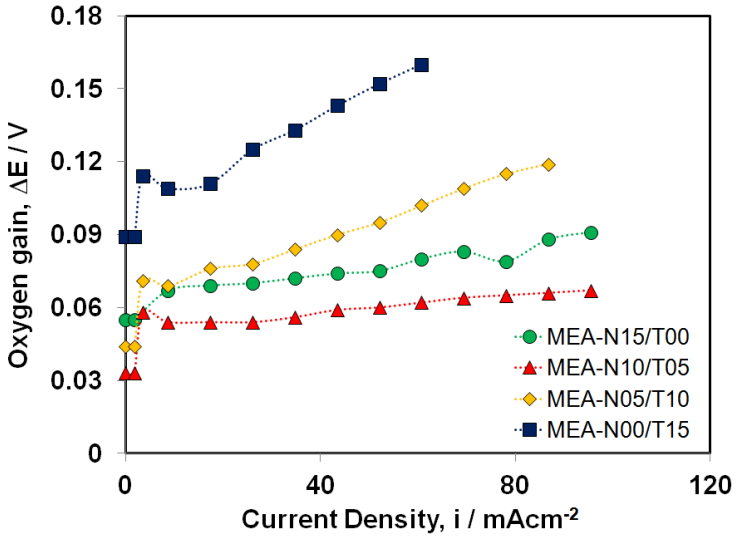

Figure 4.20 : Oxygen gain for single DMFCs at 40 °C.

D. Electrochemical impedance spectroscopy

The performance of the MEAs was investigated by impedance spectroscopy. The impedance spectra were recorded at different potentials (0.5 – 0.2 – 0.1 V), under air and oxygen feed and were fitted with the electrical circuits reported in Chapter 3. The derived kinetic parameters related to the cathodes (double-layer capacitance, C_{dl}, charge-transfer resistance, R_{CT}, relaxation resistance, R_{CO} and mass transfer resistance, R_{MT}) are reported in Table 4.3.

The complete spectra of the DMFCs equipped with the MEA – N 15 / T 00 and MEA – N 10 / T 05, recorded at 0.2 V, in presence of air and pure oxygen are presented in Figures 4.21and 4.22. The spectra consist of two overlapping and distorted semicircles, with no inductive loop in the

low frequency region. As explained in the Chapter 3, the semicircles at high and low frequencies are representative of anodic and cathodic behaviour respectively.

Concerning the Nyquist plot of the spectra recorded under air stream, Figure 4.21a, the MEA – N 15 / T 00 and MEA – N 10 / T 05 show complete semicircles of equal amplitude and intersecting the real impedance axis at low frequency. Similar values of cathodic charge-transfer resistance and double-layer capacitance were observed for the two MEAs (1.05 ± 0.18 Ωcm^2 and 1.27 ± 0.09 Ωcm^2; 0.12 ± 0.02 Fcm^{-2} and 0.13 ± 0.01 Fcm^{-2}); these results are in agreement with the similar *E-j* response under air (Figure 4.17b). Concerning MEA – N 15 / T 00, the theta phase Bode plot, Figure 4.21b, shows the beginning of a low frequency semicircle related to the diffusion limitations. A mass transport resistance of 0.22 ± 0.06 Ωcm^2 was determined for this MEA.

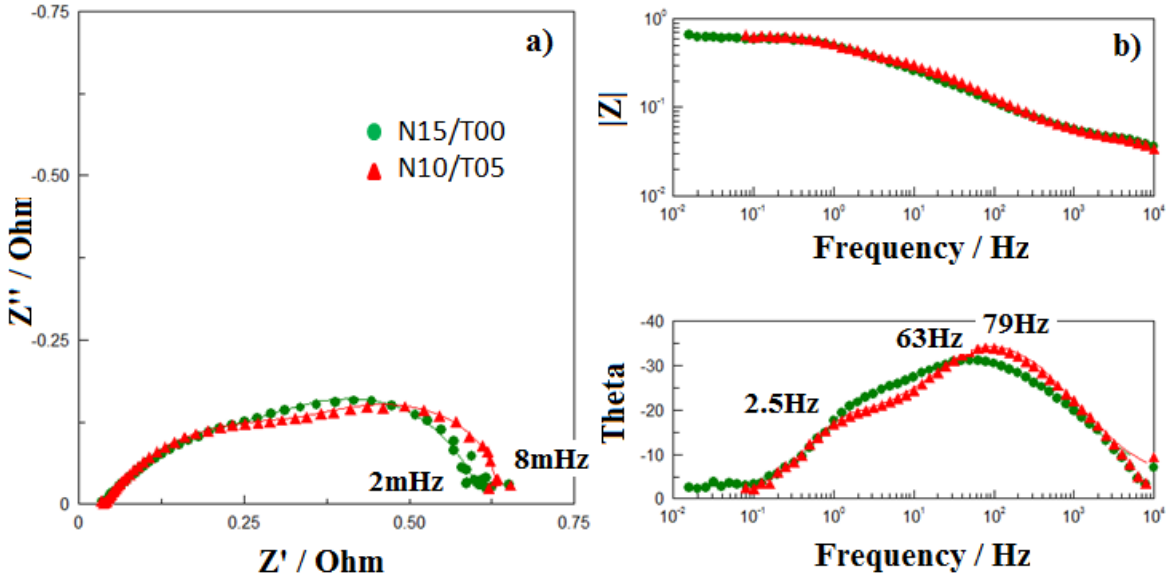

Figure 4.21 : a) Nyquist and b) Bode plots for single DMFCs equipped with MEA – N 15 / T 00 and MEA – N 10 / T 05 recorded in presence of air at 0.2 V.

Figure 4.22 shows the spectra recorded when the cathodes are fed with oxygen. The higher oxygen partial pressure favours the electrochemical processes and the amplitude of the total impedance spectra is lower with respect to those recorded in air. However, the cathodic charge-transfer resistance slightly increases when the feed is switched from air to oxygen (from 1.05 ±

0.18 Ωcm^2 to 1.62 ± 0.08 Ωcm^2 for MEA – N 15 / T 00 and from 1.27 ± 0.09 Ωcm^2 to 1.65 ± 0.05 Ωcm^2 for MEA – N 10 / T 05) indicating the occurring of diffusion limitations. For MEA – N 15 / T 00, this increase is accompanied by the appearance of a small very low frequency semicircle (0.59 ± 0.04 Ωcm^2). Since the DMFCs were operated at high overpotential and oxygen partial pressure, and the cathode does not contain any gas diffusion layer, the hypothesis of water accumulation (flooding) seems the most reasonable one. The diffusion limitations observed for this cathode during the EIS experiment (and not during the polarization curves) are probably due to the polarization of the electrode at 0.2V for 10 min as required to record the full spectrum. Longer and steady state measurements over time would help to confirm the hypothesis of flooding. As observed during the ORR studies done ex-situ (highest capacitive current and lowest charge-transfer resistance) and from the lower oxygen gain, the particular structure of MEA – N 10 / T 05 plays a key role in the performance of the MEA at high current densities and/or in the presence of water in the catalyst layer.

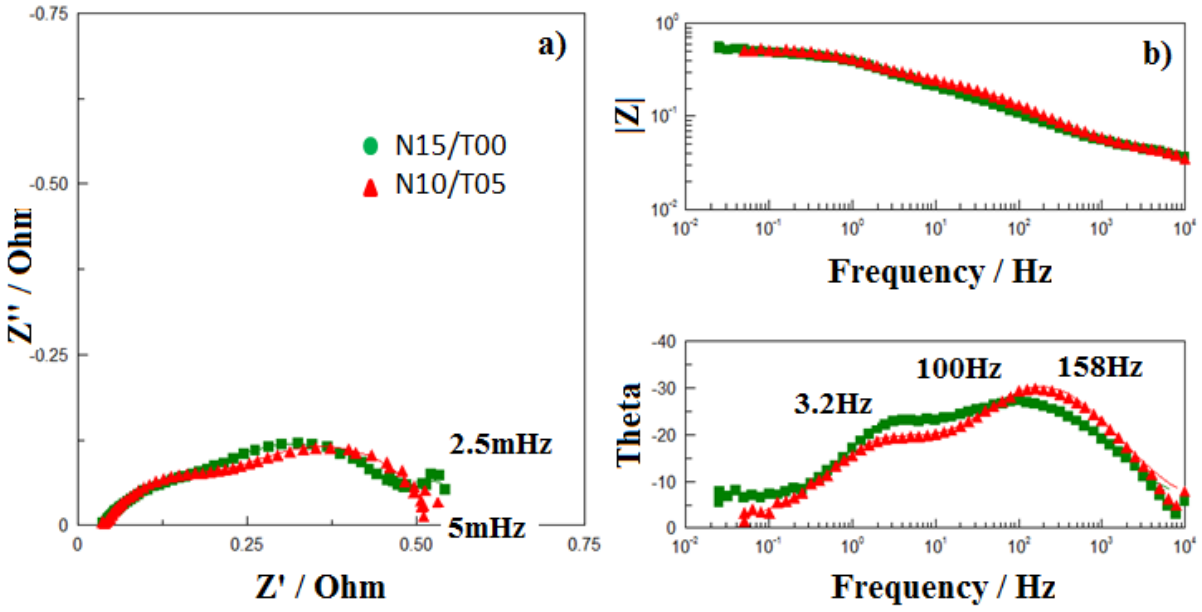

Figure 4.22 : a) Nyquist and b) Bode plots for single DMFCs equipped with MEA – N 15 / T 00 and MEA – N 10 / T 05 recorded in presence of O_2 at 0.2 V.

Table 4.3 : Cathodic parameters from fitting of impedance spectra for the four MEAs.

	Feed	**E / V**	**C_{dl} / Fcm^{-2}**	**R_{CT} / Ωcm^2**	**R_{CO} / Ωcm^2**	**R_{MT} / Ωcm^2**
MEA-N15/T00	AIR	0.5	0.36 ± 0.01	26.36 ± 0.74	26.81 ± 4.28	-
		0.2	0.12 ± 0.02	1.05 ± 0.18	-	0.22 ± 0.06
		0.1	0.04 ± 0.01	1.87 ± 0.21	-	0.74 ± 0.81
	O_2	0.5	0.30 ± 0.02	10.91 ± 0.77	9.80 ± 1.21	-
		0.2	0.04 ± 0.00	1.62 ± 0.08	-	0.59 ± 0.04
		0.1	0.03 ± 0.01	1.91 ± 0.14	-	0.86 ± 0.07
MEA-N10/T05	AIR	0.5	0.30 ± 0.01	52.86 ± 2.60	55.03 ± 17.41	-
		0.2	0.13 ± 0.01	1.27 ± 0.09	-	-
		0.1	0.08 ± 0.01	1.25 ± 0.09	-	-
	O_2	0.5	0.32 ± 0.01	28.93 ± 1.23	23.52 ± 4.61	-
		0.2	0.04 ± 0.00	1.65 ± 0.05	-	-
		0.1	0.04 ± 0.01	1.57 ± 0.17	-0	0.33 ± 0.09
MEA-N05/T10	AIR	0.5	0.27 ± 0.01	49.59 ± 2.21	50.71 ± 18.83	-
		0.2	0.17 ± 0.01	1.23 ± 0.07	-	-
		0.1	0.16 ± 0.01	1.00 ± 0.07	-	-
	O_2	0.5	0.30 ± 0.01	48.89 ± 2.40	48.59 ± 8.99	-
		0.2	0.05 ± 0.00	1.61 ± 0.06	-	-
		0.1	0.02 ± 0.00	2.08 ± 0.13	-	1.15 ± 0.81
MEA-N00/T15	AIR	0.5	0.38 ± 0.01	70.73 ± 3.54	86.46 ± 49.68	-
		0.2	0.06 ± 0.02	2.56 ± 0.82	-	-
		0.1	0.05 ± 0.02	2.50 ± 0.83	-	-
	O_2	0.5	0.23 ± 0.01	8.71 ± 0.42	69.52 ± 0.95	-
		0.2	0.17 ± 0.01	0.82 ± 0.04	-	-
		0.1	0.15 ± 0.02	0.86 ± 0.13	-	-

E. Cathode humidification

In order to confirm the benefits of using the N 10 / T 05 cathode with respect to N 15 / T 00, the effect of cathode humidification on the performance of DMFCs was investigated. The polarization curves were recorded at 40, 50, 60 and 70 °C, and at each temperature the cathode humidification was set in order to record the polarization curves at different relative humidity, 50 % RH, 100 % RH and higher than 100 % RH.

The polarization curves recorded at 50 °C are reported in Figure 4.23. At RH 50% (Figure 4.23a), the MEA – N 10 / T 05 shows a lower OCV (0.57 V vs. 0.61 V) and performance in the activation and ohmic zones but the two polarization curves overlap at high current density (123 $mAcm^{-2}$ at 0.07 V). By increasing the water content in the incoming air, the performance of MEA - N 10 / T 05 improves, in particular in the activation zone, due to a better hydration of the catalyst layer; the performance of MEA - N 15 / T 00 is the same in the activation zone but it decreases at higher current densities. Indeed, for RH ≥100% (Figure 5.23b-c) the MEA – N 10 / T 05 outperforms MEA – N 15 / T 00 at high current densities (132 vs. 113 $mAcm^{-2}$) indicating that a better transport of reactants and water removal occurs in the porous structure of this catalyst layer under high hydration conditions and at this temperature. Similar results were obtained at 40 °C. However, at 60 °C and 70 °C the MEA – N 15 / T 00 performs slightly better than MEA – N 10 / T 05, especially at high % RH (data shown in the appendix). The increase of the cell temperature accelerates the water evaporation and reduces the probability of flooding phenomena. Under these conditions, the presence of the hydrophobic component in the N 10 / T 05 cathode impairs the DMFC performance due to the poor hydration of the catalyst layer (7).

The potential to increase the performance of DMFC (equipped with this type of cathode) in terms of open circuit voltage, current density and oxygen utilization by improving the Pt distribution is very high. The effect of the Pt distribution for the N 10 / T 05 cathode was investigated and the results are reported in the next paragraph.

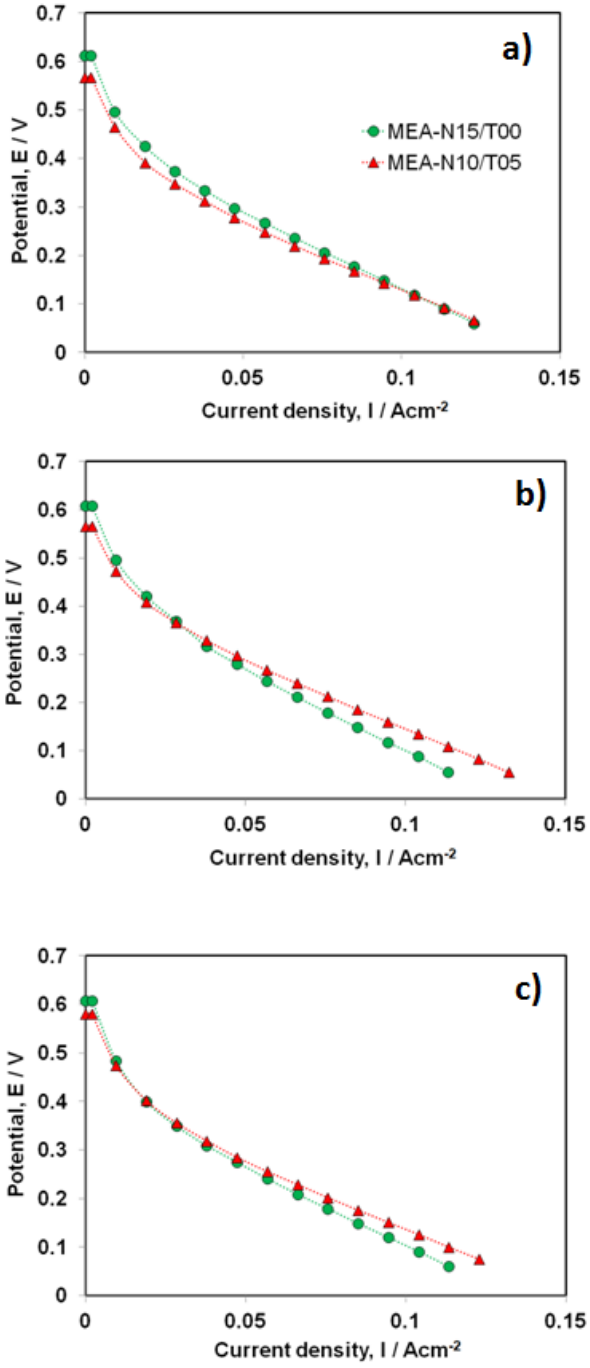

Figure 4.23 : Polarization curves recorded under air at 50 °C and a) RH 50 %, b) RH 100 %, c) RH >100%.

4.3. Cathode N 10 / T 05 – P

4.3.1. Physicochemical characterization

Table 4.4 contains the physicochemical parameters for the N 10 / T 05 and N 10 / T 05 - P cathodes. Instead of a spray gun, an airbrush with a smaller and precise spray pattern was used to prepare the new cathode (Chapter 2). The N 10 / T 05 - P cathode has a Pt distribution more concentrated on the cathode' surface, as shown in the cartography of the cathode' cross-section in Figure 4.24.

Table 4.4 : Physicochemical parameters for N 10 / T 05 and N 10 / T 05 – P cathodes.

Cathode	**N10/T05**	**N10/T05-P**
Water vapor uptake / %	1.04 ± 0.31	1.44 ± 0.52
Liquid water uptake / %	24.8 ± 1.8	27.0 ± 1.5
Contact Angle (ACA-RCA) / °	143.09 ± 1.38 140.60 ± 2.33	120 ± – 110 ± –
Thickness / μm	443 ± 49	502 ± 72
Total pore volume / cm^3g^{-1}	0.061	0.061

The Figure 4.24 reports as well the surface images of the two cathodes at different magnifications. The N 10 / T 05 – P shows a more dense coating with agglomerates on the surface (25x); however, in both cases, the deposit covers well the fibers. Uniform and dense structures formed around the fibers are observed in the images at 160x of the N 10 / T 05 – P cathode.

Slightly higher vapor water and liquid water uptake were measured for this cathode (1.44 ± 0.52 % and 27.0 ± 1.5 %) with respect to cathode N 10 / T 05. The lower advancing contact angle (120°) suggests that the surface of N 10 / T 05 - P cathode is more wettable so it may be supposed that water penetrates through some larger pores. The higher hysteresis (10° vs. 2.5°) shows that the cathode surface is more rough than for N 10 / T 05 cathode. The N 10 / T 05 - P cathode is thicker than the N 10 / T 05 cathode (502 ± 72 μm vs. 443 ± 49 μm) and no variation is observed in the total micro- and meso-pore volume (0.061 cm^3g^{-1}). Since the cathodes have the

same chemical composition, the thickness increase must be due to an higher macro-porosity in the N 10 / T 05 - P cathode catalyst layer. This hypothesis needs to be verified by Mercury Porosimetry measurements. The DMFC performance of MEAs containing the N 10 / T 05 – P cathodes was investigated and compared to N 10 / T 05 based MEA.

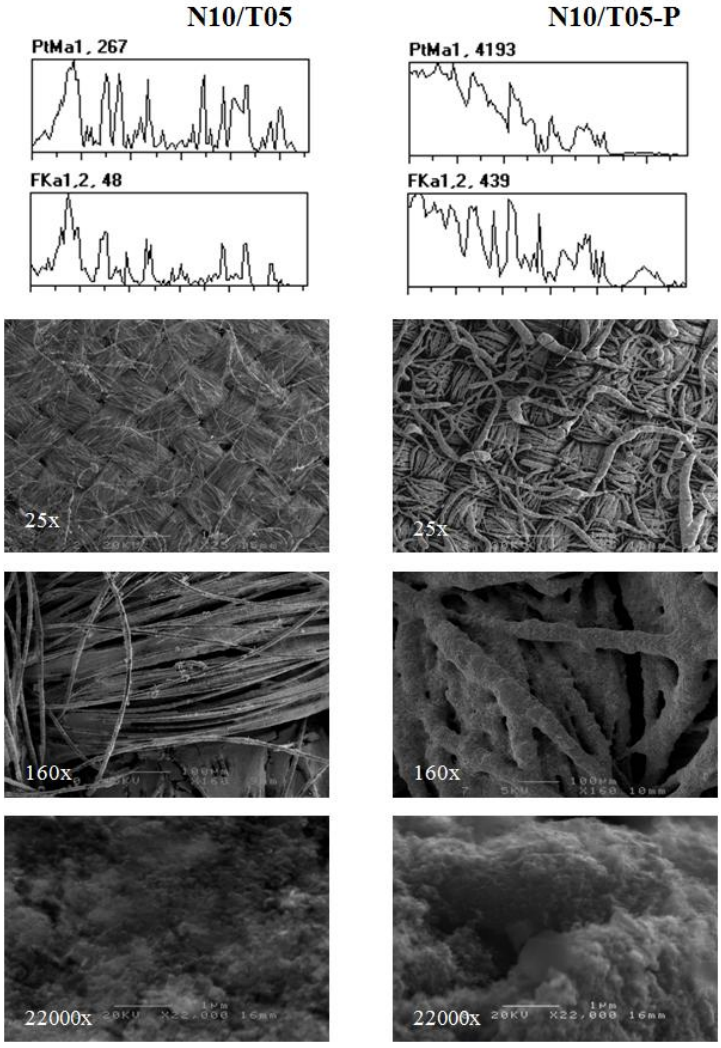

Figure 4.24 : Cartography of cross-section and surface images for N 10 / T 05 and N 10 / T 05 - P cathodes.

4.3.2. DMFC characterization

A. Conditioning

The Figure 4.25 shows the variation of the OCV over time for DMFCs equipped with MEA – N 10 / T 05 and MEA – N 10 / T 05 – P. The period for the conditioning varied between 72 and 100 minutes. The DMFCs equipped with the two MEAs shows similar behaviour, their OCVs

increase sharply in the first 40 minutes of conditioning to reach approximately the 86-93 % of the final values. For the MEA – N 10 / T 05 – P it is observed a sharper increase and a higher final OCV (0.54 V vs. 0.48 V) which suggest a faster hydration of the cathode, as expected from the slightly higher water uptake of the N 10 / T 05 – P cathode, and a more efficient supply of reagents to the catalyst sites.

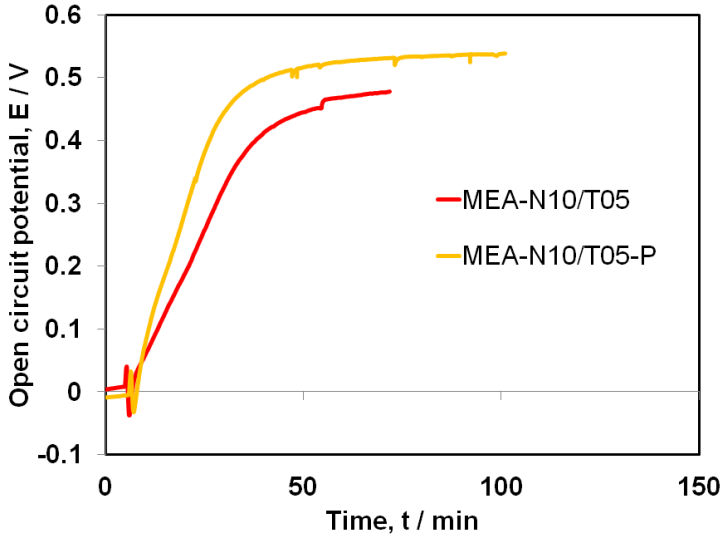

Figure 4.25 : Open circuit voltage over time for DMFCs in presence of air (220 ccmin^{-1}, atmospheric pressure) and 1 moldm^{-3} MeOH solution at 25 °C.

B. Polarization curves under air

The Figure 4.26 shows the polarization curves recorded at 25 °C, 40 °C and 80 °C during the second temperature cycle. As above, the curves show the characteristic activation and ohmic regions and no limiting current. Again, the performance of the MEA improves with the increasing of the operating temperature. For all the temperatures, the performance of MEA – N 10 / T 05 – P is always superior with remarked higher OCVs (0.58 V, 0.62 V, 0.68 V), higher catalyst utilization at the anode and the cathode and higher current densities (66 mAcm^{-2}, 104 mAcm^{-2}, 236 mAcm^{-2} at 0.1 V). The same increase was observed in the polarization curves recorded under oxygen stream at 40 °C. These results shows that this Pt distribution profile is more effective in terms of catalyst utilization, and higher support of reagent and better water removal to and from the catalyst layer are derived from the supposed higher porosity of this cathode.

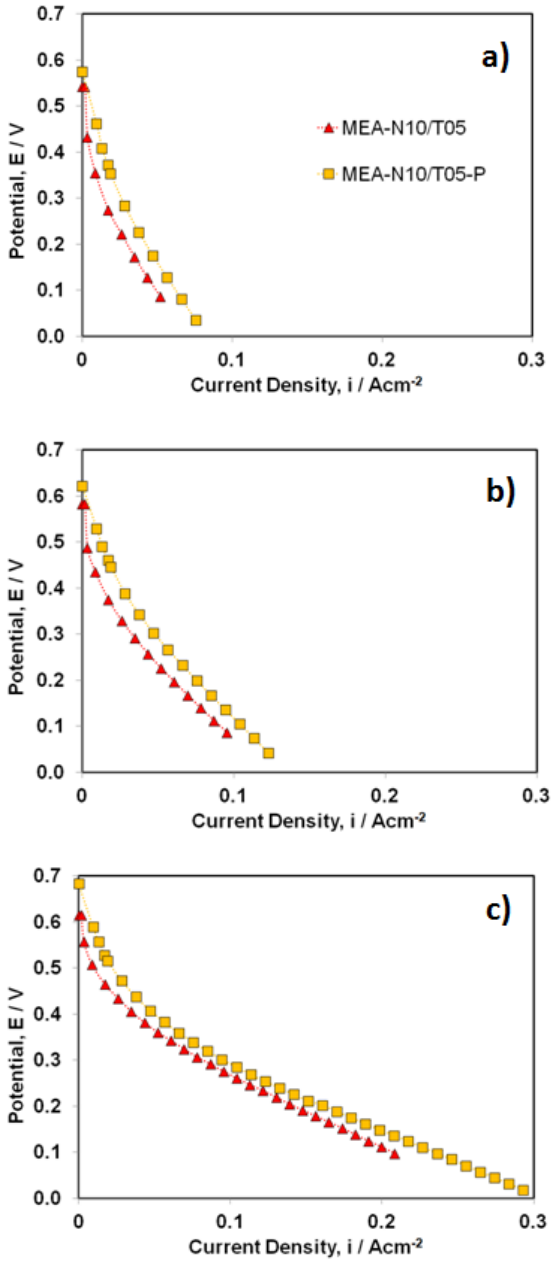

Figure 4.26 : Polarization curves recorded under air (220 ccmin^{-1}) at (a) 25 °C, (b) 40 °C, (c) 80 °C.

C. Electrochemical Impedance Spectroscopy

The complete spectra of the DMFCs equipped with the MEA – N 10 / T 05 and MEA – N 10 / T 05 - P, recorded at 0.5 V and 0.2 V, under air and oxygen, are presented in Figure 4.27. The cathodic electrochemical parameters obtained from the fitting (Chapter 3) are reported in Table 4.5. In the Nyquist plot, Figure 4.27a, the spectra show complete semicircles which amplitude

decreases from air to oxygen. Lower values of cathodic charge-transfer resistance are observed for the N 10 / T 05 – P (11.78 ± 0.36 Ωcm^2 and 7.49 ± 0.25 Ωcm^2) and consistently, a shift of the phase maximum towards higher frequencies in observed in the Bode plot, Figure 4.27b. Concerning the spectrum recorded under oxygen at 0.2 V, a third semicircle related to diffusion limitations is present in the very lower frequency region. As above, because of the operating conditions (high overpotential and oxygen partial pressure) and the particular cathodic structure (no gas diffusion layer), it is reasonable to suppose that this semicircle is related to the flooding.

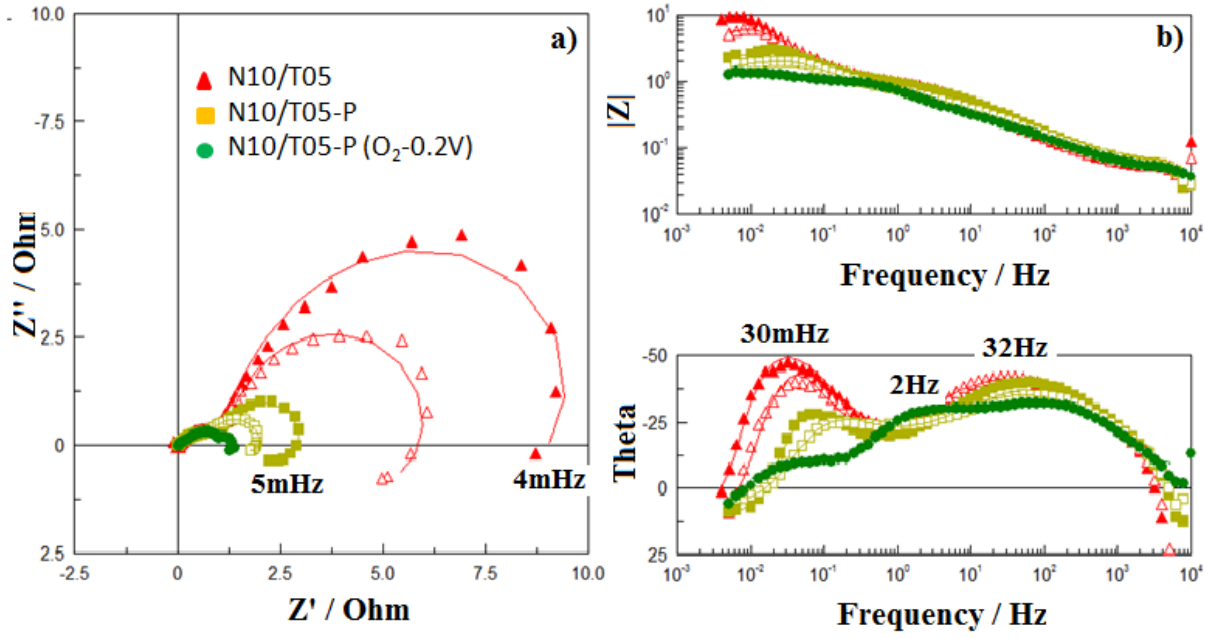

Figure 4.27 : a) Nyquist and b) Bode plots for single DMFCs equipped with MEA – N 10 / T 05 and MEA – N 10 / T 05-P recorded in presence of air (full mark) and O_2 (empty mark) at 0.5 V.

Table 4.5 : Cathodic parameters for the MEA-N10/T05 and MEA-N10/T05-P.

		MEA-N10/T05			MEA-N10/T05-P		
Feed	**E / V**	**C_{dl} / Fcm^{-2}**	**R_{CT} / Ωcm^2**	**R_{MT} / Ωcm^2**	**C_{dl} / Fcm^{-2}**	**R_{CT} / Ωcm^2**	**R_{MT} / Ωcm^2**
AIR	0.5	0.30 ± 0.01	52.86 ± 2.60	-	0.28 ± 0.01	11.78 ± 0.36	-
	0.2	0.13 ± 0.01	1.27 ± 0.09	-	-	-	-
O_2	0.5	0.32 ± 0.01	28.93 ± 1.23	-	0.16 ± 0.00	7.49 ± 0.25	-
	0.2	0.04 ± 0.00	1.65 ± 0.05	-	0.02 ± 0.01	3.98 ± 0.16	0.33 ± 0.09

D. Cathode humidification

The effect of cathode humidification on the performance of MEA – N 10 / T 05 – P was investigated. The polarization curves recorded at 40 and 50°C, and at different relative humidities, 50 % RH, 100 % RH and higher than 100 % RH, are reported in Figure 4.28.

At all tested relative humidity, the MEA – N 10 / T 05 – P shows higher OCVs, higher catalyst utilization and higher current densities than MEA – N 10 / T 05 indicating a better transport of reactants in the porous structure of the new catalyst layer under high hydration conditions and at these temperatures. However, by increasing the water content in the incoming air, the performance of MEA - N 10 / T 05 – P is compromised by the water accumulation in the cathode. Indeed, potential drops are observed in the curves for RH ≥100% (Figure 4.28c-f).

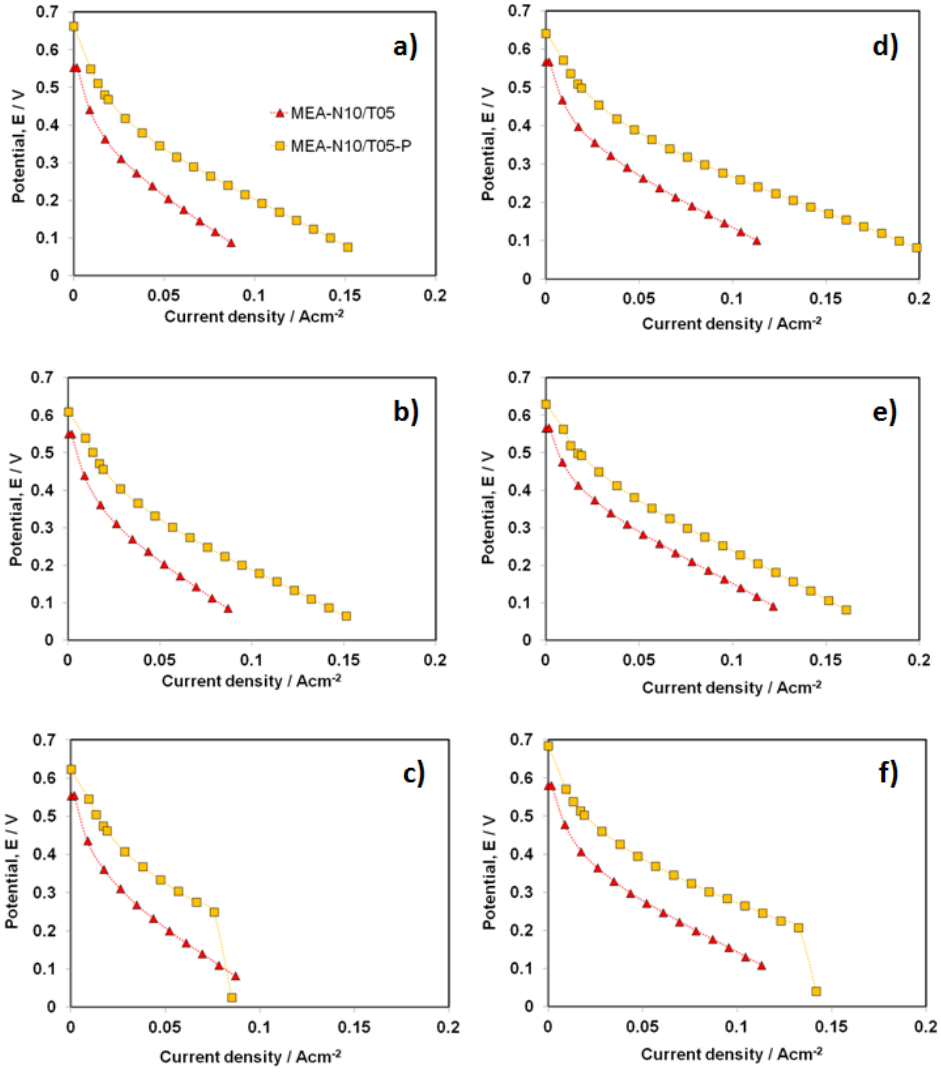

Figure 4.28 : Polarization curves recorded under air (220 ccmin^{-1}) at a) 40 °C, RH 50%; b) 40 °C, RH 100%; c) 40 °C, RH>100%; d) 50 °C, RH 50%; e) 50 °C, RH 100%; f) 50 °C, RH>100%.

4.4. Conclusions

This study aimed to investigate if the partial substitution of Nafion by PTFE can improve the diffusion of oxygen and protons through the catalyst layers.

- The physicochemical characterization has showed that partial replacement of Nafion by PTFE in the catalyst layer reduces the hydrophilicity of the cathodes (liquid W_{up} from 32.46 ± 1.86 wt% to 16.53 ± 1.46 wt%), causes a variation in the morphology of the cathode' surface (lower ACA for N 00 / T 15 cathode, 131.67° ± 1.30°) and determines the total micro- and meso-pore volume of the cathodes (0.109 cm^3g^{-1} for the N 15 / T 00 and 0.061 cm^3g^{-1} for N 10 / T 05 cathodes).
- The electrochemical characterization has shown that the Pt utilization and the capacitance increases with the hydrophilicity of the cathodes (25.50 ± 0.70 % and 104.00 ± 5.70 $mFcm^{-2}$ for N 15 / T 00). However, the benefits of including PTFE in the cathode catalyst layer are shown in the resistance to the proton transport in the catalyst layer (minimum of 5.10 ± 0.10 Ωcm^2 for N 00 / T 15) and in the ORR current density (38 $mAcm^{-2}$ at 0.2 V for N 00 / T 15). The lowest charge-transfer resistance (36.86 ± 0.47 Ωcm^2) and highest capacitance (48.74 ± 0.40 $mFcm^{-2}$) of N 10 / T 05 show that the proper balance between the 10 wt% of Nafion and the 5 wt% of PTFE ensures the proton conductivity in the catalyst layer, the continuous supply of O2 to the Pt active sites and avoids the early flooding of the cathode catalyst layer.
- The DMFC tests at different cathodic relative humidity have shown that the N 10 / T 05 cathode is suitable to work in a low temperature DMFC up to 50 °C without early flooding of the cathode catalyst layer

The Pt distribution for the N 10 / T 05 cathode was concentrated more on the surface and the performance were investigated. The N 10 / T 05 - P cathode has showed slightly higher water uptake (27.0 ± 1.5 %), higher wettability of the cathode' surface (ACA 120 °), larger thickness (502 ± 72 μm) and a suspected higher macro-porosity that needs to be verified by Mercury Porosimetry measurements. The DMFC characterization has shown higher catalyst utilization and performance but higher probability of flooding was also found for the MEA based on the N 10 / T 05 – P cathode when operated at low temperatures (40 and 50 °C). It is well-known that the

macro-pores improve the mass transport (6), but, in this cathodic configuration (no GDL) and under these operating conditions (low temperature), the pores behave as "water basins" and easily accumulate water.

These results show that the key to resolve the flooding in low temperature DMFCs lays more in the cathode porosity than in the hydrophilic/hydrophobic content of the catalyst layer. Therefore, the proper pore dimension can be substantial in the preparation of anti-flooding cathodes.

The DMFC test data and the ex-situ characterization (variation of the catalyst utilization, of the ion resistance of the catalyst layer, efficiency of oxygen transport through the catalyst layers) shown to be consistent with each other. Therefore, the electrochemical characterization of DMFC cathodes imbibed in H_2SO_4 solution might be a simple and efficient tool to test ex-situ the flooding phenomena.

4.5. References

1. **J.Xie, K.L. More, T.A. Zawodzinski, W.H. Smith.** Porosimetry of MEAs Made by ''Thin Film Decal'' Method and Its Effect on Performance of PEFCs. *Journal of The Electrochemical Society.* 2004, Vol. 151, 11, pp. A1841-A1846.

2. **T.V. Reshetenko, H.-T. Kim, H.-J. Kweon.** Cathode structure optimization for air-breathing DMFC by application of pore-forming agents. *Journal of Power Sources.* 2007, Vol. 171, p. 433.

3. **J. Lobato, P. Canizares, M.A. Rodrigo, C.R.-Lopez, J.J. Linares.** Influence of the Teflon loading in the gas diffusion layer of PBI-based PEM fuel cells. *Journal of Applied Electrochemistry.* 2008, Vol. 38, p. 793.

4. **X. Zhao, W. Li, Y. Fu, A. Manthiram.** Influence of ionomer content on the proton conduction and oxygen transport in the carbon-supported catalyst layers in DMFC. *International Journal of Hydrogen Energy.* 2012, Vol. 37, pp. 9845-9852.

5. **D.L. Wood III, C. Rulison, R.L. Borup.** Surface properties of PEMFC gas diffusion layers. *Journal of Electrochemical Society.* 2010, Vol. 157, 2, pp. B195-B206.

6. **H.M. Yu, C. Ziegler, M. Oszcipok, M. Zobel, C. Hebling.** Hydrophilicity and hydrophobicity study of catalyst layers in proton exchange membrane fuel cells. *Electrochimica Acta.* 2006, 51, pp. 1199–1207.

7. **A. Di Blasi, V. Baglio, T. Denaro, V. Antonucci, A.S. Aricò.** Optimization of Electrode Properties for Low Temperature DMFC Applications. *Journal of New Materials for Electrochemical Systems.* 2008, 11, p. 165.

8. **G. Li, P.G. Pickup.** Ionic Conductivity of PEMFC Electrodes. *Journal of The Electrochemical Society.* 2003, Vol. 150, 11, p. C745.

9. **B. Krishnamurthy, S. Deepalochani.** Experimental analysis of platinum utilization in a DMFC cathode. *Journal of Applied Electrochemistry.* 2009, Vol. 39, p. 1003.

10. **V. Baglio, A. Di Blasi, E. Modica, P. Creti, V. Antonucci, A.S. Aricò.** Influence of Catalyst Utilization on the Electrochemical Behaviour of Low Temperatures DMFCs. *Journal of New Materials for Electrochemical Systems.* 2006, Vol. 9, p. 41.

11. **A. Pozio, M. De Francesco, A. Cemmi, F. Cardelleni, L. Giorgi.** Comparison of high surface Pt/C catalysts by cyclic voltammetry. *Journal of Power Sources.* 2002, Vol. 105, pp. 13-19.

12. **E.B. Easton, P.G. Pickup.** An electrochemical impedance spectroscopy study of fuel cell electrodes. *Electrochimica Acta.* 2005, Vol. 50, p. 2469.

13. **A. Kamat, A. Huth,O. Klein, S. Scholl.** Chronoamperometric Investigations of the Electrode–Electrolyte Interface of a Commercial High Temperature PEM Fuel Cell. *Fuel Cells.* 2010, Vol. 4, p. 1.

14. **D.B. ZHou, H.VANDER POORTEN.** ELECTROCHEMICAL CHARACTERISATION OF OXYGEN REDUCTION ON TEFLON-BONDED GAS DIFFUSION ELECTRODES. *Electrochimica Acta.* 1995, Vol. 40, 12, p. 1819.

15. **B. Krishnamurthy, S. Deepalochani.** Effect of PTFE content on the performance of a Direct Methanol fuel cell. *International Journal of Hydrogen Energy.* 2009, Vol. 34, p. 446.

16. **C. He, Z. Qi, M. Hollett, A. Kaufman.** An Electrochemical Method to Improve the Performance of Air Cathodes and Methanol Anodes. *Electrochemical and Solid-State Letters.* 2002, Vol. 5, 8, p. A181.

17. **B. Krishnamurthy, S. Deepalochani, K.S. Dhathathreyan.** Effect of Ionomer Content in Anode and Cathode Catalyst Layers on Direct Methanol Fuel Cell Performance. *Fuel Cells.* 2008, Vol. 8, p. 404.

18. **Zhang, J.** *PEM Fuel Cell Electrocatalysts and Catalyst Layers.* London : Springer. p. 599.

19. **M. Prasanna, H.Y. Ha, E.A. Cho, S.-A. Hong, I.-H. Oh.** Investigation of oxygen gain in polymer electrolyte membrane fuel cells. *Journal of Power Sources.* 2004, Vol. 137, p. 1.

20. **F. Liu, C.-Y. Wang.** Optimization of cathode catalyst layer for direct methanol fuel cells Part I. Experimental investigation. *Electorchimica Acta.* 2006, Vol. 52, p. 1417.

21. **C. Rayment, S. Sherwin.** *Introduction to Fuel Cell Technology.* University of Notre : s.n. p. 27.

22. **V. Baglio, A. Stassi, F.V. Matera, H. Kim, V. Antonucci, A.S. Aricò.** AC-Impedance Investigation of Different MEA Configurations for Passive-Mode DMFC Mini-Stack Applications. *Fuel Cells.* 2010, Vol. 10, p. 124.

CHAPTER 5 : INVESTIGATION OF THE N 00 / T 15 CATHODE - THE ASSEMBLY PRESSURE AND THE CATHODE MORPHOLOGY

5.1. Summary

As seen in the previous chapter, the characterization of the Nafion-PTFE based-electrodes showed that the N 00 / T 15 cathode suffered from poor hydration, low total pore volume and reduced Pt utilization. The performance of the MEA containing this cathode was drastically low, especially under air feed. However, the surprising lower resistance to the proton conduction and the higher limiting-current for the oxygen reduction reaction made the N 00 / T 15 cathode an interesting subject for further studies.

Three different approaches aimed at improving the fuel cell performance through enhancing the hydration, the porosity and the Pt utilization of the N 00 / T 15 cathode are reported in this chapter. The first approach focussed onto decreasing the pressure of assembly in order to reduce the compression of the cathode during the MEA fabrication and maximize the cathode's available pore volume. The second approach consisted on the application of a thin layer of Nafion (coating method) on the cathode surface to improve the hydration and/or the catalyst utilization. The third approach explored the use of TFE-treated carbon cloth to facilitate the O_2 diffusion into the N 00 / T 15 cathode catalyst layer and to extend the three-phase boundary. In addition, the effect of the sintering process at 350 °C on the physicochemical and electrochemical properties of the N 00 / T 15 cathode was investigated.

5.2. Optimization of membrane-electrodes assembly pressure

Three MEAs containing the N 00 / T 15 cathode (Chapter 2), Nafion 117 membrane and the commercial anode (ElectroChem, 3 $mgcm^{-2}$ PtRu from 60 wt% PtRu/Vulcan XC-72 catalyst and 1 $mgcm^{-2}$ Nafion loading on TFE-treated C-cloth) were assembled using the standard pressure 500 lbs and two lower values of pressure: 375 lbs and 250 lbs. The DMFC performance was investigated as follow.

A. Conditioning and cell resistance

Before performing any polarization curves, the fuel cells were conditioned at 25 °C, feeding the anode with 1 moldm^{-3} methanol solution (2.5 mlmin^{-1}) and the cathode with air (220 mlmin^{-1}, RH 100%) and waiting for a stable value of the open circuit potential (OCV). The variation of the OCV over time for the single DMFCs equipped with MEA – N 00 / T 15 – 500, MEA – N 00 / T 15 – 375 and MEA – N 00 / T 15 – 250 is reported in Figure 5.1. Depending on the behaviour of the single DMFC, the period for the conditioning was varied between 1 hour and 1 hour and 30 minutes. In the first 30 minutes, the single DMFCs showed distinct behaviour which is related to the time required to reach the equilibrium. The OCV of the DMFC equipped with MEA – N 00 / T 15 – 375 (intermediate pressure) increased sharply to the 85 % of its final value, then continued to increase smoothly and stabilized at 0.5 V. For the other two DMFCs, and especially for the one equipped with MEA – N 00 / T 15 – 250 (lower pressure), the variation was less abrupt but slightly higher values of OCV (0.52 V) were reached.

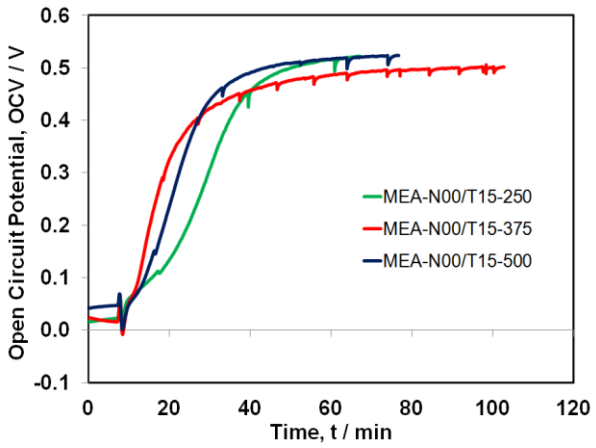

Figure 5.1 : Open circuit voltage over time for single DMFCs in presence of air (220 ccmin^{-1}, atmospheric pressure) and 1 moldm^{-3} MeOH solution at 25 °C.

The variation of the assembly pressure can strongly affect the contact between the electrodes and the membrane (1; 2). As a result, the DMFC resistance can be influenced as well. The Figure 5.2 reports the cell resistance (R_{cell}) of the DMFCs measured at the end of the conditioning process. The R_{cell} varies between 0.6 Ωcm^2 and 0.47 Ωcm^2 with a minimum for the MEA – N 00 / T 15 – 375. The graph shows that lower pressures are adequate to minimize the contact resistance between the membrane and the electrodes, but a very high assembly pressure compresses too much the electrodes and prevents the diffusion of the reactants. From the minimum of resistance

reported for MEA – N 00 / T 15 – 375 it is suggested that the intermediate pressure is the best compromise for a proper electrodes-membrane contact and an easy diffusion of the reagents to the catalytic sites.

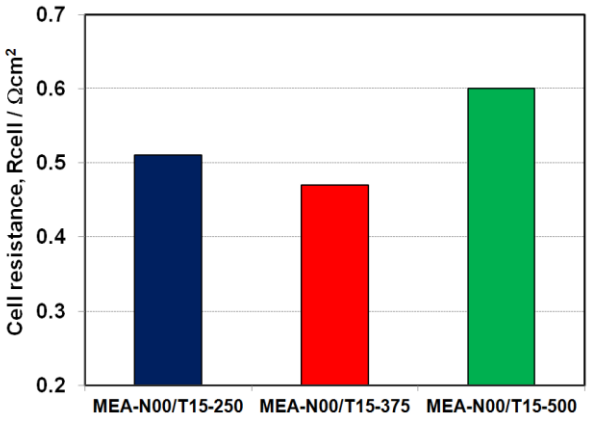

Figure 5.2 : Cell resistance of MEAs assembled at pressure 250 – 375 – 500 lbs measured at 25 °C.

B. Polarization curves under air

The performance of the three MEAs was investigated between 40 °C and 80 °C and is reported in Figure 5.3. The DMFC polarization curves show the characteristic activation zone at low overpotential (between OCV and 0.45 V) and the ohmic region at higher overpotential (from 0.45 V until 0.1 V). Except for the MEA – N 00 / T 15 – 500 at 80 °C, no limiting current due to mass transport control was evidenced for these experiments. As expected, the performance of all MEAs improved with the operating temperature. At 40 °C, Figure 5.3a, higher OCV (0.58 V vs. 0.54 V) and catalyst utilization (activation zone (3; 4)) are observed for the MEA – N 00 / T 15 – 375 but all MEAs perform almost equally at high overpotential. At 60 °C, Figure 5.3b, the MEA – N 00 / T 15 – 375 shows again higher OCV (0.63 V vs. 0.57 V) and performs better than the other MEAs in all the regions of the polarization curves. At 80 °C, Figure 5.3c, this MEA shows a distinguished and higher E-j curve and it seems not to be affected by the higher methanol cross-over and the natural evaporation of water occurring at high temperature. In fact, the OCV increased up to 0.67 V, whereas a decrease of circa 30 mV is noticed for the other two MEAs.

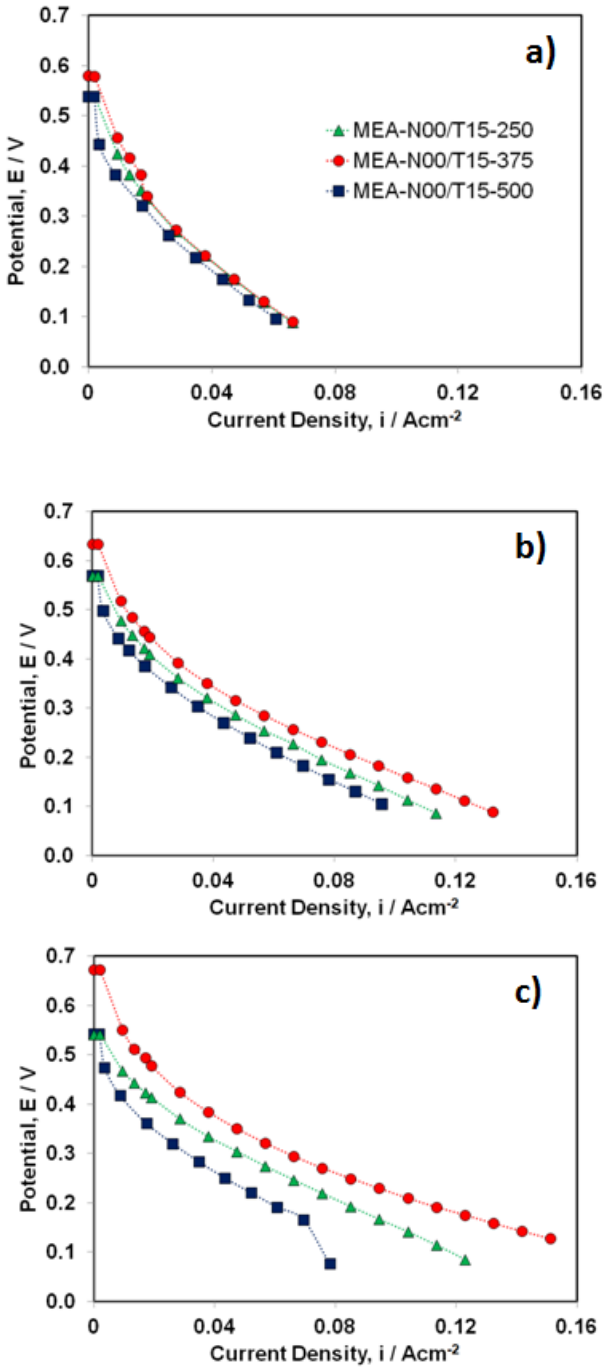

Figure 5.3 : Polarization curves recorded under air (220 cc min^{-1}) at (a) 40 °C, (b) 60 °C, (c) 80 °C.

The variation of the open circuit potential as a function of the temperature is reported in Figure 5.4. The DMFCs equipped with MEA – N 00 / T 15 – 250 and MEA – N 00 / T 15 – 500 show the same volcano trend with the highest OCV at 60 °C (0.569 V). A distinct behaviour is reported for the MEA – N 00 / T 15 – 375 which shows higher and increasing OCV values in all the range of temperature. As for the polarization curves reported in Figure 5.3, the constant increase of the

OCV indicates higher catalyst utilization at the anode and the cathode, and resulting in a lower rate of methanol cross-over.

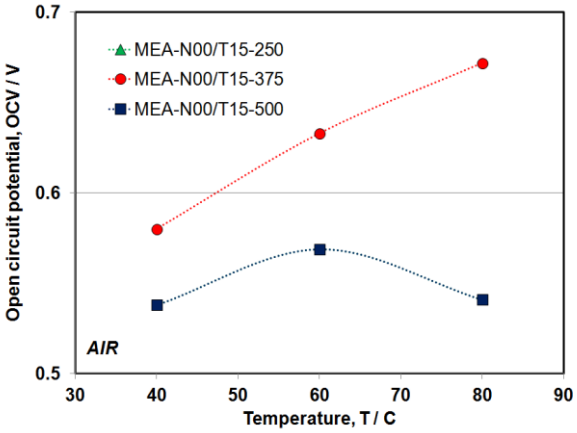

Figure 5.4 : Open circuit potential of single DMFCs measured at 40 °C, 60 °C and 80 °C.

The DMFCs cell resistances measured at 40 °C, 60 °C and 80 °C are reported in Figure 5.5. The Rcell were found to decrease with the operating temperature indicating that the membranes were constantly well-hydrated (5). It was also observed that the resistance increased with the assembly pressure and it varied between 0.23 Ωcm^2 and 0.37 Ωcm^2.

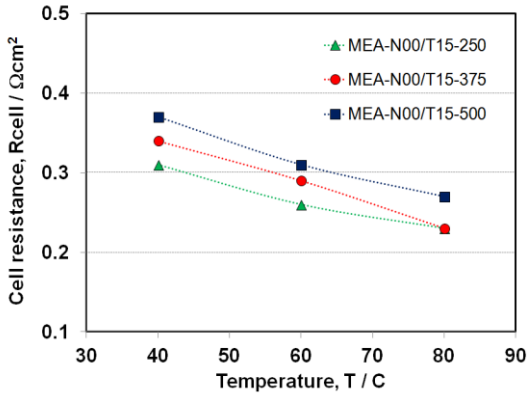

Figure 5.5 : Cell resistance for DMFCs assembled at 250 – 375 – 500 lbs, measured at 40, 60 and 80 °C.

C. Polarization curves under O_2

The performance of the MEAs was further investigated under oxygen stream. Figure 5.6 shows the polarization curves recorded at 40 °C, 60 °C and 80 °C. The oxygen stoichiometry was kept the same with respect to the tests in air; as expected, due to the higher oxygen partial pressure the performance of the fuel cells, in terms of OCV, catalyst utilization and current densities, improved with respect to the ones recorded under air stream (Figure 5.3a). At 40 °C, Figure 5.6a,

the MEAs show similar polarization curves, however a slightly higher catalyst utilization (activation zone (3; 4)) is observed for the MEA – N 00 / T 15 – 375. At 60 °C, Figure 5.6b, the two MEAs pressed at 375 lbs and 250 lbs perform better than the MEA – N 00 / T 15 – 500 in all the regions of the polarization curves. At 80 °C, Figure 5.6c, the MEA– N 00 / T 15 – 375 shows higher E-j curve and distinguishable performance in all the range of potentials.

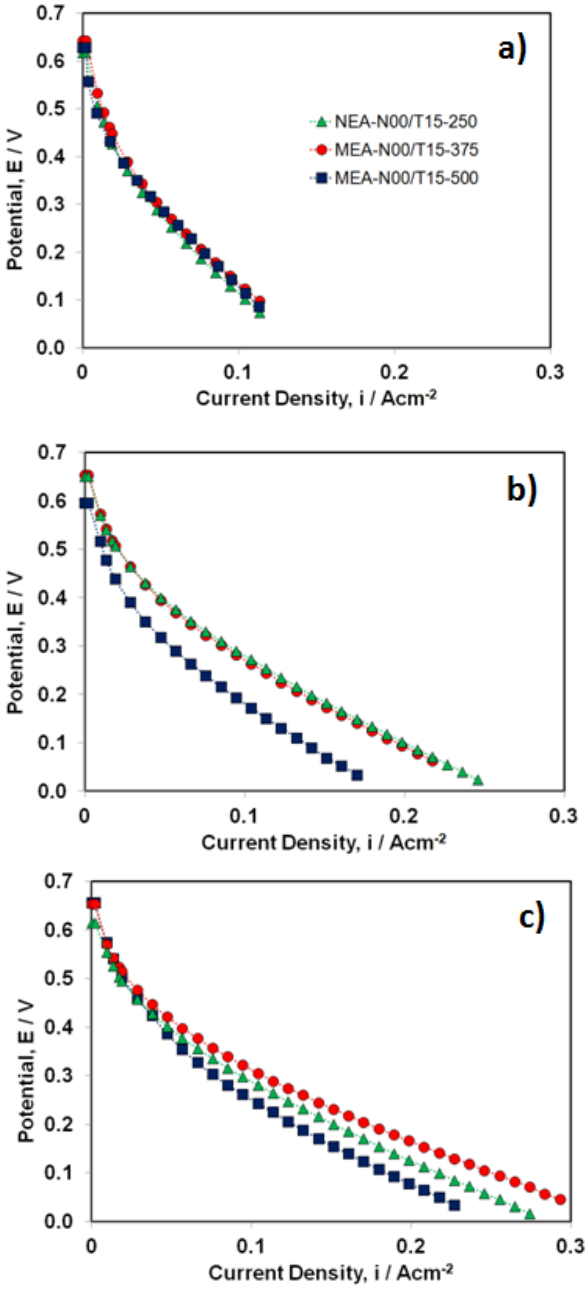

Figure 5.6 : Polarization curves recorded under O_2 (48 cc min^{-1}) at (a) 40 °C, (b) 60 °C, (c) 80 °C.

The optimization of the assembly pressure has proven to be advantageous to increase the performance of MEAs based on N 00 / T 15 cathodes. As shown in Figures 5.3 and 5.6, the MEA – N 00 / T 15 – 375 has higher performance under both air and oxygen streams. An higher catalyst utilization was found at low temperature (40 °C), Figure 5.3a and 5.6a, but the improved performance extended to the entire E-j curve at low and higher temperatures (60 °C and 80 °C), Figure 5.3b-c and 5.6b-c.

D. Electrochemical Impedance Spectroscopy

The performance of the MEAs was also investigated by electrochemical impedance spectroscopy (EIS) to have a better understanding of the phenomena occurring at the cathode under different operating conditions (low-high overpotential, air-oxygen feed). The impedance spectra were recorded and fitted with the equivalent circuits proposed in the Chapter 3.

The complete DMFC spectra (Nyquist and Bode plots) recorded at 0.5 V, in air and pure oxygen, at 40 °C are presented in Figure 5.7. The Nyquist plots, Figure 5.7a, show the two overlapping semicircles, and negative loop in the lower frequencies region. As previously, the semicircles at high and low frequencies are representative of anodic and cathodic behaviour respectively. The derived kinetic parameters for the cathode (C_{dl}, R_{CT}, R_{CO} and R_{MT}) are reported in Figure 5.8.

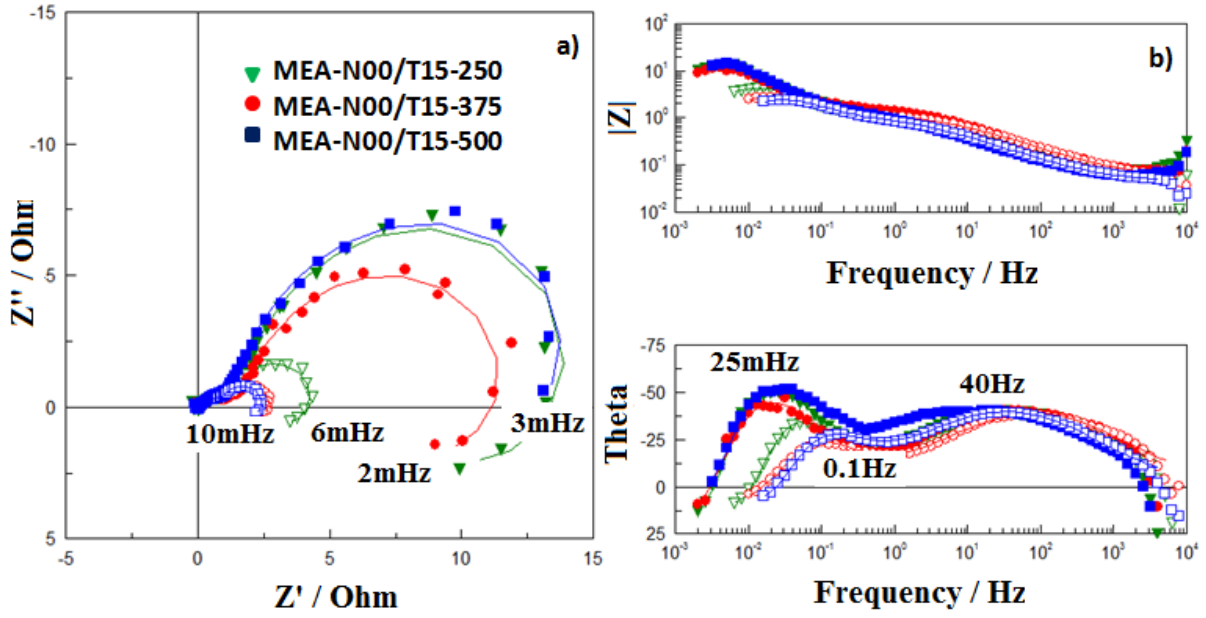

Figure 5.7 : a) Nyquist, b) Bode plots for spectra at 0.5 V under air and O_2 (full and empty marks, respectively).

The MEAs show complete semicircles of different amplitude under air stream, Figure 5.7a. The cathodic total charge-transfer resistance varies between 70.73 ± 3.54 Ωcm^2 and 48.56 ± 2.91 Ωcm^2 with a minimum for MEA – N 00 / T 15 – 375. The cathodic double-layer capacitance increases with decreasing applied pressure (0.37 ± 0.01 Fcm^{-2} at 500 lbs, 0.47 ± 0.02 Fcm^{-2} at 375 lbs, 0.48 ± 0.02 Fcm^{-2} at 250 lbs) as the transport of reactants through the porous structure is facilitated. The high double-layer capacitance and the low Pt-poisoning (L_{CO} and R_{CO}) found for the MEA – N 00 / T 15 – 375 explains the highest catalyst utilization found for this MEA when operated with air (Figure 5.3a).

Concerning the spectra recorded under oxygen feed, the charge-transfer resistances are lower and vary between 19.42 ± 1.33 Ωcm^2 and 8.63 ± 0.66 Ωcm^2 with minimum for MEA – N 00 / T 15 – 500 and MEA – N 00 / T 15 – 375. Lower methanol cross-over (L_{CO} and R_{CO}) from air to oxygen is also observed.

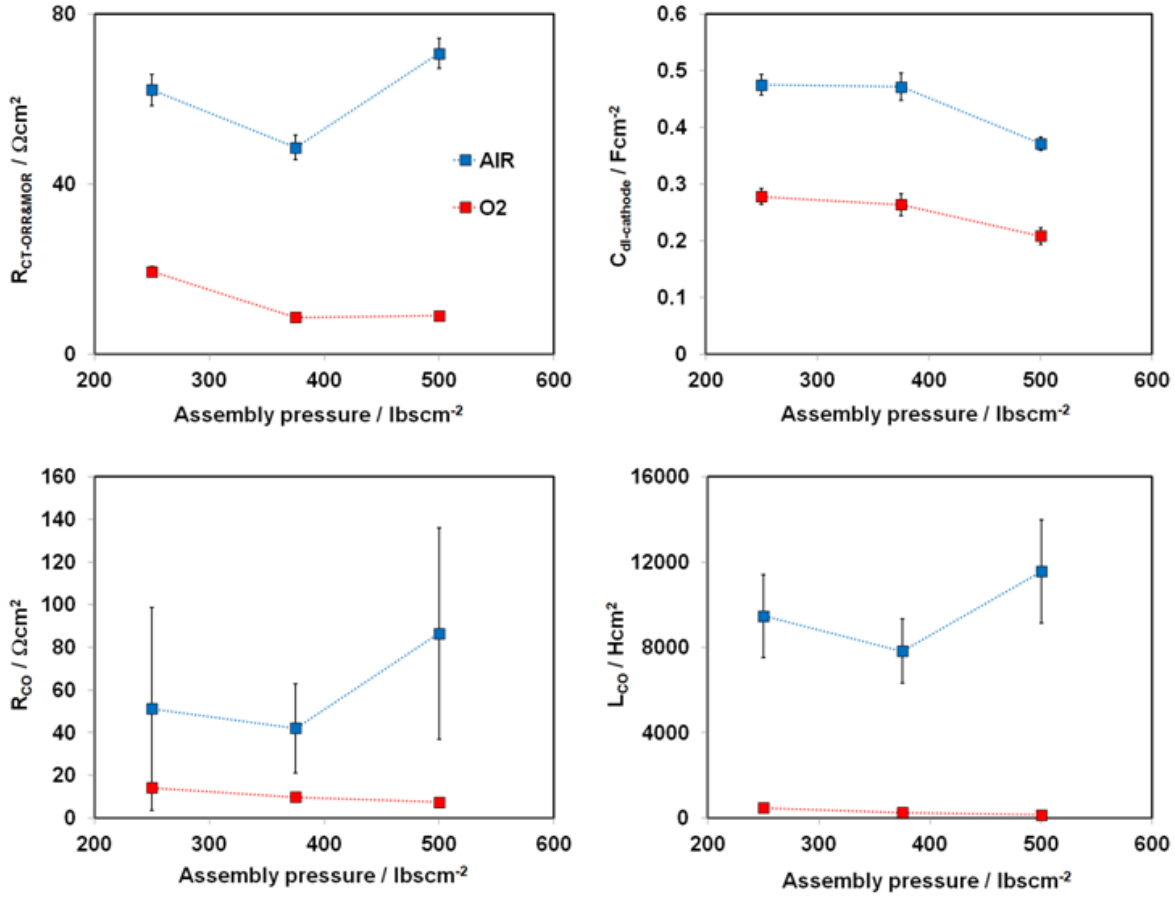

Figure 5.8 : Kinetic parameters at 0.5 V for the DMFC cathodes in function of the assembly pressure.

The complete DMFC spectra (Nyquist and Bode plots) recorded at 0.15 V, in air and pure oxygen, are presented in Figure 5.9. The derived kinetic parameters are reported in Figure 5.10.

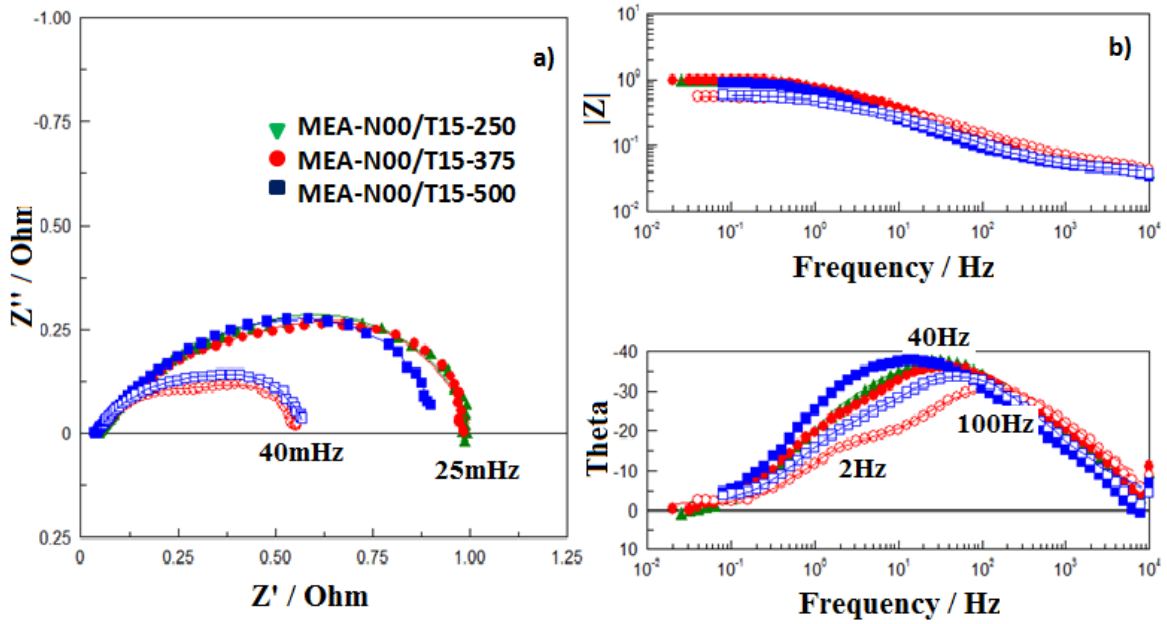

Figure 5.9 : a) Nyquist, b) Bode plots for spectra at 0.15 V under air and O_2 (full and empty marks).

Under both air and oxygen conditions, the semicircles almost overlap, Figure 5.9a. The cathodic charge-transfer resistance measured under air, Figure 5.10, slightly varies between 2.50 ± 0.83 and 1.64 ± 0.03 Ωcm^2, whereas similar values are observed under oxygen (0.86 ± 0.14 and 0.89 ± 0.06 Ωcm^2). In the same way, small variations are observed in the double-layer capacitance with slightly higher values in presence of oxygen (0.10 ± 0.01 and 0.15 ± 0.02 Fcm^{-2}).

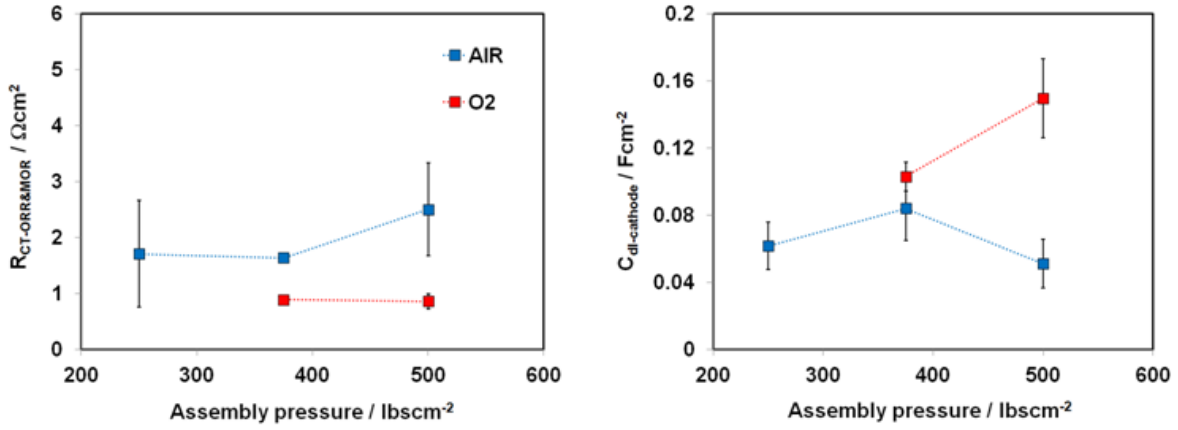

Figure 5.10 : Kinetic parameters at 0.5 V for the DMFC cathodes in function of the assembly pressure.

E. Conclusion

The optimization of the assembly pressure in MEAs equipped with N 00 / T 15 cathodes was investigated. The purpose of this study was to demonstrate that lower assembly pressure can be beneficial to improve the performance of the N 00 / T 15 cathodes' based MEAs due to an easier diffusion of oxygen and protons through the catalyst layers resulting in a higher catalyst utilization at both anode and cathode. Three MEAs, equipped with the same cathode and anode, were prepared using the following pressure: 500 lbs – 375 lbs – 250 lbs. The MEAs were tested with 1 mol dm^{-3} methanol solution at the anode and humidified air and oxygen at the cathode. With respect to the MEA pressed at the standard pressure 500 lbs, the best results were reported for the MEA pressed at 375 lbs:

- Lower cell resistance at 25 °C (0.47 Ωcm^2).
- Higher OCV in all the range of operating temperature (0.58 – 0.63 – 0.67 V at 40, 60 and 80 °C).
- Higher catalyst utilization (activation zone) in the E-j curves recorded at 40 °C under air and oxygen.
- Superior performance over the entire E-j curve at 60 °C and 80 °C (132 and 151 32 $mAcm^{-2}$ at 0.1 V under air).
- Minimum in the cathodic charge-transfer resistance, $R_{CT\text{-}ORR\&MOR}$ (48.56 ± 2.91 Ωcm^2), high double-layer capacitance, $C_{dl\text{-}cathode}$ (0.47 ± 0.02 Fcm^{-2}).

However, a comparison between the performance of MEA – N 00 / T 15 – 375 and a MEA – N 15 / T 00 (Chapter 5) is necessary. The Figure 5.11a-b shows the E-j curves recorded at 40 °C and 80 °C in presence of air. Considering that a fuel cell has to operate at high potential (higher efficiency), the performances are compared at 0.4 V. At low temperature, 40 °C, the MEAs show same performance (16 $mAcm^{-2}$), while at higher temperature, 80 °C, the MEA – N 15 / T 00 performs better (43 vs. 32$mAcm^{-2}$) as expected from the higher hydration of the Nafion-based catalyst layer.

We can conclude that for low temperature fuel cells, the optimization of the assembly pressure is beneficial in improving the catalyst utilization as seen for the MEA – N 00 / T 15. Other

approaches aimed to further improve the performance of the N 00 / T 15 cathode in the high current density region were therefore explored and described in the following section.

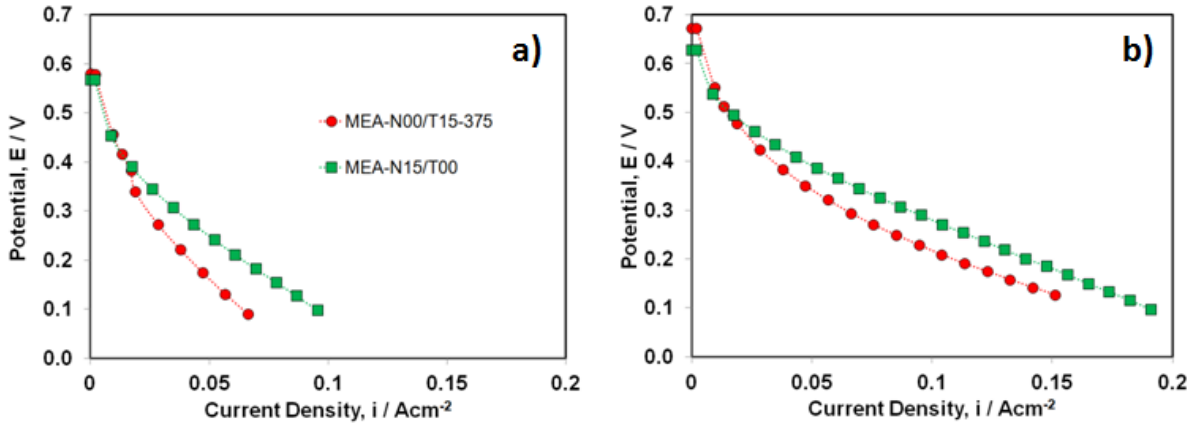

Figure 5.11 : Polarization curves of single DMFCs with 1 moldm^{-3} MeOH at (a) 40 °C and (b) 80 °C.

5.3. Modification of N 00 / T 15 cathode morphology: sintering at 350 °C, TFE-treated support and Nafion coating

Following the optimization of the assembly pressure, other approaches aimed to improve the hydration and the oxygen diffusion of the porous N 00 / T 15 cathode were explored. Three N 00 / T 15 based-cathodes were modified as following: sintering at 350 °C (N 00 / T 15 – 350), deposition of the catalyst layer on a TFE-treated carbon cloth (N 00 / T 15 – TFE), and Nafion coating on the top of the Teflon based catalyst layer (N 00 / T 15 – N 05). The details on the preparation of the cathodes are reported in Chapter 2. The cathodes underwent physicochemical, ex-situ electrochemical and fuel cell characterization.

5.3.1. Physicochemical characterization

A. Thickness

The cathodes' thickness was measured by scanning electron microscopy (SEM) (Chapter 2). The images and cartography of the cross-sections for the N 00 / T 15 – 350, N 00 / T 15 – N 05 and N 00 / T 15 – TFE cathodes are reported in Figure 5.12. Compared to N 00 / T 15 cathode which showed a continuous distribution of Pt along all the cross-section, the N 00 / T 15 – 350 cathode shows catalyst distribution over half of the cross-section. The N 00 / T 15 – N 05 cathode shows a more homogeneous and compact catalyst layer; the Nafion on the top of PTFE-based cathode

coats the electrode and binds all the components of the catalyst layer creating a more homogeneous structure. The deposition of the catalyst layer on the TFE-treated carbon cloth produces a thicker and dense catalyst layer which coats uniformly the fibres on one side of the support.

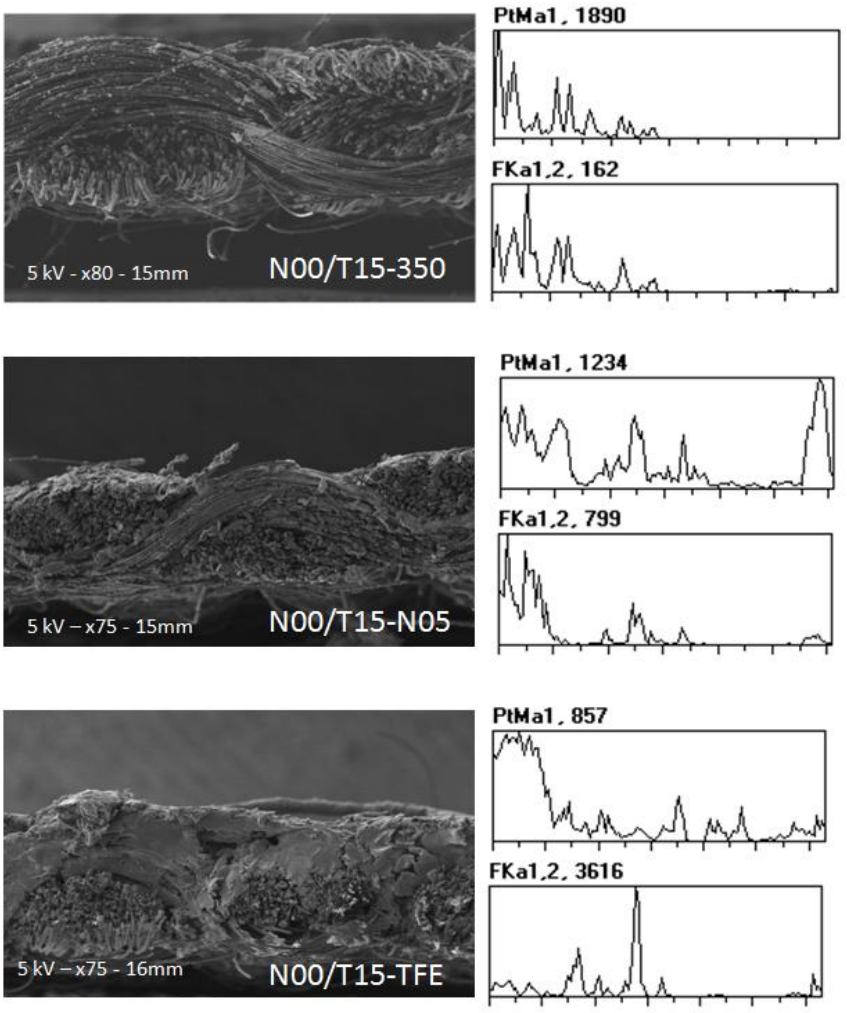

Figure 5.12 : Image and cartography of cathode' cross-sections for the N 00 / T 15-based cathodes.

The Figure 5.13 reports the thickness of the N 00 / T 15 based-cathodes. Data for the TFE-treated carbon cloth is included as reference. The thickness of the cathodes varies between 402 and 460 μm. The sintering process at 350 °C did not change the thickness of the cathode; the Nafion coating has decreased it a little (5 %), while the deposition on the TFE-treated support has increased it slightly (8 %) as expected from the utilization of a thicker support.

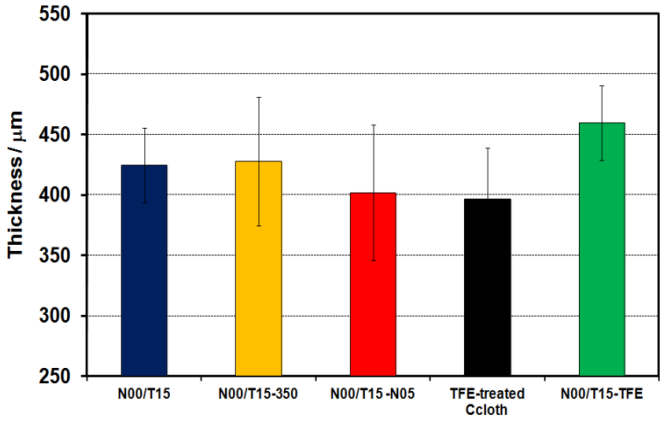

Figure 5.13 : Thickness of the N 00 / T 15-based cathodes.

B. Water uptake

The cathodes' water vapor absorption was determined by Dynamic Vapor Sorption technique while the liquid water absorption was measured by immersion of the sample in water (Chapter 2), Figure 5.14. Data for TFE-treated carbon cloth is included as reference.

The water uptake from the vapor phase is reported in Figure 5.14a. Compared to the N 00 / T 15 cathode, the N 00 / T 15 – 350 and the N 00 / T 15 – TFE cathodes show a gain of water absorption by 20%, whereas the N 00 / T 15 – N 05 has increased by half its water uptake. Comparing to the Nafion-based cathodes reported in the previous chapter, similar values were found between the most hydrophilic and hydrophobic cathodes of this and the previous chapters: N 00 / T 15 – N 05 (1.54 ± 0.32 wt%) vs. N 15 / T 00 (1.60 ± 0.34 wt%), and N 00 / T 15 – TFE (0.97 ± 0.27 wt%) vs. N 05 / T 10 (0.95 ± 0.34 wt%).

The water uptake from the liquid phase is reported in Figure 5.14b. The variations are more pronounced than for water vapor uptake. Compared to N 00 / T 15, the N 00 / T 15 – 350 cathode show a loss of the water absorption capacity by 60 %, while the N 00 / T 15 – PTFE and the N 00 / T 15 – N 05 cathodes report an higher uptake (21.60 ± 1.60 wt% and 33.80 ± 0.90 wt%, respectively). Once again, similar liquid water uptake were found between the most hydrophilic cathodes N 00 / T 15 – N 05 and N 15 / T 00 (32.46 ± 1.86 wt%) and the most hydrophobic cathodes N 00 / T 15 – TFE and N 05 / T 10 (20.59 ± 2.31 wt%).

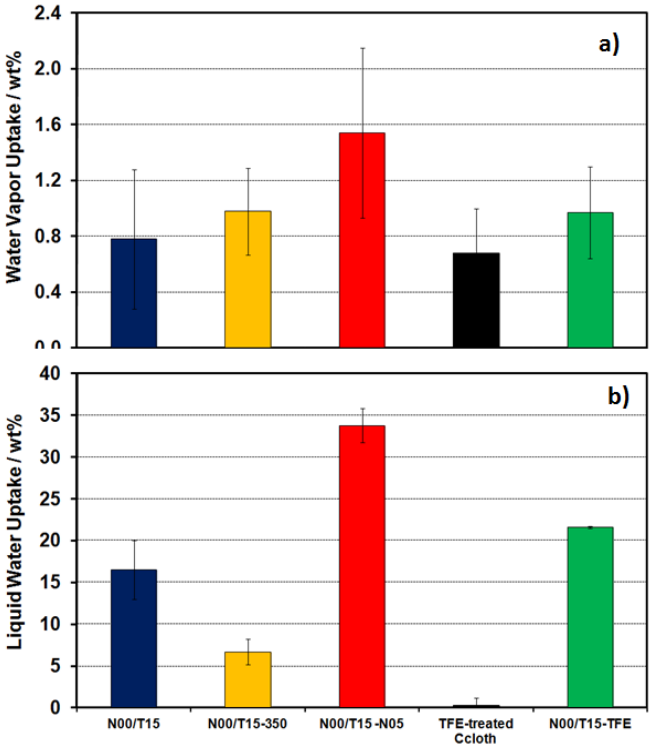

Figure 5.14 : a) Water vapor and b) Liquid water uptakes of the N 00 / T 15-based cathodes.

C. Sessile-drop contact angle

The wetting of the cathode catalyst layer surface was evaluated by the static sessile-drop contact angle measurements (Chapter 2) and the resulting advancing and receding contact angles (ACA – RCA) are reported in Figure 5.15.

The cathodes prepared on untreated carbon cloth support show very low wettability and similar ACA between 124.77° ± 1.62° and 131.67° ± 1.30°. For N 00 / T 15 – N 05, the application of Nafion on the cathode surface does not produce any drastic change in the morphology of the cathode surface. Similar behaviour was observed for the Nafion-based cathodes reported in the previous chapter. Concerning the N 00 / T 15 – 350 cathode, a smaller hysteresis with respect to N 00 / T 15 is observed. This can be related to the sintering process which enhances the hydrophobic characteristics of the catalyst layer (6).

The cathode prepared on TFE-treated carbon cloth support shows higher wettability with respect to the N 00 / T 15 cathode (100.17° ± 2.76° vs. 131.67° ± 1.30°) and N 00 / T 15 – TFE cathode (100.17° ± 2.76° vs. 139.76° ± 1.66°) . The higher wettability of the N 00 / T 15 – 350 cathode is confirmed by the water vapor and liquid water uptake values, and it is suggested that water can

penetrate into the catalyst layer through large pores. The remarked hysteresis (50°) shows that the cathode surface is highly rough. Recalling the result reported in the previous chapter for the Nafion-based cathode, it is suggested that the PTFE binder determines the morphology of the cathode in addition to its hydrophobicity.

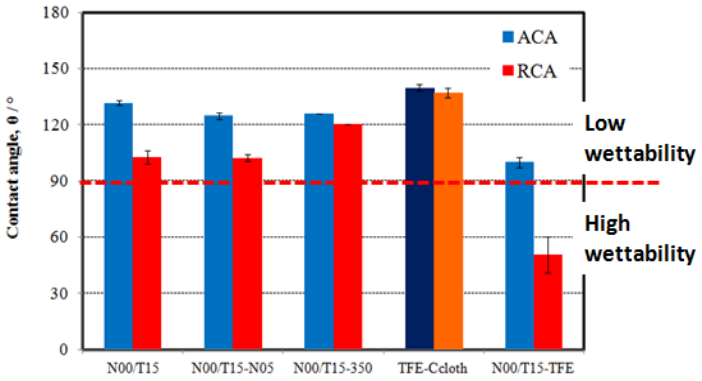

Figure 5.15 : Contact angles of the N 00 / T 15-based cathodes.

D. Total pore volume

The cathodes' total pore volume as determined from the nitrogen sorption isotherms (Chapter 2) is presented in Figure 5.16. The N 00 / T 15 – TFE and N 00 / T 15 – N 05 cathodes show only a slight variation of the total pore volume with respect to the N 00 / T 15 cathode (0.07 cm^3g^{-1} and 0.09 cm^3g^{-1} versus 0.08 cm^3g^{-1}), whereas for the N 00 / T 15 – 350, the total pore volume has decreased by half (0.04 cm^3g^{-1}). The loss of porosity for this cathode is in agreement with the results reported in Figures 5.14 and 5.15 and explains its lower liquid water uptake.

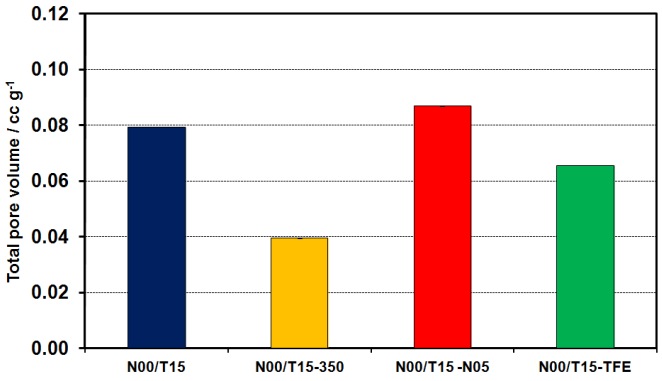

Figure 5.16 : Total pore volume of the N 00 / T 15-based cathodes.

The physicochemical characterization of the N 00 / T 15-based cathodes has showed that there is a positive effect in coating the N 00 / T 15 cathode with Nafion or in using a TFE-treated support for the catalyst layer deposition whereas no benefit results from sintering the cathode at 350 °C. After the "Nafion coating" and the "TFE-treated support" treatments, the total micro- and meso-porosities of the cathodes remain unvaried. However, the cathode water uptakes are improved and evident changes are occurred in the morphology of N 00 / T 15 – TFE cathode. For these cathodes it is expected an higher catalyst utilization. On the contrary, the sintering process reduces the porosity and the hydrophilicity of the cathode and a lower catalyst utilization is expected.

5.3.2. Ex-situ electrochemical characterization

The N 00 / T 15 based-cathodes were electrochemically characterized in nitrogen and oxygen saturated 0.5 $moldm^{-3}$ sulphuric acid solutions to determine: the platinum utilization and the electrochemical surface area, the double layer capacitance, the resistance to the ionic transport through the catalyst layer, the limiting current for the oxygen reduction reaction.

A. Pt utilization and Electrochemical Surface Area

The Figure 5.17 shows the cyclic voltammogram of the N 00 / T 15 and N 00 / T 15 – N 05 cathodes. As expected, the typical shape of a polycrystalline platinum electrode: the hydrogen adsorption and desorption peaks are clearly identified in the potential interval between -0.28 V and 0 V, the oxidation peaks of platinum between 0.6 – 0.9 V, and the platinum oxide reduction peaks between 0.2 – 0.7 V. As shown in Figure 5.17, the cyclic voltammogram of N 00 / T 15 – N 05 cathode shows higher current density indicating higher catalyst utilization respect to the N 00 / T 15 cathode.

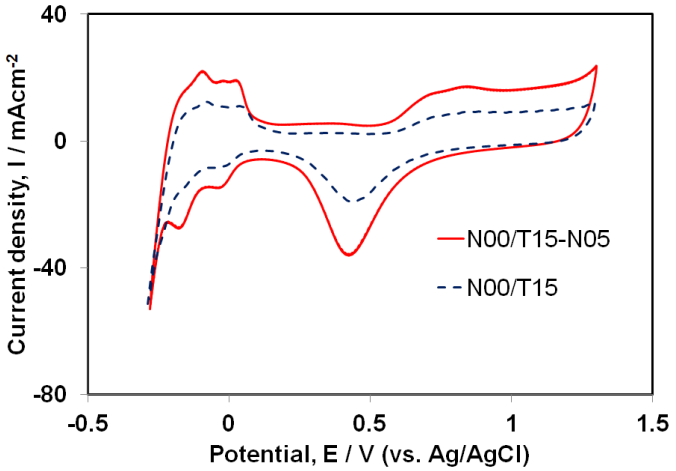

Figure 5.17 : Cyclic voltammogram (10^{th} cycle) in N_2 sat. 0.5 $moldm^{-3}$ H_2SO_4, recorded at 20 mV s^{-1}.

The Pt electrochemical surface areas were calculated from the charge of the hydrogen adsorption peaks developed during the cathodic sweep after correction of the double layer charging base line. The *ESA* (m^2g^{-1}) values were used to determine the Pt utilization. The average *ESA* and Pt utilization values determined for the cathodes are reported in Figure 5.18. It was found that the ESA varied between 2.02 ± 0.01 and 24.60 ± 1.70 m^2g^{-1} and the Pt utilization varied between 2.60 ± 0.20 and 31.70 ± 4.40 %.

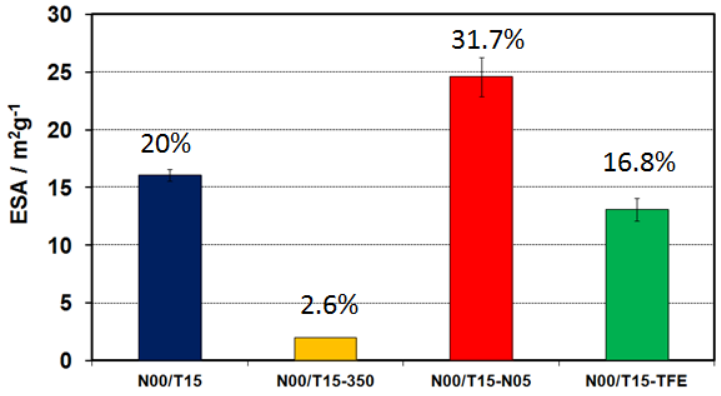

Figure 5.18 : ESA and Pt utilization estimated for the N 00 / T 15-based cathodes.

The Figure 5.19 reports the ESA and Pt utilization as a function of the liquid water uptake. The ESA and Pt utilization increase with the hydrophilicity of the cathodes, as expected, and are higher for the N 00 / T 15 – N 05 cathode. Despite the relatively high water uptake, the N 00 / T 15 – TFE cathode shows a lower ESA value respect to the N 00 / T 15 cathode which can be explained considering its lower total pore volume, Figure 5.20. As shown in the graph, the ESA

follows the variation of the total pore volume for all cathodes except for the N 00 / T 15 – N 05 which shows a sharp increase of the ESA. From the Figure 5.19 and 5.20 it can be conclude that both the hydrophilicity and the morphology of the cathodes contribute to the catalyst utilization. Indeed, N 00 / T 15 – N 05 shows superior Pt utilization than the N 15 / T 00 cathode, Figure 5.20.

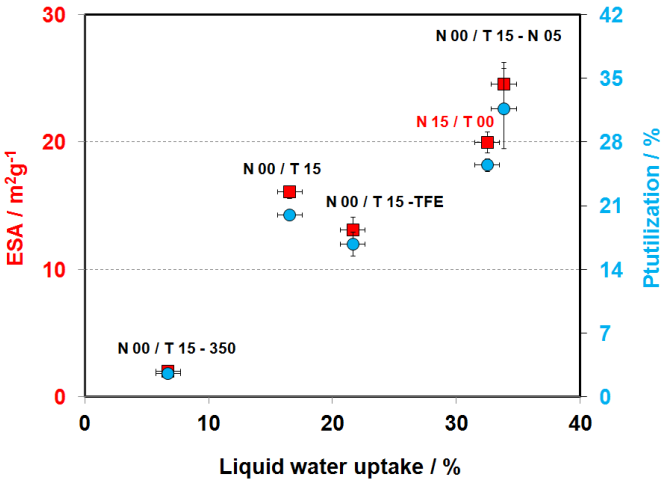

Figure 5.19 : ESA (■) and Pt utilization (●) vs. liquid water uptake.

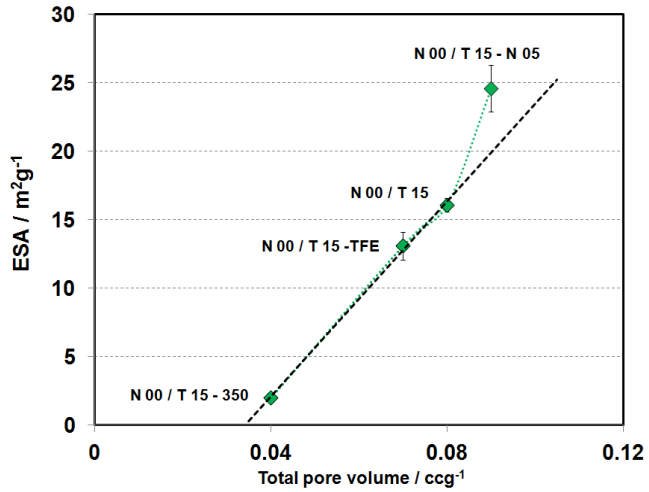

Figure 5.20 : ESA vs. BET total pore volume.

B. Double-Layer Capacitance and Ionic Resistance

The extent of the double layer formed between the cathode and the electrolyte solution, and the resistance for the ionic transport through the catalyst layer were determined by electrochemical

impedance spectroscopy. The impedance spectra were recorded at in the center of the capacitance zone. The Figure 5.21 shows the impedance spectra (Nyquist and Bode plots) corrected to the serial resistance of the N 00 / T 15, N 00 / T 15 – 350, N 00 / T 15 – TFE and N 00 / T 15 – N 05 cathodes. The lower part of Figure 5.21 shows a zoom of the high frequency region for the N 00 /T 15 – N 05 cathode. The spectra show at high frequency the characteristic Warburg impedance for the ion transport through a porous electrode structure and at low frequencies the capacitive element.

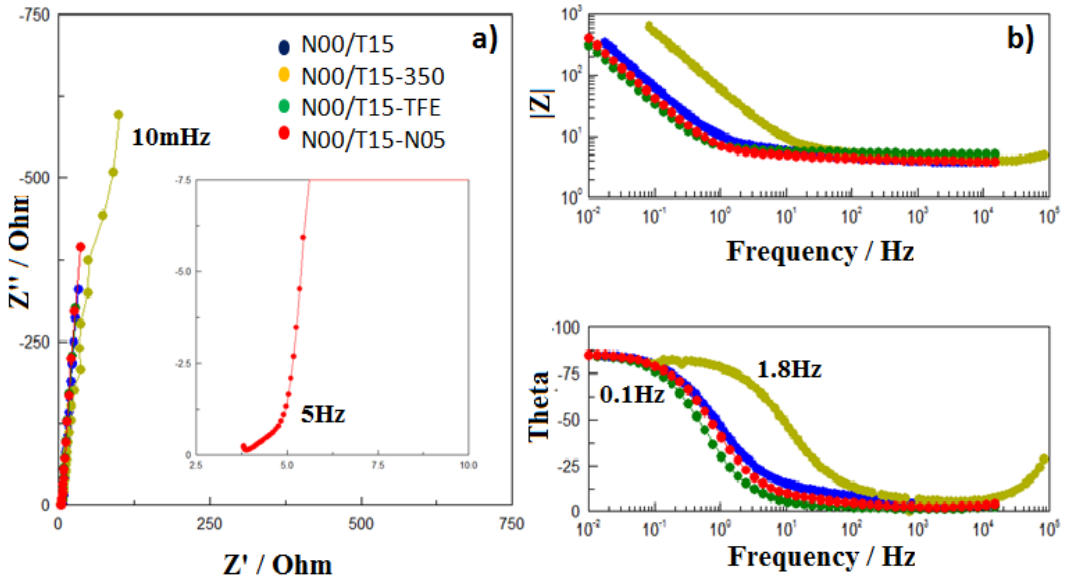

Figure 5.21 : Electrochemical impedance spectra recorded at 0.2 V (vs. Ag/AgCl), a) Nyquist b) Bode plots.

Figure 5.22 reports the *Cdl* and the *Rionic* for the four N 00 / T 15 based-cathodes. The capacitance varies between 6.89 ± 0.04 and 181.50 ± 21.9 $mFcm^{-2}$, with lowest value for the N 00 / T 15 – 350 cathode, and the highest values for N 00 / T 15 – N 05 and N 00 / T 15 – TFE cathodes. On the other hand, the resistance to the proton transport in the cathode catalyst layer varies between 3.20 ± 0.80 and 6.59 ± 0.51 Ωcm^2 with lower values for the N 00 / T 15 – N 05 and N 00 / T 15 – TFE cathodes. Since these cathodes have showed similar porosity, similar values of ionic resistance were expected. However, the higher water uptake of the N 00 / T 15 – N 05 accounts for the higher proton conduction through its porous structure. Compared to the previous results, this cathode shows an ionic resistance twenty times smaller than the N 15 / T 00 cathode and an almost two times the capacitance (Chapter 5).

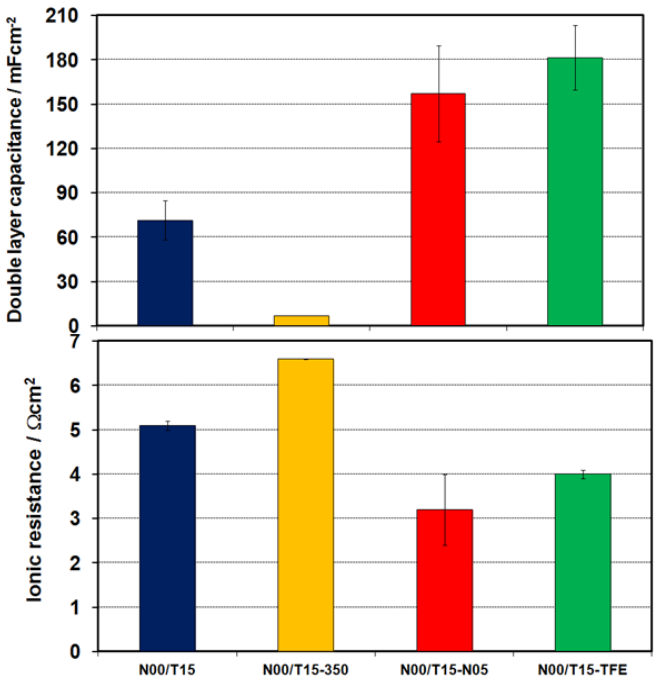

Figure 5.22 : Double layer capacitance and ionic resistance for the N 00 / T 15-based cathodes.

C. Oxygen Reduction Reaction

The activity of the cathodes towards the ORR was investigated by the meaning of linear sweep voltammetry and impedance spectroscopy. As reported in Chapter 3, the higher limiting-current of the N 00 / T 15 cathode compared to the Nafion-based cathodes demonstrated the benefits of using PTFE in the cathode catalyst layer. The Figure 5.23 shows the linear voltammograms of the N 00 / T15-based cathodes in the range of potential 1 – 0 V. The onset potential was found to be ca. 0.7V for all four cathodes, but the electrodes have a distinct behavior at higher overpotential. The N 00 / T 15 cathode has the lowest limiting current (40 $mAcm^{-2}$). Higher values of current density and no evidence of a limiting-current were found for N 00 / T 15 – 350 and N 00 / T 15 – TFE cathodes, but the overpotential for the ORR is clearly very high. A remarkably higher value of limiting current (300 $mAcm^{-2}$) and low overpotential were observed for the N 00 / T 15 – N 05 cathode clearly demonstrating the benefit of combining the Nafion coating (higher catalyst utilization) on a PTFE-based cathode (low Rionic and low tendency to flood).

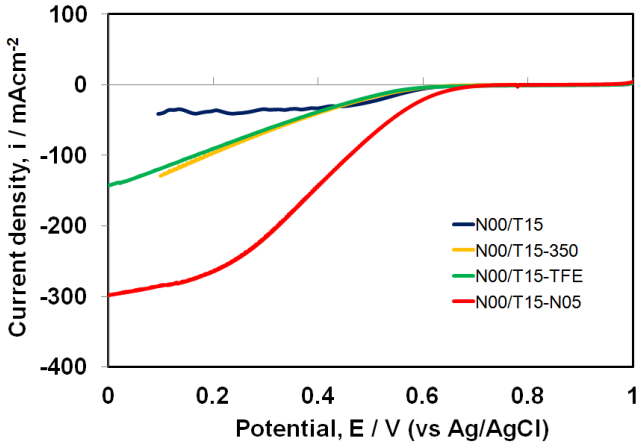

Figure 5.23 : Linear sweep voltammetry in O_2 sat. 0.5 mol dm^{-3} H_2SO_4, recorded at 5 mVs^{-1}.

The variation of the current density at 0.1 V as a function of the liquid water uptake of the cathodes is reported in Figure 5.24. In opposition to what observe for the series I of Nafion/PTFE-based cathodes (Chapter 5), here the current density increases with the liquid water uptake with a maximum for the N 00 / T 15 – N 05 cathode. This trend confirms once again that there are variations in the morphology of the PTFE-based cathode and shows that the water uptake cannot be used as a parameter to anticipate the flooding of the cathodes.

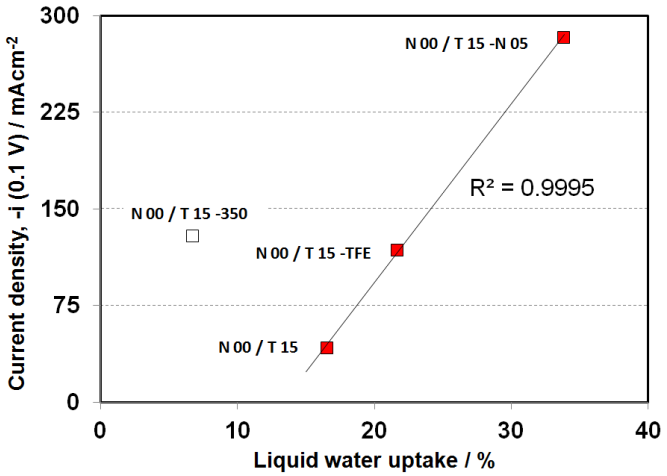

Figure 5.24 : Current density at 0.1 V vs. liquid water uptake.

The ohmic resistance was determined from the slope of ORR polarization curves. An higher resistance was found for the N 00 / T 15 cathode (5.3 Ωcm^2), lower values were observed for the N 00 / T 15 – 350 and N 00 / T 15 – TFE (3.5 – 3.6 Ωcm^2), whereas the minimum was measured for the N 00 / T 15 – N 05 cathode (1.4 Ωcm^2). The variation of the ohmic resistance as a

function of the ionic resistance through the catalyst layer (from impedance measurements in N_2 saturated sulphuric acid solution) is presented in Figure 5.25. Except for the N 00 / T 15 – 350, there is a linear relationship between the two parameters with minimum for the N 00 / T 15 – N 05 cathode. It can be concluded, that the addition of Nafion on the top of the PTFE-based cathode allows higher protons diffusion into the catalytic sites, therefore the ORR is favored and higher current densities are reached.

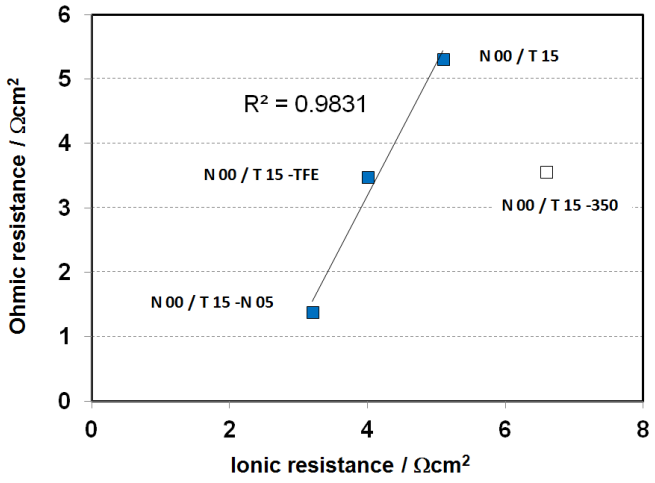

Figure 5.25 : Ohmic resistance estimated from ORR curves vs. ionic resistance estimated from impedance measurements in N_2 sat. H_2SO_4 solution.

A further investigation on the performance of the cathodes towards the ORR was done by impedance spectroscopy. Impedance spectra were recorded at 0.65 V (activation zone of the polarization curve) and 0.3 V (mass transport control zone); the kinetic parameters derived from the fitting of the spectra (Chapter 3) are reported in Table 5.1.

The Nyquist and Bode plots of spectra recorded at 0.65 V are reported in Figure 5.26. Very high values of charge-transfer resistance were estimated for the N 00 / T 15 – TFE and N 00 / T 15 – 350 cathodes (496.43 ± 7.41 Ωcm^2 and 93.11 ± 0.00 Ωcm^2), whereas for N 00 / T 15 and N 00 / T 15 – N 05 were considerably smaller (49.44 ± 0.56 Ωcm^2 and 25.61 ± 1.02 Ωcm^2, respectively). The maximum C_{dl} was measured for N 00 / T 15 – N 05 cathode (116 ± 0.02 $mFcm^{-2}$), whereas lower values between 21.72 $mFcm^{-2}$ and 66.29 ± 0.43 $mFcm^{-2}$ were found for the other cathodes. This result is consistent with the voltammetric study which showed an higher catalyst utilization for N 00 / T 15 – N 05. Concerning the theta phase Bode plot, Figure 5.26b, the combined effect of the charge-transfer resistance and the double-layer capacitance is visible

in the shift of the maximum. The high value of R_{CT} found for N 00 / T 15 – TFE shifts the theta maximum to very low frequencies (0.07 Hz).

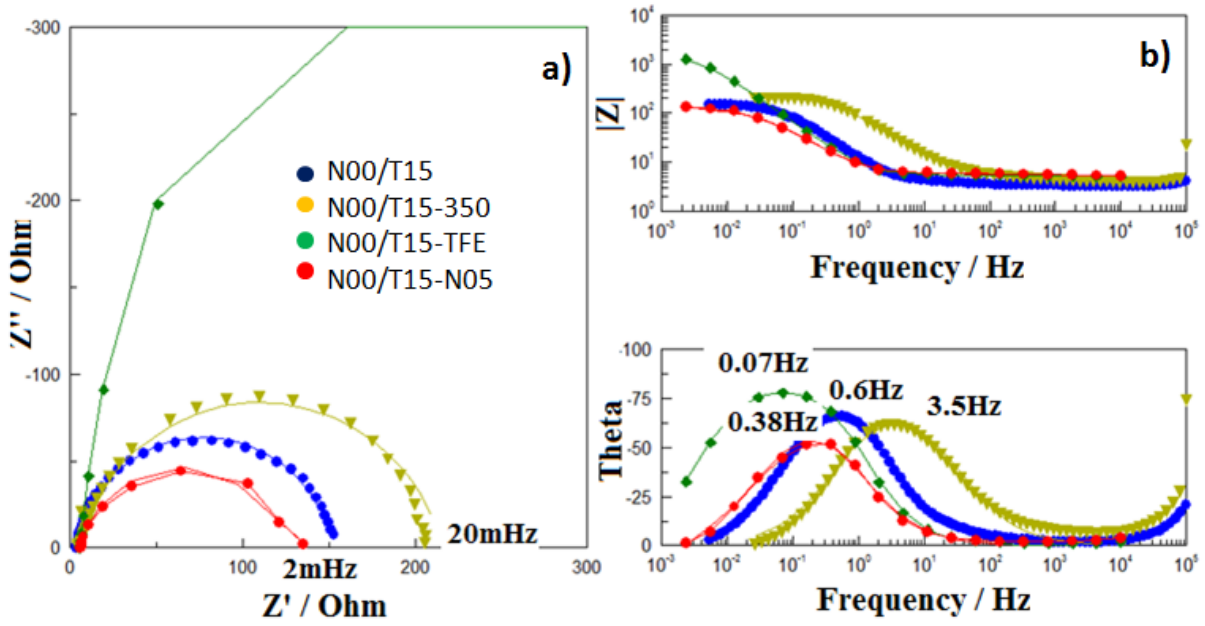

Figure 5.26 : Impedance spectra in O_2 sat. 0.5 mol dm^{-3} H_2SO_4 at 0.65 V, a) Nyquist b) Bode plots).

The EIS spectra recorded at 0.3 V are presented in Figures 5.27. Completed semicircles with small amplitude were recorded for the N 00 / T 15 - TFE and N 00 / T 15 – 350 cathodes, whereas an uncompleted semicircle reflecting oxygen diffusion limitations was observed for the N 00 / T 15 – N 05 cathode. The charge-transfer resistance varies between 10.54 ± 0.20 Ωcm^2 and 2.24 ± 0.07 Ωcm^2 with a minimum for the N 00 / T 15 – TFE cathode which reflects the benefit of using an hydrophobic support to avoid the early flooding phenomena. The highest capacitance is reported for the N 00 / T 15 – N 05 cathode (170.7 ± 0.04 $mFcm^{-2}$) and this is in agreement with the higher performance observed in the ORR polarization curves (Figure 5.23). Again, the combined effect of the charge-transfer resistance and the double-layer capacitance is visible in the shift of the maximum in the theta Bode plot. The low R_{CT} and C_{dl} values for N 00 / T 15 – 350 justify the shift towards higher frequencies.

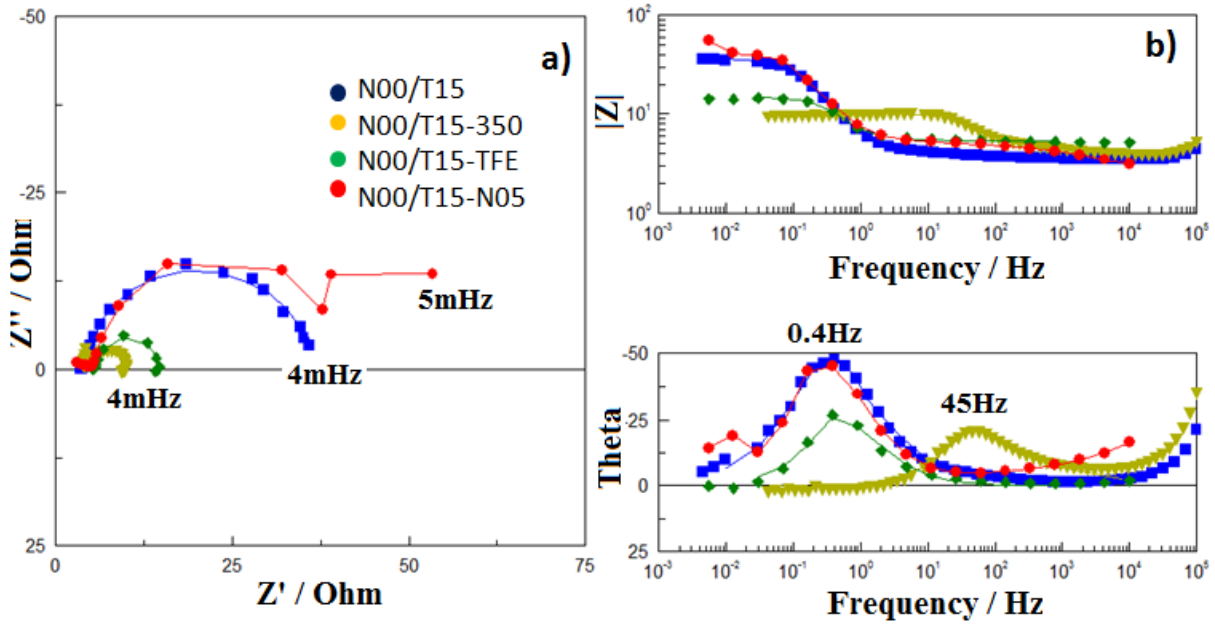

Figure 5.27 : Impedance spectra in O_2 sat. 0.5 mol dm^{-3} H_2SO_4 at 0.3 V, a) Nyquist b) Bode plots).

Table 5.1 : EIS parameter for PTFE-based cathodes in 0.5 moldm^{-3} H_2SO_4 at 0.65 V and 0.3 V.

	0.65 V		**0.3 V**	
Cathode	**$R_{CT\text{-}ORR}$ / Ωcm^2**	**C_{dl} / mFcm^{-2}**	**$R_{CT\text{-}ORR}$ / Ωcm^2**	**C_{dl} / mFcm^{-2}**
N00/T15	49.44 ± 0.56	35.06 ± 0.38	10.54 ± 0.20	96.29 ± 0.23
N00/T15 – 350	93.11 ± 0.00	21.72 ± 0.00	2.43 ± 0.04	17.39 ± 0.00
N00/T15 – TFE	493.43 ± 7.41	66.29 ± 0.04	2.24 ± 0.07	145.4 ± 0.07
N00/T15 – N05	25.61 ± 1.02	116 ± 0.02	7.24 ± 0.22	170.7 ± 0.04

The benefits of the Nafion coating and deposition of the catalyst layer on a TFE-treated carbon cloth on the performance of the cathodes were investigated in the fuel cell system and the results will be presented in the next paragraph. Since advantages in using the N 00 / T 15 – 350 cathode were not reported, the DMFC performance of this cathode was not investigated.

5.3.3. DMFC characterization

The DMFC performance of MEAs containing the N 00 / T 15 – N 05 and N 00 / T 15 – TFE cathodes was investigated to verify if the Nafion coating and/or deposition of the catalyst layer on

a TFE-treated carbon cloth can improve the performance of the N 00 / T 15 cathode. The MEAs were prepared at the optimized pressure 375 lbs and compared to the MEA – N 00 / T 15 - 375.

A. Conditioning and cell resistance

The variation of the OCV over time for the single DMFCs equipped with MEA – N 00 / T 15 – N 05, MEA – N 00 / T 15 – TFE and MEA – N 00 / T 15 – 375 is reported in Figure 5.28. The period for the conditioning varied between 1 hour and 1 hour and 20 minutes, but after 30 minutes the single DMFCs showed already a distinct behaviour. The OCV of the DMFC equipped with MEA – N 00 / T 15 – N 05 increased sharply to 96% of its final value (0.508 V), while for the DMFC equipped with MEA – N 00 / T 15 – 375 the variation was less abrupt and the OCV was only 85% of its final value. For the DMFC with the MEA – N 00 / T 15 – TFE, the conditioning required more time and in the first 30 minutes the OCV increased only to the 16% of its final value (0.493 V). The lower equilibration time of the MEA – N 00 / T 15 – N 05 is consistent with the higher water uptake and catalyst utilization (from ex-situ cyclic voltammetry) found for this cathode. The cell resistance was measured at the end of the conditioning process and varied between 0.47 Ωcm^2 and 0.52 Ωcm^2.

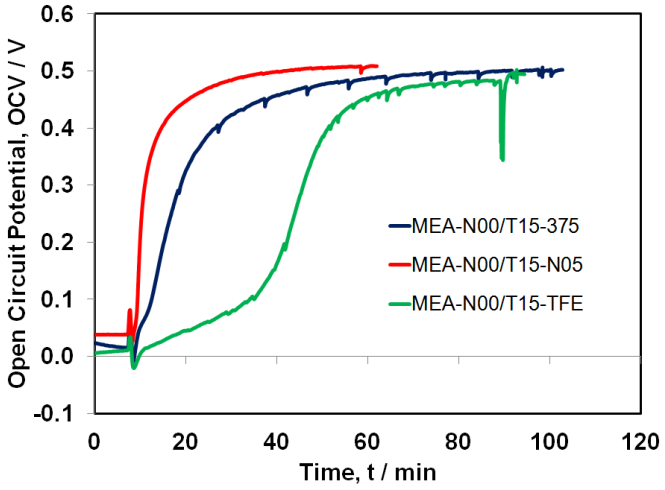

Figure 5.28 : Open circuit voltage over time for DMFCs in presence of air (220 $ccmin^{-1}$,atmospheric pressure) and 1 $moldm^{-3}$ MeOH solution at 25 °C.

B. Polarization curves under air

The Figure 5.29 reports the polarization curves recorded at 40 °C, 60 °C and 80 °C during the second temperature cycle.

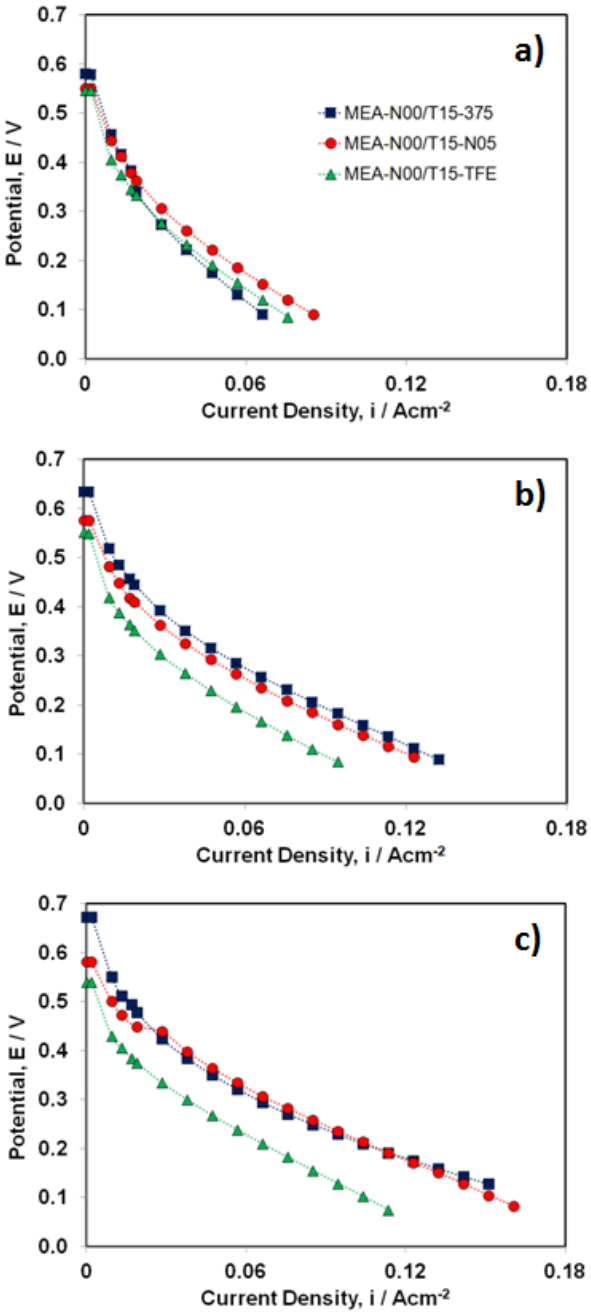

Figure 5.29 : Polarization curves recorded under air (220 cc min^{-1}) at (a) 40 °C, (b) 60 °C, (c) 80 °C.

At 40 °C, Figure 5.29a, the MEA – N 00 / T 15 – 375 shows higher OCV (0.58 V vs. 0.55 V) and same catalyst utilization (activation zone) than MEA – N 00 / T 15 – N 05 but higher performance in the ohmic region is found for MEA – N 00 / T 15 – N 05. At 60 °C, Figure 5.29b, the MEA – N 00 / T 15 – 375 shows the highest OCV (0.63 V) and performs slightly better than

the MEA – N 00 / T 15 – N 05, whereas MEA – N 00 / T 15 – TFE shows a lower E-j curve. At 80 °C, Figure 5.29c, the MEA – N 00 / T 15 – 375 shows a further increase of the OCV (0.67 V) and higher catalyst utilization, whereas it performs as MEA – N 00 / T 15 – N 05 in the rest of the E-j curve. Again, the MEA – N 00 / T 15 – TFE shows lower performance.

The variation of the open circuit potential as a function of the temperature is reported in Figure 5.30. The DMFCs equipped with the three MEAs show distinguish behaviours. The MEA – N 00 / T 15 – TFE reports same OCV (0.55 V) at 40 °C and 60 °C and it starts to decrease when the temperature rises to 80 °C. The OCV of MEA – N 00 / T 15 – N 05 increase from 40 °C to 60 °C (0.55 V to 0.58 V) and it remains constant. A distinct behaviour is observed for the MEA – N 00 / T 15 – 375 which shows higher and increasing OCV values in all the range of temperature. As for the polarization curves reported in Figure 5.29, the constant increase of the OCV indicates higher catalyst utilization at the anode and the cathode and a lower rate of methanol cross-over. From these results it can be concluded that reducing the assembly pressure is more beneficial in improving the catalyst utilization in the MEA - N 00 / T 15 compared to coating the cathode with Nafion, or to deposit the cathode catalyst layer on a TFE-treated carbon cloth.

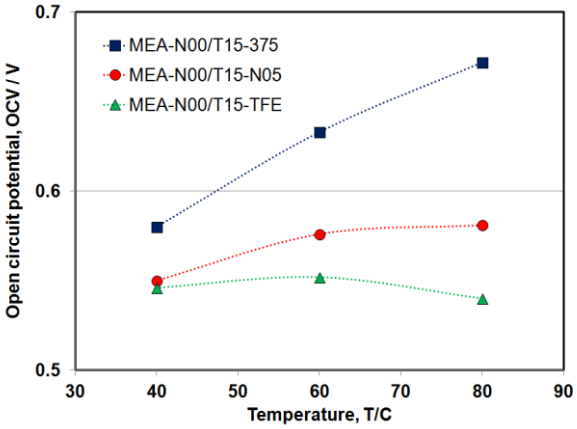

Figure 5.30 : Open circuit potential of single DMFCs measured at 40 °C, 60 °C and 80 °C.

The current density at 0.1 V and 40 °C correlated to the cathodes' water vapor uptake is reported in Figure 5.31. The current density increases with the water vapor uptake of the cathodes with a maximum for the MEA – N 00 / T 15 – N 05 (85 $mAcm^{-2}$). As expected, the higher water uptake and catalyst utilization of the N 00 / T 15 – N 05 cathode allowed higher performance for this MEA when operated at the low temperature of 40 °C.

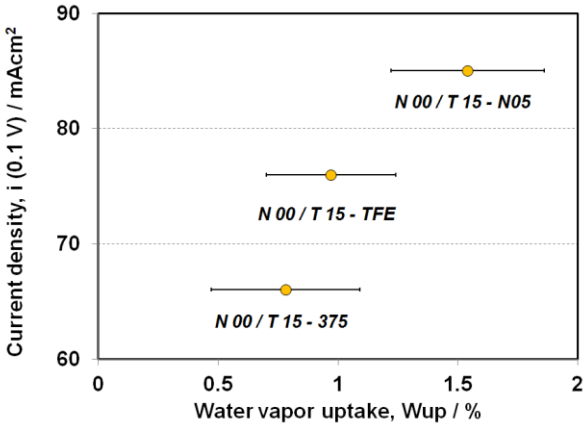

Figure 5.31 : Current density (0.1 V) at 40 °C vs. water vapor uptake cathodes.

C. Polarization curves under O_2 and oxygen gain

The performance of the MEAs was further investigated recording polarization curves under oxygen stream, Figure 5.32. The oxygen stoichiometry was kept the same with respect to the tests in air; as expected, due to the higher oxygen partial pressure the performance of the fuel cells, in terms of OCV, catalyst utilization and current densities, improved with respect to the ones recorded under air stream (Figure 5.29a). However, the most significant improvement was seen on the MEA – N 00 / T 15 – N 05 which performed better than the MEA – N 00 / T 15. The higher water uptake of the N 00 / T 15 – N 05 cathode and its high catalyst utilization have a positive effect on the performance of MEA – N 00 / T 15 – N 05 when the DMFC is operated at 40 °C. On the contrary, the low catalyst utilization found for the N 00 /T 15 – TFE cathode (16.80 ± 1.30 %) limits the performance of the MEA – N 00 / T 15 – TFE.

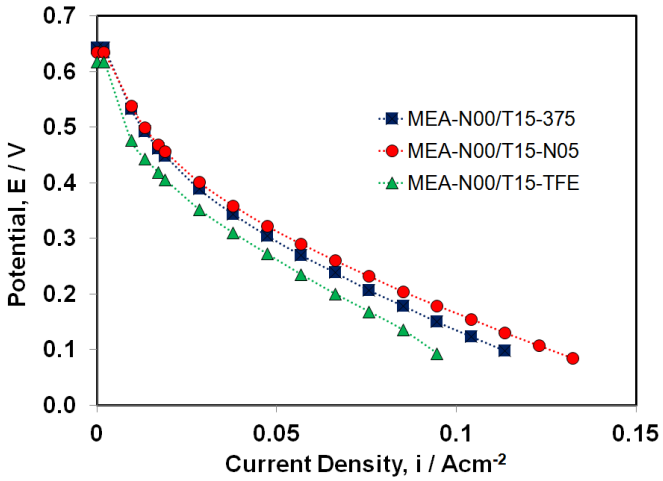

Figure 5.32 : Polarization curves recorded under O_2 (48 $ccmin^{-1}$) at 40 °C.

As explained in the Chapter 4, the oxygen gain is used to estimate the voltage loss associated with mass transport in the cathode operating with air and is evaluated in the 20 – 80 $mAcm^{-2}$ current density interval, where the methanol crossover is negligible. For all three MEAs the oxygen gain, Figure 5.33, increases with the current density. Lowest oxygen gain (80 mV) is observed in the MEA – N 00 / T 15 – TFE for which the deposition of the catalyst layer on a TFE-treated carbon cloth should have improved the support of oxygen to the catalytic sites; however, this result may be also an artifact. In fact, the low catalyst utilization in N 00 /T 15 – TFE cathode limits the performance under oxygen and that can be responsible of this low oxygen gain. On the contrary, the highest and very pronounced increase of the oxygen gain with the current observed for the MEA – N 00 / T 15 - 375 was expected from the low performance reported in Figure 5.29a. The higher proton conduction and the higher catalyst utilization observed for the N 00 / T 15 – N 05 cathode explain the lower oxygen gain of MEA – N 00 / T 15 – N 05 with respect to MEA – N 00 / T 15 – 375. This is quite in agreement with the results observed in the previous chapter, where the Nafion based-cathodes showed much lower and less pronounced oxygen gain than the N 00 / T 15 cathode.

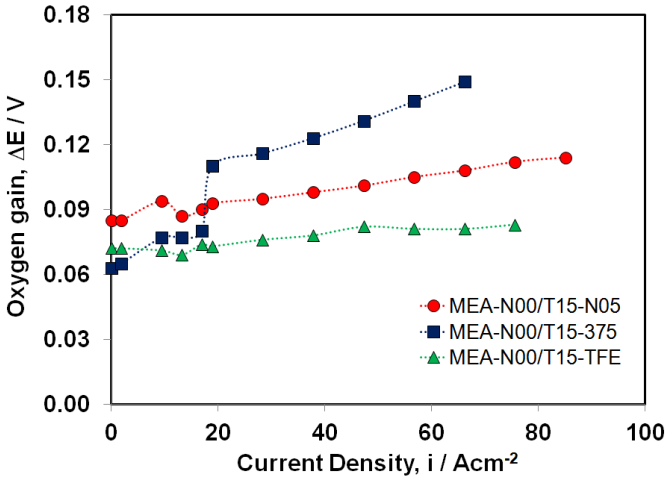

Figure 5.33 : Oxygen gain for single DMFCs at 40 °C.

D. Electrochemical impedance spectroscopy

The performance of the MEAs was investigated by impedance spectroscopy. The spectra were recorded at different potentials (0.5 – 0.4 – 0.3 – 0.2 – 0.1 V) in presence of air and oxygen and

fitted with equivalent circuits (Chapter 3). The cathodic kinetic parameters (C_{dl}, R_{CT}) derived from the spectra recorded in presence of oxygen are reported in Figure 5.34. As expected, the cathodic charge-transfer resistance decreases with the applied potential. Higher values are observed for the MEA – N 00 / T 15 – TFE (between 19.54 ± 0.86 and 1.89 ± 0.19 Ωcm^2) and with a slight increase at high overpotential (2.50 ± 0.33 Ωcm^2). Similar values are observed for MEA – N 00 / T 15 and MEA – N 00 / T 15 – N05 in all range of applied potentials (between 8.63 ± 0.66 and 0.85 ± 0.03 Ωcm^2). The cathodic double-layer capacitance decreases with the applied potential as well. At 0.5 V, it is similar for the three MEAs (0.30 ± 0.02 Fcm^{-2}) and it is much smaller for MEA – N 00 / T 15 – TFE at lower potentials (0.024 ± 0.005 Fcm^{-2} at 0.2 V and 0.004 ± 0.002 Fcm^{-2} at 0.1 V). The increase of the charge-transfer resistance (from 0.2 to 0.1 V) and the low capacitance show that the MEA – N 00 / T 15 – TFE suffers from mass-transport diffusion limitations at high overpotential. This is in agreement with the low performance of this MEA under oxygen (Figure 5.33) and its oxygen gain (Figure 5.32).

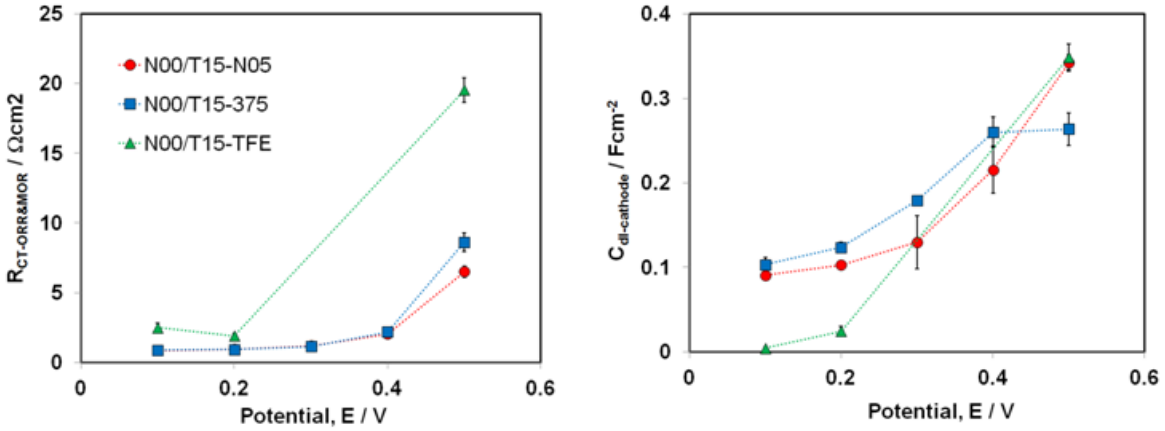

Figure 5.34 : Kinetic parameters in O_2 for the DMFC cathodes in function of the potential.

5.4. Conclusions

N 00 / T 15 based-cathodes were modified using the following treatments: sintering at 350 °C, deposition on a TFE-treated carbon cloth and Nafion coating. This study aimed to investigate which treatment may be beneficial at improving the fuel cell performance through enhancing the hydration, the porosity and the Pt utilization of the N 00 / T 15 cathode.

- The physicochemical characterization showed that there is a positive effect in coating the N 00 / T 15 cathode with Nafion or in using a TFE-treated support for the catalyst layer deposition whereas no particular benefit results from sintering the cathode at 350 °C. The water uptake of the N 00 / T 15 – N 05 and N 00 / T 15 – TFE cathodes improved (32.46 ± 1.86 and 20.59 ± 2.31 wt%, respectively), the morphology of the N 00 / T 15 – TFE cathode showed changes and the total micro- and meso-pore volume of the cathodes remains almost unvaried (0.07 - 0.09 cm^3g^{-1}). On the contrary, the sintering process reduces the water capacity of the cathode by 60% and its porosity (0.04 cm^3g^{-1}).
- The electrochemical characterization has shown higher Pt utilization (31.70 ± 4.40 %), capacitance (181.50 ± 21.9 $mFcm^{-2}$), ionic resistance (3.20 ± 0.80 Ωcm^2) and current density of the ORR (300 $mAcm^{-2}$ at 0.1 V) for the most hydrophilic cathode N 00 / T 15 – N 05. However, in the impedance spectra recorded at 0.3 V the cathode showed evidence of diffusion problems at 0.3 V.
- The DMFC characterization of the MEAs prepared with the optimized pressure 375 lbs shown that the replacement of the N 00 / T 15 cathode with the N 00 / T 15 – N 05 cathode allowed a small improvement of the DMFC performance at 40 °C. In fact, the higher water uptake and catalyst utilization of the N 00 / T 15 – N 05 cathode guaranties a higher proton conduction inside the cathode catalyst layer and higher current densities in the E-j curves are reached. However, the lack of linearity shown in Figure 6.31, revealed that the structure of this cathode is not optimized. A higher and selected porosity of the cathode catalyst layer is required to take completely advantage of the higher water uptake and optimize the performance of this cathode. Pore formers can be suggest to improve the porosity of the cathode catalyst layer and their possible application will be evaluated.

  Concerning the utilization of the N 00 / T 15 – TFE cathode, no particular advantages was found. In fact, the low catalyst utilization found for this cathode limits the cell performance under air and oxygen. Therefore, the utilization of a TFE-treated support in a PTFE-based cathode is not suggested to improve the DMFC performance.

5.5 References

1. **C. Song, P.G. Pickup.** Effect of hot pressing on the performance of direct methanol fuel cells. *Journal of Applied Electrochemistry.* 2004, Vol. 34, p. 1065.

2. **C.Y. Chen, C.S. Tsao.** Characterization of electrode structures and the related performance of direct methanol fuel cells. *International Journal of Hydrogen Energy.* 2006, Vol. 31, p. 391.

3. **T.V. Reshetenko, H.-T. Kim, H.-J. Kweon.** Cathode structure optimization for air-breathing DMFC by application of pore-forming agents. *Journal of Power Sources.* 2007, Vol. 171, p. 433.

4. **C. He, Z. Qi, M. Hollett, A. Kaufman.** An Electrochemical Method to Improve the Performance of Air Cathodes and Methanol Anodes. *Electrochemical and Solid-State Letters.* 2002, Vol. 5, 8, p. A181.

5. **A.S. Aricò, S. Srinivasan, V. Antonucci.** DMFCs: From Fundamental Aspects to Technology Development. *Fuel Cells.* 2001, Vol. 1, 2, p. 133.

6. **A. Di Blasi, V. Baglio, T. Denaro, V. Antonucci, A.S. Aricò.** Optimization of Electrode Properties for Low Temperature DMFC Applications. *Journal of New Materials for Electrochemical Systems.* 2008, Vol. 11, pp. 165-174.

CHAPTER 6 : CONCLUSIONS

This project was focused on studying the flooding of DMFC cathode catalyst layers, in order to improve the water removal from the electrode. To attend this objective different protocols for the investigation of the flooding were explored and it was established a baseline for a future work concerning the preparation of novel cathodes using other co-polymers than Nafion and PTFE.

The partial substitution of Nafion by PTFE and the simultaneous deposition of the two binders with the Pt catalyst were explored as a strategy to improve the water removal, and to guarantee the continuous supply of oxygen to the catalyst sites during the DMFC operation. For this purpose, three series of Pt-based cathodes where I) the relative Nafion and PTFE content was varied between 0 and 15 wt% but the total amount of binder was maintained constant; III) the Pt distribution on a Nafion/PTFE-based cathode was improved; and III) PTFE-based cathodes with distinct morphologies were prepared and characterized by physicochemical, ex-situ electrochemical and fuel cell techniques. The ex-situ electrochemical characterization in 0.5 M sulphuric acid solution was proposed for a pre-screening of the cathodes before their test in fuel cell. This procedure is less-time and materials consuming than in a fuel cell and was thought to be representative of the flooding condition encountered in a fuel cell.

The first part of this work was devoted to the use of the Electrochemical Impedance Spectroscopy technique and fitting procedure to characterize cathodes immersed in the sulphuric acid solution and in direct methanol fuel cell. First, we describe the procedures used in the analysis of the impedance spectra recorded in sulphuric acid solution. For the spectra acquired in nitrogen saturated solution, the Nyquist plot were analysed and elaborated to determine the ionic resistance and double-layer capacitance (1; 2). For the spectra recorded in oxygen saturated solution, the experimental data were fitted with an equivalent circuit built for the determination of the kinetic parameters. The equivalent circuit contained the series resistance for the electrolyte solution, the charge-transfer resistance for the electrochemical oxygen reduction reaction, the constant phase element representing the double-layer capacitance and the finite Warburg element related to the diffusion of the species in the electrode porous structure. The coherence of the results showed that the equivalent circuit was properly built to model our electrochemical system.

Concerning the use of the EIS technique in a DMFC system, an unique and simple method for the analysis of the full DMFC impedance spectra does not exist as yet. The simultaneous and related processes occurring in the system make the investigation of the DMFC not straightforward. Therefore, the objective of our study was to find an easy and not time dispending approach for the investigation of the total DMFC spectra. We proposed the analysis of the impedance spectra of two MEAs built using the same anode and membrane but different cathode, MEA-Pt_3Co/KB and MEA-Pt/KB, but previously studied by us (3). The total impedance spectra were fitted by the modelled equivalent circuits (Figure 6.1) which were built to consider the electrochemical processes occurring at the cathode, the anode and the electrolyte membrane. The results showed that the model used for the fitting properly attributed the cathodic impedance to the semi-circle at low frequencies and the anodic impedance to the semi-circle at high frequencies. The cathodic parameters responded coherently to the variation of cell potential, type of reactant (air/O_2), air flow rate and cathode composition. On the contrary, the anodic parameters did not show significant variation with the operative conditions, as expected from the high fuel stoichiometry used in these experiments (4).

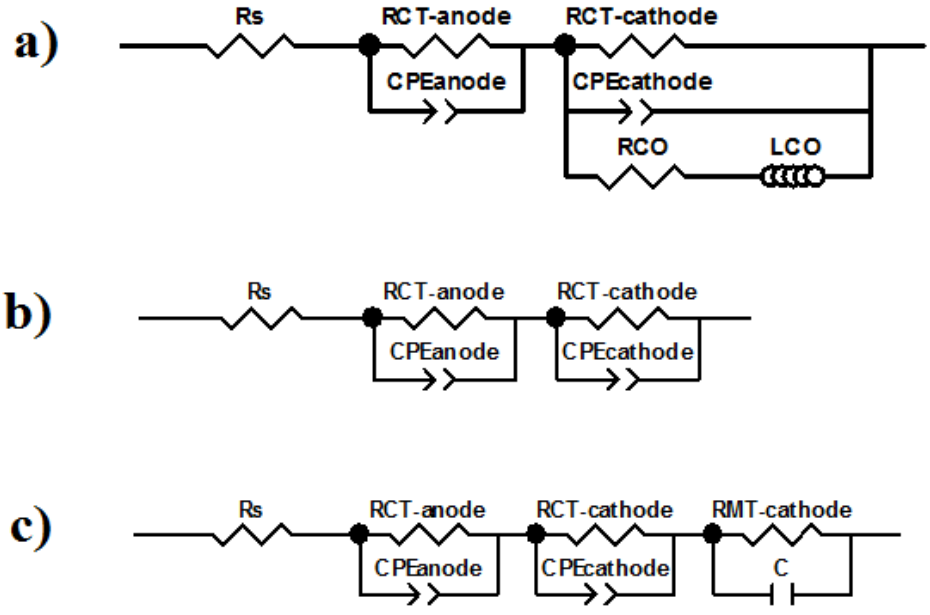

Figure 6.1: Equivalent circuits used to fit the EIS spectra of DMFCs (Chapter 3 - Figure 3.23).

This study was expedient to extend the fitting process to the MEAs that were the specific subject of this thesis and to validate our hypothesis that for these MEAs operated under excess of methanol, the semicircle at low frequency was representative of the cathode behaviour. Therefore, the impedance spectra of two other MEAs, MEA-N15/T00 and MEA-Pt/XC72, were analyzed. The results confirmed that the semicircle appearing in the low frequency region was representative of the cathode behaviour. Indeed the analysis of the Bode plot showed that the cathodic phase-shift maximum responds to the type of reactant (air/oxygen) and to the variation of cell potential, whereas the anodic maximum was unvaried. In addition, this investigation showed as well features in the EIS spectra recorded at low overpotential that might be associated to mass-transport limitations due to the flooding of the cathode catalyst layer.

The second part of this work concerned the investigation of four Nafion/PTFE-based cathodes with relative Nafion and PTFE content varying between 0 and 15 % and named N 15 / T 00, N 10 / T 05, N 05 / T 10, N 00 / T 15. The cathodes were investigated to understand if the simultaneous deposition of the two binders in a specific ratio can improve the performance of the cathodes in terms of flooding. Physicochemical, ex-situ electrochemical and in-situ fuel cell techniques were adopted for the analysis. The physicochemical characterization showed that the partial replacement of Nafion by PTFE in the catalyst layer reduced the hydrophilicity of the cathode (liquid water uptake from 32.46 ± 1.86 wt% for N 15 / T 00 to 16.53 ± 1.46 wt% N 00 / T 15), caused variation in the morphology of the cathode' surface (lower ACA for N 00 / T 15 cathode, 131.67° ± 1.30°) and determined the total pore volume of the cathodes (0.109 cm^3g^{-1} for the N 15 / T 00 and 0.061 cm^3g^{-1} for N 10 / T 05 cathodes). The ex-situ electrochemical characterization showed that the Pt utilization and the capacitance increased with the hydrophilicity of the cathodes and were maximum for the N 15 / T 00 cathode (25.50 ± 0.70 % and 104.00 ± 5.70 $mFcm^{-2}$); however the benefits of including PTFE in the cathode catalyst layer were shown in the lower value of resistance to the proton transport in the catalyst layer and in the higher ORR current density. In this case, higher values were reported for the N 00 / T 15 cathode (5.10 ± 0.10 Ωcm^2 and 38 $mAcm^{-2}$ at 0.2 V). Finally, the electrochemical characterization showed lowest charge-transfer resistance and highest capacitance for the N 10 / T 05 cathode (36.86 ± 0.47 Ωcm^2 and 48.74 ± 0.40 $mFcm^{-2}$). It was suggested that the proper balance between the 10 wt% of Nafion and the 5 wt% of PTFE ensured the proton conductivity in the catalyst layer, the continuous supply of O_2 to the Pt active sites and avoided the early flooding of the

cathode catalyst layer. The DMFC tests at different relative humidity confirmed this hypothesis and showed that the N 10 / T 05 cathode is suitable to work in a low temperature DMFC up to 50 °C without early flooding of the cathode catalyst layer.

The ex-situ characterization (variation of the catalyst utilization, of the ion resistance of the catalyst layer, efficiency of oxygen transport through the catalyst layers) and the DMFC test data shown to be consistent with each other. Therefore it could be concluded that the electrochemical characterization of DMFC cathodes imbibed in H_2SO_4 solution might be a simple and efficient tool to test the potential flooding of the cathodes.

It was observed that the DMFC performance of the N 10 / T 05 cathode could be further improved by optimizing the Pt utilization. Therefore, the Pt distribution was concentrated more on the surface and the performance of a new cathode was investigated. The new cathode, N 10 / T 05 – P showed slightly higher water uptake (27.0 ± 1.5 %), higher wettability of the cathode' surface (ACA 120 °) and larger thickness (502 ± 72 μm). Since the cathode has the same chemical composition of the N 10 / T 05 cathode and no variation was observed in the total micro- and meso-pore volume (0.061 cm^3g^{-1}), it was suspected that the thickness increase should be due to a higher macro-porosity of the cathode catalyst layer. This hypothesis needs however to be verified by Mercury Porosimetry measurements. The DMFC characterization of the MEA containing this cathode showed higher catalyst utilization and performance but also higher probability of flooding when the DMFC was operated at low temperatures (40 and 50 °C). It is well-known that the macro-pores improve the mass transport (5), but, in this cathodic configuration (no GDL) and under these operating conditions (low temperature), it was found that the macro pores behaved as "water basins" and easily accumulated water.

These results suggest that the key to resolve the flooding in low temperature DMFCs lays more in the cathode's porosity than in the hydrophilic/hydrophobic content of the catalyst layer. Therefore, the proper pore dimension can be crucial in the development of anti-flooding cathodes.

The last part of this work concerned a further investigation of PTFE-based cathode. The performance of the MEA containing this cathode was drastically low, especially under air feed. However, the surprising lower resistance to the proton conduction and the higher limiting-current for the oxygen reduction reaction made the N 00 / T 15 cathode an interesting subject for further

studies. Two different approaches were followed aimed at improving the fuel cell performance through enhancing the hydration, the porosity and the Pt utilization of the N 00 / T 15 cathode: optimization of the assembly pressure of the MEA and morphological variations of the N 00 / T 15 cathode.

In the first approach, the assembly pressure was decrease in order to reduce the compression of the cathode during the MEA fabrication and maximize the cathode's available pore volume. Three MEAs were prepared using the following pressure: 500 lbs – 375 lbs – 250 lbs. The DMFC results showed that lower assembly pressure can be beneficial to improve the performance of the N 00 / T 15 cathodes' based MEAs due to an easier diffusion of oxygen and protons through the catalyst layers resulting in higher catalyst utilization at both anode and cathode. Indeed, the best results were reported for the MEA pressed at 375 lbs: higher OCVs in all the range of operating temperature (0.58 – 0.63 – 0.67 V at 40, 60 and 80 °C), higher catalyst utilization in the E-j curves recorded at 40 °C under air and oxygen, superior performance over the entire E-J curve at 60 °C and 80 °C (132 $mAcm^{-2}$ and 151 $mAcm^{-2}$ at 0.1 V). The performance of this MEA was then compared with the one of MEA – N 15 / T 00. Considering that a fuel cell has to operate at high potential (higher efficiency), the comparison was done at 0.4 V. At 40 °C, the MEAs have the same performance (16 $mAcm^{-2}$), however at higher temperature 80 °C, the MEA – N 15 / T 00 performed better (43 vs. 32$mAcm^{-2}$) as expected from the higher hydration of the Nafion-based catalyst layer. It was concluded that the optimization of the assembly pressure is beneficial in improving the catalyst utilization of the N 00 / T 15 cathode; however other approaches were necessary to further improve the performance of the N 00 / T 15 cathode in the high current density region.

In the second approach, the morphology of the N 00 / T 15 cathode was varied by the following treatments: sintering at 350 °C, deposition on a TFE-treated carbon cloth and Nafion coating. The cathodes, named N 00 / T 15 – 350, N 00 / T 15 – TFE and N 00 / T 15 – N 05 were then investigated by physicochemical, ex-situ electrochemical and fuel cell characterization to understand which treatment was beneficial at improving the N 00 / T 15 cathode performance. The physicochemical results showed that there is a positive effect in coating the N 00 / T 15 cathode with Nafion or in using a TFE-treated support for the catalyst layer deposition whereas no particular benefit results from sintering the cathode at 350 °C. Indeed, the water uptake of the N 00 / T 15 – N 05 and N 00 / T 15 – TFE cathodes improved (32.46 ± 1.86 and 20.59 ± 2.31

wt%, respectively), the morphology of the N 00 / T 15 – TFE cathode showed changes and the total micro- and meso-pore volume of the cathodes remains almost unvaried (0.07 - 0.09 cm^3g^{-1}). On the contrary, the sintering process reduced the water capacity of the cathode by 60% and its porosity (0.04 cm^3g^{-1}). From the electrochemical characterization the best results are related to the N 00 / T 15 – N 05 cathode which showed higher Pt utilization (31.70 ± 4.40 %), capacitance (181.50 ± 21.9 $mFcm^{-2}$), ionic resistance (3.20 ± 0.80 Ωcm^2) and current density of the ORR (300 $mAcm^{-2}$ at 0.1 V). However, in the impedance spectra recorded at 0.3 V the cathode showed evidence of diffusion problems at 0.3 V. The DMFC characterization of the MEAs prepared with the optimized pressure 375 lbs showed the replacement of the N 00 / T 15 cathode with the N 00 / T 15 – N 05 cathode allowed a small improvement of the DMFC performance at 40 °C. However, the lack of linearity between the cathode water uptake and the highest current density reached in the polarization curve revealed that the structure of this N 00 / T 15 – N 05 cathode was not optimized. Therefore, a higher and tuned porosity of the cathode catalyst layer is required to take completely advantage of the higher water uptake of this cathode. The use of pore formers can be suggested to improve the porosity of the cathode catalyst layer and their possible application will be evaluated.

Concerning the N 00 / T 15 – TFE cathode, no particular advantages were found. In fact, the low catalyst utilization found for this cathode limited the cell performance under air and oxygen. Therefore, the utilization of a TFE-treated support in a PTFE-based cathode is not suggested to improve the DMFC performance.

6.1. Future work

The results reported in this thesis showed that the preparation of cathodes by partial substitution and simultaneous deposition of Nafion and PTFE binders is a good method to understand which parameters of the DMFC cathode catalyst layer contribute to flooding. Indeed the cathodes prepared by this methodology showed different hydrophilic/hydrophobic degree and morphology. The investigation of these cathodes brought to the conclusion that the key to resolve the flooding in low temperature DMFCs lays more in the cathode porosity than in the hydrophilic/hydrophobic content of the catalyst layer and the proper pore dimension can be substantial in the preparation of anti-flooding cathodes. For the cathodes presented in this work, it is suspected that the macro-pores behaved as “water basins” and are responsible of the water

accumulation. However, as it was mentioned several times in this thesis, the macro-porosity of the cathodes needs to be quantified and the mercury porosimetry technique would be the perfect method of analysis (6; 7; 8).

In this work, the hydrophilic and hydrophobic character of the cathodes was measured by liquid water and hexane absorption and no relevant uptake was observed in the case of hexane. This result suggested that the choice of using a non polar solvent to measure the hydrophobicity of the cathodes was not appropriate. Most probably the high hydrophobicity of the hexane molecule prevented completely the cathode from getting wet. In alternative, the wettability of the cathodes may be study with different polar organic solvents (methanol, 1-butanol, 4-octanol, 1-decanol) and by measurement of internal contact angle which seems to give a better idea of the hydrophilicity of the samples (9).

Finally, for the PTFE-based cathodes presented in the Chapter 5 of this work it is suggested a more detailed investigation of the impedance spectra recorded in N_2 saturated H_2SO_4 solution. Indeed, these cathodes did not show clear evidence of a Warburg diffusion region in the Bode plots of the impedance spectra. This behaviour can be related either to a non homogeneous distribution on the pores in the cathode (1) or to the presence of clogged pores which do not count for the proton diffusion (10); therefore two different models can be taken in consideration for the analysis of the impedance spectra.

Beside to understand which are the causes of water flooding in the DMFC cathode, the partial substitution and simultaneous deposition of Nafion and PTFE binders was meant to improve the water removal from the cathode. The presence of the PTFE binder was found to be beneficial to avoid the water accumulation in the cathode and the N 10 / T 05 cathode was suitable to work in a low temperature DMFC up to 50 °C without evidence of early flooding. However, for optimized Pt distribution and improved DMFC performance higher probability of flooding were reported. These results showed that increasing the hydrophobicity of the cathode catalyst layer is not enough to prevent the water flooding since in this cathodic configuration the macro-pores behaved as water basin. For a better control of catalyst layer morphology, it should be consider the preparation of DMFC cathodes with gas diffusion layers. Indeed, GDL is still the best tool to prevent the water flooding even for low temperature DMFC (10; 11; 12; 13). Since macro-pores

facilitate the mass transport (5), if necessary the porosity of the catalyst layer can be improved by the addition of pore-formers (7).

In this work, the cathodes were prepared by deposition of the catalyst layer on the porous support. This configuration was chosen based on the need to characterize the cathodes ex-situ by physicochemical and electrochemical techniques before the assembly procedure and the DMFC characterization. An extension of this work can take in consideration the preparation of more performing cathodes. In that case, it should be consider the deposition of the catalyst layer directly on the membrane (catalyst coated membrane, CCM), followed by GDL addition. As reported in the literature, CCMs show higher cell open circuit voltages and higher limiting current density compared to the MEAs prepared in the traditional mode (catalyzed diffusion media, CDM) (14).

The third objective of this work was to develop a protocol for the investigation of the flooding of the DMFC cathodes. As reported above, the electrochemical characterization of DMFC cathodes imbibed in H_2SO_4 solution was found to be a simple and efficient tool to pre-screen the cathodes before the fuel cell tests. Though EIS technique was found to be the most useful technique to observe the mass-transport diffusion limitations, steady-state measurements over time on optimized MEAs should be added to the protocol even if they are time consuming. Other in-situ techniques/approaches should be evaluated as well to elaborate a better protocol.

Finally, this work was meant to set a baseline for the preparation of cathodes using other co-polymers than Nafion and PTFE. The specific choice of the hydrophilic/hydrophobic sections of non-fluorinated co-polymers can be the appropriate tool to control and prevent the water flooding of the cathode and at the same time to guarantee the ion conductivity in the catalyst layers. This approach addresses specifically the fabrication of membrane electrode assemblies using novel composite membranes based on zeolites functionalized with sulfonic acid groups and high density polyethylene as polymer binder as the ones developed in our group (16).

6.2. References

1. **E. B. Easton, P. G. Pickup.** An electrochemical impedance spectroscopy study of fuel cell electrodes. *Electrochimica Acta.* 2005, Vol. 50, p. 2469.

2. **M. Lefebvre, Z. Qi, D.Rana, P.G. Pickup.** Chemical Synthesis, Characterization, and Electrochemical Studies of Poly(3,4-ethylenedioxythiophene)/Poly(styrene-4-sulfonate) Composites. *Chemical Materials.* 1999, Vol. 11, pp. 262-268.

3. **S. Siracusano, A. Stassi, V. Baglio, A.S. Aricò, F. Capitanio, A.C. Tavares.** Investigation of carbon-supported Pt and PtCo catalysts for oxygen reduction in direct methanol fuel cells. *Electrochimica Acta.* 2009, Vol. 54, p. 4844.

4. **J. T. Mueller, P. M. Urban, W. F. Hölderich.** Impedance studies on direct methanol fuel cell anodes. *Journal of Power Sources.* 1999, Vol. 84, p. 157.

5. **H.M. Yu, C. Ziegler, M. Oszcipok, M. Zobel, C. Hebling.** Hydrophilicity and hydrophobicity study of catalyst layers in proton exchange membrane fuel cells. *Electrochimica Acta.* 2006, 51, pp. 1199–1207.

6. **J.Xie, K.L. More, T.A. Zawodzinski, W.H. Smith.** Porosimetry of MEAs Made by ''Thin Film Decal'' Method and Its Effect on Performance of PEFCs. *Journal of The Electrochemical Society.* 2004, Vol. 151, 11, pp. A1841-A1846.

7. **T.V. Reshetenko, H.-T. Kim, H.-J. Kweon.** Cathode structure optimization for air-breathing DMFC by application of pore-forming agents. *Journal of Power Sources.* 2007, Vol. 171, p. 433.

8. **X. Zhao, W. Li, Y. Fu, A. Manthiram.** Influence of ionomer content on the proton conduction and oxygen transport in the carbon-supported catalyst layers in DMFC. *International Journal of Hydrogen Energy.* 2012, Vol. 37, pp. 9845-9852.

9. **D.L. Wood III, C. Rulison, R.L. Borup.** Surface properties of PEMFC gas diffusion layers. *Journal of Electrochemical Society.* 2010, Vol. 157, 2, pp. B195-B206.

10. **R. Dugas, A.C. Tavares, D. Guay.** 3D-Percolating Model of Hydrous Ruthenium Oxide Dispersed in an Inert Polymer Matrix: An Impedance Spectroscopy Study. *Journal of Electrochemical Society.* 2012, Vol. 159, 9, pp. F1-F7. in press..

11. **V.B. Oliveira, C.M. Rangel, A.M.F.R. Pinto.** Water management in direct methanol fuel cells. *International Journal of Hydrogen Energy.* 2009, Vol. 34, pp. 8245-8256.

12. **C. Xu, T.S. Zhao, Y.L. He.** Effect of cathode gas diffusion layer on water transport and cell performance in direct methanol fuel cells. *Journal of Power Sources.* 2007, Vol. 171, pp. 268–274.

13. **G.Q. Lu, F.Q. Liu, C.-Y. Wang.** Water Transport Through Nafion 112 Membrane in DMFCs. *Electrochemical and Solid-State Letters.* 2005, Vol. 8, 1, p. A1.

14. **G. Jewett, Z. Guo, A. Faghri.** Water and air management systems for a passive direct methanol fuel cell. *Journal of Power Sources.* 2007, Vol. 168, pp. 434-446.

15. **Zhang, J.** *PEM fuel cell electrocatalysts and catalyst layers: fundamentals and applications.* s.l. : Springers, 2008. p. 895.

16. **Felice, V.** *Novel Silicate-based Membranes for Direct Methanol Fuel Cells.* INRS-EMT. 2010. PhD Thesis.